Wind Tunnel Investigation of the Effects of Surface Porosity and Vertical Tail Placement on Slender Wing Vortex Flow Aerodynamics at Supersonic Speeds

Gary E. Erickson
Langley Research Center, Hampton, Virginia

Since its founding, NASA has been dedicated to the advancement of aeronautics and space science. The NASA Scientific and Technical Information (STI) Program Office plays a key part in helping NASA maintain this important role.

The NASA STI Program Office is operated by Langley Research Center, the lead center for NASA's scientific and technical information. The NASA STI Program Office provides access to the NASA STI Database, the largest collection of aeronautical and space science STI in the world. The Program Office is also NASA's institutional mechanism for disseminating the results of its research and development activities. These results are published by NASA in the NASA STI Report Series, which includes the following report types:

- TECHNICAL PUBLICATION. Reports of completed research or a major significant phase of research that present the results of NASA programs and include extensive data or theoretical analysis. Includes compilations of significant scientific and technical data and information deemed to be of continuing reference value. NASA counterpart of peer-reviewed formal professional papers, but having less stringent limitations on manuscript length and extent of graphic presentations.

- TECHNICAL MEMORANDUM. Scientific and technical findings that are preliminary or of specialized interest, e.g., quick release reports, working papers, and bibliographies that contain minimal annotation. Does not contain extensive analysis.

- CONTRACTOR REPORT. Scientific and technical findings by NASA-sponsored contractors and grantees.

- CONFERENCE PUBLICATION. Collected papers from scientific and technical conferences, symposia, seminars, or other meetings sponsored or co-sponsored by NASA.

- SPECIAL PUBLICATION. Scientific, technical, or historical information from NASA programs, projects, and missions, often concerned with subjects having substantial public interest.

- TECHNICAL TRANSLATION. English-language translations of foreign scientific and technical material pertinent to NASA's mission.

Specialized services that complement the STI Program Office's diverse offerings include creating custom thesauri, building customized databases, organizing and publishing research results ... even providing videos.

For more information about the NASA STI Program Office, see the following:

- Access the NASA STI Program Home Page at *http://www.sti.nasa.gov*

- E-mail your question via the Internet to help@sti.nasa.gov

- Fax your question to the NASA STI Help Desk at (301) 621-0134

- Phone the NASA STI Help Desk at (301) 621-0390

- Write to:
  NASA STI Help Desk
  NASA Center for AeroSpace Information
  7115 Standard Drive
  Hanover, MD 21076-1320

Wind Tunnel Investigation of the Effects of Surface Porosity and Vertical Tail Placement on Slender Wing Vortex Flow Aerodynamics at Supersonic Speeds

Gary E. Erickson
Langley Research Center, Hampton, Virginia

October 2007

Acknowledgments

Table of Contents

This page is left intentionally blank.

Abstract

A wind tunnel experiment was conducted in the NASA Langley Research Center (LaRC) Unitary Plan Wind Tunnel (UPWT) to determine the effects of passive surface porosity and vertical tail placement on vortex flow development and interactions about a general research fighter configuration at supersonic speeds. Optical flow measurement and flow visualization techniques were used that featured pressure sensitive paint (PSP), laser vapor screen (LVS), and schlieren, These techniques were combined with conventional electronically-scanned pressure (ESP) and six-component force and moment measurements to quantify and to visualize the effects of flow-through porosity applied to a wing leading-edge extension (LEX) and the placement of centerline and twin vertical tails on the vortex-dominated flow field of a 65° cropped delta wing model. Test results were obtained at free-stream Mach numbers of 1.6, 1.8, and 2.1 and a Reynolds number per foot of 2.0 million. LEX porosity promoted a wing vortex-dominated flow field as a result of a diffusion and weakening of the LEX vortex. The redistribution of the vortex-induced suction pressures contributed to large nose-down pitching moment increments but did not significantly affect the vortex-induced lift. The trends associated with LEX porosity were unaffected by vertical tail placement. The centerline tail configuration generally provided more stable rolling moments and yawing moments compared to the twin wing-mounted vertical tails. The strength of a complex system of shock waves between the twin tails was reduced by LEX porosity.

Introduction

The control of vortex flows to improve the longitudinal and lateral-directional aerodynamic characteristics is an important design consideration for military and commercial aircraft, missiles, and reusable launch vehicles. Wings, bodies, stabilizing and control surfaces, engine inlets, and surface protuberances are several sources where controlled flow separation in the form of vortices can occur. Furthermore, disorganized and/or unsteady flow separation issues are often addressed by adding devices ranging from small vortex generators to energize the local boundary layer to larger wing leading-edge extensions and strakes to control the global flow field. The aerodynamic benefits of vortex flows can be extended, or undesired effects mitigated, by tailoring the vehicle geometry or incorporating additional passive and active flow control concepts. The vortex flow topology can also be significantly affected by the placement of a vertical tail(s) on the fuselage or wings if the vortices are in proximity to, or directly interact with, the tail surfaces. Passive porosity has been successfully applied to control vortices shed from slender bodies at subsonic through supersonic speeds (reference 1) and to mitigate the adverse effects of shock waves on wings at transonic and supersonic speeds (reference 2). The present experimental investigation focuses on flow-through porosity applied to the leading-edge extension of a 65° cropped delta wing to control the leading-edge vortex development and interactions at supersonic speeds. Figure 1 shows a photograph of the generic fighter model that was used in the current experiment. This configuration was selected since it was representative of fighter aircraft designs with subsonic/transonic maneuver and supersonic cruise capabilities. In addition, it had provision for a centerline tail and twin, wing-mounted vertical tails, which are of interest to this class of fighter aircraft. Porosity was applied to the LEX, since it is situated ahead of the moment reference center (MRC) and generates a strong vortex flow that affects the global wing flow field. Four model configurations were tested

1

and included non-porous (solid) and porous LEX in combination with centerline and wing-mounted vertical tails. This matrix provided a sufficient range of configurations to assess the effects of LEX porosity and any mutual aerodynamic interactions with vertical tail surfaces at supersonic speeds. Emphasis in this report is on the application of PSP, ESP, and strain-gage balance measurement techniques and LVS and schlieren flow visualization methods to identify flow mechanisms and aerodynamic effects of LEX porosity and vertical tail placement. The wind tunnel testing was performed in the NASA LaRC UPWT Test Section 1 at free-stream Mach numbers of 1.6, 1.8, and 2.1, which are representative supersonic cruise Mach numbers. The test results that are presented in this report were obtained at a fixed Reynolds number per foot of 2.0 million at selected angles of attack and sideslip.

Nomenclature

AMS	angle measurement system
AVI	audio video interleave
b	span distance, inches (in.)
b_w	reference span, 18.726 in.
B.L.	model butt line, in.
BMC	balance moment center, M.S. 21.475
c	chord length, in. (also $c_{r,w}$)
$c_{r,w}$	wing centerline chord, 23.622 in.
$\overline{c}_w$	mean aerodynamic chord, 16.056 in.
C_A	axial force coefficient, $\dfrac{Axial\ Force}{q_\infty (S_w)}$
C_D	drag force coefficient, $\dfrac{Drag}{q_\infty (S_w)}$
C_l	rolling moment coefficient, $\dfrac{Rolling\ Moment}{q_\infty (S_w) b_w}$

C_L	lift coefficient, $\dfrac{Lift\ Force}{q_\infty (S_w)}$
C_m	pitching moment coefficient, $\dfrac{Pitching\ Moment}{q_\infty (S_w) c_{r,w}}$
C_n	yawing moment coefficient, $\dfrac{Yawing\ Moment}{q_\infty (S_w) b_w}$
C_N	normal force coefficient, $\dfrac{Normal\ Force}{q_\infty (S_w)}$
C_Y	side force coefficient, $\dfrac{Side\ Force}{q_\infty (S_w)}$
C_p	static pressure coefficient, $(p - p_\infty)/q_\infty$
CP	surface static pressure coefficient from PSP processing software
$C_{p,u}$	upper surface static pressure coefficient
$C_{p,v}$	vacuum pressure coefficient, $-2/\gamma M_\infty^2$
$C_{p(PSP)}$	PSP pressure coefficient
$\hat{C}_p$	estimated mean value of the pressure coefficient
$\widehat{C}_{p(PSP)_h}$	point estimate of the mean pressure coefficient response at a selected PSP pixel location
CCD	charge coupled device
CCU	camera control unit
C.L.	confidence limit
ΔC_p	differential pressure coefficient
delcm	delta pitching moment coefficient due to flow angle
Dewpt	dewpoint, degrees Fahrenheit (°F)
ESP	electronically-scanned pressure

ESP_i	pressure measurement at i^{th} orifice		S_w	reference wing area, 254.3553 sq. in.
I/I_o	PSP intensity ratio		$SCSI$	Small Computer Systems Interface
$\overline{I/I_o}$	PSP intensity ratio averaged over all N pixels		*thetaf*	flow angle, deg
$l_{0.25\overline{c}}$	tail length, distance between 25% tail mean aerodynamic chord to MRC, in.		$t(1-\alpha_S/2)$	critical value from the Student-t distribution
KPG	known pressure generator		T_0	stagnation temperature, ^oF
LEX	leading-edge extension		UV	ultraviolet
LVS	laser vapor screen		V	vertical tail volume, cubic inches (cu. in.)
M_∞	free-stream Mach number		$W.L..$	model water line, in.
MRC	moment reference center, M.S. 21.144		x	local axial distance measured along the wing centerline chord from the wing apex, in.
$M.S.$	model station, in.		y	local semispan distance measured from the wing centerline, positive to the right, in.
MSE	mean square error			
N	number of ESP taps			
$NTSC$	National Television System Committee		$\overline{y}$	span location of mean aerodynamic chord, in.
p	local static pressure, pounds per square foot (psf)		α	angle of attack, degrees
p_0	stagnation pressure, psf		α_s	level of statistical significance
p_∞	free-stream static pressure, psf		ε	mean relative error, percent
$psfa$	pounds per square foot absolute		λ	taper ratio
$psia$	pounds per square inch absolute		γ	ratio of specific heats
$psid$	pounds per square inch differential		Λ_{LE}	leading-edge sweep angle, deg
Δp	differential pressure, psf		Λ_{TE}	trailing-edge sweep angle, deg
PCU	pressure calibration unit			
PRT	platinum resistance temperature			
PSP	pressure-sensitive paint			
PSP_i	pressure measurement at PSP pixel location corresponding to i^{th} ESP calibration orifice			
q_∞	free stream dynamic pressure, psf			
Re	Reynolds number, millions per foot			
$RMSE$	Root mean square error			
s	local semispan measured from the wing centerline to the leading edge, in.			
$s.d.$	standard deviation			
S	reference area, square inches (sq. in.)			

Subscripts

cl	centerline
lex	leading-edge extension
r	root
t	tip
tw	twin
w	wing

Model Description and Test Apparatus

A generic fighter model featuring a 65-degree cropped delta wing with sharp leading edges was used in this test. The model was designed and fabricated in the 1980's for surface

pressure and force and moment testing in subsonic, transonic, and supersonic wind tunnel facilities in support of a multi-national Euler code validation program (reference 3) that focused on the prediction of vortex flow effects on slender wings at high angles of attack. The wing had an NACA 64A005 airfoil section from the 40-percent chord station to the trailing edge. A sharp leading edge was obtained by fairing a biconvex circular-arc section into the NACA profile from the 40-percent chord station to the wing leading edge. The wing was mounted in a high position on a fuselage that served as a housing for balance and pressure instrumentation. Although not part of the current experiment, it was possible to test the model in a wing-alone configuration. This was the primary configuration of interest in the Euler code validation program summarized in reference 3. In this case, the fuselage tapered down to a small radius along approximately the forward 35-percent portion of its length, and it terminated 0.50 inches (model scale) from the apex of the wing. This portion of the fuselage could be replaced with an alternate forward fuselage section having an integral strut, or "gooseneck." The model as designed in the 1980's included the installation of a canard to the gooseneck to provide a closely-coupled canard-wing arrangement. Modifications were made to the model in more recent years to include a wing leading-edge extension (LEX) mounted to the gooseneck, a centerline vertical tail on the fuselage, and twin vertical tails on the wings. A flat-plate, 0.25-inch thick LEX having a $65^{o}/90^{o}$ planform and symmetrically-beveled leading edges was fabricated for the investigation described in this report. The exposed area of the LEX (left and right sides) was 15% of the reference wing area. The LEX incorporated a pattern of 0.050-inch diameter through holes spaced 0.10 inch apart on center to provide a total porosity level of 14.75% relative to the LEX exposed area. The fuselage and wings were modified with pockets to allow the installation of a centerline vertical tail or twin vertical tails with integral mounting pads. The model with porous LEX, wing, and twin wing-mounted vertical tails is shown installed in Test

Section 1 of the NASA LaRC UPWT in figure 1. A close-up view of the porous LEX is presented in figure 2. Note that the bevels along the LEX leading and side edges were not porous because of constraints in the machining process that precluded drilling holes near the edges. In addition, a 0.625-inch wide strip along the centerline of the LEX was solid, since the LEX was bolted to the gooseneck in this region. Similarly, a 0.75-inch wide strip along each trailing edge of the LEX was solid where the LEX overlapped the wing leading edge in a tongue-and-groove arrangement. The same LEX was tested with 0% porosity (solid LEX) by applying sealing tape having 1.8 mil thickness (0.0018 inches) along the lower surface to cover all of the through holes. The white strips along the juncture of the wing and LEX in figure 1 correspond to plaster which was used to provide a smooth transition between the two components. The size and positioning of the centerline and twin vertical tails were selected to provide approximately the same tail volume, which is the product of the total exposed tail area and the distance from the moment reference center (MRC) to the 25% mean aerodynamic chord location of the tail. Planview and sideview sketches of the wing, LEX, fuselage, and tails are provided in figures 3-5. Geometric details of the model are summarized in table I.

The right wing upper surface was instrumented with a total of forty five (45) 0.020-inch diameter pressure orifices distributed in three spanwise rows. The pressure rows were located at 30%, 60%, and 80% of the distance, x, along the wing centerline chord, $c_{r,w}$, measured from the apex of the wing ($x/c_{r,w}$ = 0.30, 0.60, and 0.80, respectively). Sketches of the pressure orifice layout are shown in figures 3 and 6, and the pressure orifice locations are listed in table II. The orifice nondimensional semispan location, y/s, is expressed in terms of the semispan distance, y, measured from the wing centerline divided by the wing local semispan, s. Consequently, y/s values of 0.0 and 1.0 correspond to the wing centerline and the right wing leading edge,

4

respectively. There were 13 orifices at $x/c_{r,w}$ = 0.30, 17 orifices at $x/c_{r,w}$ = 0.60, and 15 orifices at $x/c_{r,w}$ = 0.80. The distribution of taps in each row was intended to capture the pressure signature of a leading-edge vortex at high angles of attack. Cross sections of the wing at the three pressure measurement stations are sketched in figure 7. The pressures were measured using a single 48-port, 10 psid ESP module located inside the model as shown in figures 3-5. The ESP module featured a purge air option that was used to prevent contamination of the pressure orifices during the application of pressure sensitive paint (PSP) to the wing upper surface. The 0.040-inch outer diameter (O.D.) stainless steel pressure lines inside the model were connected to the ESP module using 0.040-inch O.D. urethane jumpers. Two thermocouple wires were attached to the sides of the ESP module to monitor the module surface temperature. The ESP electronics cable, reference and calibration pressure lines, purge air lines, and thermocouple wires were routed through channels machined into the internal balance strongback and then out along the model sting. The instrumentation bundle was then encased in a protective conduit that extended from the model support system to the test cell region outside the test section.

The model forces and moments were measured using an internally-mounted, six-component strain gage balance designated UT-52A. Sketches of the balance inside the model are shown in figures 4 and 5. The balance incorporated three platinum resistance temperature (PRT) devices to monitor the temperatures in the forward, center, and rear sections of the balance. The balance and PRT wiring were routed internally to the sting as illustrated in figure 8. The balance moment center (BMC) was located at model station (M.S.) 21.475 which corresponded to approximately 58.4% of the distance along the wing centerline chord measured from the apex ($x/c_{r,w}$ = 0.584). The MRC was taken about the 57% centerline chord location ($x/c_{r,w}$ = 0.57) or M. S. 21.144 as shown in figures 3-5. The force

and moment coefficients for all configurations were based on the reference wing area, S_w.

Two diagonally-opposed 0.060-inch O.D. stainless steel tubes were run along the sting and extended approximately 2.5 inches inside the model fuselage cavity to measure the chamber pressures using 5 psid Druck transducers located outside the test section. The tubes were run underneath a model fouling strip on the sting as shown in figure 8. A non-conductive layer of tape was applied between the pressure tubes and the fouling strip tape.

The sting served a dual role of providing an internal passageway for the balance and PRT wiring bundle and adapting the model and balance assembly to the tunnel support hardware. The sting featured a cylindrical aft end, which was a sliding slip fit to the UPWT roll coupling. The sting was affixed to the roll coupling with two set screws that pressed against dimples machined into the sting aft end. The roll coupling was installed to the UPWT standard articulated pitch mechanism. Figure 9 shows a sketch of the overall installation of the model, balance, sting, and main support system hardware which was attached to a horizontal blade strut spanning the width of the test section. The axial position of the model in the test section was adjusted during the installation process by translating the horizontal blade strut. The strut position was fixed when the model was judged to be in a position for satisfactory viewing of schlieren flow visualization patterns throughout the desired range of angle of attack. The vertical bars in the sketch in figure 9 are structural support bars in the test section side walls which partitioned several 1.5-inch thick windows constructed of optical quality glass.

Transition grit was not applied to the model, since the flow was assumed to separate at the sharp leading edges at all conditions of interest in the current experiment. In addition, a suitable gritting strategy based on the criteria in reference 4 to cause transition of the boundary layer associated with vortex-induced reattached flow on the wing upper surface has not been

established. Reference 5 summarizes many of the challenges associated with transition grit applications for high angle-of-attack experimentation.

Wind Tunnel Facility and Test Conditions

The wind tunnel test was conducted in the NASA LaRC UPWT, which is a continuous-flow, variable pressure supersonic wind tunnel. The tunnel contains two test sections which are approximately 4 feet square and 7 feet long. Each test section encompasses only part of the Mach number range of the tunnel. The nozzle ahead of each test section consists of an asymmetric sliding block which allows continuous Mach number variation during tunnel operations from 1.5 to 2.86 in the low Mach number test section and 2.3 to 4.63 in the high Mach number test section. A complete description of the facility along with test section calibration information is contained in reference 6.

The experiment was performed in UPWT Test Section 1 and was designated Test 1958. Table III shows the average free stream conditions in Test 1958. Testing was performed from M_∞ = 1.6 to 2.1 at a constant Reynolds number per foot of 2.0 million. The tolerances for the tunnel condition setpoints for the total pressure and temperature were typically +/-2 pounds per square foot absolute (psfa) and +/-2 degrees Fahrenheit (°F), respectively. The tunnel air dew point was maintained at sufficient levels to minimize water vapor condensation effects during all phases of the test. The dewpoint setpoints for each Mach number are also tabulated in table III. The tolerance for the dewpoint setpoint was +0 °F to any value less than the setpoint. The automated tunnel controls system allowed data acquisition only when the total pressure, temperature, and dewpoint were simultaneously within tolerances.

The testing was performed in multiple phases to accommodate several test techniques used in Test 1958. Phase I focused on the acquisition of

PSP images on the model with solid LEX and porous LEX and with centerline and twin vertical tails. Figures 10 and 11 show the porous LEX model with centerline and twin vertical tails, respectively, and PSP coating applied to the wing upper surface. The Experimental Techniques section of this report provides details of the PSP technique. The model was rolled +90 degrees to a wings-vertical orientation for the PSP testing, since the optical access was from the test section side wall. PSP images were obtained at angles of attack of 2, 4, 6, and 8 degrees. The maximum angle of attack was approximately 8 degrees in this roll orientation, since angle of attack was varied using a twin-screw arrangement on the main support system horizontal blade strut. This mechanism is typically used to vary the yaw angle when the model is in a wings-level orientation. Electronically-scanned pressures were also obtained to perform in-situ calibrations of the PSP. Six-component force and moment measurements were acquired and were used to estimate the model, balance, and sting assembly deflections due to aerodynamic loading. The PSP testing was performed at free-stream Mach numbers of 1.6 and 2.1 at a Reynolds number per foot, Re, of 2.0 million and a stagnation temperature, T_o, of 125 °F. The model angle of attack and angle of sideslip were determined via appropriate Euler angle transformations using the output from an accelerometer mounted in a protective housing on the knuckle component of the model support system, the output (in counts) from the twin-screw mechanism, the potentiometer output from a mechanized roll coupling, balance-to-support system and balance-to-model misalignment angles, and corrections applied to account for aeroelastic or mechanical deflections of the model, balance, and sting assembly due to aerodynamic loads.

Phase II consisted of laser vapor screen (LVS) flow visualization. The model was in an upright orientation for this phase of testing. In this phase, the dewpoint was allowed to vary in order to promote condensation in the test section. LVS flow visualization was conducted on the model with solid and porous LEX and centerline vertical tail and with the solid LEX

and twin vertical tails. Video and still images of the LVS cross-flow patterns were obtained at selected angles of attack and model stations at M_∞ = 1.6, 1.8, and 2.1. The LVS images were useful in the interpretation of the PSP and ESP upper surface static pressure distributions. A more detailed description of the UPWT LVS system is provided in the Experimental Techniques section.

Schlieren flow visualization was obtained with the model in the upright orientation in Phase III. The acquisition of schlieren and LVS images was mutually exclusive, which required separate phases for each technique. Schlieren video and digital images were acquired at M_∞ = 1.6, 1.8, and 2.1 at selected angles of attack for the model with solid and porous LEX and centerline and twin vertical tails. The UPWT schlieren system is described in more detail in the Experimental Techniques section.

Dedicated ESP and six-component force and moment measurements were obtained on the unpainted model in the upright orientation in Phase IV. Data were acquired at M_∞ = 1.6, 1.8, and 2.1. The angle of attack was varied from -4 degrees to +12 degrees at M_∞ = 1.6 and from -4 degrees to +22 degrees at M_∞ = 1.8 and 2.1. Sideslip sweeps were also conducted at an angle of attack of 10°. Angle of attack sweeps were performed at sideslip angles of 0 degrees and +4 degrees. The Experimental Techniques section describes the ESP and force and moment measurement techniques.

Experimental Techniques

Pressure-Sensitive Paint Technique

PSP is a global surface static pressure measurement technique. The key elements of a PSP system include photoluminescent material in the form of a paint applied to the test article, illumination source to excite the paint, imaging device to document the paint in the excited state, and a data acquisition and processing system. A PSP system based on the work described in reference 7 has been in use at UPWT since 1996. Descriptions of the primary components and their practical applications at UPWT are described in this section.

The PSP method is based on the oxygen-quenching characteristics of certain luminescent materials. The emitted light intensity varies inversely with the local oxygen partial pressure and, therefore, the air pressure, since oxygen is a fixed mole fraction of air. A PSP formulation typically consists of three components. The luminescent material (luminophore) is the sensor component. For oxygen quenching to occur, the luminophore must be soluble in a suitable binder material. Finally, a compatible solvent is used for the application of the paint, via a spray gun, to the test article. Prior to the paint application, the model surface is primed with white paint. The white undercoat to the PSP coating serves a critical function in that it amplifies the PSP emission signal (reference 8). Certain characteristics of PSP coatings induce measurement error: photodegradation and temperature sensitivity. Specifically, the emission response of the PSP decreases with time of exposure to the excitation radiation, and the luminescence intensity is sensitive to changes in the temperature. An earlier formulation successfully applied at UPWT was designated IEMA/PtT(PFP)P which used a proprietary University of Washington copolymer. Laboratory calibrations at NASA LaRC indicated that the relationship between the PSP intensity ratio and the pressure ratio was linear over a wide range of pressures. This linear relationship is referred to as the Stern-Volmer equation (reference 9). The laboratory calibrations also showed that photodegradation was reduced compared to prior-generation paints used at UPWT. Consequently, this was a robust and responsive formulation at the low static pressures typical of the supersonic testing at UPWT. Poly-2,2,2-trifluoroethylmethacrylate-co-isobutlymethacrylate (FEM) and platinum tetra (pentafluorphenyl) porphyrin, PtT(PFP)P, applied to a Prime'N Seal base coat was used in the UPWT testing discussed in this report. Reference 10 describes more recent PSP applications that include dual luminophores and

uni-coat PSP chemistries that do not require the acquisition of wind-off reference images or the application of a base coat to the model surface.

The intensity of the light emitted by PSP is proportional to the excitation light that is absorbed. A stable illumination source must be used that is tailored to the absorption wavelength band of the PSP coating. Ultraviolet long wave (365 nanometer (nm)), 250-watt lamps connected to a regulated power supply were used in continuous mode to provide the illumination source in the UPWT system. The optical filters attached to these lamps allowed passage of light at the absorption wavelength of the coating but prevented transmission of light at the luminescence wavelengths that could compromise the images acquired by the PSP cameras.

Electronic CCD imaging devices of two types were used: conventional video and scientific grade digital cameras. The original PSP system upon which the UPWT system was developed (reference 7) featured an 8-bit resolution image acquisition and processing system using standard NTSC format video cameras. These cameras were used in UPWT Test 1958 as monitoring devices only, since they had the advantage of providing real-time viewing of the PSP response to aerodynamic flow changes. Scientific-grade, thermoelectrically-cooled digital cameras connected to a regulated power source were used exclusively for PSP image acquisition because of their low noise, excellent linear response, and good signal-to-noise ratio. These cameras acquired an electronic snapshot only, and the exposure or integration time was set from the host computer. Cooled CCD digital cameras of 12-bit and 14-bit resolution and 1280 x 1024 and 1024 x 1024 pixel arrays were used. Each camera was commanded to acquire an image with the lens closed in order to acquire a "dark image". A dark-level correction was applied to all wind-off and wind-on images to subtract out the CCD dark current and noise of the overall imaging system. Optical filters centered about 650 nm were installed on the conventional video

and scientific-grade digital cameras to permit the passage of the luminescence emission wavelengths, while preventing the transmission of the excitation light source wavelengths to the acquisition cameras. The incursion of extraneous sources of light from the test cell area into the test section was prevented by sealing the sidewall access doors with coverings and enclosures.

Acquisition of the PSP images was controlled by UNIX- and PC-based workstations in the UPWT Data Room. The cable run length between the host computers and the cameras installed in the test cell was approximately 125 feet. The 12-bit, 1280 x 1028 pixel array digital camera and its electronic camera control unit (CCU) were interfaced to a UNIX workstation via a 200-foot fiber optic-based, Small Computer Systems Interface (SCSI) bus extender system. The 14-bit, 1024 x 1024 pixel array camera and its CCU were connected to a proprietary PCI-based image acquisition board installed in the PC via a custom electronics cable. Image acquisition on the UNIX system was performed using a NASA LaRC-developed program that allowed user control of the camera integration time and camera gain, and determined the minimum, maximum, and average pixel intensity values for the most recently-acquired image. The proprietary image acquisition software on the PC provided a more full-featured suite of utilities to evaluate the characteristics of an acquired image. However, the time-critical nature associated with the acquisition of production images during the testing typically precluded the use of anything but the most basic features. Images were stored on high-capacity disk arrays for off-line processing and archiving. Image processing was performed exclusively on a UNIX workstation using the software package described in reference 11 and referred to as PAINTCP. This software package is one of several PSP processing tools in use by the technical community (see reference 12, for example), and it has been successfully applied at UPWT since 1996.

Optical access to both test sections of UPWT was provided by two doors that formed the sidewalls of the test sections. Each of the test section doors featured nine 5.5-in. by 48-in. windows, separated by 1.25-in solid webs. The windows were 1.5-in thick glass of optical quality to provide minimum distortion for schlieren and other flow visualization methods. There was no optical access to the test section from the ceiling. The test section was isolated from extraneous light sources by the installation of a wooden panel on one door and a wooden enclosure on the other door, which provided sufficient volume to set up and access a large array of cameras and lights. The test section layout offered both advantages and disadvantages to the implementation of the PSP technique. The primary advantages were the ease with which cameras and lights could be attached to the webbing. In addition, all instrumentation was located in ambient conditions, which eliminated the need for special pressure- and thermally-controlled enclosures for the imaging and illumination hardware. The test section and equipment were very accessible during tunnel operation, which allowed regular system checks, close-up viewing of the paint status and its real-time response to pressure-field changes, and manual shuttering of the UV lights, as necessary. The primary disadvantages were the proximity of the cameras and lamps to the model and the optical quality glass, which affected the field of view, limited the positioning of cameras and lights relative to the model and to each other, increased the susceptibility to the adverse effects of reflections from the windows, raised concerns regarding thermal effects induced by the UV lamps on the glass, increased the effects of model dynamics on image quality, and amplified the effects of small spatial differences between the wind-off and wind-on images. In addition, the sidewall optical access required the model to be rolled 90 degrees to a wings-vertical position. As discussed in the previous section, the model angle of attack was then obtained by the twin-screw arrangement on the horizontal strut that was normally used to vary the yaw angle. As a result, the angle of attack was limited to a maximum of approximately +8 degrees. The model support system was translated off-center (away from the camera) by about 4 inches to maintain field of view and focus at the higher angles of attack.

The installation of the PSP cameras and UV lamps for Test 1958 is shown in figure 12. The camera locations, pointing angles, and lenses were chosen to maximize the viewing area of the right-hand, pressure-instrumented wing to which the PSP coating was applied, while striving to avoid undesired reflections from the optical glass. The light sources were carefully selected and positioned to reduce the nonuniformity of illumination at the model. This procedure involved the activation of two lamps and a survey of the illumination source intensity at the model for a range of angle of attack. A hand-held digital long-wave radiometer was used to acquire local measurements and to guide the camera installation. A reading of approximately 300 microwatts per square centimeter (μW/cm^2) at the model was used as a general guideline based on previous experience. Consistent readings in the 400 to 500 μW/cm^2 range were avoided due to concerns with more rapid and nonuniform photodegradation. The mutual proximity of the cameras and lamps raised the concern of electromagnetic interference that could damage the sensitive electronic components in the digital cameras. This might occur as the result of inadvertent power cycling of the UV lamps while the cameras were operational. The webbing of the test section door afforded some protection, but this was augmented by the placement of metal shields between the cameras and lamps.

The paint application and curing process required one or more shifts to complete. This operation required a skilled painter equipped with protective gear, including full face mask and a continuous air supply. The run schedule was tailored, whenever possible, to conduct the painting after operating hours to avoid the resultant facility down time. The model was cleaned with solvents, and all model components except the region of interest were masked off. The 45 discrete surface static pressure orifices

on the right wing were plumbed to an internal ESP module with purge air capability. The purge air pressure was applied and adjusted to provide adequate flow through all pressure lines to avoid contamination of the orifices during the paint application while avoiding local mounding around the holes caused by excessive, jet-like flow. This was the desired effect but rarely achievable because of different flow rates through the individual pressure lines. Approximately 4 hours were required for the curing of the base coat, and a comparable period of time was allotted after the PSP coating was applied. The PSP image registration process required reference marks, or control points, to be placed on the model. The locations of these registration marks were defined by placing a Mylar transfer sheet containing a 1:1 scale drawing of the wing with pre-punched holes on the fully-cured PSP coating. After the hole centers were marked, the Mylar template was removed and black dots were drawn on the model using a plastic circle template and marker pen. Latex gloves were worn during this process to avoid contamination of the PSP coating. A final step prior to securing the test section for operation was to clean the test section windows and to confirm that the transmission and absorption filters on the PSP light sources and cameras were free of contaminants.

Wind-off images were acquired at several angles of attack with the test section evacuated to low pressures, typically 200 psfa (1.389 psia) to 400 psfa (2.778 psia). This pumpdown condition was more representative of the static pressure levels that existed on the painted wing during wind-on runs, and it provided an opportunity to define the digital camera integration times that were used throughout the testing. In general, a range of integration time was determined from the wind-off run such that the maximum pixel intensity was approximately 60-70 percent of the saturation level of the camera. This approach provided a buffer against saturation during the wind-on runs where lower static pressures occurring locally on portions of the wing promoted even higher pixel intensities at the same integration times. Integration times

of 500 milliseconds (msec) to 1500 msec were typical. The longer integration time was not a problem, since model dynamics were not an issue in UPWT Test 1958. Wind-off images were acquired in smaller angle-of-attack increments to provide a better range of available reference images that were spatially aligned with the wind-on images. For example, depending on the aerodynamic loads on the model, a wind-off image acquired at $\alpha = 7.5^{\circ}$ was more spatially aligned with a wind-on image acquired at $\alpha = 8.0^{\circ}$.

Wind-on data acquisition consisted of the discrete pressures measured from the ESP taps and the PSP images at the desired angles of attack. Full on-line calibrations of the ESP modules were performed to ensure they met the instrumentation performance criteria discussed in a following section, since the acquisition of high-quality ESP data was essential to the in-situ PSP calibration performed during the off-line image processing. The PSP illumination source was shielded during all transitional phases of tunnel operation (tunnel start-up and shutdown, Mach number changes, ESP calibrations) in order to reduce the overall exposure time of the PSP coating. The PSP image acquisition was performed independently of the data acquisition performed by the wind tunnel host computer. The test conditions, ESP data, and other parameters were obtained off-line for use in input files required by the PSP image processing software. The wind-on, real-time response of the PSP was observed and recorded using the 8-bit video camera mounted in the test section door webbing. The signatures of particularly strong flow-field features such as shock waves and vortices were clearly visible in the video display. A repeat set of wind-off images and dark images were acquired after the wind-on runs. Comparisons of the initial and final wind-off pixel intensities at the same camera integration times provided an indication of the level of photodegradation that had occurred. In some cases, the final wind-off images were used in the image processing, since they were acquired closer in time to the wind-on images that were being processed.

The image processing method features the subtraction of the dark image from the wind-off and wind-on images, identification of wind-off and wind-on control points, image registration, image ratioing, resection transform, and global calibration of the paint. Registration, or spatial alignment, of the two model images was performed to correct for nonalignment caused by model motion and/or deformation. A second-order biquadratic transform was used to align the wind-on image with the wind-off image. This process depended on finding the respective control points, or registration marks, which were used to determine the transform coefficients. The wind-off and wind-on intensity field images were ratioed, and the intensity field of the resultant image was proportional to pressure (Stern-Volmer relation). Note that the image ratioing process was effective in factoring out the effects of spatial nonuniformities in the light source intensity and PSP coating thickness. A resection transform based on photogrammetry techniques was performed next, which related each point in the final intensity ratio image plane to a corresponding point on the model surface. The effectiveness of this transform depended on an accurate determination of the spatial locations of the model registration marks. The image mapping in UPWT Test 1958 was exclusively a two-dimensional (2-D) plane view representation of the wing. Quantification of the pressure field in the final intensity ratio image required a calibration of the paint to determine the Stern-Volmer sensitivity coefficients. This was accomplished using an in-situ calibration method. In this method, the paint intensity was calibrated from the ESP pressure tap data at spatially corresponding locations. The in-situ calibration process was iterative, since the first pass through the calibration rarely provided a completely satisfactory global match between the ESP and PSP pressure data. In practice, the paint cannot be calibrated at the exact location of the pressure orifice. This required that the PSP image pixel locations used for calibration be slightly offset from the orifices. In some cases, additional offsets were necessary since the purge air flow during the painting process was excessive and local mounding of the paint occurred about the orifice.

Laser Vapor Screen Technique

The vapor screen technique was used in UPWT Test 1958 to visualize the cross-flow patterns about the porous LEX model at supersonic speeds. This technique has been used at UPWT for many years, and reference 13 provides a detailed account of the system currently in use at this facility.

Water was injected into the tunnel circuit in a controlled manner and in sufficient quantity to promote condensation and the formation of a thin, uniformly distributed fog in the test section. The cross-flow patterns were illuminated by an intense sheet of light produced by an argon-ion laser. The presence of the model in the flow field altered the uniform distribution of fog and, consequently, the degree of illumination. Several flow features were manifested in the LVS images. The change in flow density through oblique shock waves resulted in a similar change in fog density so that shock positions and shapes were clearly defined. Separated flows such as wakes, vortex feeding sheets, and vortex core regions appeared dark or transparent, since condensate did not appear to be convected across the shear lines.

The laser system consisted of a laser head and power supply and fiber optic components that refocused and directed the laser beam to an optics package to generate a thin sheet of light of controllable thickness and spread angle (reference 14). The light sheet optical package was secured to the test section side wall and remained fixed during the flow visualization runs. The flow patterns at different model longitudinal stations were observed by forward and aft traversal of the model support mechanism. A flat paint was uniformly applied to the model and sting to reduce the flare when the laser light impinged on the metal surfaces. Proper control of the water injection allowed extended vapor screen runs for ranges of angle of attack and Mach number.

Observation and documentation of the flow patterns were accomplished with a 70mm Hasselblad film camera and a miniature black-and-white video camera with 360 television lines of horizontal resolution and fixed focal length lens. Both cameras were mounted in the test section in protective enclosures. The real-time output from the miniature video camera was routed to videocassette recorder. This camera provided a perspective aft of the model which looked upstream parallel to the model centerline. The video image perspective remained constant throughout the pitch angle range because there was little relative motion between the camera and the model. Selected portions of the videocassette recording were digitized and converted to AVI format using a video frame grabber installed in a personal computer. The frame grabber software allowed the capture and limited enhancement of individual LVS video frames that appear in this report along with selected images obtained from the Hasselblad camera.

Schlieren Technique

The UPWT schlieren system provides a two-dimensional image of the density gradients in a three-dimensional flow field, since this method is related to light refraction along the entire optical path. Each test section at UPWT is equipped with a single-pass, off-axis schlieren system in a Z-layout similar to that described in reference 15. The light source passes through the test gas only once (hence, single-pass), and large spherical mirrors are used in this system in order to provide a 49-inch field of view. The complete system consists of a light source, two spherical mirrors, knife-edge, optical beam splitter, still camera, flat mirror, video camera, and image screen. The entire system is supported from a beam as a unit and can be positioned along the longitudinal axis of the test section to provide schlieren images of any part of the test section. The light source is provided by a xenon vapor arc lamp that is operated continuously. An optical beam splitter is located just behind the knife edge and is used to provide a schlieren image for still and video cameras. A

more detailed description of the UPWT schlieren system is provided in reference 13.

Still photographic images were acquired using a 70mm Hasselblad camera. Output from the video camera was supplied to a videocassette recorder. Selected portions of the videocassette recording were digitized and converted to AVI format using a video frame grabber installed in a personal computer. In a manner similar to the LVS image processing, the frame grabber software allowed the capture and limited enhancement of individual schlieren video frames that appear in this report. The schlieren system revealed the shock waves generated from the LEX, wings, and tails. In addition, the vortex flows shed from these surfaces often induced sufficiently large density gradients that the vortex paths were visible. The results presented in this paper correspond to the solid and porous LEX with twin vertical tails at M_∞ = 1.6, 1.8, and 2.1 and selected angles of attack.

ESP Measurements

Surface static pressure measurements were obtained at 45 discrete locations on the model using a single, internally-mounted 48-port ESP module. The UPWT ESP system features System 8400 data acquisition instrumentation manufactured by Pressure Systems, Incorporated (PSI). The System 8400 is interfaced with the wind tunnel data acquisition system, and uses external modules or modules mounted internally to the model. The internal volume of the porous LEX model was sufficient to contain a single 10 psid ESP model with purge air capability. A 15 psia pressure calibration unit (PCU) was used in this experiment with a digitally-controlled pneumatic source that provided valve control and generated calibration pressures for the ESP scanner. Calibration pressure accuracy specified by the manufacturer was +/-0.02% full-scale (F.S.). The ESP module pressure range was selected on the basis of prior supersonic testing of this model with solid LEX (reference 16). The manufacturer-specified uncertainty as a percent of full-scale was +/-0.1% (95% confidence limits (C.L.)) for the 10 psid module.

The uncertainties for this module expressed in terms of the static pressure coefficient for the test conditions that were run in the UPWT Test 1958 are listed in table IV. The differential ESP module was used in absolute mode by evacuating the reference side of the module using a vacuum source. A turbo-molecular vacuum pump was used to provide the reference pressure to the module. The vacuum level was measured by a DIGIQUARTZ calibration standard (a high-accuracy vibrating quartz pressure standard manufactured by Paroscientific, Inc.).

The ESP data acquisition rate during the testing was 10 frames per second for 2 seconds, for a total of 20 frames per data point. A dwell time of 5 seconds was specified to allow the pressures to stabilize before acquiring a data point.

The standard ESP calibration consisted of five points that were used to determine a quartic polynomial representation of the pressure-voltage signature of each transducer or sensor. The calibration pressure range was from approximately 0.2 psia to 10 psia. Full calibrations were performed prior to each run series and prior to each change in the free-stream Mach number. More frequent calibrations were performed, as necessary, based on certain instrumentation diagnostics as described next.

Several ESP system verification techniques were used during the testing. Two thermocouple wires were affixed to the sides of the ESP module, and the thermocouple output was routed to the data acquisition system for display and recording. This data provided an indication of the ESP module temperature stability during wind-on runs. A 5-degree change in the module temperature was a general guideline based on operational experience to perform a full online ESP calibration. Units referred to as known pressure generators (KPGs) were used to generate and maintain specified pressures that were plumbed to selected module ports as a system diagnostic tool for real-time accuracy checks. Three module ports were dedicated to the known pressures, which were typically 50 psfa, 200 psfa, and 700 psfa. The differences between the measured and applied pressures at these ports were displayed in real-time, including time histories of the differences using the wind tunnel on-line graphics software. Differences that were outside a specified range of +/-1 psfa led to the application of check pressures to all module transducers. In general, if approximately 25% of the ports were reading more than +/-0.5 psfa different than a given check pressure, a full online ESP calibration was performed. Another opportunity for an ESP system check occurred during the acquisition of wind-off zeroes at the beginning and end of each run series when the tunnel pressure was evacuated to a stable pressure between 200 psfa and 400 psfa. This provided an opportunity to verify the responses of all 45 pressure transducers relative to the tunnel static pressure measurement obtained via a direct read from a Ruska pressure transducer.

The ESP module featured a purge air option which involved a modification to the calibration valve to manifold purge pressure inputs to the measurement ports during calibration. With the valve placed in the calibrate position, the application of a purge air supply pressure of approximately 40 psi prevented contamination of the pressure measurement lines during the PSP application process.

Strain Gage Balance Measurements

Force and moment data were obtained with a 6-component electrical strain gage balance designated NASA LaRC UT-52A. Three four-wire platinum resistance temperature (PRT) devices were located on the front, middle, and aft sections of the balance to monitor the balance temperatures during the test. The measured temperatures were averaged and used to adjust the balance primary sensitivities. The PRT measurements were also used to monitor balance temperature gradients. There is no method currently available to correct the balance output for thermal gradients. Consequently, these gradients were minimized to values of

approximately 1-2 ^{o}F by allowing the balance temperatures to stabilize during wind-on operations before acquiring any force and moment data.

The UT-52A balance design loads and the balance calibration accuracies (95% confidence level) expressed in percent full-scale (% F.S.) are shown in table V. The balance accuracies were converted to microvolts (µV) and, also, to pounds (lbs) or inch-pounds (in-lbs) as shown in table V. The latter values were used to estimate the measurement accuracies in the aerodynamic force and moment coefficients for the conditions in Test 1858 as shown in table VI.

The balance data acquisition rate during the testing was 30 frames per second for 2 seconds, for a total of 60 frames per data point. All force and moment data were acquired in a pitch-pause mode. A dwell time of 5 seconds at each setpoint was dictated by the simultaneous acquisition of the ESP data.

Force and moment and surface pressure measurements are typically obtained in separate phases of testing at UPWT since the on-board ESP cable, reference and calibration pressure lines, known pressure lines, and thermocouple wires bridge the balance. These measurements were combined in Test 1958 in order to also obtain the PSP measurements and LVS and schlieren flow visualization within the available tunnel occupancy time. Precautions were taken to mitigate any bridging effects on the balance by distributing the ESP cable, pressure lines, purge air lines, and wiring along the interior surface of the model and providing a flexible bridge from the model to the sting, where the ESP instrumentation bundle was run externally to a protective conduit near the roll coupling. A hydraulic load cell and double knife edge assembly was used to apply prescribed check loads to the balance normal force, side force, pitching moment, and yawing moment components after the model installation was completed. Rolling moments were applied by placing calibrated weights at selected locations on the wing surfaces. A hand-held force gage

interfaced to the wind tunnel data acquisition system was used to apply axial check loads. The applied loads to all six balance components were compared to the computed loads from the wind tunnel data system, which indicated that simultaneous acquisition of the balance and ESP measurements was a valid testing approach in the current application.

Model Chamber Pressure Measurements

Model chamber pressures were measured at two diagonally-opposed locations approximately 2.5 inches upstream of the model fuselage exit plane. The 0.060-inch outer diameter (O.D.) stainless steel pressure tubes were run underneath the model fouling strip and along the sting to a protective conduit near the roll coupling. The tubes extended approximately 15 feet from the model to individual 5 psia Druck pressure transducers that were located outside the test section. The manufacturer-specified measurement accuracy (95% confidence level) as a percent of full-scale is +/-0.1% for these transducers (+/-0.005 pounds per square foot absolute (psia) or +/-0.72 psfa). The corresponding estimates for the measurement accuracies expressed in terms of the chamber pressure coefficient for the conditions in Test 1858 are presented in table VII.

A within-test check of the chamber pressure measurements was provided during the acquisition of the initial and final wind-off zeroes with the test section evacuated to a stable pressure (typically about 300 psfa). Differences between the tunnel static pressure and the individual Druck transducers no greater than approximately +/-0.5 psfa were typical. These zeroes were useful in verifying the functionality of the transducers and as a partial check of the integrity of the pressure tubing.

Pitch Angle Measurements

The primary type of instrumentation in use at UPWT for pitch angle measurement is a gravity-sensing servo accelerometer (QFlex). Direct and indirect methods of model attitude measurement are used. The direct measurement

uses an accelerometer mounted in the model. The indirect measurement features an accelerometer installed in a protective housing on the knuckle component of the model support system with corrections applied to account for aeroelastic or mechanical deflections of the model, balance, and sting assembly. There was insufficient internal volume in the porous LEX model to accommodate a QFlex package. Consequently, the indirect method of attitude measurement was used in Test 1858. For static (unaccelerated) model conditions, the QFlex measures changes in angle relative to the horizontal by determining the differences in the component of the force due to gravity acting parallel to its sensitive axis. Although the instrument response to acceleration is linear, its response to changes in attitude relative to the local gravity vector in unaccelerated conditions is sinusoidal. The knuckle pitch angle was computed using the following equation:

$$pitch = sin^{-1}\left(\left(reading - bias\right)/sens\right) - zero$$

where *reading* is the QFlex output in millivolts, and *bias* (bias in millivolts), *sens* (sensitivity in millivolts/g), and *zero* (in degrees) are derived from the in-tunnel QFlex calibration. The QFlex calibration was performed by installing a NASA LaRC angle measurement system (AMS) package to a precision-machined plate affixed to the knuckle component of the model support system. The AMS is a self-contained instrumentation package consisting of three orthogonally-mounted QFlex accelerometers mounted in a titanium housing with precision base and interfaced to a signal conditioning unit and a laptop computer system. The AMS is capable of measuring absolute pitch and roll angles to within +/-0.001 degrees. An 11-point calibration was performed at knuckle plate pitch angles from approximately -8 degrees to +30 degrees. The standard deviation from the QFlex calibration was approximately 0.002 degrees.

Corrections to account for aeroelastic or mechanical deflections of the model, balance, and sting assembly due to aerodynamic loads were based on in-tunnel sting and balance deflection calibrations. Deflections due to normal force, pitching moment, side force, and yawing moment were obtained using a hydraulic load cell with double knife-edge assembly. Prescribed loads were applied at predetermined locations relative to the balance moment center (BMC), and the corresponding deflections were recorded using an AMS package installed on the balance calibration fixture and from the knuckle QFlex accelerometer. The rolling moment deflection calibration was conducted by applying calibrated weights suspended from two opposing horizontal arms bolted to the sides of the calibration fixture via weight pans and double knife edges. The weights were transferred from one pan to the other, and the corresponding deflections due to rolling moment were measured directly using the AMS package on the balance calibration fixture.

Roll Angle Measurements

The UPWT mechanized roll coupling provided the primary measurement for the model roll angle. Output from the roll coupling was obtained using an onboard potentiometer. The roll coupling was calibrated using the AMS package mounted to the balance calibration fixture as a reference standard. The roll coupling output was converted to degrees using linear interpolation from a look-up table obtained from the in-tunnel calibration.

Corrections

Flow angularity

The force and moment data were corrected for tunnel flow angularity (*thetaf*) and delta pitching moment (*delcm*). The *delcm* correction term is a result of non-uniform flow angularity across the test section and model asymmetries that result in a pitching moment. If the flow angularity in the tunnel was constant throughout the test section and there were no model asymmetries, then *delcm* would be zero. Flow angle runs were performed on the model with porous LEX and twin vertical tails in the upright and inverted orientations at the outset of Test 1858. Upright and inverted runs were

conducted at each Mach number. The estimated flow angle corrections including *thetaf* and *delcm* are presented in table VIII. Flow angle runs with the model in the wings vertical orientation were not performed.

Chamber pressures

The model chamber pressure measurements were used to correct the balance axial force to a condition of free-stream static pressure at the model base. Base pressure corrections were not applied, since the model base area was essentially zero.

Discussion of Results

Phase I – Pressure Sensitive Paint Measurements

PSP Accuracy

Table IX shows the percent error and intervals corresponding to +/- two sample standard deviations for the PSP pressure measurements relative to the ESP tap data for four configurations corresponding to the solid and porous LEX and centerline and twin vertical tails. A new PSP coating was applied to each configuration. The selected test conditions were M_∞ = 1.6 and 2.1 and α = 8°. Listed in the table are the Mach number, the number of ESP taps used to calibrate the PSP, the range of pressure spanned by the ESP taps, the mean relative error in PSP measurement, and an interval corresponding to two sample standard deviations for the PSP measurements relative to the ESP data.

The mean relative error is calculated using the following equation from reference 17:

$$\varepsilon = \frac{\sum_{i-1}^{N}\left(100 \times \frac{|ESP_i - PSP_i|}{ESP_i}\right)}{N}$$

where ESP_i is the pressure value at the ith pressure tap, PSP_i is the pressure value using the PSP technique corresponding to ESP_i, N is the number of ESP taps used, and ε is the mean relative error in pressure measurement using the PSP technique.

Table IX indicates that the range of mean relative error in pressure measurement is approximately 0.97 – 1.85 percent at M_∞ = 1.6 and approximately 1.89 – 3.25 percent at M_∞ = 2.10. For any given configuration, the mean relative error increases as the Mach number is increased from 1.6 to 2.1. Possible contributing factors to this trend are (1) error in the intensity measurement, which results in a larger relative error in the measurement of the lower pressures at the high supersonic Mach number (reference 17); (2) more pronounced surface temperature variations at the higher Mach number (surface temperature measurements were not made during this experiment); and (3) photodegradation effects. It is noted that the estimated mean relative errors are an order of magnitude greater than the manufacturer's estimated ESP measurement uncertainties for the 10 psid module shown previously in table IV. Similar results were obtained in previous PSP testing conducted at UPWT and in other NASA LaRC facilities (see reference 17, for example).

Assessment of PSP Aerodynamic Intrusiveness

The model without PSP coating was tested in Phase IV of the current experiment to obtain dedicated ESP and six-component balance measurements with the solid and porous LEX and centerline and twin vertical tails. This section compares the ESP measurements obtained on the unpainted model to the corresponding data obtained with the PSP coating applied to the wing upper surface. The model was tested in the upright (wings horizontal) orientation in Phase IV and in a wings-vertical orientation during the PSP testing in Phase I. Consequently, the pressure data comparisons will include any effects caused by differences in the model location in the test section. In addition, the tunnel flow angularity at M_∞ = 1.6 and 2.1 was manifested as a yaw

angle when the model was rolled $+90^{\circ}$. Adjustments to the model yaw angle to offset the flow angle correction at each Mach number were not made during the PSP testing, since this would have affected the spatial alignment of the wind-on and wind-off (reference) images.

Figures 13-16 compare the spanwise distributions of the ESP upper surface static pressure coefficient, $C_{p,u}$, at the three chord stations on the right wing upper surface ($x/c_{r,w}$ = 0.30, 0.60, and 0.80) at $\alpha = 8^{\circ}$ with PSP off and PSP on corresponding to the configurations with solid LEX/centerline tail, solid LEX/twin tails, porous LEX/centerline tail, and porous LEX/twin tails, respectively. Each figure shows results obtained at M_{∞} = 1.6 and 2.1. The pressure distributions are superimposed on an isometric view of the right half of the LEX and wing extending from the apex of the LEX to the 80% wing centerline chord location. The character of the vortex-dominated pressure distributions is the same with PSP off and PSP on. For the solid LEX (figures 13 and 14), the pressure signatures of two vortices are apparent. In figure 13(a), for example, the influence of the wing vortex is evident at $x/c_{r,w}$ = 0.60 and $x/c_{r,w}$ = 0.80 outboard of y/s = 0.6 as a suction pressure peak or suction pressure plateau. The effect of the LEX vortex is manifested at these same measurement stations as a suction pressure peak of lower magnitude centered at y/s approximately 0.4 and 0.3, respectively. In contrast, the pressure distributions with the porous LEX in figures 15 and 16 reveal a single, broader vortex-induced pressure signature. Differences exist between the PSP off and PSP on cases, however, and the suction pressure levels are typically higher with PSP on. These differences appear to diminish as the Mach number increases from 1.6 to 2.1.

A quantitative assessment of the differences in the pressure data with PSP off and PSP on is provided in figures 17-20 for the same configurations and test conditions presented in figures 13-16. In the lower frame of each figure, the ESP pressure coefficients with PSP off and PSP on are plotted versus the pressure tap for all 45 taps on the right wing upper surface. For example, pressure taps 1 through 13 are located in the first spanwise row ($x/c_{r,w}$ = 0.30) and extend from the tap closest to the wing centerline at y/s = 0.10 to the tap near the wing leading edge at y/s = 0.94. Similarly, pressure taps 14 through 30 are located in the second spanwise row ($x/c_{r,w}$ = 0.60), and taps 31 through 45 are in the third spanwise row ($x/c_{r,w}$ = 0.80). The upper frame in each figure plots the difference in the pressure coefficients with PSP off and PSP on ($\Delta C_{p,u}$) at each pressure tap location. Horizontal dashed lines above and below $\Delta C_{p,u}$ = 0 correspond to upper and lower uncertainty limits on the pressure coefficient using the manufacturer's uncertainty (95% confidence) for the 10 psid ESP module. The differences are typically much greater (often by an order of magnitude) than the estimated ESP measurement accuracies. There is evidence of systematic error, since the $\Delta C_{p,u}$ values are typically positive, rather than being randomly distributed about zero. An exception to this trend is in figure 20(b), which corresponds to the porous LEX with twin vertical tails at M_{∞} = 2.1. Here, the differences are primarily negative. In general, however, the unpainted and painted model comparisons provided assurance that the PSP coating was not causing a significant effect on the flow topology of interest in the current experiment.

Assessment of PSP-Derived Surface Pressure Measurements

Composite plots are presented in the following sections showing the distributions of the calibrated PSP upper surface static pressure coefficient corresponding to the locations of the discrete ESP pressure orifices at the three axial measurement stations $x/c_{r,w}$ = 0.30, 0.60, and 0.80. The surface pressure coefficient (denoted CP in the figures) is plotted against the nondimensional local span distance y/s. The composite plots also include the corresponding ESP pressure measurements, false-colored PSP global surface pressure field response and, when available, LVS flow visualization images. Additional LVS flow visualization images are presented in a later section of this report.

A global calibration of the PSP was obtained for each configuration (solid LEX with centerline and twin vertical tails, porous LEX with centerline and twin vertical tails) and test condition (angle of attack and Mach number combination) by selecting pixel locations in the processed PSP image that were as close as possible to the ESP pressure orifices but in a region where the paint thickness was considered uniform. The PSP image processing software, PAINTCP, performed a simple linear regression to compute the intercept and slope of the global calibration for each PSP image. The values of the intensity ratios and ESP pressure coefficients were also exported to a statistical software application (reference 18) to conduct an independent linear regression and analysis of residuals. Table X presents the estimated regression functions for the eight cases (four configurations and two test conditions) that are the subject of this report. The table also shows the root mean square error (RMSE), which is an estimate of the standard deviation of the random error and 95% confidence limits about the estimated mean response. A residuals analysis was performed for all of the regression functions to confirm that the assumptions of normally-distributed errors and constancy of error variance were satisfied. In addition, checks were performed for the presence of outlying or influential observations. An assessment of the independence of error terms could not be made since the data were not acquired in any time order.

The false-colored PSP pressure maps were created after performing image registration, ratioing, and resection transform. Lines are superimposed on the pressure maps at the three pressure measurement stations with leaders pointing to the appropriate pressure coefficient plot. Color bars are included to show the corresponding range of pressure coefficient. In general, green, blue, and purple colors correspond to regions of low pressure (that is, higher suction pressures), with purple representing the highest suction pressure levels. Regions of higher surface pressures (lower suction pressures or slightly positive pressures) are represented by yellow and red colors.

The available LVS cross-plane images are positioned to the left of the pressure measurement station that closely matches the location where the laser light sheet impinged on the model surface. The LVS images are scaled relative to each other to reflect the growth of the vortices from the forward to aft portions of the wing. The main purpose of these composite plots is to show the level of agreement between the two pressure measurement techniques and to provide pertinent information on the topology of the vortex flows that induce these pressure distributions.

Solid LEX with Centerline and Twin Tails

Comparisons of the distributions of the PSP and ESP upper surface static pressure coefficient at $M_\infty = 1.6$ and 2.1 and $\alpha = 8^\circ$ are shown in figures 21 and 22 corresponding to the solid LEX with centerline and twin vertical tails, respectively. The pressure distributions are plotted on a common scale to facilitate comparisons of the vortex pressure signatures at the three measurement stations. The false-colored PSP images provide a map of the surface pressure field response at each Mach number. In general, the pressure signature, or footprint, of the wing leading-edge vortex is revealed by a broad band of predominantly purple, blue and green colors. The footprint of the LEX vortex is typically characterized by a faint, narrow band of blue color within a predominantly green region. Regions of vortex-induced reattached flow near the central region of the wing are characterized by yellow and red colors. Similarly, the pressure rise downstream of a shock wave at the centerline tail or downstream of intersecting shock waves between the twin tails produces regions of yellow and red colors. In an attempt to extract pertinent features in the false-colored PSP images, the selected color range extremes would sometimes cause local saturation. This would produce regions of white and black in the PSP surface pressure maps.

The spanwise distributions of the PSP upper surface static pressure coefficients derived from the in-situ global calibrations compare favorably with the corresponding ESP pressure distributions in figures 21 and 22. The highest suction pressures occur underneath the wing leading-edge vortex. The wing vortex pressure signature is more clearly seen in the distributions at $x/c_{r,w}$ = 0.60 and 0.80 as a region of higher suction pressures along approximately the outer 30% to 40% of the local wing semispan. The solid LEX vortex induces a less pronounced suction pressure peak farther inboard. The pressure distributions correlate with the false-colored PSP pressure maps and the available LVS flow visualization images, which show the wing vortex as a broader, elliptically-shape region close to the wing upper surface and the LEX vortex as a more confined structure with approximately circular cross section. Increasing the Mach number from 1.6 to 2.1 decreases the peak vortex-induced suction pressures at $x/c_{r,w}$ = 0.60 and 0.80. The vertical tail placement does not affect the character of the pressure distributions, since the presence of the tails is not communicated to the upstream pressure measurement stations at the supersonic speeds. Quantitative differences in the pressure distributions with the centerline and twin vertical tails are more likely due to systematic error associated with different PSP coating applications for the two configurations. More detailed comparisons of the pressure distributions obtained with the centerline and twin tail arrangements are provided in a later section of this report for the unpainted model.

Porous LEX with Centerline and Twin Tails

Comparisons of the distributions of the PSP and ESP upper surface static pressure coefficient at M_∞ = 1.6 and 2.1 and α = 8° are shown in figures 23 and 24 corresponding to the porous LEX with centerline and twin vertical tails, respectively. Reasonable quantitative agreement is obtained between the PSP and ESP pressure distributions. The pressure distributions at all three measurement stations reveal a single, broad wing leading-edge vortex pressure

signature. A LEX vortex-induced pressure footprint is not apparent. The pressure distribution trends correlate with the PSP pressure maps which show an extended region of higher suction pressures induced by an apparent single vortex system. These results are also consistent with the LVS cross-flow images (available only for the centerline tail configuration at M_∞ = 1.6 and 2.1 in figure 23), which reveal a broad, elliptically-shaped wing leading-edge vortex that extends over a greater spanwise extent of the wing compared to the results obtained with the solid LEX (see figure 21). More detailed comparisons of the results obtained with the solid LEX and porous LEX are presented in the next section.

Comparison of PSP Pressure Maps, LVS Images, and Spanwise Pressure Distributions

Figure 25 presents a composite of false-colored PSP images with solid and porous LEX and centerline and twin vertical tails at M_∞ = 1.6 and 2.1 and α = 8°. The PSP images clearly show that LEX porosity broadens the surface pressure response to the wing leading-edge vortex while masking the presence of a distinct LEX vortex pressure signature. The broadening of the wing vortex with the porous LEX also promotes a direct interaction of the wing vortex with the twin vertical tails. In contrast, the solid LEX configuration exhibits an apparent direct interaction of the LEX vortex with the twin tails, while the wing vortex passes unimpeded along the outer region of the wing. The vertical tail placement does not promote any observable differences in the character of the surface pressure response upstream of the tail surfaces with either the solid LEX or porous LEX. A footprint of an oblique shock wave emanating from the apex region of the centerline tail is visible in figure 25. This shock intersects the pressure footprints of the LEX and/or wing leading-edge vortices but does not appear to cause any discontinuities in the local pressure response along the rear portion of the wing. The flow topology is significantly different with the twin verticals tails, however, where two intersecting oblique shock waves promote a

rapid pressure rise between the tails (indicated by an abrupt color change from green to red across the shocks). The surface pressure response outboard of the tails is very different, however. The flow field in which the tails are embedded consists of a superposition of shock waves and cross flow induced by the LEX and/or wing leading-edge vortices. An indication of this cross flow can be inferred from the LVS image at $x/c_{r,w} = 0.80$ in figure 22(a). The local angle of attack at the tail leading edges may be sufficiently high to cause flow separation in the form of vortices outboard of the twin tails. The regions of higher suction pressures outboard of the tails (denoted by blue and black (saturated) false coloring) are indicative of vortex-induced pressure signatures. In addition, the vortex-dominated flow along the outer portion of the wing appears to significantly reduce the shock footprint outboard of the vertical tails.

Figure 26 provides a composite display of PSP pressure maps, LVS flow visualization, and spanwise pressure distributions for the solid LEX and porous LEX at $M_\infty = 1.6$ and 2.1, $\alpha = 8^{\circ}$, and centerline tail. The LVS images and pressure distributions were obtained at $x/c_{r,w} = 0.80$, and the corresponding location in the PSP pressure maps is denoted by a horizontal dashed line. The results at this model station indicate that the flow field with solid LEX is dominated by a dual-vortex system from the LEX and wing, whereas a single, broader wing leading-edge vortex is the dominant flow-field feature with the porous LEX.

The calibrated PSP pressure distributions with estimated error bars corresponding to the solid LEX and porous LEX at $M_\infty = 1.6$ and 2.1 and $\alpha = 8^{\circ}$ are compared in figures 27-30. Results are shown for the configurations with centerline and twin vertical tails. The simple linear regression functions summarized in table X were used to estimate the mean response at selected pixel locations in the PSP images. The point estimate for the mean response and the corresponding 95% confidence intervals for

the mean response at these pixel locations were constructed using the following equation (from reference 19):

$$\left(\widehat{C}_{p(PSP)}\right)_h \pm t\left(1 - \alpha_S/2,\, N-2\right) s.d.\left\{\left(\widehat{C}_{p(PSP)}\right)_h\right\}$$

where

$$\left(\widehat{C}_{p(PSP)}\right)_h$$

is the point estimate of the mean response at the desired PSP pixel location. The corresponding estimated standard deviation, $s.d.$, of the mean response is

$$s.d.\left\{\left(\widehat{C}_{p(PSP)}\right)_h\right\} =$$

$$\left(MSE\left[\frac{1}{N} + \frac{\left(\left(I/I_o\right)_h - \overline{I/I_o}\right)^2}{\sum_{i=1}^{N}\left(\left(I/I_o\right)_i - \overline{I/I_o}\right)^2}\right]\right)^{1/2}$$

The critical value from the t-distribution corresponding to a 5 percent level of significance, α_s, and 43 degrees of freedom is

$$t\left(1 - \alpha_s/2,\, N-2\right) = t\left(0.975, 43\right) = 2.017$$

The mean square error, MSE, is an unbiased estimator of the population variance. A point estimate of MSE was determined from each regression analysis and was based on 43 degrees of freedom. The intensity ratios at (1) the desired pixel location, (2) the pixel location corresponding to the ith ESP tap, and (3) averaged over all N pixel locations are expressed, respectively, as

$$\left(I/I_o\right)_h,\ \left(I/I_o\right)_i,\ \overline{I/I_o}$$

The 95% confidence intervals are depicted in the following figures as error bars centered about the estimated mean PSP pressure coefficient. Non-overlapping error bars indicate statistically significant differences between the solid and porous LEX pressure coefficients at a given pixel location. The false-colored PSP pressure maps for the solid and porous LEX are shown as

20

inserts in each figure and a horizontal dashed line denotes the corresponding pressure measurement location.

LEX porosity causes statistically significant differences in the pressure distributions at all three measurement stations in figures 27-30, and the overall suction pressure levels at these stations appear to be higher with the porous LEX. The transformation from a dual-vortex pressure signature with solid LEX to a broader single-vortex pressure signature with porous LEX is apparent. The pressure distribution trends are similar at $M_\infty = 1.6$ and 2.1 and with the centerline and twin vertical tails.

Detailed Chordwise PSP Pressure Distributions

An advantage of the PSP technique compared to the discrete measurements using the ESP system is that every pixel in the painted portion of the PSP digital image is effectively a pressure tap. Consequently, the pressure distributions can be resolved to much greater detail in all applicable regions on the wing. Figures 31-34 plot the pressure coefficients at $\alpha = 8^\circ$ corresponding to all available pixels from approximately the wing leading edge to the trailing edge in two selected chordwise rows at $y/s = 0.25$ and $y/s = 0.40$. The twin vertical tails are installed on the model in each figure, and the two chordwise rows bound the right-hand tail. For reference, the nondimensional span locations of the LEX-wing junction and the right-hand tail correspond to $y/s = 0.265$ and $y/s = 0.333$, respectively.

Figure 31 shows the chordwise pressure distributions obtained with the solid LEX at $M_\infty = 1.6$. The PSP static pressure coefficient is plotted against pixals in the digital image starting near the leading edge of the wing. There were approximately 742 pixels in the chordwise row at $y/s = 0.25$ and 632 pixels in the chordwise row at $y/s = 0.40$. The chordwise location of the vertical tail apex extended to the two pressure rows corresponds to pixel 587 at $y/s = 0.25$ and pixel 477 at $y/s = 0.40$. The

locations of the pressure rows are shown in the PSP pressure map to the right of the data plots. In addition, an LVS cross-flow image near the wing trailing edge is shown directly below the PSP pressure map. The LVS image is scaled so that the spanwise locations of significant flow-field features such as leading-edge vortices can be correlated with the surface pressure response directly above it. The pressure distributions exhibit scatter from pixel-to-pixel, which could be caused by surface irregularities in the PSP coating and variation in the intensity of light emitted by the PSP. A marked discontinuity in the estimated pressure coefficients between adjacent pixels is typically caused by a discontinuity in the model surface, for example, a part line in the model or the presence of a pressure orifice. It is noted, however, the data scatter would be bounded reasonably well by the 95% confidence limits for the estimated overall mean response previously presented in table X. The region near the wing apex is characterized by red and yellow colors in the PSP pressure map, which is attributed to flow reattachment and recompression inboard of the LEX vortices. The pressure row at $y/s = 0.25$ captures a portion of this reattachment region, which is manifested as a pressure rise near the wing leading edge. The pressure row at $y/s = 0.25$ is situated near the inboard edge of the LEX vortex pressure footprint, and the corresponding pressure distribution indicates a flow expansion to an approximately constant pressure level along the main portion of the wing up to the region of the vertical tail. This is indicated by the predominantly green color in the PSP pressure map. A significant flow recompression occurs downstream of an oblique shock wave generated at the tail. The estimated shock front position corresponds to pixel 599 at $y/s = 0.25$. The rapid pressure rise correlates with the abrupt change in the false-colored PSP image from green to red across the shock. The pressure row at $y/s = 0.40$ intersects the wing vortex pressure signature near the leading edge, which appears as a blue region in the PSP pressure map. The pressure distribution reveals a corresponding vortex-induced suction pressure peak in this region. The pressure row at $y/s = 0.40$ is situated

between the wing and LEX vortex pressure footprints farther aft, and it captures a region of approximately constant pressure level on the wing (depicted as green in the pressure map) up to the vicinity of the vertical tail. The PSP pressure map suggests the presence of a weak shock front extending outboard from the tail, which is consistent with the minor flow recompression beginning at approximately pixel 465 in the pressure distribution at $y/s = 0.40$. The superposition of a strong vortex flow field in this region reduces the shock strength, however. Farther aft, the pressure distribution reveals a significant increase in the suction pressure level and a well-defined suction pressure peak that is approximately centrally located in a region of blue color in the PSP pressure map. The transition from green to blue colors at $y/s = 0.40$ in the PSP pressure map occurs at approximately pixel 485. The pressure distribution and pressure map in this region are consistent with the induced effects of a vortex flow. The LVS image near the trailing edge of the wing that is shown directly below the pressure map confirms the presence of a vortex that is situated at the outboard junction of the tail and wing upper surface. This vortex appears as a dark region with essentially no water vapor condensate surrounded by a lighter region of condensation. The PSP pressure map shows the LEX vortex pressure footprint directly impinging on the vertical tail. The LVS image indicates that the LEX vortex retains its structure despite the direction interaction with the tail and the passage of the vortex across the oblique shock. The central region of the LEX vortex is shown as a dark area at about midspan on the inboard side of the vertical tail. The induced effect of the LEX vortex on the external flow field can be inferred from the roughly circular pattern of condensate surrounding the dark center region. The wing leading-edge vortex also appears in the LVS image as a flattened region of low water vapor condensate near the wing upper surface, and its spanwise extent correlates with the broad region of blue color in the PSP pressure map. Finally, a wing tip vortex appears as a dark circular region outboard of the flattened wing vortex in the LVS image.

Figure 32 shows the chordwise pressure distributions obtained with the porous LEX at $M_\infty = 1.6$. The pressure row at $y/s = 0.25$ intersects the inboard region of a broadened wing leading-edge vortex in the presence of the porous LEX. The flow recompression and corresponding pressure rise that appeared near the wing leading edge with solid LEX does not occur with porous LEX because the induced effects of the wing vortex extend farther inboard. The blue region in the PSP pressure map that denotes the wing vortex pressure signature extends as far inboard as the vertical tail. The wing vortex-induced effects appear to reduce the oblique shock strength at the vertical tail, since the flow recompression downstream of the shock is not as severe and the intensity and extent of the red color region in the pressure map are diminished. The chordwise row at $y/s = 0.40$ is situated within the boundary of the wing vortex pressure signature and reveals an approximately linearly increasing suction pressure level from the wing leading edge to the location of a weak shock front outboard of the vertical tail. A minor flow recompression occurs, which is followed by a flow expansion as the pressure row traverses through a vortex flow region outboard of the tail. LVS flow visualization images were not obtained for this configuration.

The chordwise pressure distributions obtained with the solid LEX and porous LEX at $M_\infty = 2.1$ and $\alpha = 8^\circ$ are shown in figures 33 and 34, respectively. The trends obtained at the higher Mach number are similar to those observed in figures 31 and 32 at $M_\infty = 1.6$, and no further discussion is presented.

Figures 35 and 36 present side-by-side comparisons of the PSP pressure maps and chordwise pressure distributions at $y/s = 0.25$ and $y/s = 0.40$, respectively, with solid LEX and porous LEX at $M_\infty = 1.6$ and $\alpha = 8^\circ$. Similar comparisons are shown in figures 37 and 38 corresponding to $M_\infty = 2.1$. The twin vertical tails are installed in all cases. The primary effects of LEX porosity in figures 35 and 36 at $M_\infty = 1.6$ are to promote a single, broadened

vortex pressure signature, mitigate the shock-induced flow recompression along the inboard side of the vertical tail, and reduce the chordwise pressure signature of a vortex that develops along the outboard junction of the tail and wing upper surface. Similar effects are observed at M_∞ = 2.1 in figures 37 and 38. The porous LEX is not as effective at M_∞ = 2.1 in mitigating the flow recompression downstream of the oblique shock at the vertical tail. This is attributed to a weaker wing leading-edge vortex at the higher Mach number (reference 20).

Phase II – Laser Vapor Screen Flow Visualization

Comparison of Solid and Porous LEX with Centerline Tail

The effect of LEX porosity on the LVS cross-flow pattern at a nominal M_∞ = 1.6, α = 8° and 10°, and $x/c_{r,w}$ = 0.80 is shown in figure 39. The light sheet location corresponds to the aft ESP pressure tap row on the right-hand wing upper surface. Porosity shifts the dominance from the LEX vortex to the wing vortex. The solid LEX images are highlighted by two distinct vortex pairs, which are revealed as darker regions lacking water vapor condensate. The left- and right-hand LEX vortices have nearly circular cross sections and are positioned along the inboard portion of the wing. A region of intense downflow is induced between these vortices. The left- and right-hand wing leading-edge vortices are flatter regions situated along the outer section of the wing. In contrast, the porous LEX images reveal one vortex pair featuring a broader, thicker wing leading-edge vortex on each side. The LEX vortices are not visible in these images, and the induced downflow above the fuselage is less discernible. It is noted that LVS flow visualization was not obtained at angles of attack higher than 10 degrees at M_∞ = 1.6 because of observed starting shock instability caused by model and wake blockage and condensation effects.

The cross-flow patterns at the same light sheet location at M_∞ = 2.1 and α = 8°, 10°, 12°

and 16° are shown in figure 40. The images obtained at α = 12° and 16° (figures 40(c) and 40(d), respectively) provide additional insight regarding the effects of porosity on the off-surface flow field. The LEX vortices are not suppressed by porosity. Instead, the vortices are weaker and diffuse because of a decrease in the vorticity shed from the leading edge. The weaker vortex produced by the porous LEX combines with the wing leading-edge vortex, and the shear layer from the wing leading edge connects the two vortices. The bulk of this vortex region is situated closer to the wing surface, which suggests a local increase in the vortex-induced suction pressures. This pattern is consistent with the schlieren flow visualization results presented in the next section that reveal vortex traces starting at the LEX and extending along the entire wing. The identities of the LEX and wing vortices can still be discerned at these higher angles of attack, but the resultant cross flow pattern is characteristic of a single, broader vortical flow. Consistent with this effect is the development of a single cross flow shock wave above the combined vortex system, in contrast to the separate shocks that develop above the LEX and wing vortices in the solid LEX images.

Comparison of Centerline and Twin Tails with Solid LEX

A comparison of the LVS cross-flow patterns obtained with the solid LEX and the centerline and twin vertical tails at M_∞ = 1.6, α = 8°, and $x/c_{r,w}$ = 0.60, 0.80, and 1.10 is shown in figure 41. There is very little difference in the cross-flow patterns at $x/c_{r,w}$ = 0.60 and 0.80 since the presence of the vertical tails is not communicated upstream to these wing stations at the supersonic speeds. In contrast, there are significant differences in the LVS patterns downstream of the tails and in the near wake of the wing. With the centerline tail, the LEX and wing vortices directly interact and begin to merge. Wake roll-up and the wing tip vortex are also visible in the image. The LEX and wing vortices do not directly interact in the presence of the twin vertical tails. Each LEX vortex is situated inboard of the wing-mounted tail, and a

cross flow-induced vortex is visible near the outboard junction of the tail and wing. Situated farther outboard is a flattened wing leading-edge vortex and the wing tip vortical flow. There was no evidence from the still images and the video recordings that embedding the twin vertical tails in the vortex-dominated flow field caused flow instability at or downstream of the tails.

Phase III – Schlieren Flow Visualization

Comparison of Solid and Porous LEX with Twin Vertical Tails

Figures 42-44 compare the schlieren flow visualization results obtained with the solid LEX and porous LEX at M_∞ = 1.6, 1.8, and 2.1 and selected angles of attack with the twin vertical tails. The vortex flows are visible in the schlieren images as lighter regions extending nearly streamwise above the model surface. Porosity causes a diffusion of these lighter regions, which suggests a weakening of the vortex shed from the LEX. The LEX vortex is not suppressed by porosity, since vorticity is still shed from the LEX leading edge, albeit to a lesser degree. These observations are consistent with the LVS cross-flow images presented in the previous section.

Phase IV – Electronically-Scanned Pressure and Strain-Gage Balance Measurements

Comparison of ESP Pressure Distributions with Solid and Porous LEX; Centerline Tail On

Figures 45-47 compare the ESP upper surface static pressure distributions obtained with the solid LEX and porous LEX at M_∞ = 1.6, 1.8, and 2.1 and selected angles of attack with the centerline vertical tail. The maximum test angle of attack was 12 degrees at M_∞ = 1.6 and 22 degrees at M_∞ = 1.8 and 2.1. The configuration with solid LEX is characterized by a dual vortex pressure signature at the lower angles of attack that is induced by the LEX and wing vortices. At higher angles of attack, these vortices directly interact, and the combined

vortex system induces a pressure signature characteristic of a single vortex flow. The configuration with porous LEX exhibits a single, broader vortex pressure signature at all measurement stations and test conditions. LEX porosity typically increases the overall suction pressure levels. This effect is most notable along the inboard region of the wing, since the broadened leading-edge vortex acts over an effectively larger portion of the wing. This trend is consistent with the redistribution of the global surface pressure response and the vortex cross-flow patterns that were observed in the PSP pressure maps and the LVS images, respectively, in previous sections of this report.

The effect of the angle of attack on the upper surface static pressure distributions with the solid LEX and porous LEX at M_∞ = 1.6, 1.8, and 2.1 is shown in figures 48-50, respectively. The range of angle of attack at M_∞ = 1.6 in figure 48 is from -4 degrees to +12 degrees in 4-degree increments. The corresponding α-range is from -4 degrees to +20 degrees at M_∞ = 1.8 and 2.1 in figures 49 and 50, respectively. Leading-edge flow separation occurs from the LEX and wing as the angle of attack increases from 0 to 4 degrees at all Mach numbers. The upper surface static pressure coefficients at $x/c_{r,w}$ = 0.30, 0.60, and 0.80 exhibit a corresponding transition from distributions characteristic of attached flow at α = 0° to distributions featuring vortex-induced suction peaks at α = 4°. At this low angle of attack, the distinct pressure footprints of the LEX and wing vortices are already apparent with the solid LEX. A dual vortex pressure signature is also apparent with the porous LEX at α = 4°, particularly at $x/c_{r,w}$= 0.60. Although the LEX vortex is weakened because of porosity, the wing vortex has not yet achieved sufficient strength to entrain the LEX vortical flow. The dual vortex pressure signatures become more prominent with the solid LEX as the angle of attack increases. The solid LEX and wing vortices directly interact along the rear portion of the wing at the higher angles of attack, and the vortices combine to induce a single vortex-induced suction pressure peak (see

reference 16). In contrast, the configuration with porous LEX exhibits a single vortex pressure signature at angles of attack of 8 degrees and higher, often resembling a "roof-top" distribution, as the broadened wing vortex dominates the flow field. The overall suction pressure level at a given pressure measurement station increases with the angle of attack for both the solid LEX and porous LEX configurations. At M_∞ = 1.8 and 2.1 in figures 49 and 50, respectively, the suction pressures increase at a diminished rate at the higher angles of attack and appear to approach a limiting value. For example, the maximum suction pressure levels at M_∞ = 1.8 and 2.1 and $\alpha = 20^o$ are approximately 85% to 90% of the vacuum limit. Table XI presents the values of the vacuum pressure coefficient at M_∞ = 1.6, 1.8, and 2.1. Similar maximum suction pressure levels were obtained on delta wings at supersonic speeds in references 21 and 22.

The effect of the angle of sideslip on the upper surface static pressure distributions with the solid LEX and porous LEX and centerline vertical tail at M_∞ = 1.6, 1.8, and 2.1 is shown in figures 51-53, respectively. The corresponding plots with the twin vertical tails are presented in figures 54-56. All of the data in figures 51-56 were obtained in a sideslip "sweep" at a constant angle of attack of 10 degrees. This was the only angle of attack at which sideslip sweeps were performed. Each frame in a given figure compares the static pressure coefficients on the right wing upper surface at $\beta = -4^o$ and $\beta = +4^o$, thereby providing the downwind (leeward) and upwind (windward) wing pressure distributions in sideslip. It has been noted in subsonic and transonic wind tunnel testing of slender wings in reference 23 that sideslip reduces the direct interaction of LEX and wing vortices on the upwind wing and increases this interaction on the downwind wing. The pressure distributions with the solid LEX in figures 51-56 are consistent with these earlier observations, since the signatures of the LEX and wing vortices are typically more distinct with a greater lateral spacing between suction pressure peaks on the

upwind wing, whereas the converse is true on the downwind wing. This trend is particularly apparent at $x/c_{r,w}$ = 0.60. A primary effect that is observed with the porous LEX is a broadening of the single vortex pressure signature on the upwind wing compared to the downwind wing. In general, the suction pressure differences between the upwind and downwind wings are greater with the solid LEX compared to the porous LEX along approximately the outer half of the wing, and the opposite trend is observed along the inboard region of the wing. These results indicate that the redistribution of the spanwise pressure distributions caused by sideslip is sensitive to LEX porosity. The implications on the rolling moment characteristics are discussed in a later section of this report. It is noted that LVS flow visualization was not obtained with the model in sideslip. Consequently, flow field inferences drawn from the pressure distributions and force and moment data are limited.

Figures 57 and 58 show the effect of the Mach number on the spanwise pressure distributions with solid LEX and porous LEX and centerline vertical tail at $\alpha = 8^o$ and $\alpha = 12^o$, respectively. Figures 59 and 60 present the corresponding plots with the twin vertical tails. The most notable and consistent effect as the Mach number is increased is a reduction in the overall vortex-induced suction pressure levels at $x/c_{r,w}$ = 0.60 and 0.80. This effect occurs for all combinations of LEX porosity and vertical tail placement. The diminished suction pressure levels act over a large region of the wing that is aft of the MRC ($x/c_{r,w}$ = 0.57). The character of the pressure distributions at these measurement stations is similar within the range of Mach number from M_∞ = 1.6 to 2.1, which suggests the flow topology in this region of the wing is unaffected by changes in the Mach number. The Mach number effect is less consistent at $x/c_{r,w}$ = 0.30. Increasing the Mach number promotes a local increase in the vortex-induced suction pressure level with the solid LEX, whereas the opposite effect occurs with the porous LEX.

Comparison of ESP Pressure Distributions with Centerline and Twin Tails

Figures 61-63 compare the spanwise pressure distributions obtained at selected angles of attack with the centerline and twin vertical tails and solid LEX at M_∞ = 1.6, 1.8, and 2.1. The corresponding pressure distributions with the porous LEX are presented in figures 64-66. The pressure distributions at $x/c_{r,w}$= 0.30, 0.60, and 0.80 with solid LEX are insensitive to the vertical tail placement. These results are consistent with the LVS cross-flow images presented in a previous section that revealed no upstream influence of the tails on the vortex-dominated flow field. Similar results are obtained with the porous LEX, except at the ESP pressure tap location corresponding to $x/c_{r,w}$= 0.80 and y/s = 0.40. In general, the magnitude of the suction pressure coefficient at this tap location decreases slightly when the twin vertical tails are installed. This pressure tap is in close proximity to the apex of the right-hand tail, which is located at $x/c_{r,w}$= 0.81 and y/s = 0.33 (see the model planview and sideview sketches in figures 3 and 5). As shown previously in the PSP pressure map in figure 24, the spanwise extent of the wing vortex with porous LEX extends from the leading edge to a location inboard of the wing-mounted tail, and a direct interaction between the vortex and tail occurs immediately downstream of the 80% chord station. It is possible that this interaction causes a disturbance to propagate upstream within the wing upper surface boundary layer to affect the pressure measurement at this tap location. On the other hand, this effect is not as obvious at the higher angles of attack at M_∞ = 2.1 in figure 66, so an ESP instrumentation issue cannot be discounted.

Comparison of Longitudinal Aerodynamic Characteristics with Solid and Porous LEX

Figures 67-69 compare the lift, drag, and pitching moment coefficients obtained with the solid LEX and porous LEX at M_∞ = 1.6, 1.8, and 2.1. Results obtained with the centerline and twin vertical tails are shown in each figure. The most notable effect is that LEX porosity causes large, nose-down increments to the pitching moment coefficient (negative ΔC_m). Concurrent effects include lower lift at angles of attack greater than approximately 12 degrees and higher drag through most of the range of lift coefficient. Below α = 12°, the lift coefficient is either unchanged or slightly higher with the porous LEX. These trends are applicable at M_∞ = 1.6 to 2.1 and with the centerline and twin vertical tails. The force and moment coefficient data suggest that porosity weakens the LEX vortex and, consequently, decreases the LEX vortex-induced lift and nose-up pitching moment increments. The overall increase in the wing vortex-induced suction pressures in the presence of the porous LEX (see figures 45-47, for example) could mitigate the lift decrease at the higher angles of attack and be sufficient to offset the weakened LEX vortex at lower α's. The flow through the porous LEX surface, the decreased vortex lift from the LEX, and the redistribution of the wing vortex-induced suction pressures are factors that contribute to the increased drag.

The effect of the Mach number on the lift, drag, and pitching moment coefficients with the solid LEX and porous LEX is shown in figures 70 and 71 corresponding to the configurations with centerline and twin vertical tails, respectively. Increasing the Mach number decreases the lift curve slope, increases the drag at moderate and high lift, and promotes nose-up pitching moment increments (positive ΔC_m) and unstable shifts in the pitching moment curves. The Mach number effects on the pitching moment coefficient are consistent with the pressure distribution trends previously observed in figures 57-60, which showed a decrease in the overall suction pressure levels downstream of the MRC as the Mach number was increased. The magnitudes of the aerodynamic coefficient increments and the trends associated with increasing Mach number are similar for the solid LEX and porous LEX configurations and with the centerline and twin vertical tails.

Comparison of Longitudinal Aerodynamic Characteristics with Centerline and Twin Tails

Figures 72 and 73 compare the lift, drag, and pitching moment coefficients obtained with the centerline and twin vertical tails at M_∞ = 1.6, 1.8, and 2.1 corresponding to the solid LEX and porous LEX, respectively. The tail placement does not have a significant effect on the lift and drag characteristics of the model with the solid LEX or porous LEX. These results are consistent with the LVS flow visualization images previously shown in figure 41 in which the flow field upstream of the tails was unaffected by the tail placement. Although embedding the twin tails within the vortex-dominated flow field changed the flow topology along the rear portion of the wing, it did not promote instability of the vortical flows. The only notable effect of the tail placement is in the pitching moment coefficient plots, which show that the twin vertical tails generally promote nose-up pitching moment increments (positive ΔC_m) but no significant longitudinal stability changes compared to the centerline tail configuration.

Comparison of Lateral-Directional Aerodynamic Characteristics with Solid and Porous LEX

Figures 74-76 compare the variation of the rolling moment, yawing moment, and side force coefficients with the angle of attack at $\beta = +4^o$ for the solid LEX and porous LEX configurations at M_∞ = 1.6, 1.8, and 2.1, respectively. Data plots are shown in each figure corresponding to the centerline and twin vertical tails. All configurations exhibit stable values of the rolling moment and yawing moment coefficients throughout the range of angle of attack that was tested at a given Mach number. LEX porosity generally results in unstable increments to the rolling moment coefficient beginning at α = 4° to 6°. These increments may be caused by the redistribution of the surface pressure distributions in sideslip that was previously shown in figures 51-56 and discussed on page 24. This effect occurs at all

Mach numbers and with the centerline and vertical tails. Unstable increments in the yawing moment coefficient are also incurred with the porous LEX, although the onset angle of attack does not exhibit a discernible pattern with Mach number or tail placement. It is speculated that a weakening of the LEX vortex reduces the dynamic pressure at the vertical tails with a concurrent decrease in the tail contribution to the stable yawing moment coefficient.

Figures 77 and 78 show the Mach number effect on the lateral-directional aerodynamic characteristics with the solid LEX and porous LEX at $\beta = +4^o$ corresponding to the centerline and twin vertical tails, respectively. The sensitivity of the rolling moment coefficient to the Mach number is small. The data suggest that increasing the Mach number typically causes small unstable increments to the rolling moment coefficient at a given angle of attack. The most significant effect in figures 77 and 78 is the large, unstable increments to the yawing moment as the Mach number is increased from 1.6 to 2.1. This effect is common to all configurations and is likely caused by a reduction in the dynamic pressure environment at the centerline and twin vertical tails. The sign of the side force coefficient increments caused by increased Mach number is consistent with a reduction in the tail effectiveness.

Comparison of Lateral-Directional Aerodynamic Characteristics with Centerline and Twin Tails

Figures 79-81 compare the rolling moment, yawing moment, and side force coefficients obtained with the centerline and twin vertical tails at M_∞ = 1.6, 1.8, and 2.1, respectively. Each figure shows results corresponding to the solid LEX and porous LEX. The centerline tail configuration generally exhibits stable rolling moment increments compared to the twin vertical tail configuration. The centerline and twin vertical tails have approximately the same tail volume. However, the larger-span centerline tail may be embedded in a higher dynamic pressure environment that, combined with the

larger distance from the tail center of pressure to the MRC, promotes larger stable increments to the rolling moment. This effect is common to the solid LEX and porous LEX configurations at M_∞ = 1.6, 1.8, and 2.1. The only departure from this trend is with the porous LEX at M_∞ = 1.6 and $\alpha = 10^o$ to 12° in figure 79. The centerline tail also exhibits stable increments to the yawing moment coefficient up to an angle of attack at which a cross-over in the yawing moment coefficient curves occurs. This cross-over angle of attack is higher with the porous LEX and is more sporadic with Mach number. It is speculated that the stable increments to the yawing moment coefficient that occur with the twin vertical tails at these higher angles of attack is associated with a favorable interaction of the LEX and wing vortices with the tail surfaces.

Concluding Remarks

Optical measurement and flow visualization techniques were used in combination with electronically-scanned pressure and strain gage balance measurements to identify the effects of passive porosity and vertical tail placement on the development and interactions of leading-edge vortex flows about a 65° cropped delta wing-LEX configuration at supersonic speeds. The conclusions from this investigation are applicable to fighter aircraft designs with subsonic/transonic maneuver and supersonic cruise capabilities. Flow-through porosity applied to the LEX significantly reduced the nose-up pitching moments that are characteristic of a LEX vortex-dominated flow field without causing a concurrent large decrease in vortex-induced lift. LEX porosity increased the drag and generally decreased the stable values of the rolling moment and yawing moment. The trends associated with LEX porosity were unaffected by vertical tail placement. Schlieren and LVS flow visualizations indicated that porosity promoted a wing vortex-dominated flow field as a result of a diffusion and weakening of the LEX vortex. The LVS and PSP results obtained with the porous LEX revealed a single, broader wing vortical flow. The redistribution of the wing vortex-induced suction pressures contributed to

the nose-down pitching moment increments and mitigated the decrease in the LEX vortex-induced lift, except at the higher angles of attack. The force and moment measurements indicated that the centerline tail configuration generally provided more stable rolling moments and yawing moments compared to the twin wing-mounted vertical tails. The twin tails were embedded in a complex flow field characterized by multiple vortices and interacting shock waves. The PSP measurements indicated that LEX porosity reduced the strength of shock waves situated between the twin tails. The PSP, LVS, and schlieren techniques were mutually exclusive because of conflicting illumination and image acquisition requirements. However, the results from these optical methods combined with the discrete ESP surface pressure and six-component force and moment measurements provided a detailed assessment of the effects of passive porosity and vertical tail placement on the high angle-of-attack flow field.

References

1. Bauer, S. X. S.; and Hemsch, M. J.: Alleviation of Side Force on Tangent-Ogive Forebodies Using Passive Porosity. AIAA-92-2711, June 1992.

2. Bauer, S. X. S.; and Hernandex, G.: Reduction to Cross-Flow Shock-Induced Separation with a Porous Cavity at Supersonic Speeds. AIAA-88-2567, June 1988.

3. Elsenaar, A.: How It All Started: The International Vortex Flow Experiment on Euler Code Validation in Retrospect. *Symposium on International Vortex Flow Experiment on Euler Code Validation – Proceedings*, A. Elsenaar and G. Eriksson, eds., FFA, Flygtekniska Forsoksanstalten (Sweden), Oct. 1986, pp. 17-19.

4. Braslow, A. L.; Hicks, R. M.; and Harris, R. V., Jr.: *Use of Grit-Type Boundary-Layer Transition Strips on Wind-Tunnel Models*. NASA TN D-3579, 1966.

5. Hall, R. M.; Erickson, G. E.; and Fox, C. H., Jr.: *Evaluation of Gritting Strategies for High Angle of Attack Using Wind Tunnel and Flight Test Data for the F/A-18.* NASA TP-1998-207670, May 1998.

6. Jackson, Charlie M. Jr.; Corlett, William A.; Monta, William J.: *Description and Calibration of the Langley Unitary Plan Wind Tunnel,* NASA TP 1905, November 1981

7. McLachlan, B. G.; Bell, J. H.; Kennelly, R. A.; Schreiner, J. A.; Smith, S. C.; Strong, J. M.; Gallery, J.; and Gouterman, M.: Pressure Sensitive Paint Use in the Supersonic High-Sweep Oblique Wing (SHOW) Test. AIAA-92-2686, June 1992.

8. McLachlan, B. G.; and Bell, J. H.: Pressure-Sensitive Paint in Aerodynamic Testing. *Experimental Thermal and Fluid Science*, Vol. 10, 1995, pp. 470-485.

9. Oglesby, D. M.; Puram, C. K.; and Upchurch, B. T.: *Optimization of Measurements with Pressure Sensitive Paints.* NASA TM 4695, 1995.

10. Carroll, Bruce; Abbitt, John; Lukas, Erick; Winslow, Andy; Schanze, Kirk; Morris, Marty: "Pressure Sensitive Paint Time and Frequency Response", Workshop on Pressure, Temperature and Shear Sensitive Coatings, University of Florida, Gainesville, Florida, May 1995.

11. Trosin, J.; and Hermstad, D.: *PAINTCP V2.3 User's Guide.* TN-94-8006-0000-48, Technical Note No. 48, Revision 1, NASA Ames Research Center, May 1995.

12. *GreenBoot User's Guide*, Version 2.10, Boeing Company, November 1997.

13. Erickson G. E.: *Overview of Supersonic Aerodynamics Measurement Techniques in the NASA Langley Unitary Plan Wind Tunnel.* NASA-TM-2007-214894, August 2007.

14. Erickson, G. E.; and Inenaga, A. S.: *Fiber-Optic-Based Laser Vapor Screen Flow Visualization for Aerodynamic Research in Larger Scale Subsonic and Transonic Wind Tunnels.* NASA TM 4514, 1994.

15. Merzkirch, Wolfgang: *Flow Visualization*, Academic Press, 1974.

16. Erickson, G. E.: *Wind Tunnel Investigation of the Interaction and Breakdown Characteristics of Slender-Wing Vortices at Subsonic, Transonic, and Supersonic Speeds.* NASA TP 3114, 1991.

17. Jagharghi, A. J.; Cler, D. L.; Erickson, G. E.; Mitchell, M.; Lamb, M.; Gibson, L.S.; Farokhi, S.; Taghavi, R. R.; and Hazlewood, R.: Application of Pressure Sensitive Paint to Measurement of Global Surface Pressure for a Convergent-Divergent Nozzle and an Isolated Double Delta Wing at Transonic Speeds. AIAA-95-0639, January 1995.

18. Many authors: JMP Version 5, User's Guide. SAS Institute Inc., ISBN 1-59047-070-2, 2002.

19. Neter, J.; Kutner, M. H.; Nachtstein, C. J.; and Wasserman, W.: Applied Linear Statistical Models. Fourth Edition, ISBN 0-256-11736-5, SCB McGraw-Hill, 1996.

20. Hemsch, M. J.; and Luckring, J. M.: Connection Between Leading-Edge Vortex Lift and Vortex Strength for Delta Wings. *J. Aircr.*, vol. 27, no. 5, May 1990, pp. 473-475.

21. Wood, R. M.: *Supersonic Aerodynamics of Delta Wings.* NASA TP 2771, 1988.

22. Wood, R. L.; Wilcox, F. J., Jr.; Bauer, S.X.S.; and Allen, J. M.: *Vortex Flows at Supersonic Speeds.* NASA TP-2003-211950, 2003.

23. Erickson, G. E.: Wind Tunnel Application of a Pressure-Sensitive Paint Technique to a Faceted Missile Model at Subsonic and Transonic Speeds. NASA-TM-2004-212991, February 2004.

Model Geometry Details							
Wing		*LEX*		*Centerline Tail*		*Twin Tails*	
Airfoil	Modified NACA 64A005 with sharp leading edg	*Airfoil*	Flat plate with symmetrically-beveled leading edge	*Airfoil*	Flat plate with symmetrically-beveled leading edge	*Airfoil*	Flat plate with symmetrically-beveled leading edge
$\Lambda_{LE,w}$	65°	$\Lambda_{LE,lex}$	65°	$\Lambda_{LE,cl}$	45°	$\Lambda_{LE,tw}$	45.24°
$\Lambda_{TE,w}$	0°	$\Lambda_{TE,lex}$	65°	$\Lambda_{TE,cl}$	70°	$\Lambda_{TE,tw}$	0°
$c_{r,w}$	23.622 in.	$c_{r,lex}$	7.680 in.	$c_{r,cl}$	6.881 in.	$c_{r,tw}$	5.650 in.
$c_{t,w}$	3.544 in.	$c_{t,lex}$	7.680 in.	$c_{t,cl}$	3.175 in.	$c_{t,tw}$	0.880 in.
b_w	18.726 in.	b_{lex}	4.960 in.	b_{cl}	5.829 in.	b_{tw}	4.730 in.
$\overline{c}_w$	16.056 in.	$\overline{c}_{lex}$	7.680 in.	$\overline{c}_{cl}$	5.256 in.	$\overline{c}_{tw}$	3.846 in.
λ_w	0.150	λ_{lex}	1.000	λ_{cl}	0.461	λ_{tw}	0.156
S_w	254.3553 in^2 (1.7664 ft^2)	S_{lex}	38.0928 in^2 (0.2645 ft^2)	S_{cl}	29.308 in^2 (0.2035 ft^2)	S_{tw}	15.443 in^2 (0.1072 ft^2) (per tail)
MRC	0.57 $c_{r,w}$ (M.S. 21.144)			$l_{0.25\overline{c}_{cl}}$	8.647 in. (M.S. 29.791)	$l_{0.25\overline{c}_{tw}}$	8.454 in. (M.S. 29.598)
S_{cham}	4.909 in^2 (0.03409 ft^2)			V_{cl}	253.4398 in^3 (0.1467 ft^3)	V_{tw}	261.1048 in^3 (0.1511 ft^3)

Table I. Porous LEX model geometry details.

Pressure Orifice Locations											
M. S. (in.)	$x/c_{r,w}$	y (in.)	y/s	M. S. (in.)	$x/c_{r,w}$	y (in.)	y/s	M. S. (in.)	$x/c_{r,w}$	y (in.)	y/s
14.767	0.30	0.326	0.10	21.853	0.60	0.661	0.10	26.578	0.80	1.762	0.20
		0.652	0.20			1.322	0.20			2.644	0.30
		0.978	0.30			1.983	0.30			3.525	0.40
		1.304	0.40			2.644	0.40			4.847	0.55
		1.630	0.50			3.304	0.50			5.287	0.60
		1.956	0.60			3.965	0.60			5.728	0.65
		2.200	0.675			4.296	0.65			5.948	0.675
		2.363	0.725			4.626	0.70			6.389	0.725
		2.526	0.775			4.957	0.75			6.830	0.775
		2.689	0.825			5.122	0.775			7.050	0.80
		2.852	0.875			5.287	0.80			7.270	0.825
		3.000	0.92			5.452	0.825			7.490	0.85
		3.064	0.94			5.618	0.85			7.711	0.875
						5.783	0.875			8.107	0.92
						5.948	0.90			8.460	0.96
						6.212	0.94				
						6.477	0.98				

Table II. Porous LEX model pressure orifice locations.

M_∞	q_∞ (psf)	p_∞ (psf)	p_0 (psf)	Re (10^{-6})	T_0 (^0F)	$Dewpt$ (^0F)
1.60	454.8	253.8	1079	2.0	125	-31
1.80	455.5	200.8	1154	2.0	125	-30
2.10	442.8	143.4	1312	2.0	125	-28

*Table III.   Test conditions for the porous LEX model in the NASA LaRC
UPWT Test Section 1.*

M_∞	q_∞ (psf)	C_p uncertainty, ΔC_p (95% C.L.)
1.6	454.8	±0.00317
1.8	455.5	±0.00316
2.1	442.8	±0.00325

$$\Delta C_p = \frac{\Delta p}{q_\infty} = \frac{0.001 * 10 \ psi * 144 \ sq.in \,/\, sq. \ ft.}{q_\infty} = \frac{1.44 \ psf}{q_\infty}$$

*Table IV.   ESP uncertainties expressed in terms of the static pressure coefficient
(95% confidence limits (C.L.) about the mean response).*

UT-52A Balance					
Component	*Design Load (lbs or in-lbs)*	*Full Scale Output (mV)*	*Accuracy % F.S. (95% C.L.)*	*Accuracy (μV) (95% C.L.)*	*Accuracy (lbs or in-lbs) (95% C.L.)*
Normal Force	±1200	6.550	0.11	7.21	1.32
Axial Force	120	5.780	0.43	24.85	0.52
Pitching Moment	±2400	6.545	0.06	3.93	1.44
Rolling Moment	±800	5.200	0.15	7.80	1.20
Yawing Moment	±1200	5.760	0.09	5.18	1.08
Side Force	±600	5.845	0.07	4.09	0.42

Table V. NASA LaRC UT-52A balance design loads and calibration accuracies.

M_∞	q_∞, psf	C_N	C_A	C_m	C_l	C_n	C_Y
1.60	454.8	±0.00164	±0.00064	±0.000076	±0.00008	±0.000072	±0.00052
1.80	455.5	±0.00164	±0.00064	±0.000076	±0.00008	±0.000072	±0.00052
2.10	442.8	±0.00169	±0.00066	±0.000078	±0.000082	±0.000074	±0.00054

Table VI. Balance calibration accuracies expressed in terms of aerodynamic force and moment coefficients.

M_∞	q_∞ (psf)	C_p uncertainty, ΔC_p (95% C.L.)
1.6	454.8	±0.00158
1.8	455.5	±0.00158
2.1	442.8	±0.00163

$$\Delta C_p = \frac{\Delta p}{q_\infty} = \frac{0.001*5 \ psi * 144 \ sq.in \ / \ sq. \ ft.}{q_\infty} = \frac{0.72 \ psf}{q_\infty}$$

Table VII.   Chamber pressure measurement uncertainties expressed in terms of the static pressure coefficient (95% confidence limits (C.L.) about the mean response).

M_∞	$Re \ (10^{-6})$	thetaf (deg)	delcm
1.60	2.0	0.328	-0.00034
1.80	2.0	0.395	-0.00045
2.10	2.0	1.085	-0.00048

Table VIII.   Flow angle corrections for the porous LEX model in the NASA LaRC UPWT Test Section 1.

LEX	Tail	M_∞	N	Range of ESP pressures (psi)	ε (%)	2 std. dev. interval $ESP_i - PSP_i$ (psi)
Solid	Centerline	1.6	45	0.727 – 1.763	0.977	+/-0.0266
Solid	Centerline	2.1	45	0.296 – 0.980	3.146	+/-0.0400
Porous	Centerline	1.6	45	0.747 – 1.667	1.845	+/-0.0492
Porous	Centerline	2.1	45	0.266 – 0.851	3.249	+/-0.0367
Solid	Twin	1.6	45	0.708 – 1.762	1.063	+/-0.0256
Solid	Twin	2.1	45	0.276 – 0.966	2.561	+/-0.0270
Porous	Twin	1.6	45	0.755 – 1.666	0.971	+/-0.0233
Porous	Twin	2.1	45	0.257 – 0.844	1.887	+/-0.0236

Table IX. Estimates of PSP measurement accuracies at M_∞ = 1.6 and 2.1 for the solid and porous LEX with centerline and twin vertical tails.

LEX	Tail	M_∞	Estimated Regression Function	RMSE	$\pm t_{1-\alpha/2,43}(RMSE)$
Solid	Centerline	1.6	$\hat{C}_p = 0.87598\left(I_o/I\right) - 0.82317$	0.00426	+/- 0.00859
Solid	Centerline	2.1	$\hat{C}_p = 1.07827\left(I_o/I\right) - 0.6502$	0.00656	+/- 0.01323
Porous	Centerline	1.6	$\hat{C}_p = 0.79151\left(I_o/I\right) - 0.8165$	0.00788	+/- 0.01590
Porous	Centerline	2.1	$\hat{C}_p = 0.9786\left(I_o/I\right) - 0.6334$	0.00604	+/- 0.01218
Solid	Twin	1.6	$\hat{C}_p = 0.70784\left(I_o/I\right) - 0.87815$	0.00410	+/- 0.00827
Solid	Twin	2.1	$\hat{C}_p = 0.99028\left(I_o/I\right) - 0.6093$	0.00457	+/- 0.00922
Porous	Twin	1.6	$\hat{C}_p = 0.9884\left(I_o/I\right) - 0.8857$	0.00372	+/- 0.00751
Porous	Twin	2.1	$\hat{C}_p = 1.06394\left(I_o/I\right) - 0.6387$	0.00388	+/- 0.00782

Table X. Estimated regression functions from PSP in-situ calibrations; $\alpha = 8^o$.

M_∞	$C_{p,v}$
1.6	-0.5580
1.8	-0.4409
2.1	-0.3239

Table XI. Vacuum pressure coefficient at supersonic speeds.

Figure 1. Photograph of the porous LEX model installed in Test Section 1 of the NASA Langley Research Center Unitary Plan Wind Tunnel.
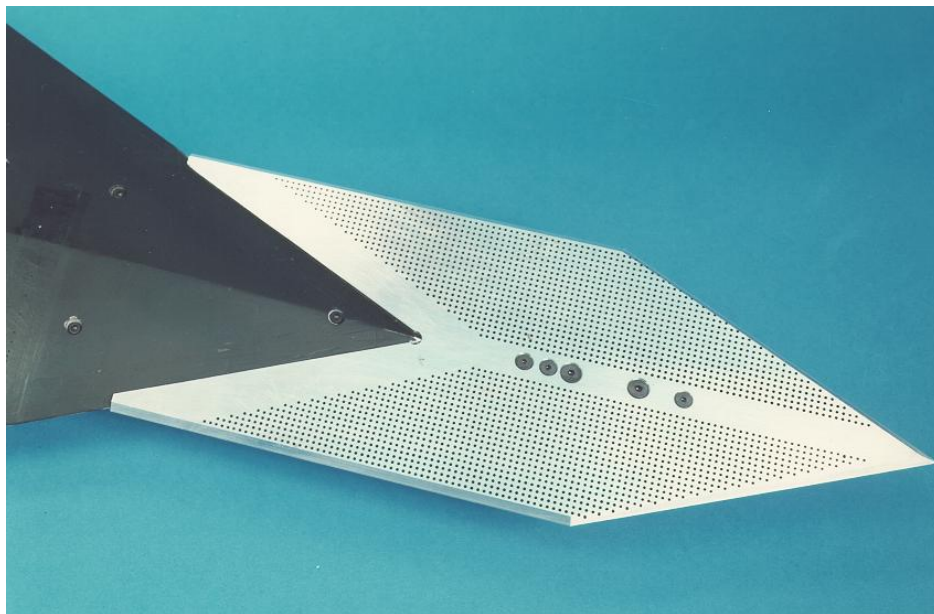
Figure 2. Close-up view of the porous LEX.
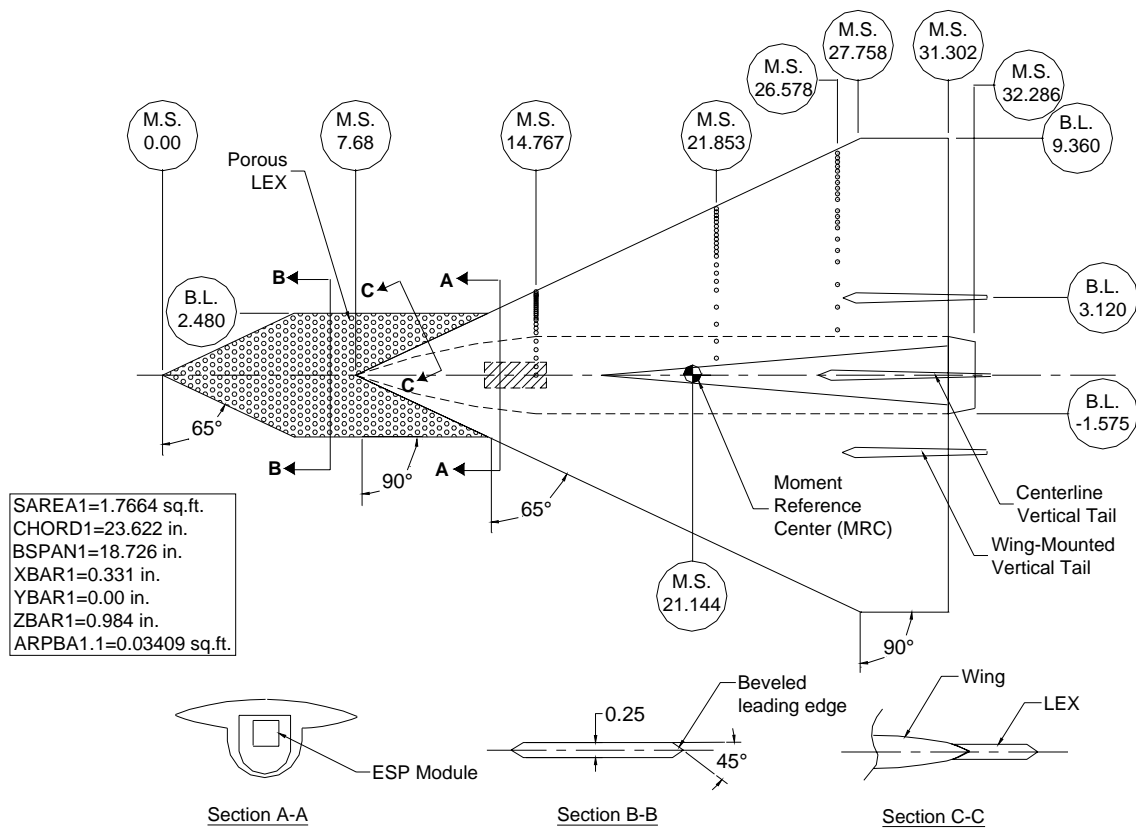
Figure 3. Planview of the porous LEX model. (Dimensions are in inches.)
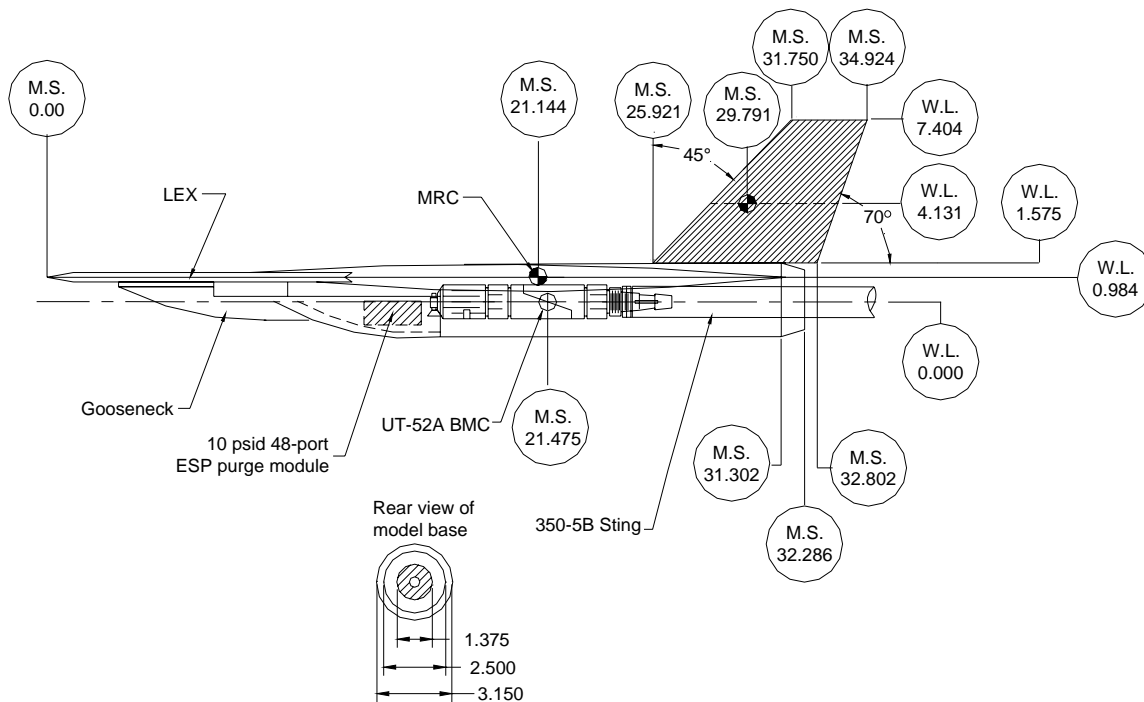
Figure 4. Sideview of the porous LEX model with centerline vertical tail.
(Dimensions are in inches.)
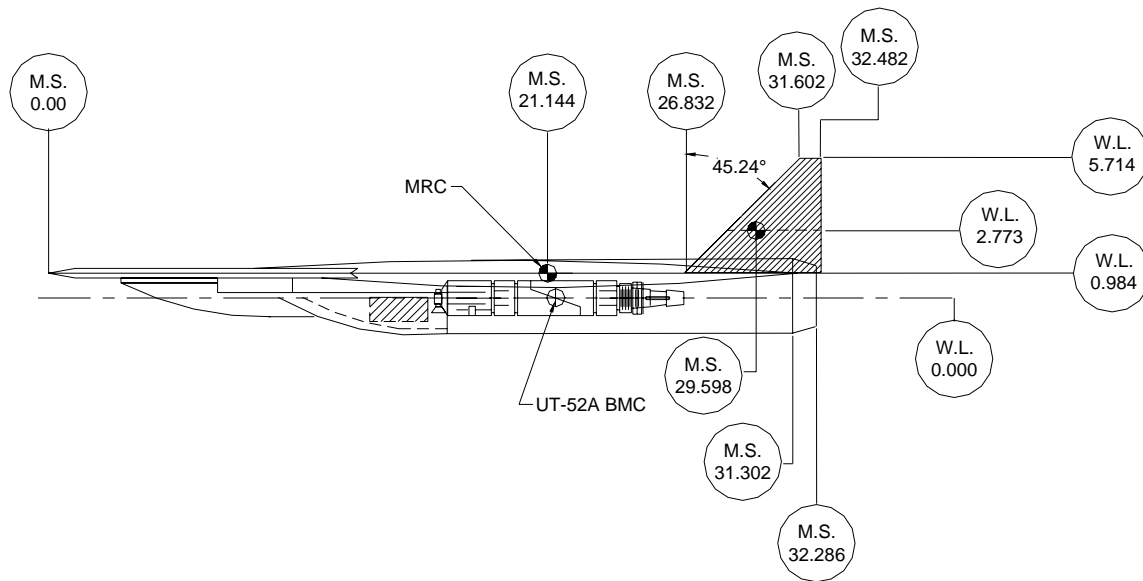
Figure 5. Sideview of the porous LEX model with twin vertical tails.
(Dimensions are in inches.)
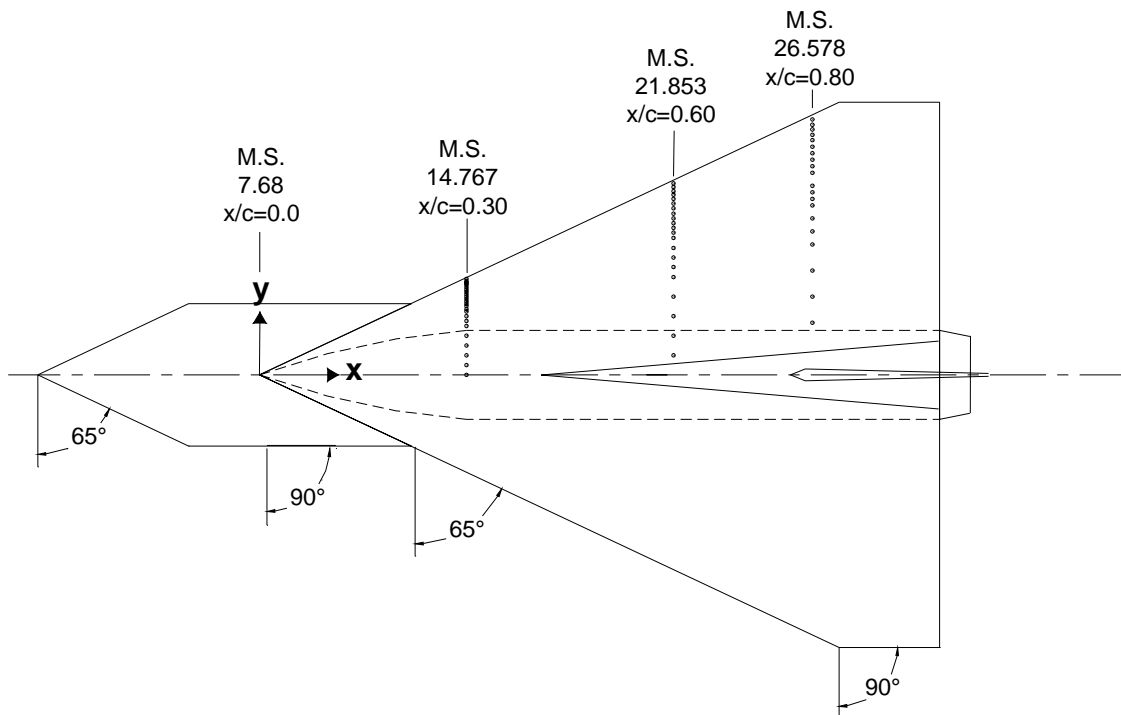
Figure 6. Upper surface static pressure measurement stations on the porous LEX model.
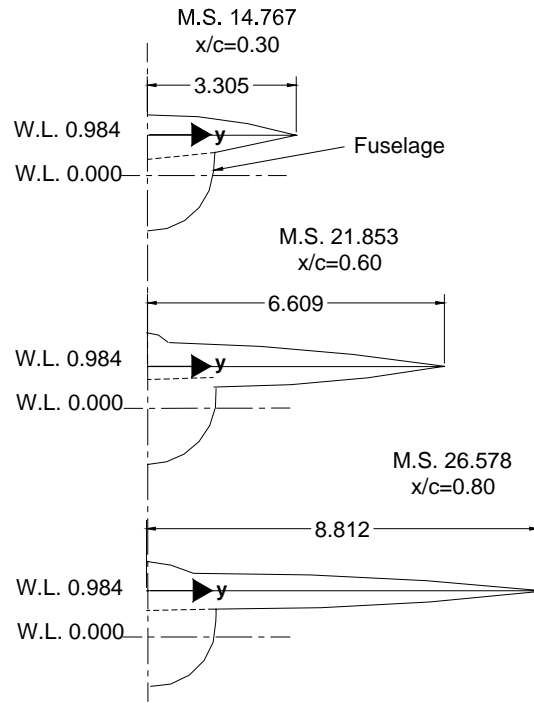
Figure 7. Cross-sections of the porous LEX model at the three pressure measurement
stations.   (Dimensions are in inches.)
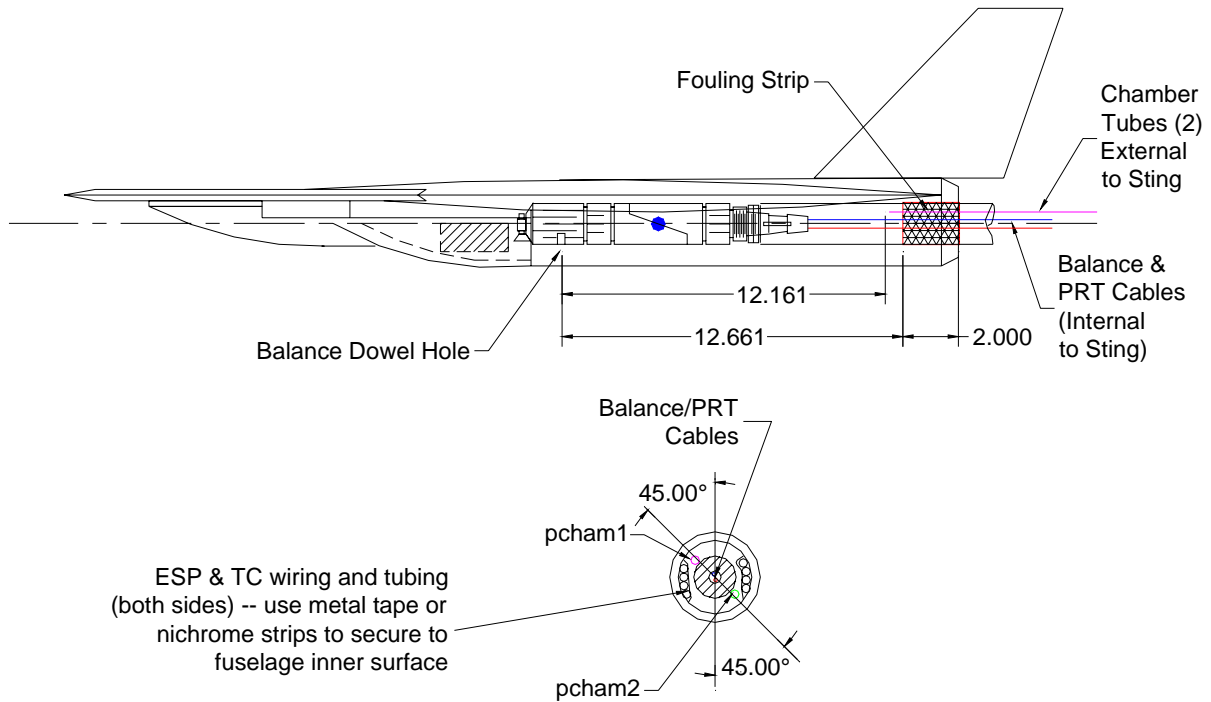
Figure 8. Chamber pressure tube and fouling strip layout on porous LEX model.
(Dimensions are in inches.)
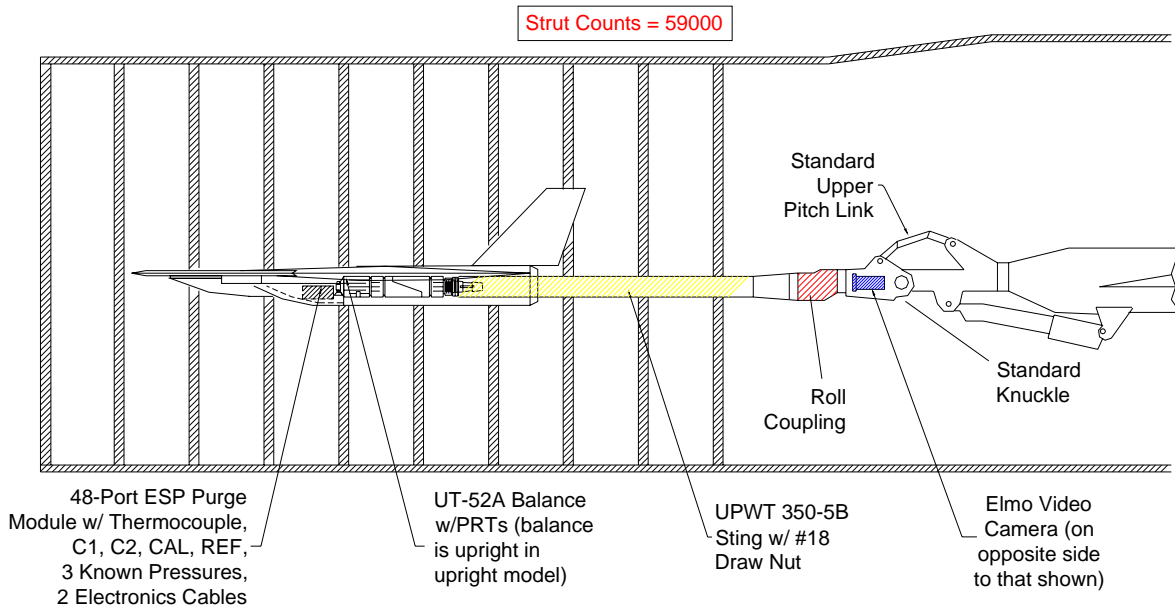
Figure 9. Sketch of porous LEX model installation hardware components.
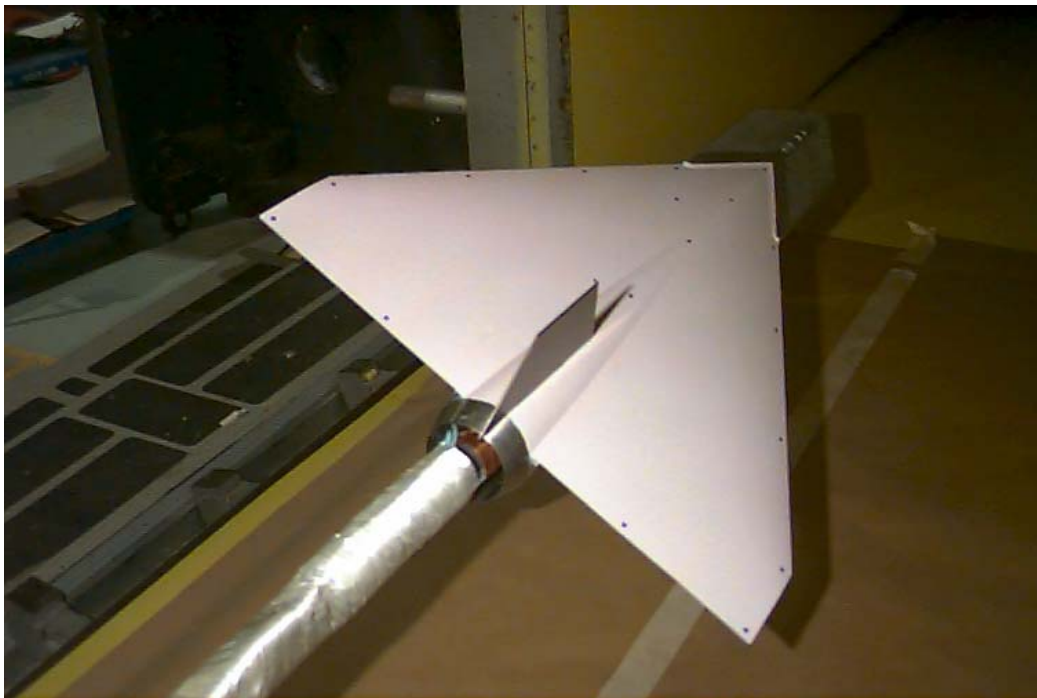
Figure 10. Photograph of the porous LEX model with PSP coating applied to the wing upper surface; centerline vertical tail on.

40
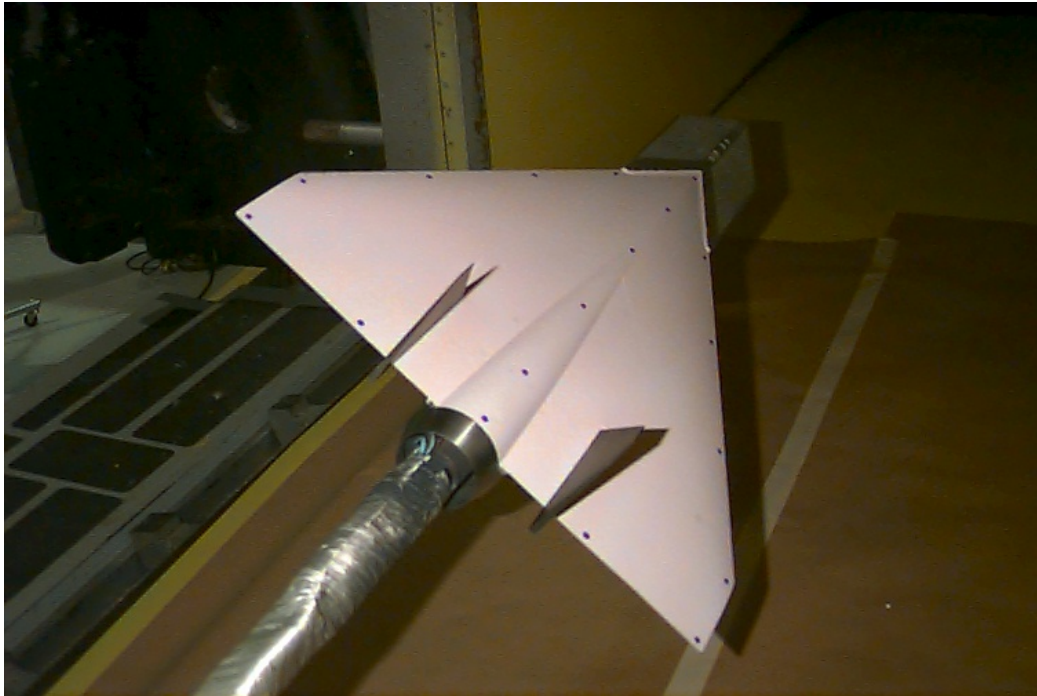
Figure 11. Photograph of the porous LEX model with PSP coating applied to the wing
upper surface; twin vertical tails on.
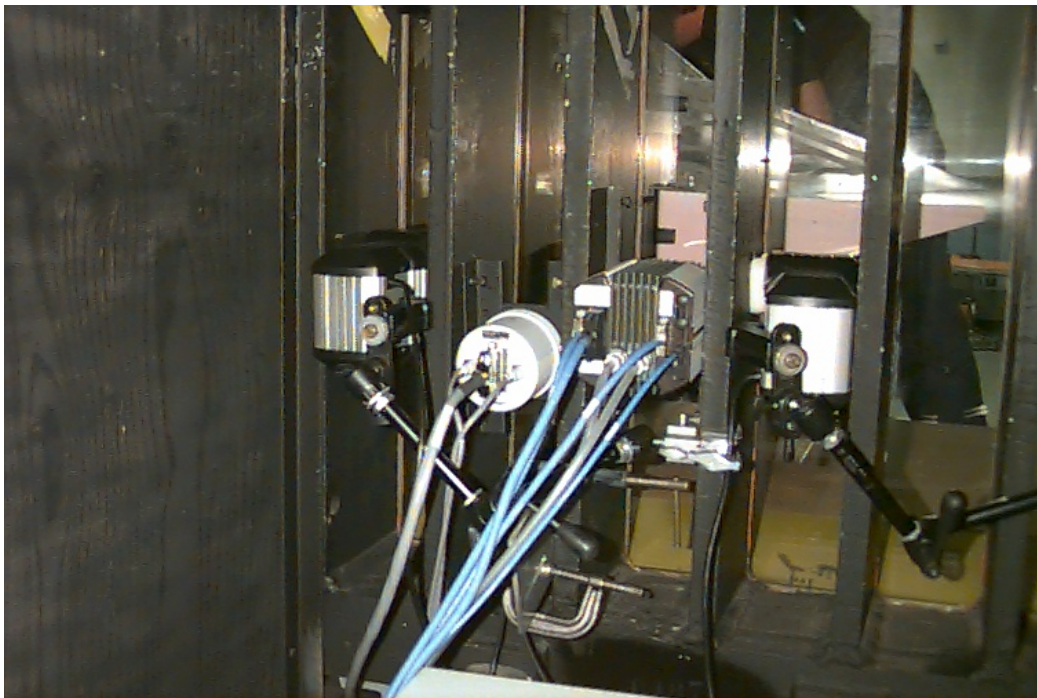
Figure 12. Photograph of PSP cameras and UV lamp installation.
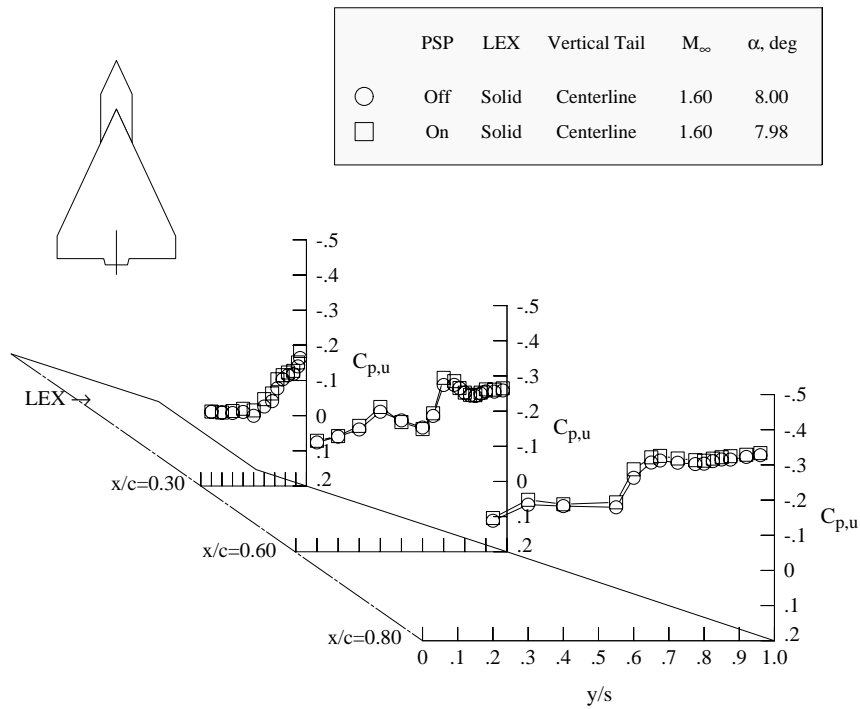
(a) $M_\infty = 1.6$.
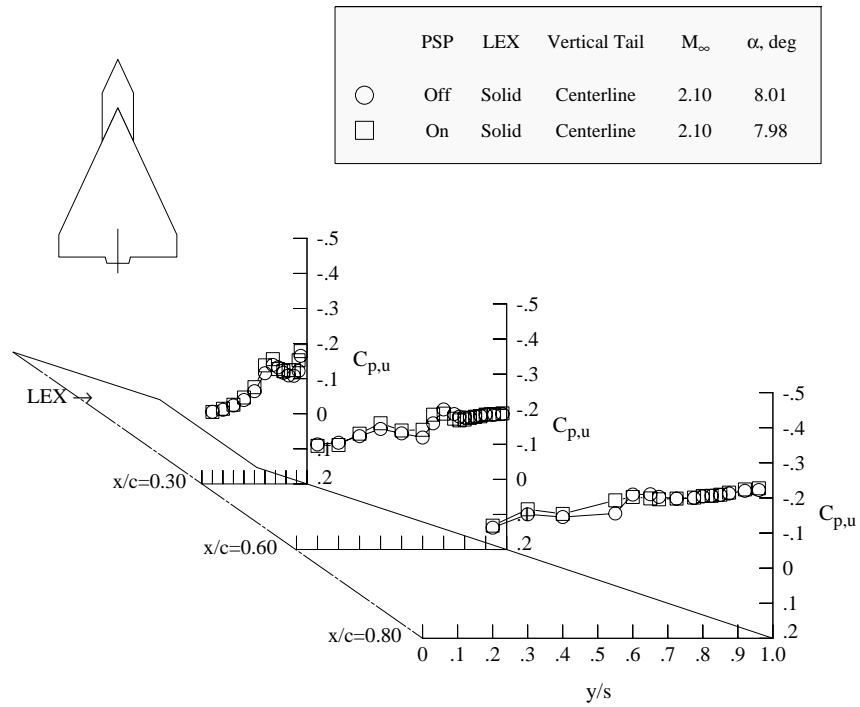
(b) $M_\infty = 2.1$.

Figure 13. Comparison of unpainted and painted wing ESP pressure measurements with solid LEX and centerline vertical tail at $\alpha = 8^\circ$.
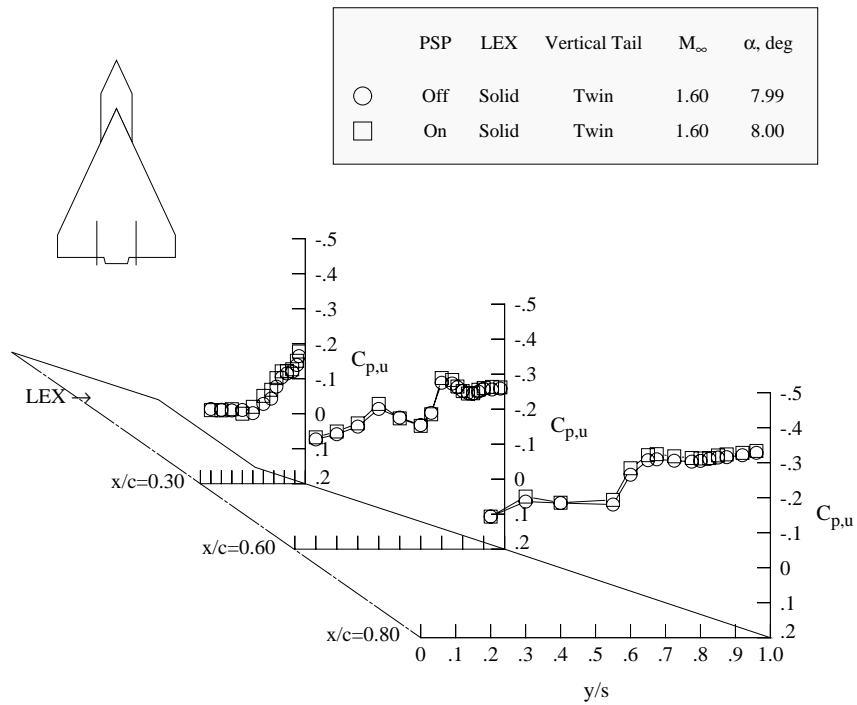
(a) $M_\infty = 1.6$.
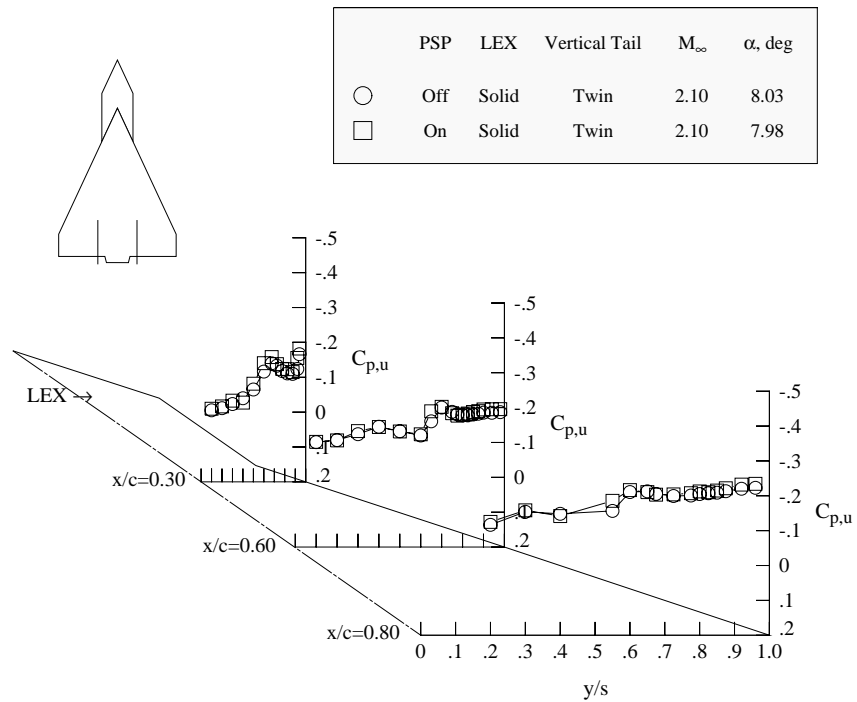
(b) $M_\infty = 2.1$.

Figure 14. Comparison of unpainted and painted wing ESP pressure measurements with solid LEX and twin vertical tails at $\alpha = 8^\circ$.
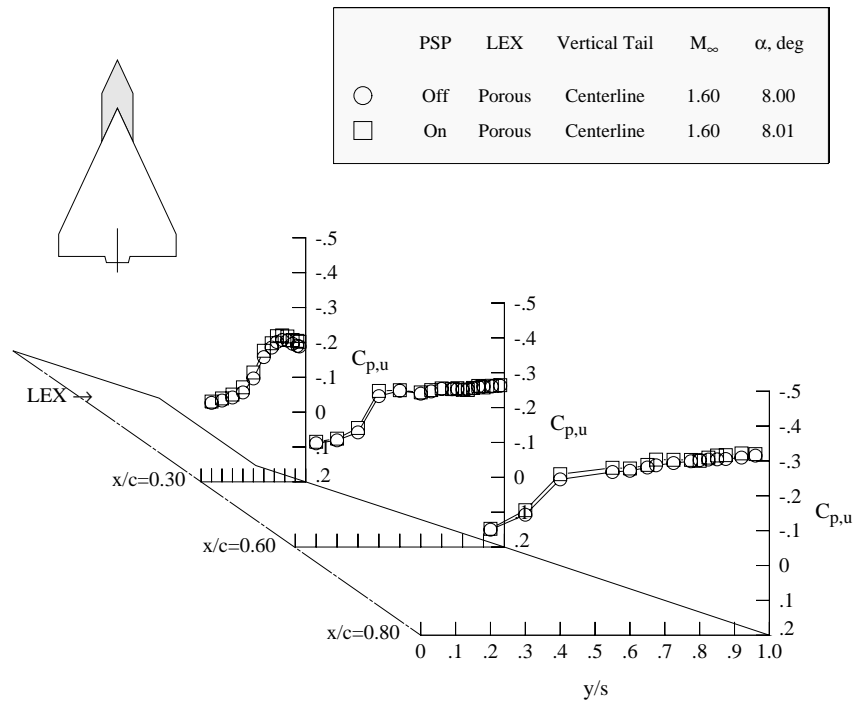
(a) $M_\infty = 1.6$.
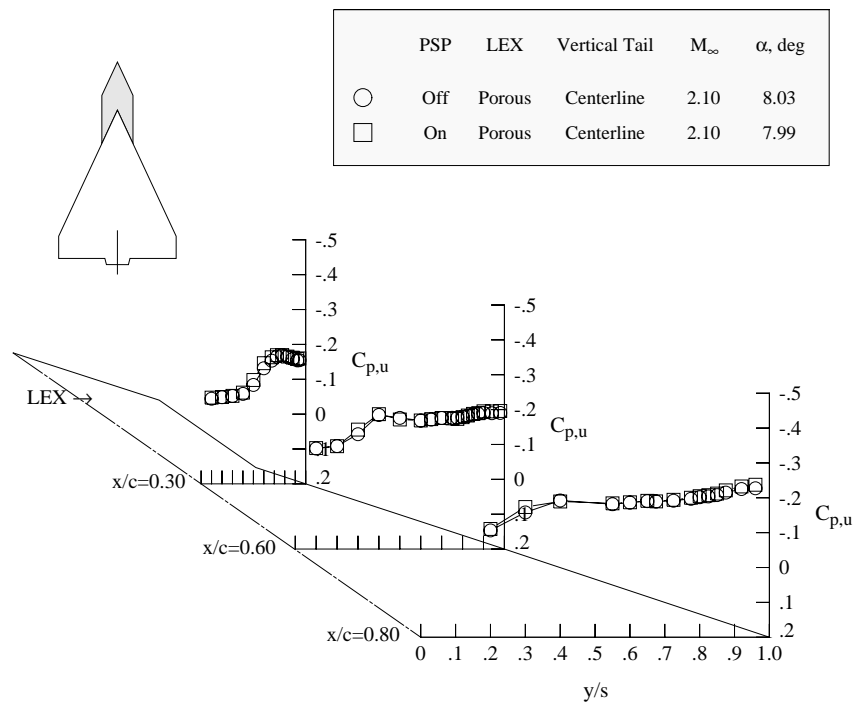
(b) $M_\infty = 2.1$.

Figure 15. Comparison of unpainted and painted wing ESP pressure measurements with porous LEX and centerline vertical tail at $\alpha = 8^\circ$.

	PSP	LEX	Vertical Tail	M_∞	α, deg
○	Off	Porous	Twin	1.60	7.99
□	On	Porous	Twin	1.60	8.00

(a) $M_\infty = 1.6$.

	PSP	LEX	Vertical Tail	M_∞	α, deg
○	Off	Porous	Twin	2.10	8.01
□	On	Porous	Twin	2.10	7.98
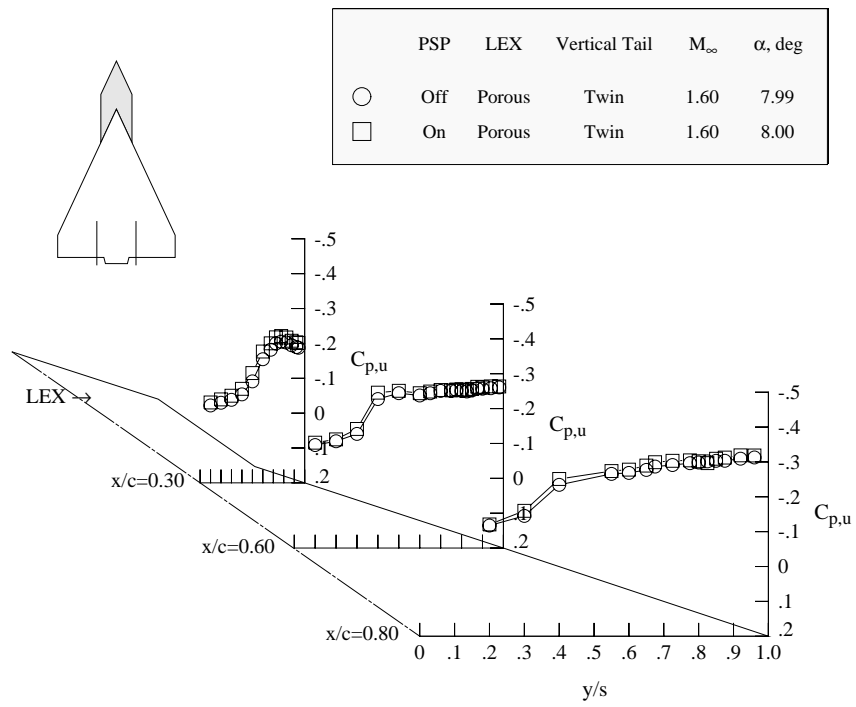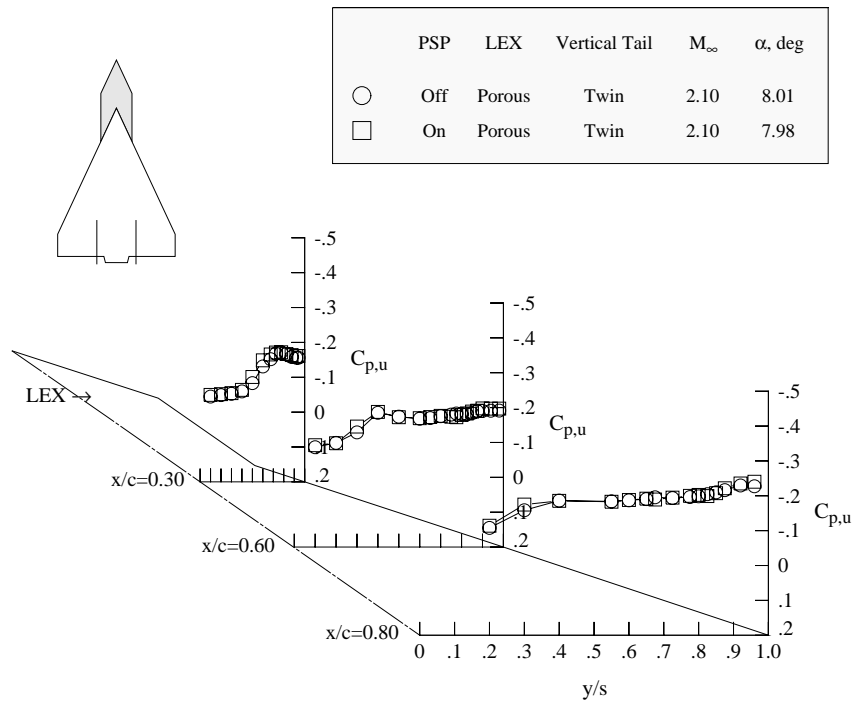
(b) $M_\infty = 2.1$.

Figure 16. Comparison of unpainted and painted wing ESP pressure measurements with porous LEX and twin vertical tails at $\alpha = 8^o$.

	Test	Run	M_∞	Point	PSP	LEX	Vertical Tail
○	1858	34	1.60	563.	Off	Solid	Centerline
□	1858	61	1.60	882.	On	Solid	Centerline

Δ's are the C_p differences between PSP off and PSP on at the nominal values of the independent variable

Dashed lines computed from manufacturer's uncertainty (95-percent confidence) for 10 psid ESP module
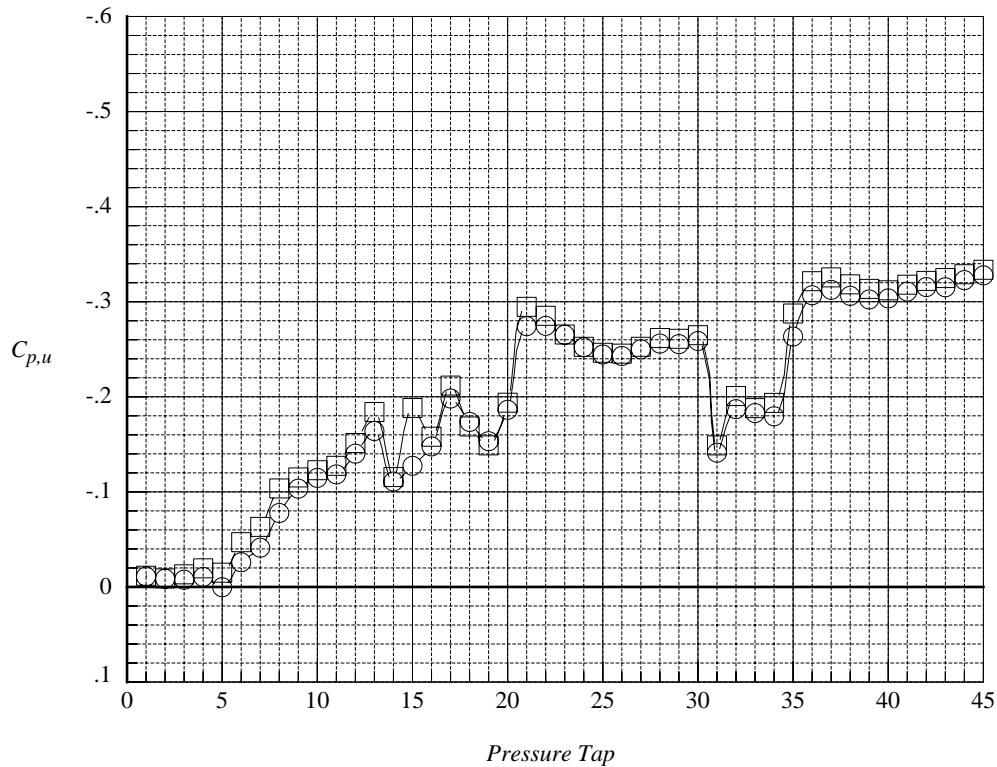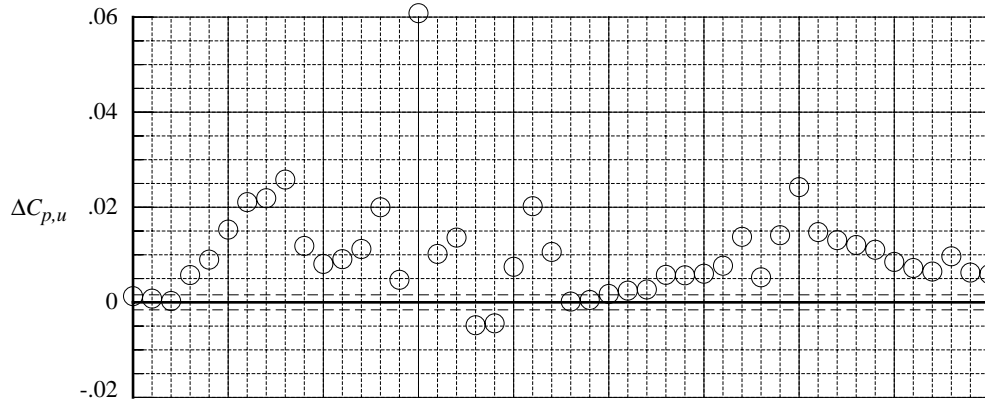
(a) $M_\infty = 1.6$.

Figure 17. Data scatter plot of unpainted and painted wing ESP pressure measurements with solid LEX and centerline vertical tail at $\alpha = 8^o$.

46

	Test	Run	M_∞	Point	PSP	LEX	Vertical Tail
○	1858	40	2.10	638.	Off	Solid	Centerline
□	1858	62	2.10	886.	On	Solid	Centerline

Δ's are the C_p differences between PSP off and PSP on at the nominal values of the independent variable

Dashed lines computed from manufacturer's uncertainty (95-percent confidence) for 10 psid ESP module
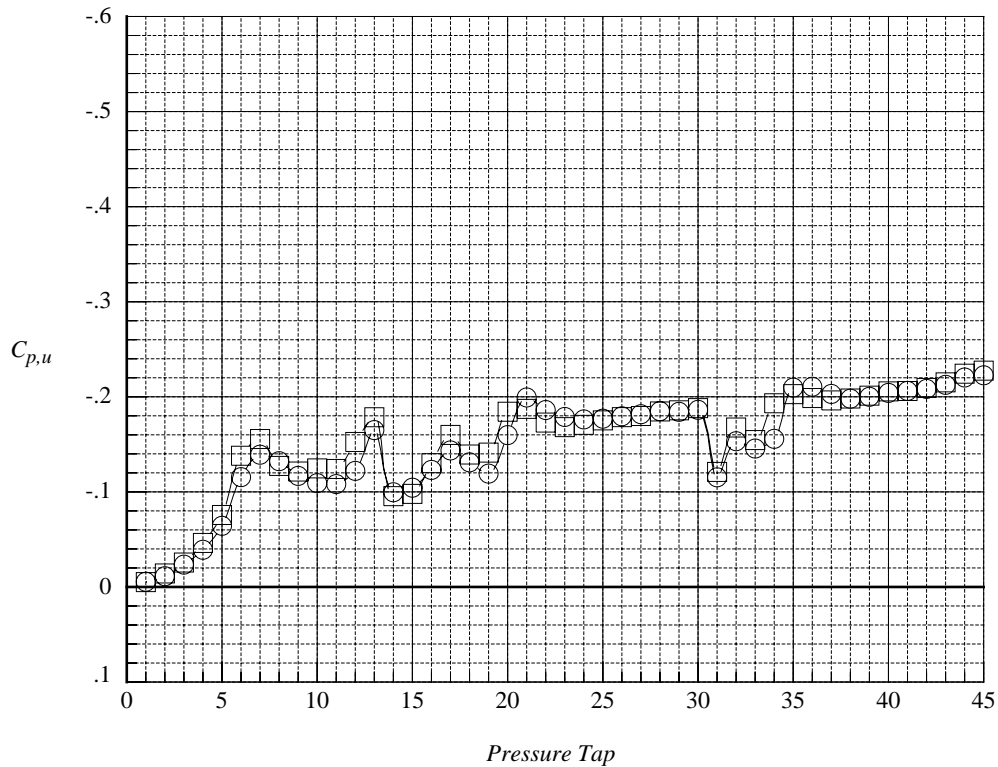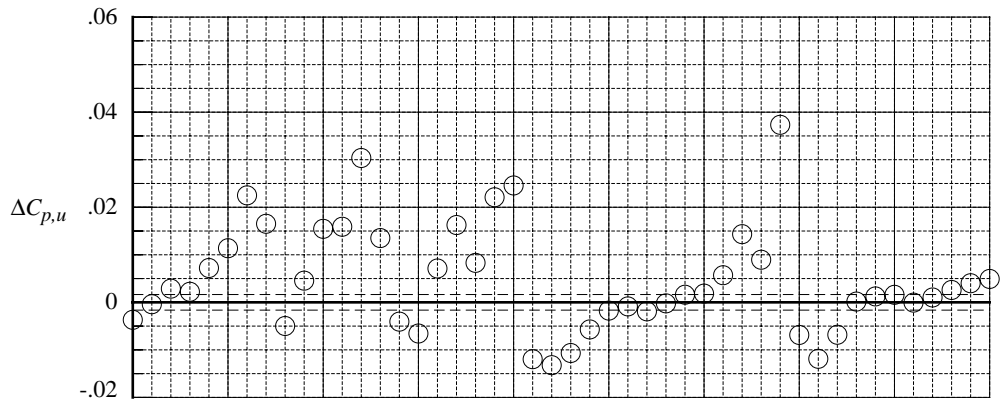
(b) $M_\infty = 2.1$.

Figure 17. Concluded.

	Test	Run	M_∞	Point	PSP	LEX	Vertical Tail
○	1858	43	1.60	698.	Off	Porous	Centerline
□	1858	57	1.60	858.	On	Porous	Centerline

Δ's are the C_p differences between PSP off and PSP on at the nominal values of the independent variable

Dashed lines computed from manufacturer's uncertainty (95-percent confidence) for 10 psid ESP module
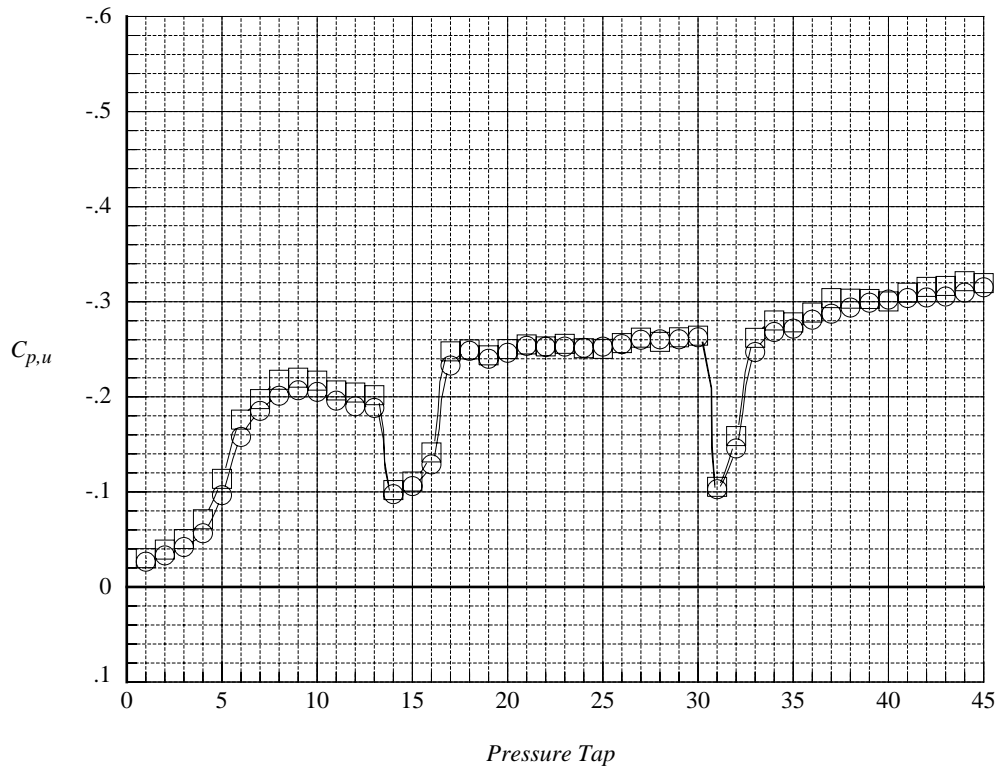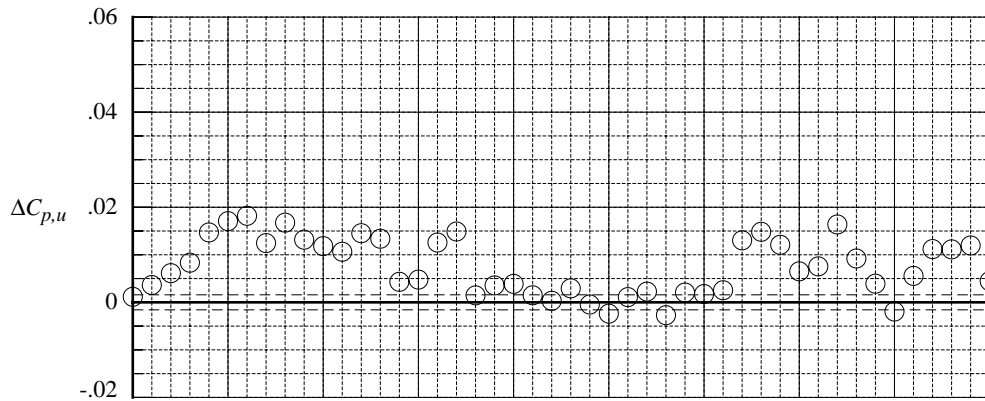
(a) $M_\infty = 1.6$.

Figure 18. Data scatter plot of unpainted and painted wing ESP pressure measurements with porous LEX and centerline vertical tail at $\alpha = 8^o$.

	Test	Run	M_∞	Point	PSP	LEX	Vertical Tail
○	1858	49	2.10	782.	Off	Porous	Centerline
□	1858	58	2.10	862.	On	Porous	Centerline

Δ's are the C_p differences between PSP off and PSP on at the nominal values of the independent variable

Dashed lines computed from manufacturer's uncertainty (95-percent confidence) for 10 psid ESP module
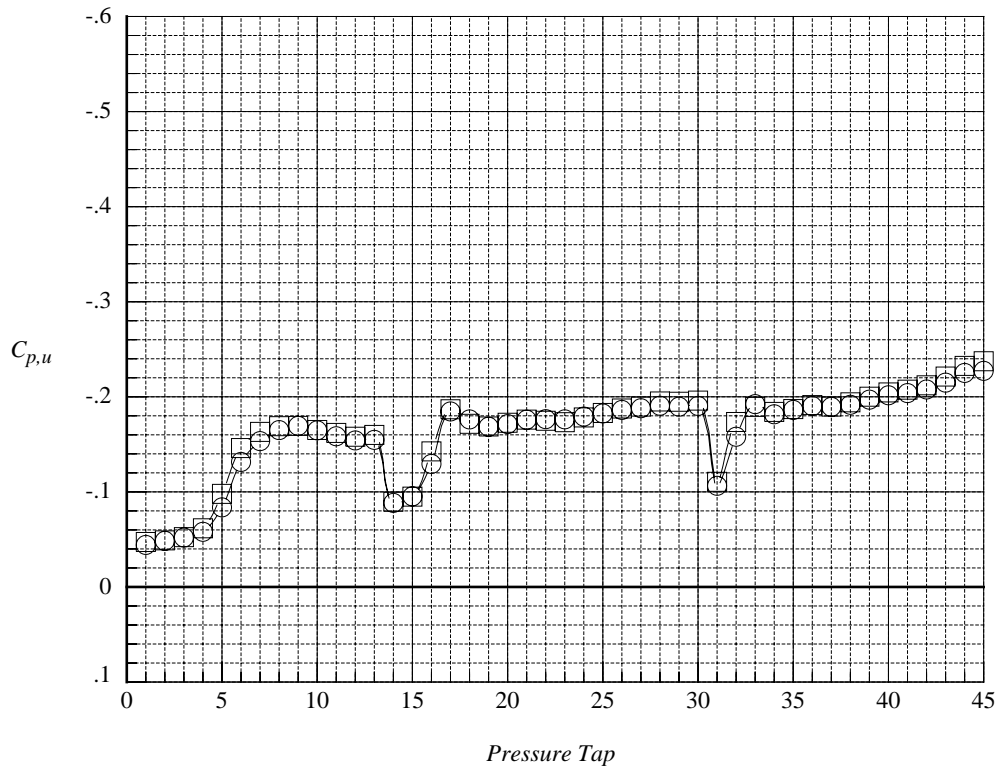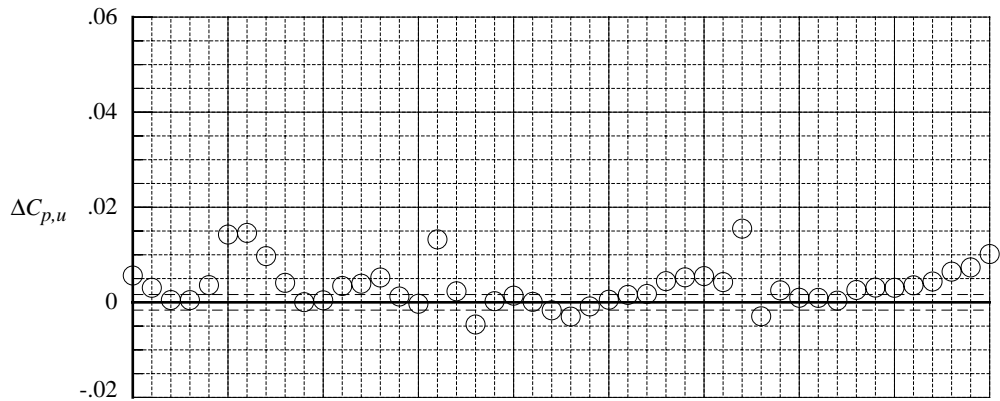
(b) $M_\infty = 2.1$.

Figure 18. Concluded.

	Test	Run	M_∞	Point	PSP	LEX	Vertical Tail
○	1858	25	1.60	422.	Off	Solid	Twin
□	1858	77	1.60	1088.	On	Solid	Twin

Δ's are the C_p differences between PSP off and PSP on at the nominal values of the independent variable

Dashed lines computed from manufacturer's uncertainty (95-percent confidence) for 10 psid ESP module
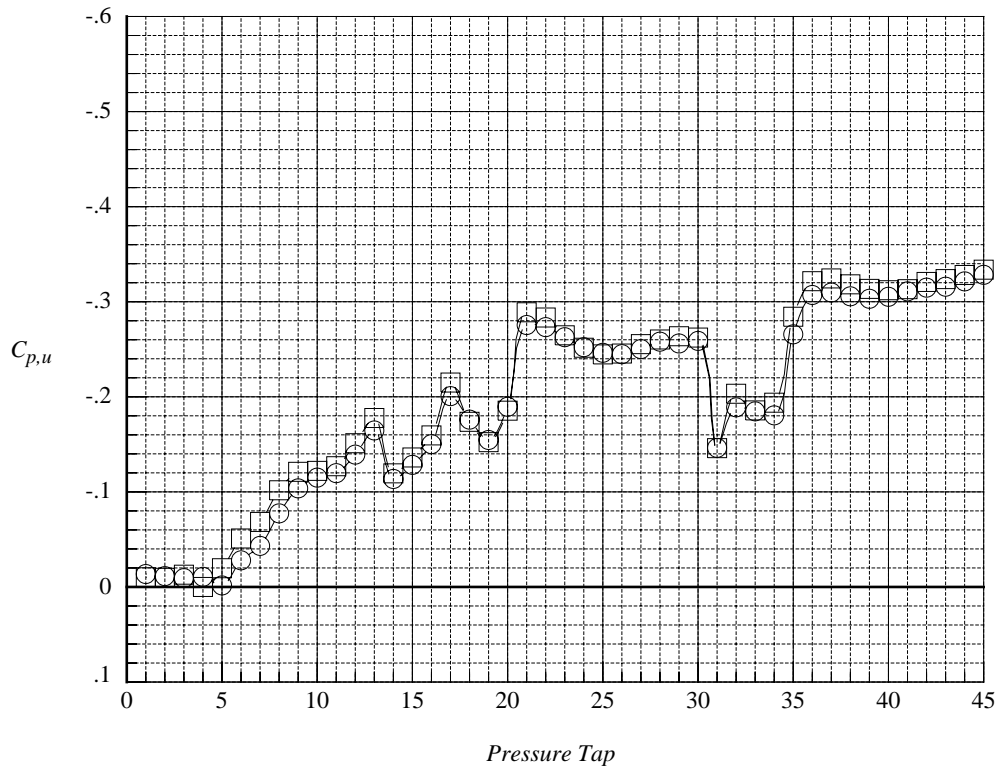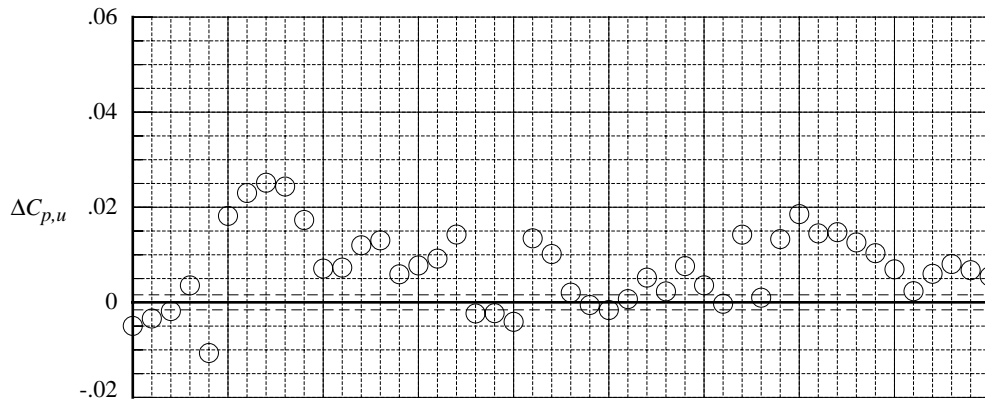
(a) $M_\infty = 1.6$.

Figure 19. Data scatter plot of unpainted and painted wing ESP pressure measurements with solid LEX and twin vertical tails at $\alpha = 8^o$.

	Test	Run	M_∞	Point	PSP	LEX	Vertical Tail
○	1858	31	2.10	505.	Off	Solid	Twin
□	1858	78	2.10	1092.	On	Solid	Twin

Δ's are the C_p differences between PSP off and PSP on at the nominal values of the independent variable

Dashed lines computed from manufacturer's uncertainty (95-percent confidence) for 10 psid ESP module
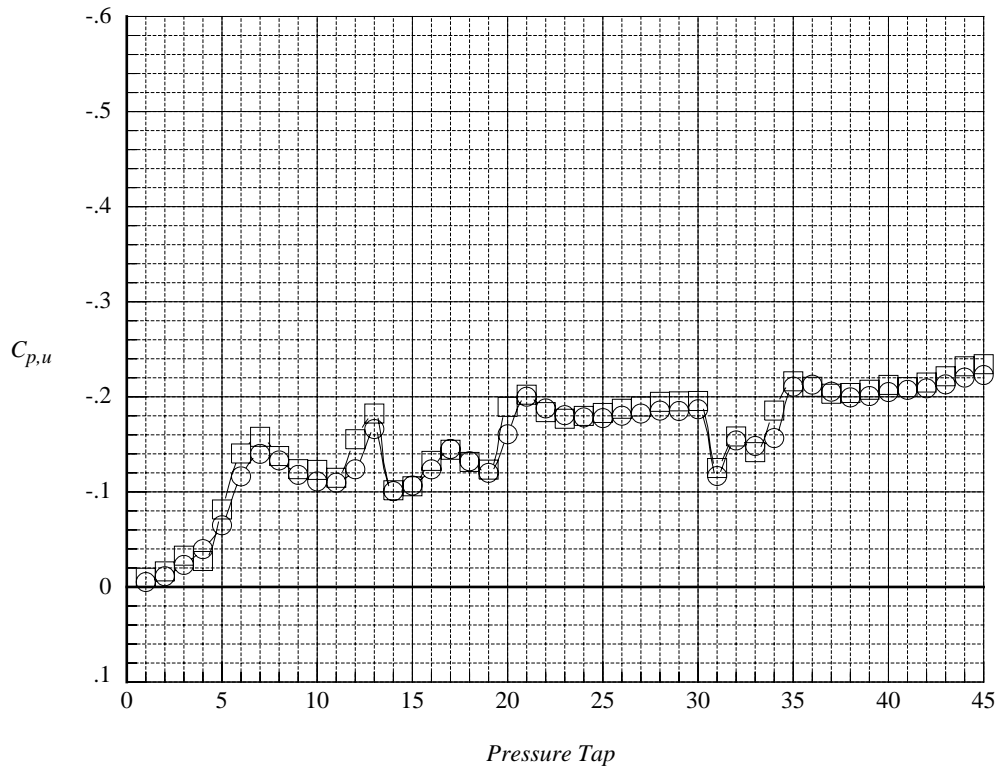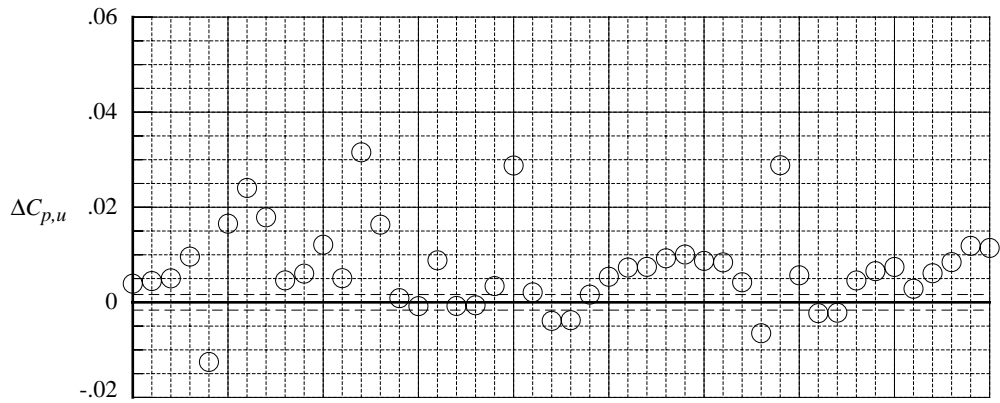
(b) $M_\infty = 2.1$.

Figure 19. Concluded.

51

	Test	Run	M_∞	Point	PSP	LEX	Vertical Tail
○	1858	10	1.60	258.	Off	Porous	Twin
□	1858	81	1.60	1125.	On	Porous	Twin

Δ's are the C_p differences between PSP off and PSP on at the nominal values of the independent variable

Dashed lines computed from manufacturer's uncertainty (95-percent confidence) for 10 psid ESP module
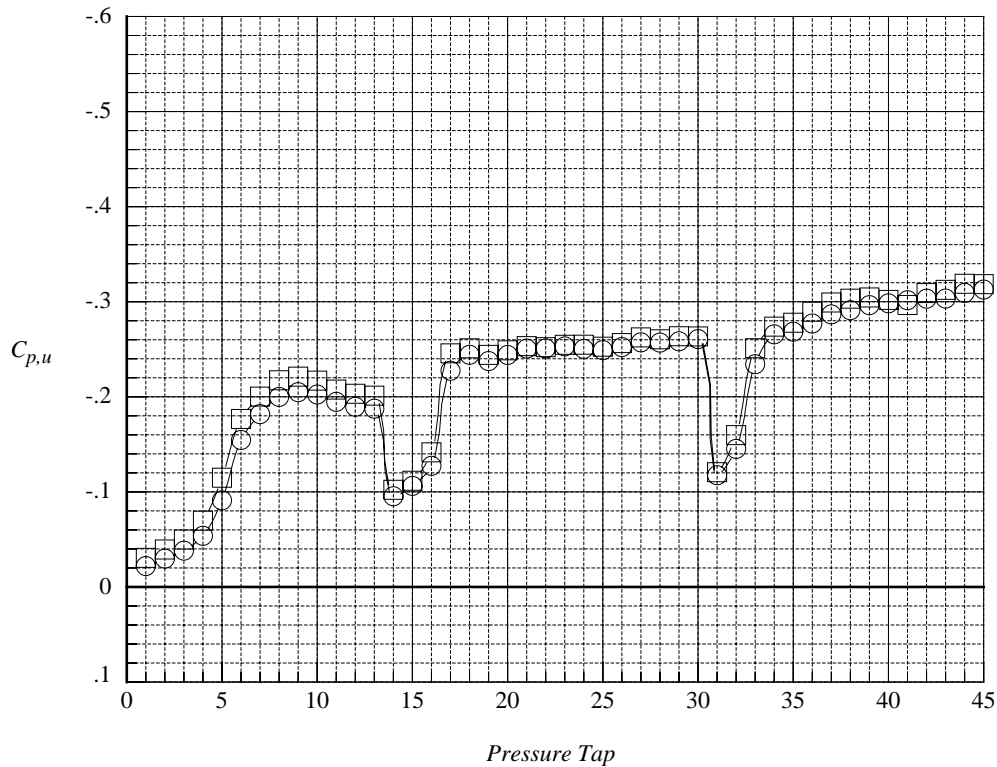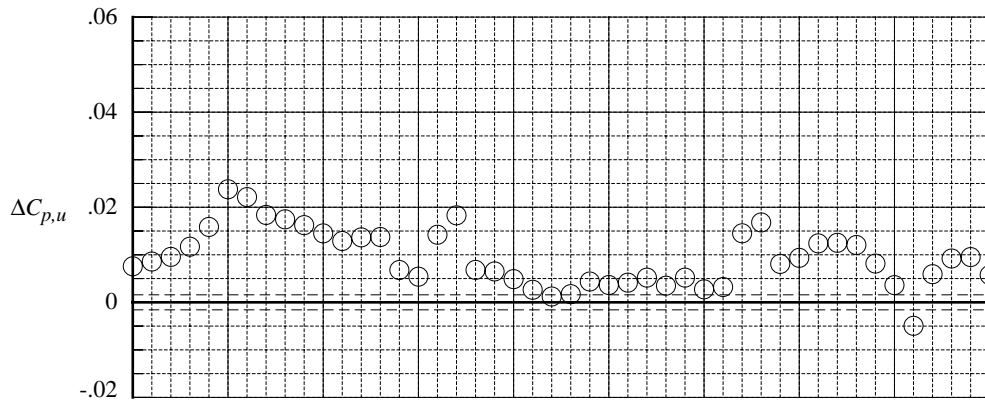
(a) $M_\infty = 1.6$.

Figure 20. Data scatter plot of unpainted and painted wing ESP pressure measurements with porous LEX and twin vertical tails at $\alpha = 8^\circ$.

	Test	Run	M_∞	Point	PSP	LEX	Vertical Tail
○	1858	13	2.10	290.	Off	Porous	Twin
□	1858	82	2.10	1129.	On	Porous	Twin

Δ's are the C_p differences between PSP off and PSP on at the nominal values of the independent variable

Dashed lines computed from manufacturer's uncertainty (95-percent confidence) for 10 psid ESP module
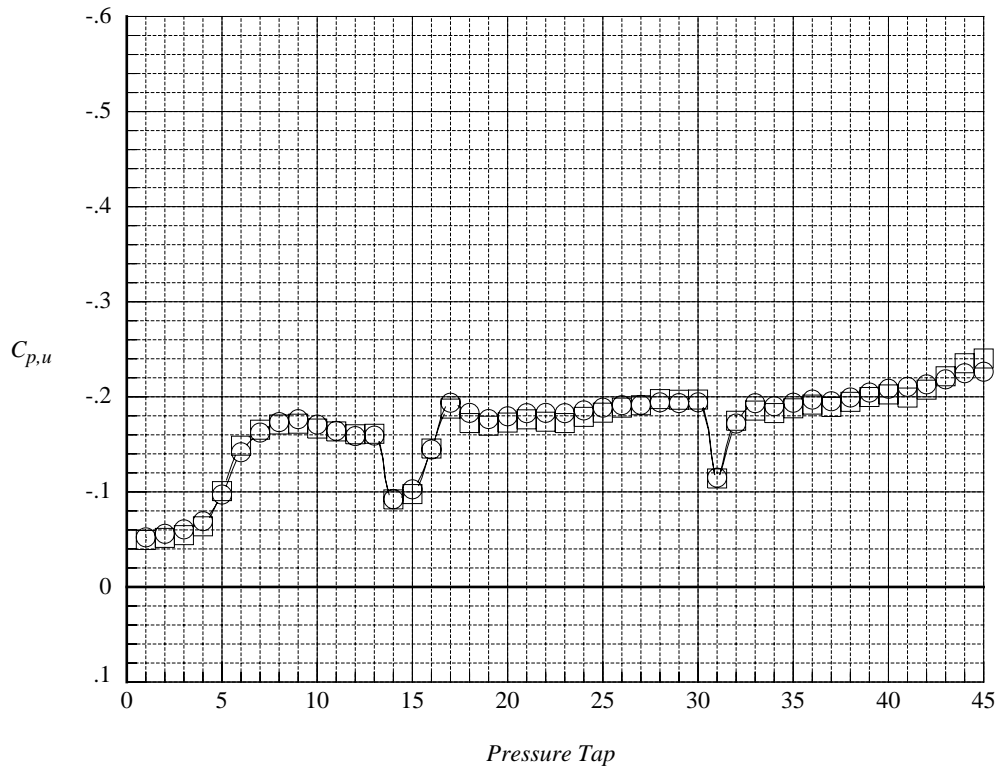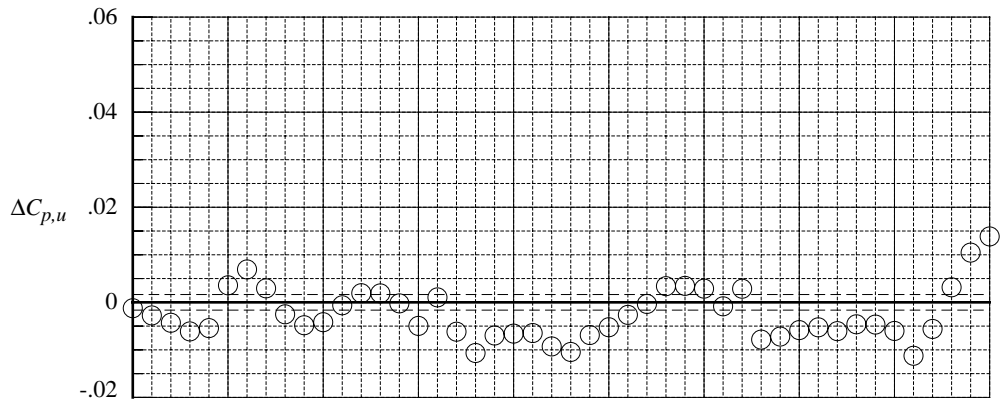
(b) $M_\infty = 2.1.$

Figure 20. Concluded.

MACH=1.60, AOA=8 DEGREES, X/C=0.30

MACH=1.60, AOA=8 DEGREES, X/C=0.60

MACH=1.60, AOA=8 DEGREES, X/C=0.80

LVS image at x/c=0.6
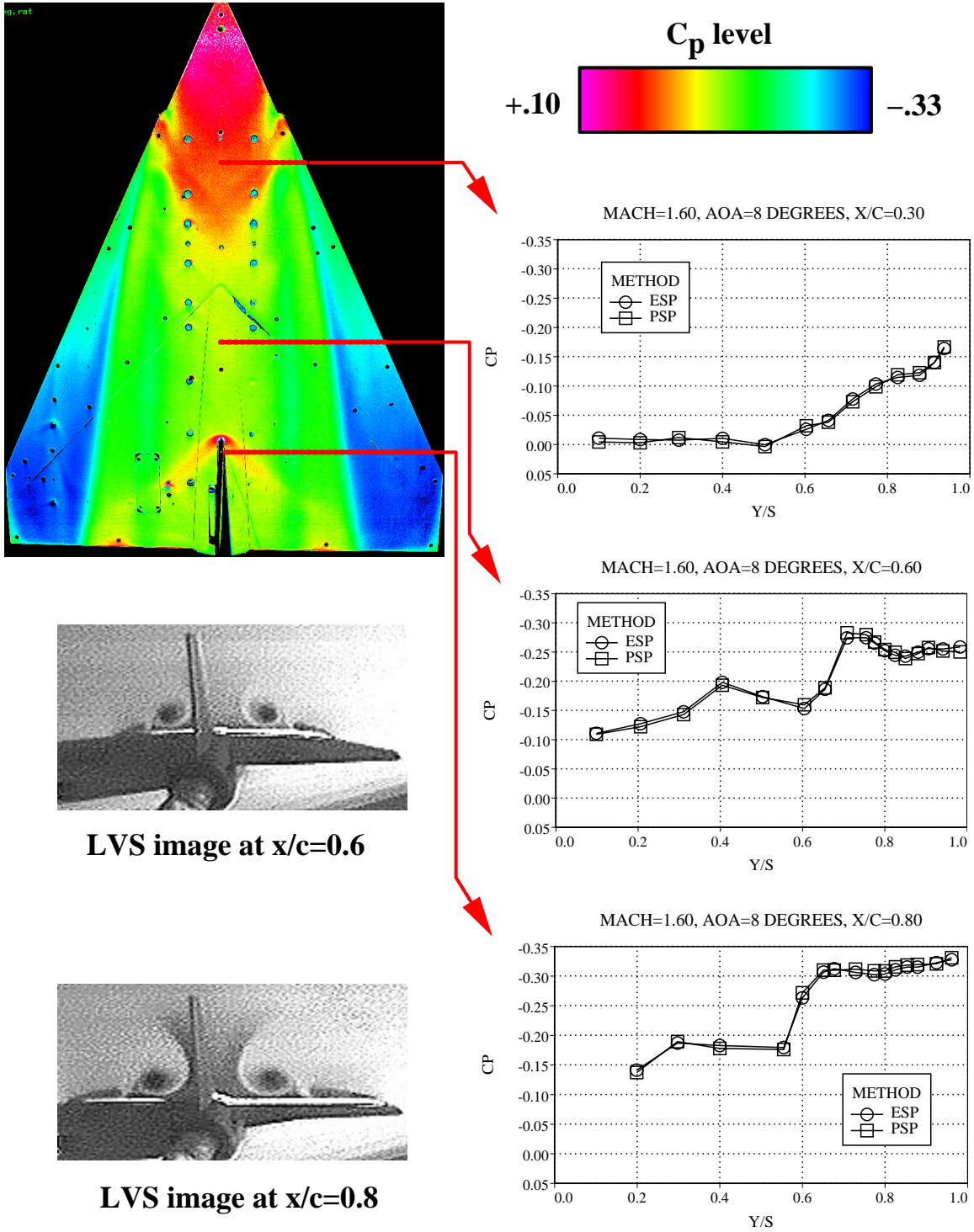
LVS image at x/c=0.8

(a) $M_\infty = 1.6$.

Figure 21. Composite plots of PSP and ESP measurements and LVS flow visualization images with solid LEX and centerline vertical tail; $\alpha = 8^\circ$.

C_p level

$+.02$ $-.22$

MACH=2.10, AOA=8 DEGREES, X/C=0.30

METHOD
ESP
PSP

CP

Y/S

LVS image at x/c=0.6

MACH=2.10, AOA=8 DEGREES, X/C=0.60

METHOD
ESP
PSP

CP

Y/S

LVS image at x/c=0.8

MACH=2.10, AOA=8 DEGREES, X/C=0.80

METHOD
ESP
PSP

CP

Y/S
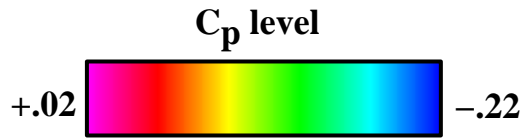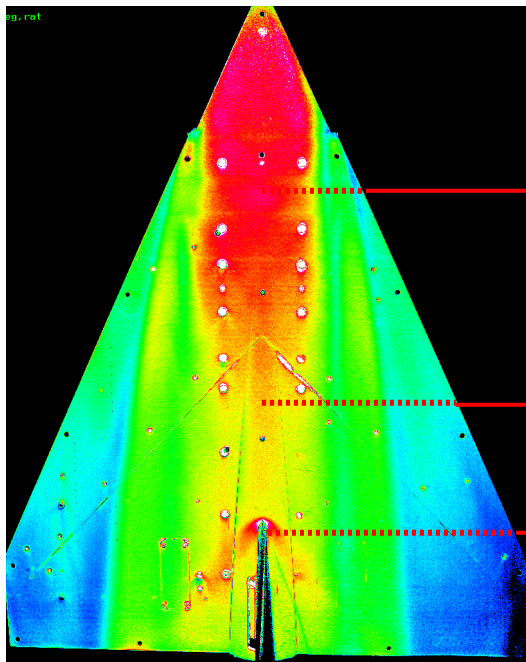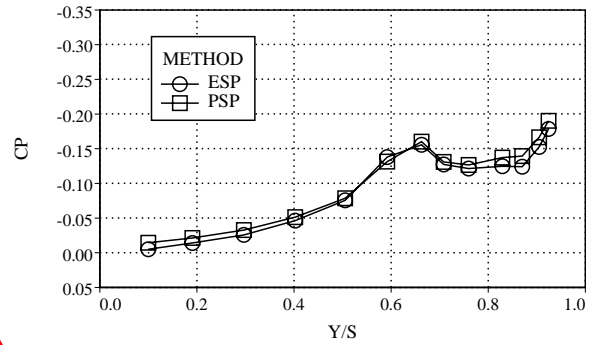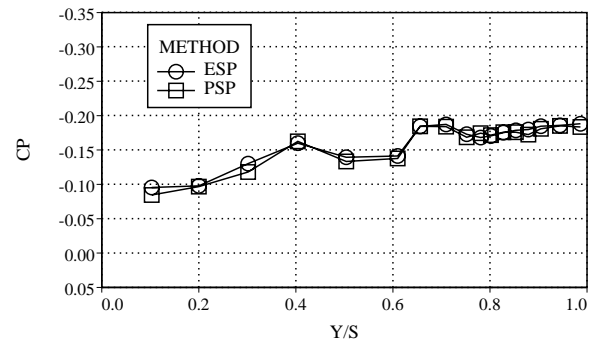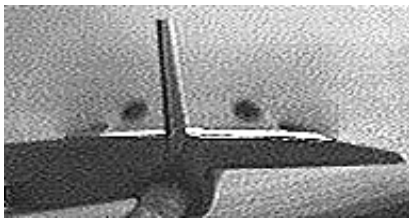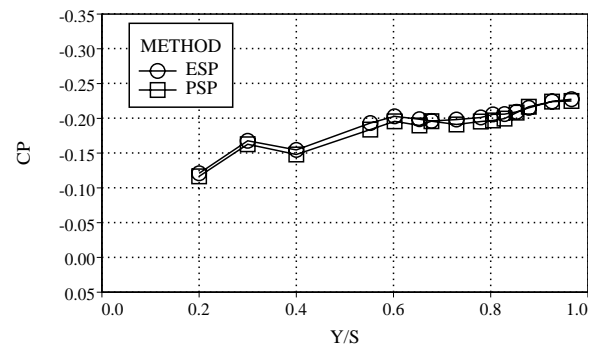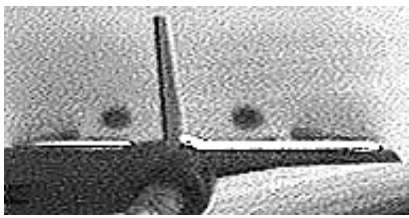
(b) $M_\infty = 2.1$.

Figure 21. Concluded.

C_p level

+.10   −.33

MACH=1.60, AOA=8 DEGREES, X/C=0.30

METHOD
ESP
PSP

MACH=1.60, AOA=8 DEGREES, X/C=0.60

METHOD
ESP
PSP

MACH=1.60, AOA=8 DEGREES, X/C=0.80

METHOD
ESP
PSP

LVS image at x/c=0.6
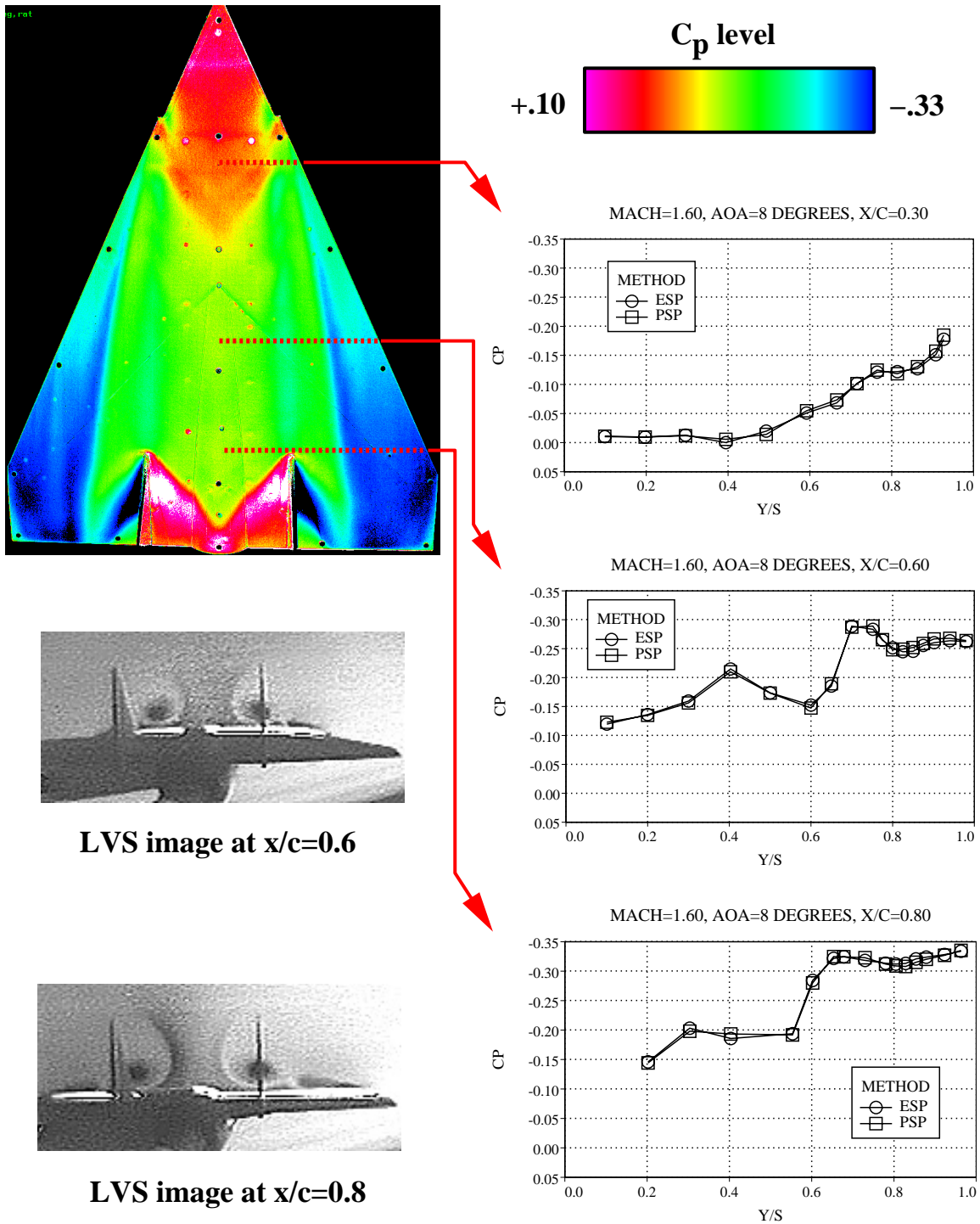
LVS image at x/c=0.8

(a) $M_\infty = 1.6$.

Figure 22. Composite plots of PSP and ESP measurements and LVS flow visualization
images with solid LEX and twin vertical tails; $\alpha = 8^\circ$.

C$_p$ level

+.02   −.22
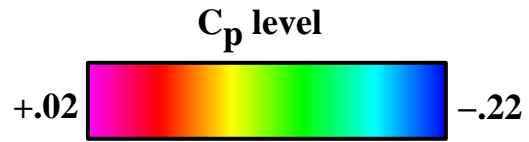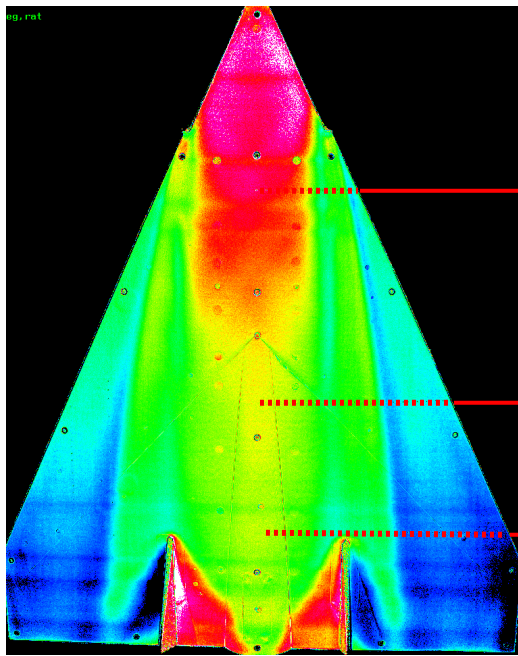
MACH=2.10, AOA=8 DEGREES, X/C=0.30
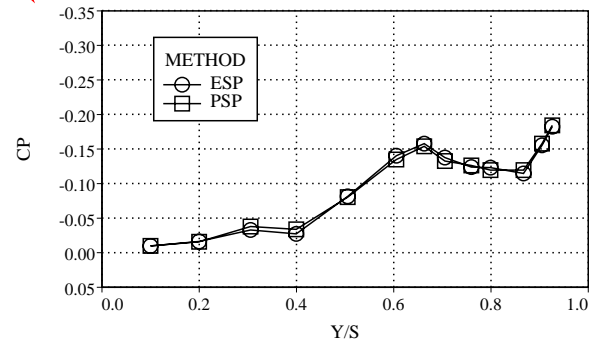
MACH=2.10, AOA=8 DEGREES, X/C=0.60
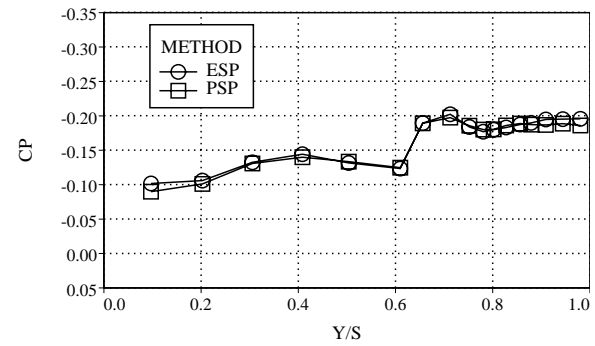
MACH=2.10, AOA=8 DEGREES, X/C=0.80
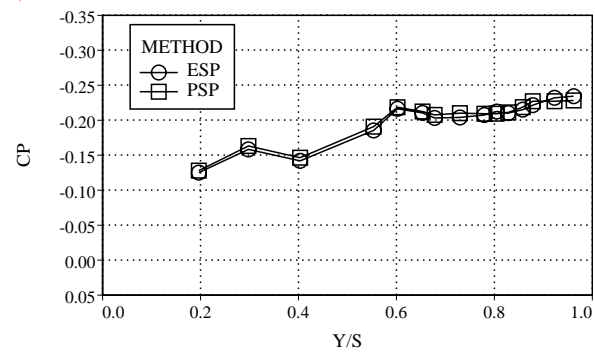
LVS image at x/c=0.8

(b) $M_\infty = 2.1$.

Figure 22. Concluded.

LVS image at x/c=0.6

LVS image at x/c=0.8

MACH=1.60, AOA=8 DEGREES, X/C=0.30

MACH=1.60, AOA=8 DEGREES, X/C=0.60

MACH=1.60, AOA=8 DEGREES, X/C=0.80
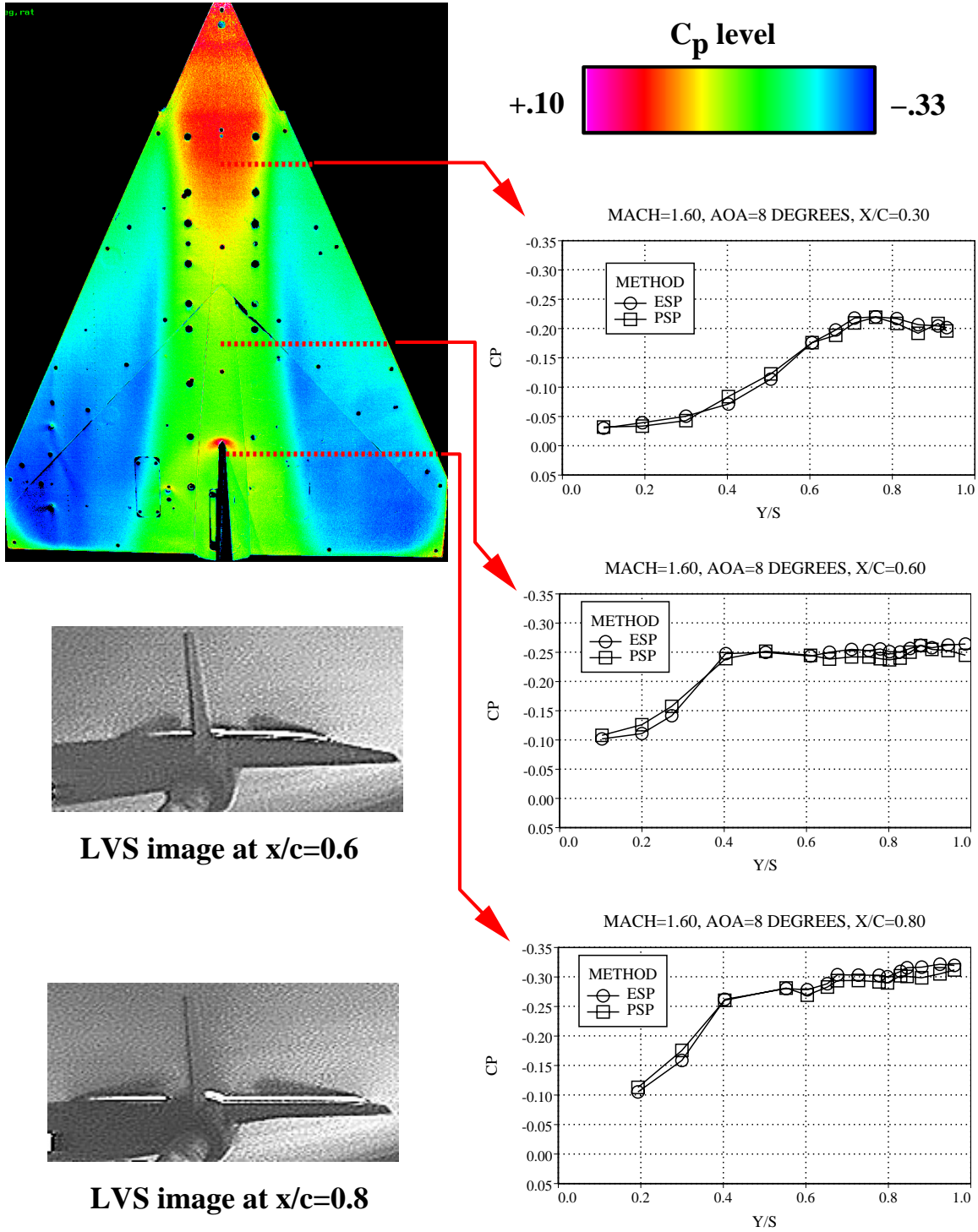
(a) $M_\infty = 1.6$.

Figure 23. Composite plots of PSP and ESP measurements and LVS flow visualization
images with porous LEX and centerline vertical tail; $\alpha = 8^\circ$.

C_p level

+.02   −.22

MACH=2.10, AOA=8 DEGREES, X/C=0.30

MACH=2.10, AOA=8 DEGREES, X/C=0.60

MACH=2.10, AOA=8 DEGREES, X/C=0.80

LVS image at x/c=0.6

LVS image at x/c=0.8

(b) $M_\infty = 2.1$.

Figure 23. Concluded.

MACH=1.60, AOA=8 DEGREES, X/C=0.30

MACH=1.60, AOA=8 DEGREES, X/C=0.60

MACH=1.60, AOA=8 DEGREES, X/C=0.80

C_p level

+.10   −.33
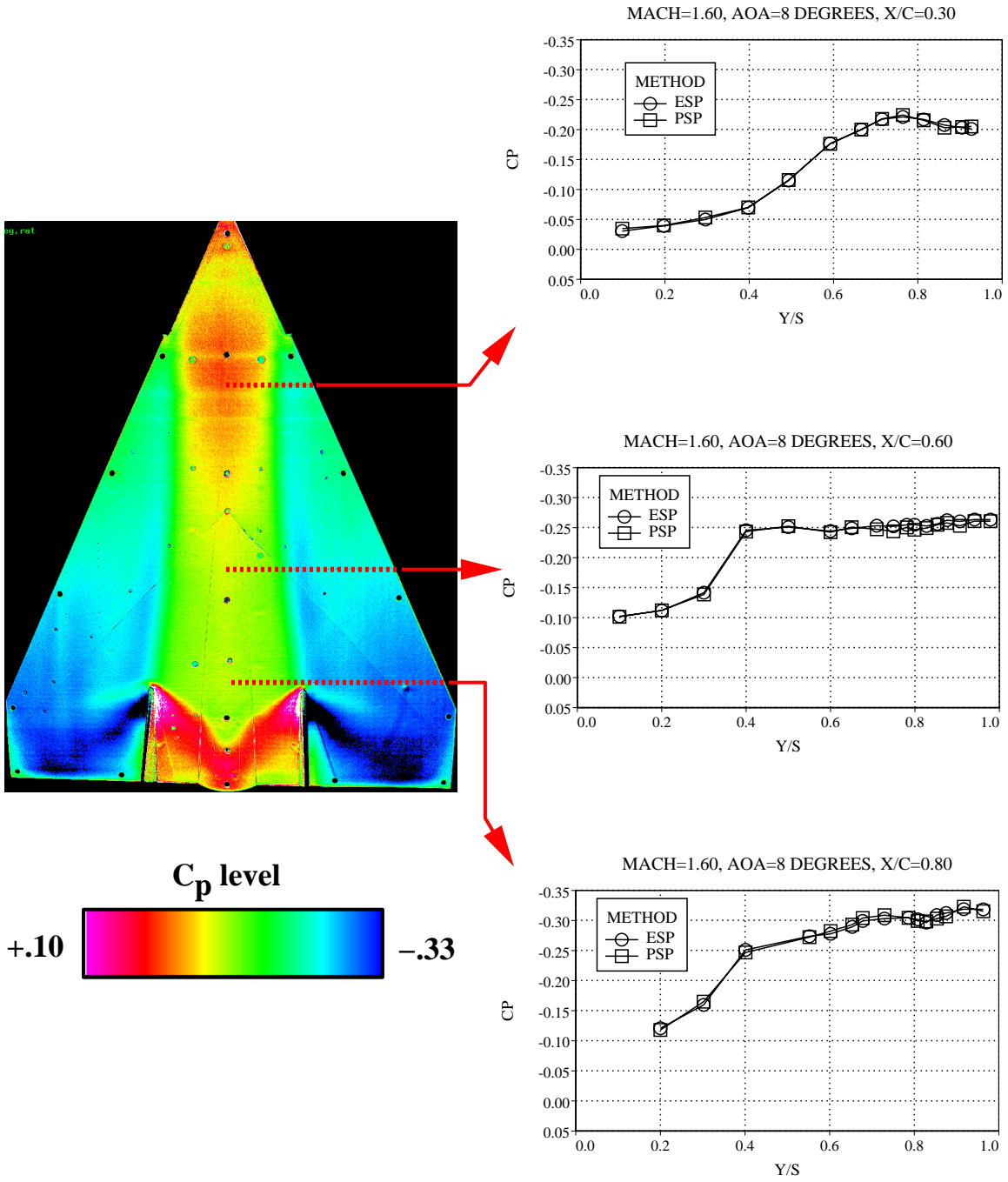
(a) $M_\infty = 1.6$.

Figure 24. Composite plots of PSP and ESP measurements with porous LEX and twin
        vertical tails; $\alpha = 8^\circ$.
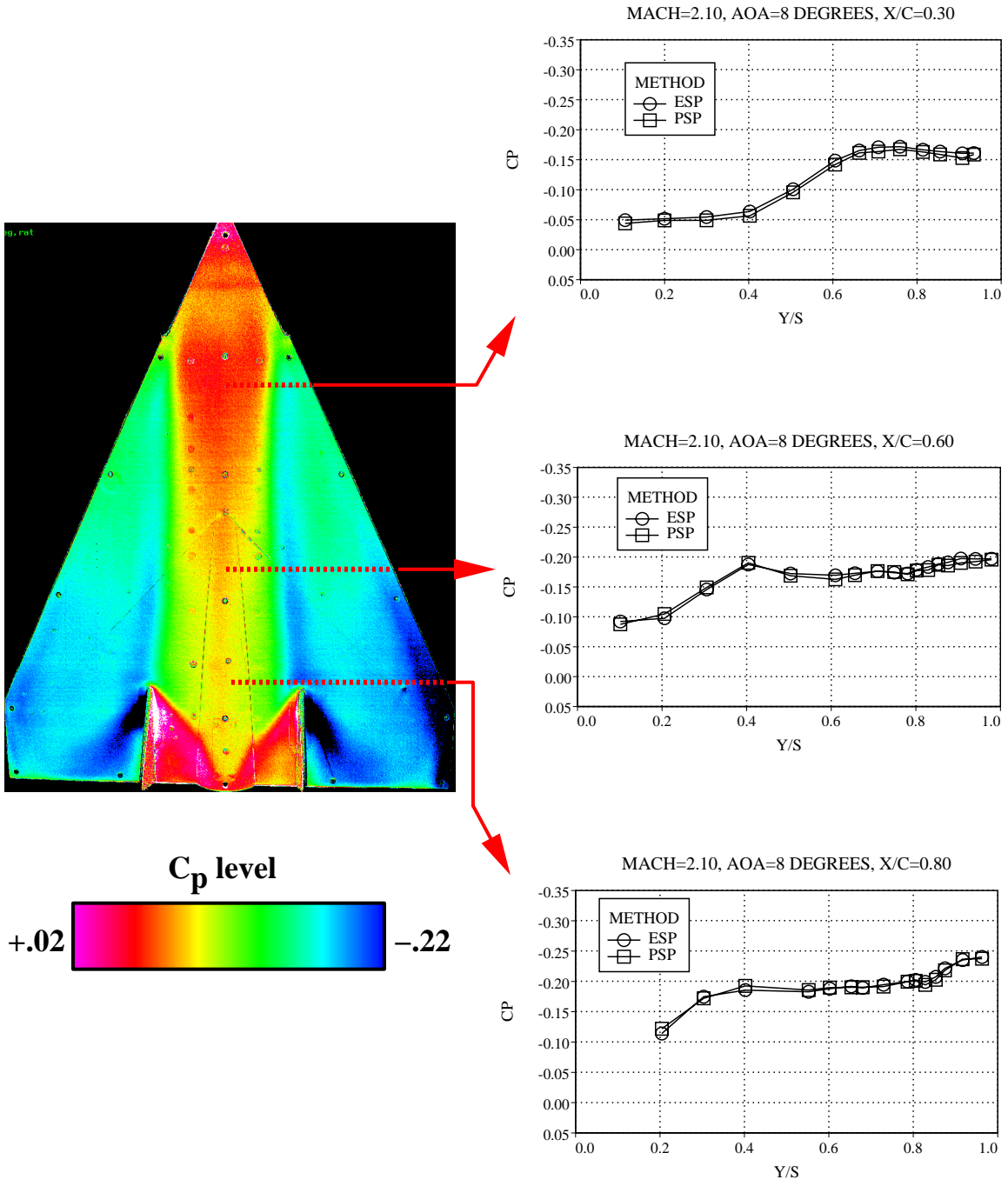
(b) $M_\infty = 2.1$.

Figure 24. Concluded.
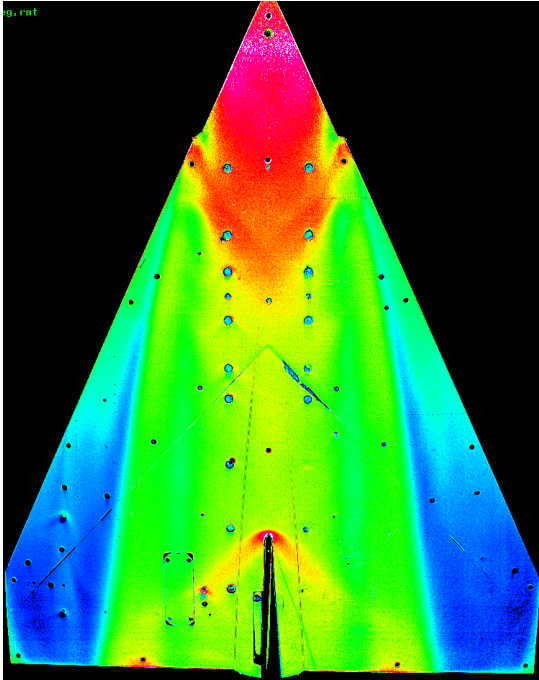
Solid LEX, Centerline Tail
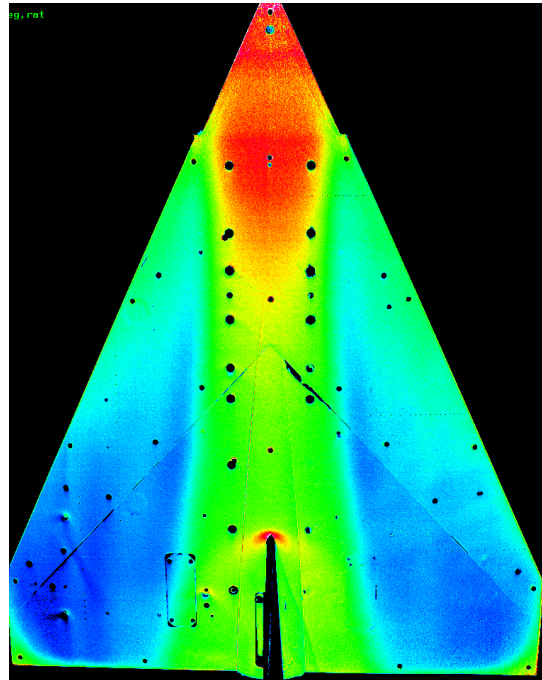
Porous LEX, Centerline Tail
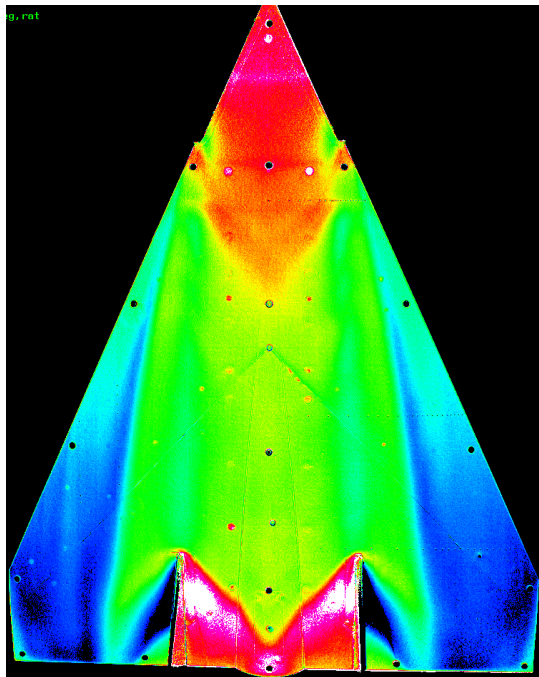
Solid LEX, Twin Tails
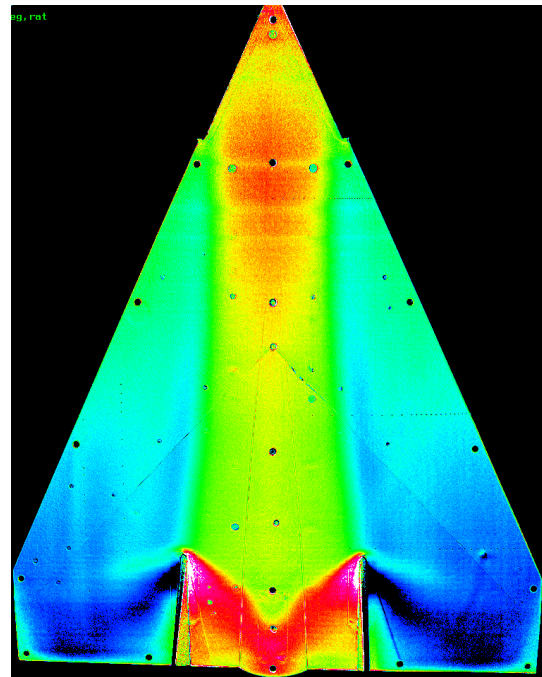
Porous LEX, Twin Tails

(a) $M_\infty = 1.6$.

Figure 25. Comparison of PSP surface pressure response with solid and porous LEX and centerline and twin vertical tails; $\alpha = 8^\circ$.
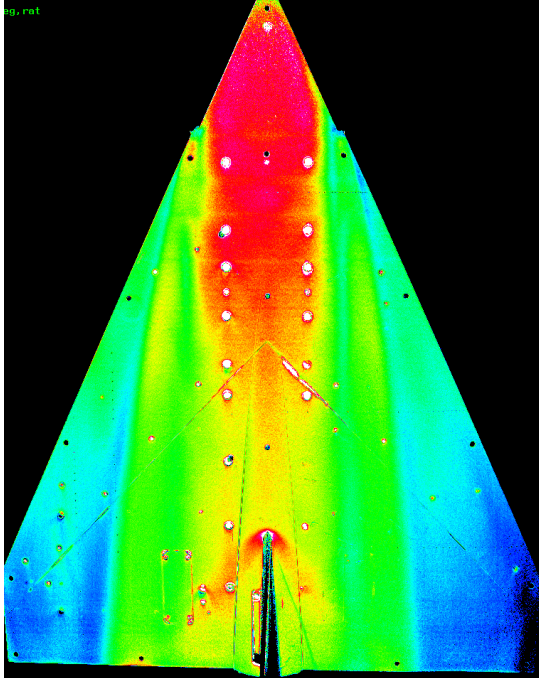
Solid LEX, Centerline Tail
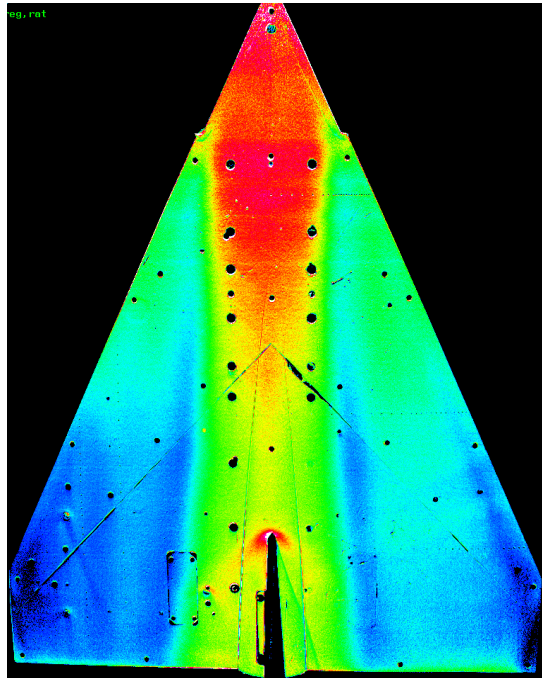
Porous LEX, Centerline Tail
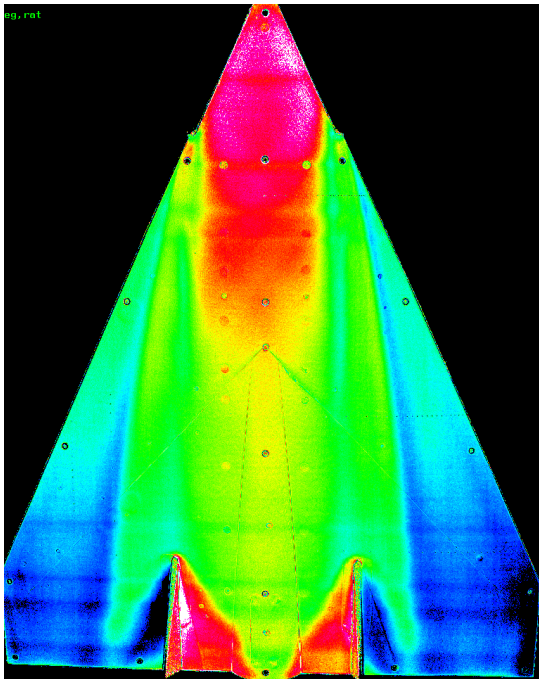
Solid LEX, Twin Tails
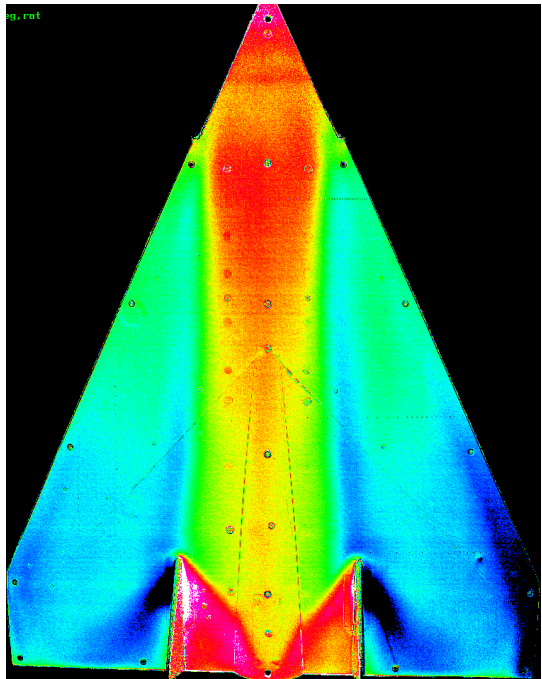
Porous LEX, Twin Tails

(b) $M_\infty = 2.1$.

Figure 25. Concluded.
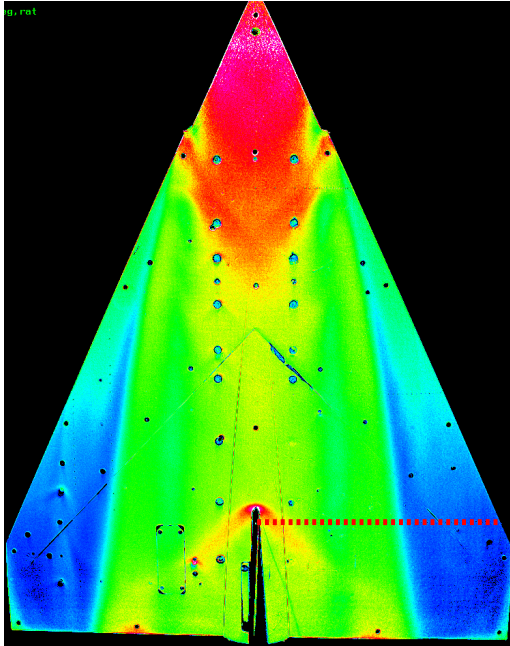
Solid LEX   **Porous LEX**
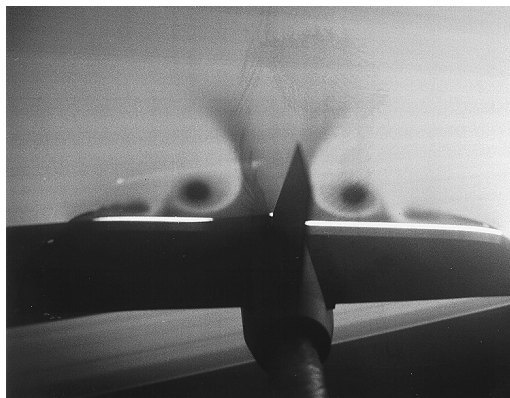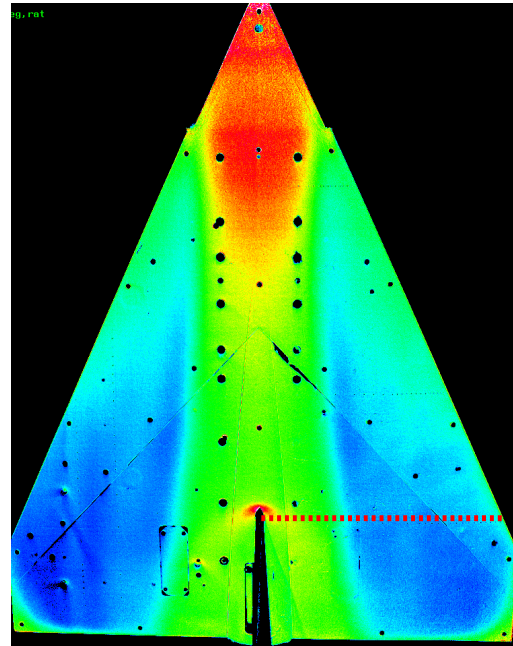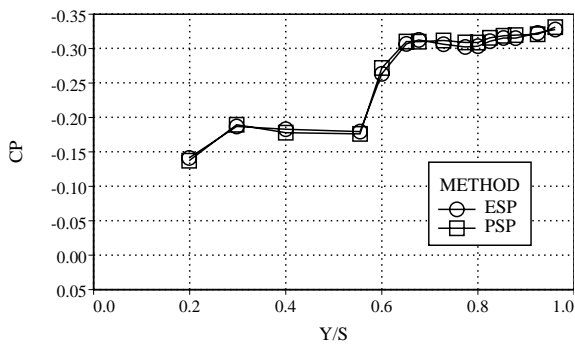
MACH=1.60, AOA=8 DEGREES, X/C=0.80
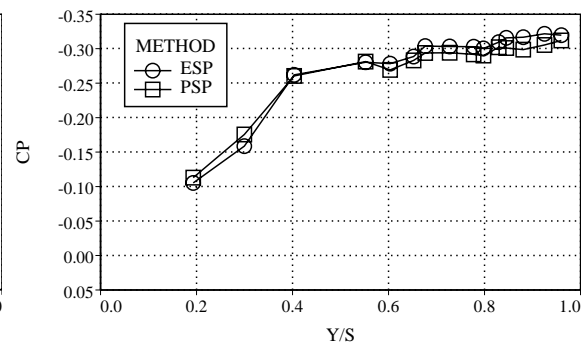
(a) $M_\infty = 1.6$.

Figure 26. Comparison of PSP surface pressure response, LVS images, and surface static pressure distributions with solid LEX and porous LEX; $\alpha = 8^{\circ}$; centerline tail.
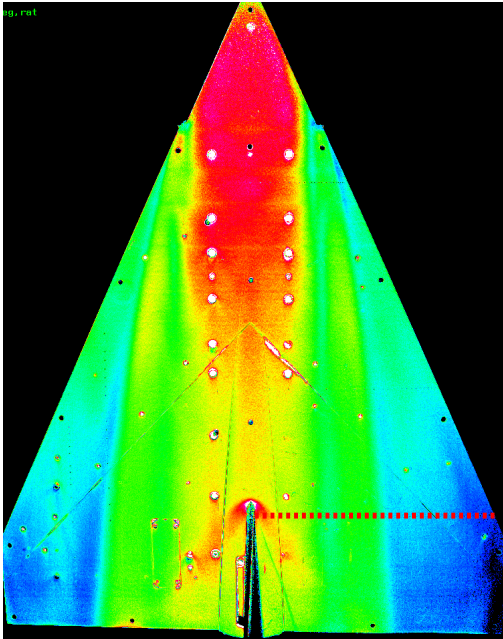
Solid LEX   **Porous LEX**
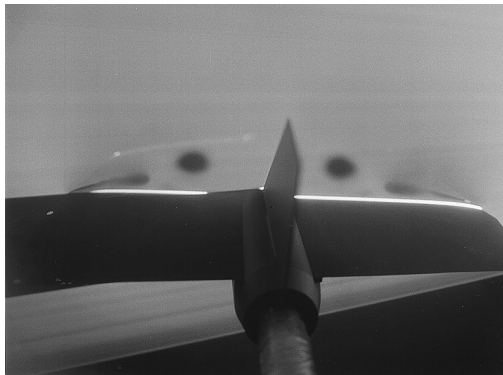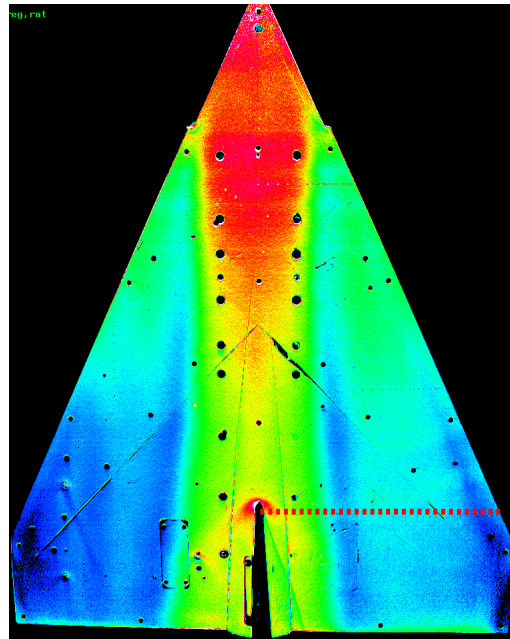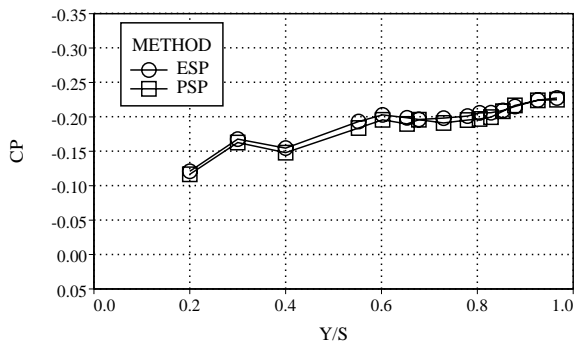
MACH=2.10, AOA=8 DEGREES, X/C=0.80   MACH=2.10, AOA=8 DEGREES, X/C=0.80
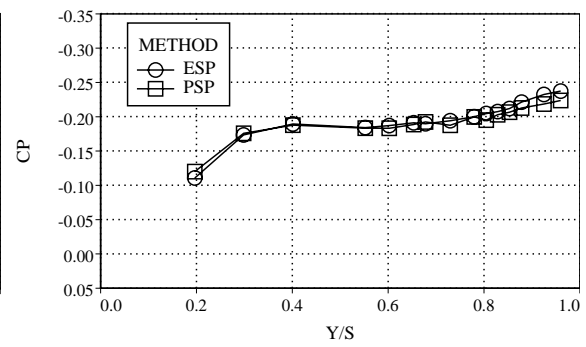
(b) $M_\infty = 2.1$.

Figure 26. Concluded.
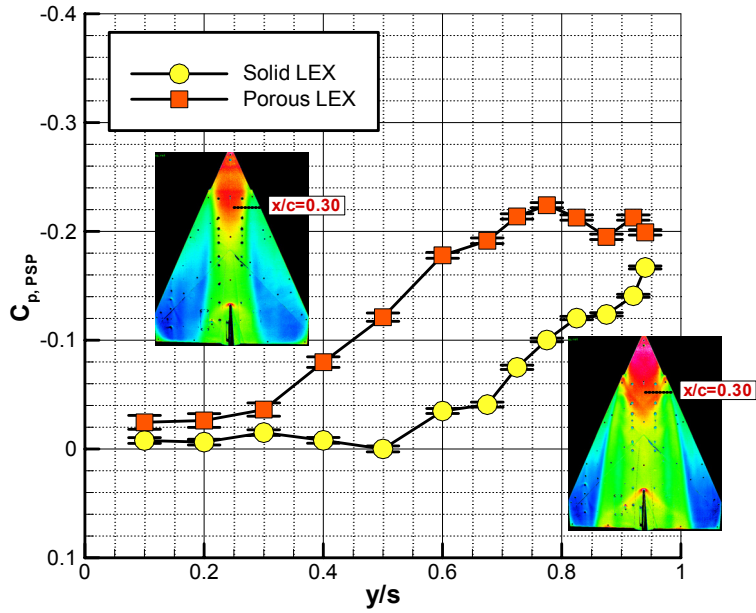
(a) *x/c=0.30.*
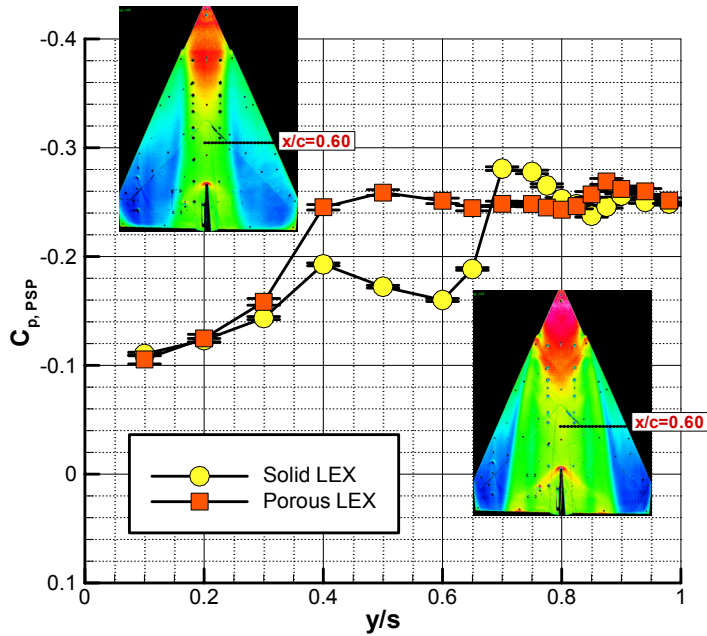
(b) *x/c=0.60.*

Figure 27. Comparison of PSP surface static pressure distributions with solid LEX and porous LEX and centerline vertical tail; $M_\infty = 1.6$, $\alpha = 8^\circ$.
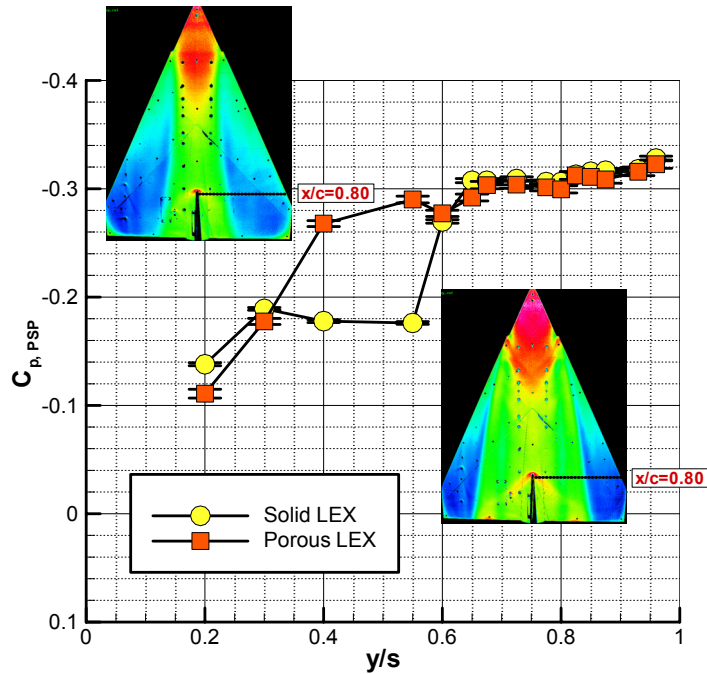
(c) *x/c=0.80.*

Figure 27. Concluded.
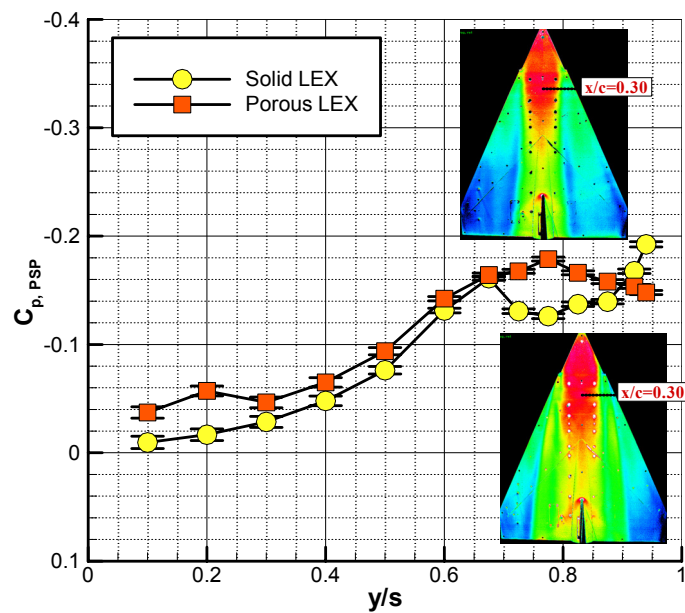
(a) *x/c=0.30.*

Figure 28. Comparison of PSP surface static pressure distributions with solid LEX and porous LEX and centerline vertical tail; $M_\infty = 2.1$, $\alpha = 8^\circ$.
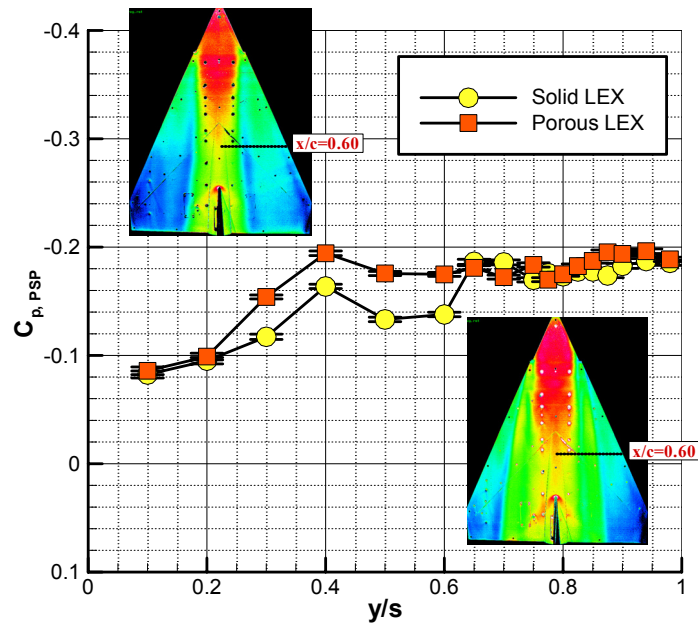
(b) *x/c=0.60.*
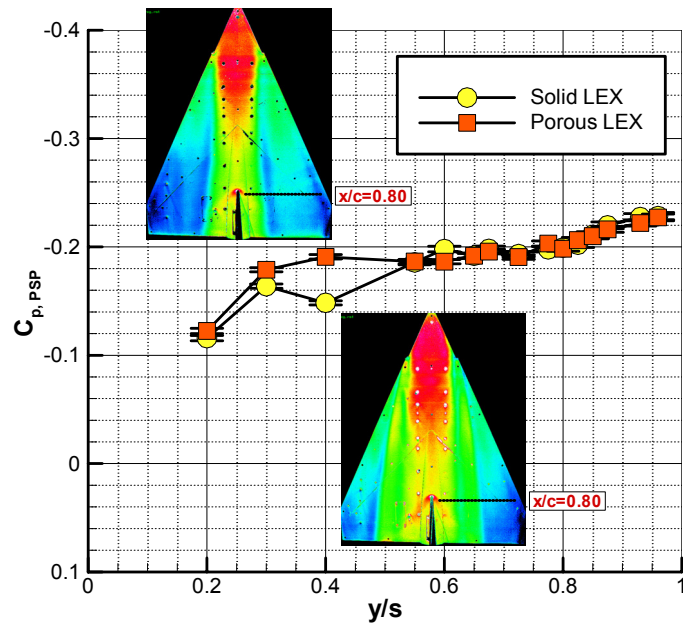
(c) *x/c=0.80.*

Figure 28. Concluded.
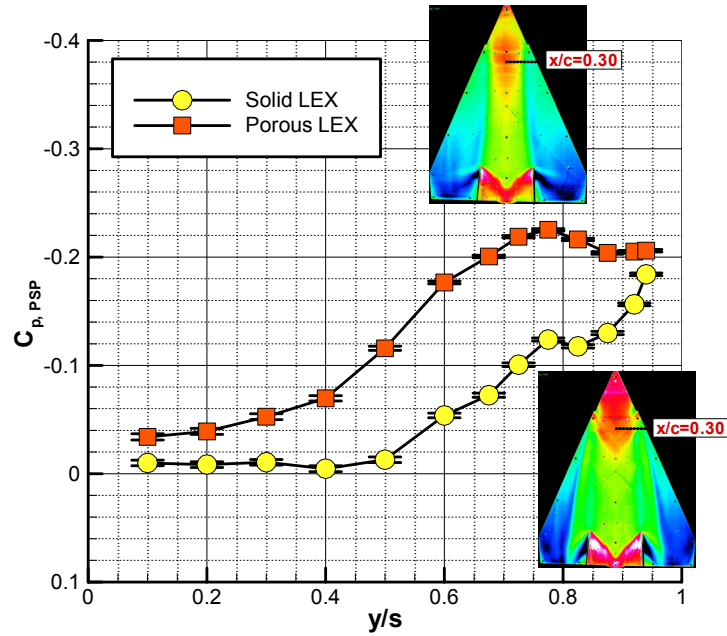
(a) *x/c=0.30.*
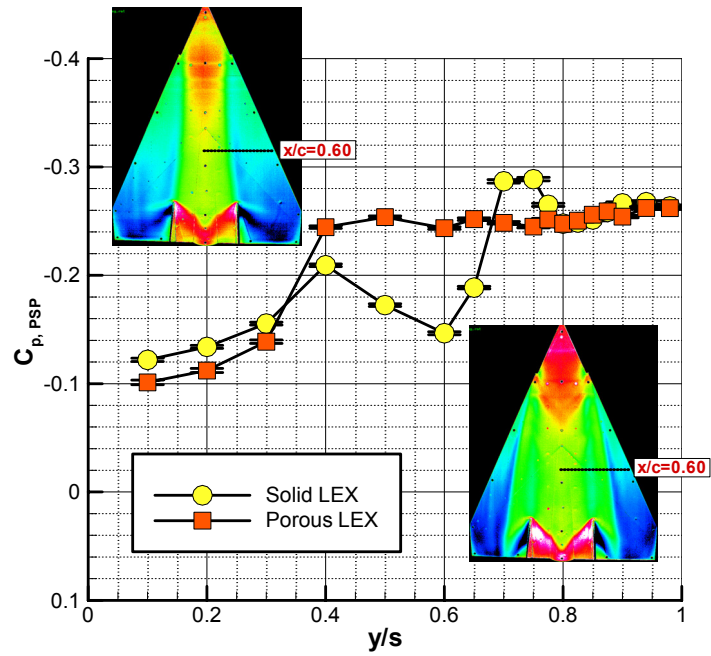
(b) *x/c=0.60.*

Figure 29. Comparison of PSP surface static pressure distributions with solid LEX and porous LEX and twin vertical tails; $M_\infty = 1.6$, $\alpha = 8^\circ$.
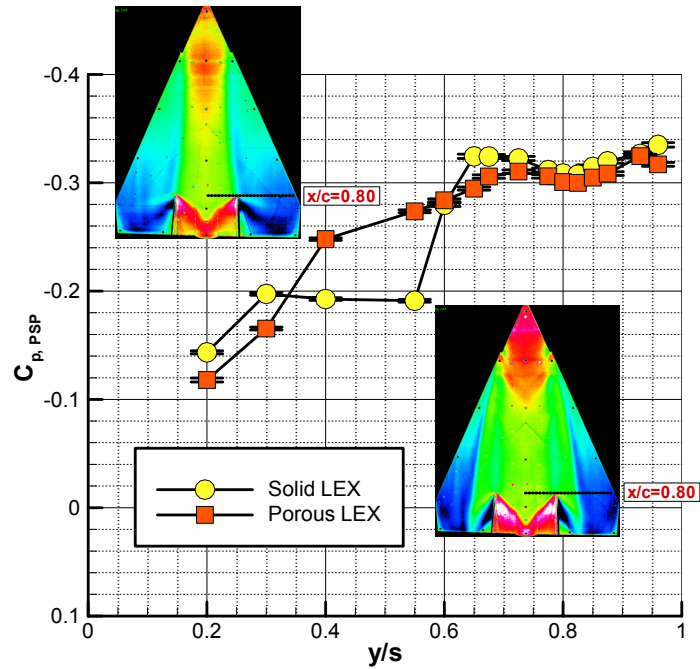
(c) *x/c=0.80.*
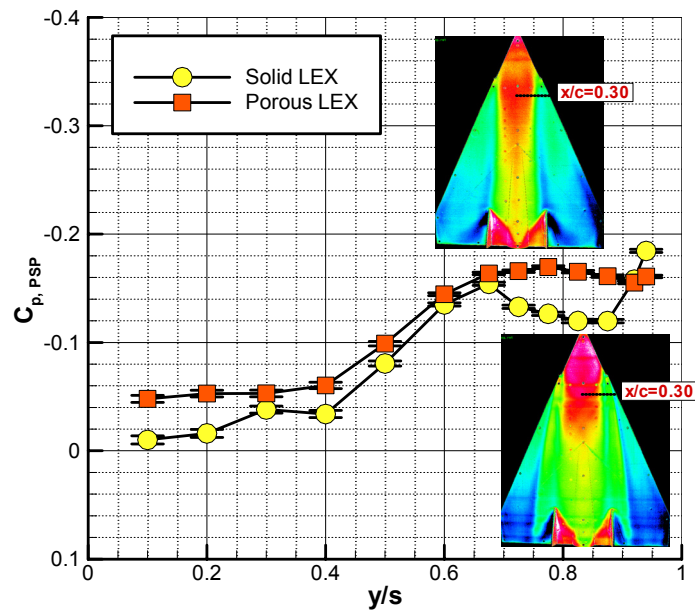
(a) *x/c=0.30.*

Figure 30. Comparison of PSP surface static pressure distributions with solid LEX and
porous LEX and twin vertical tails; $M_\infty = 2.1$, $\alpha = 8^\circ$.

70
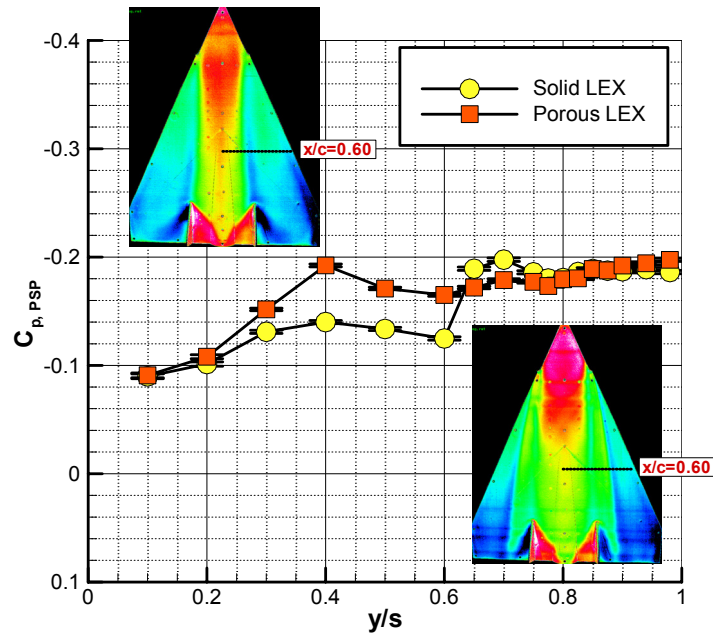
(b) *x/c=0.60.*
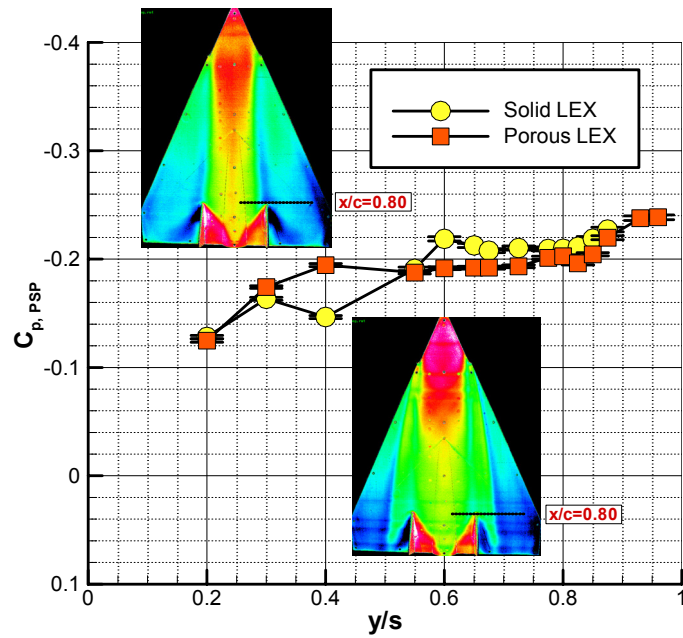
(c) *x/c=0.80.*

Figure 30. Concluded.
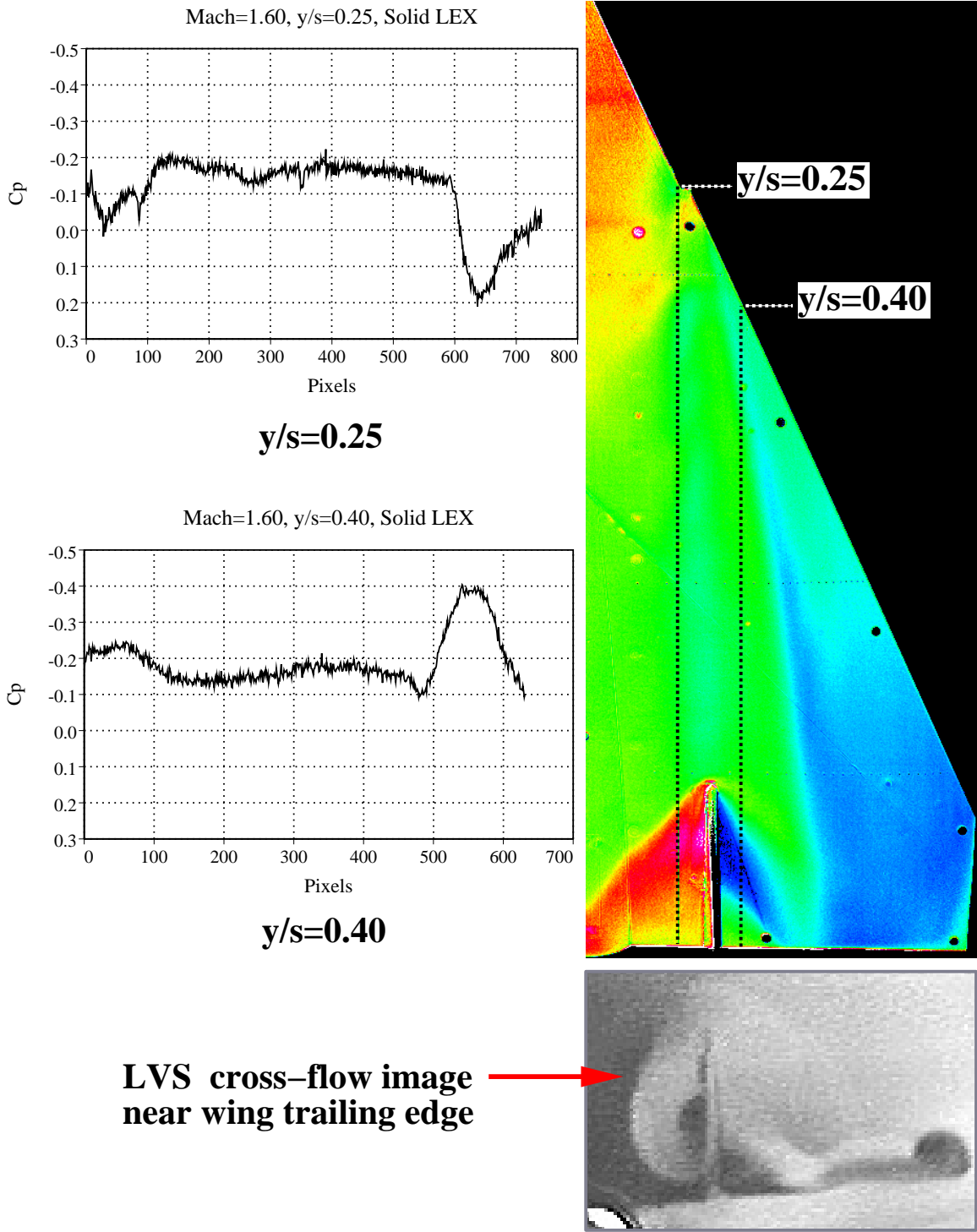
Figure 31. PSP chordwise pressure distributions at y/s = 0.25 and 0.40 with solid LEX and twin vertical tails; $M_\infty = 1.6,\ \alpha = 8^o$.
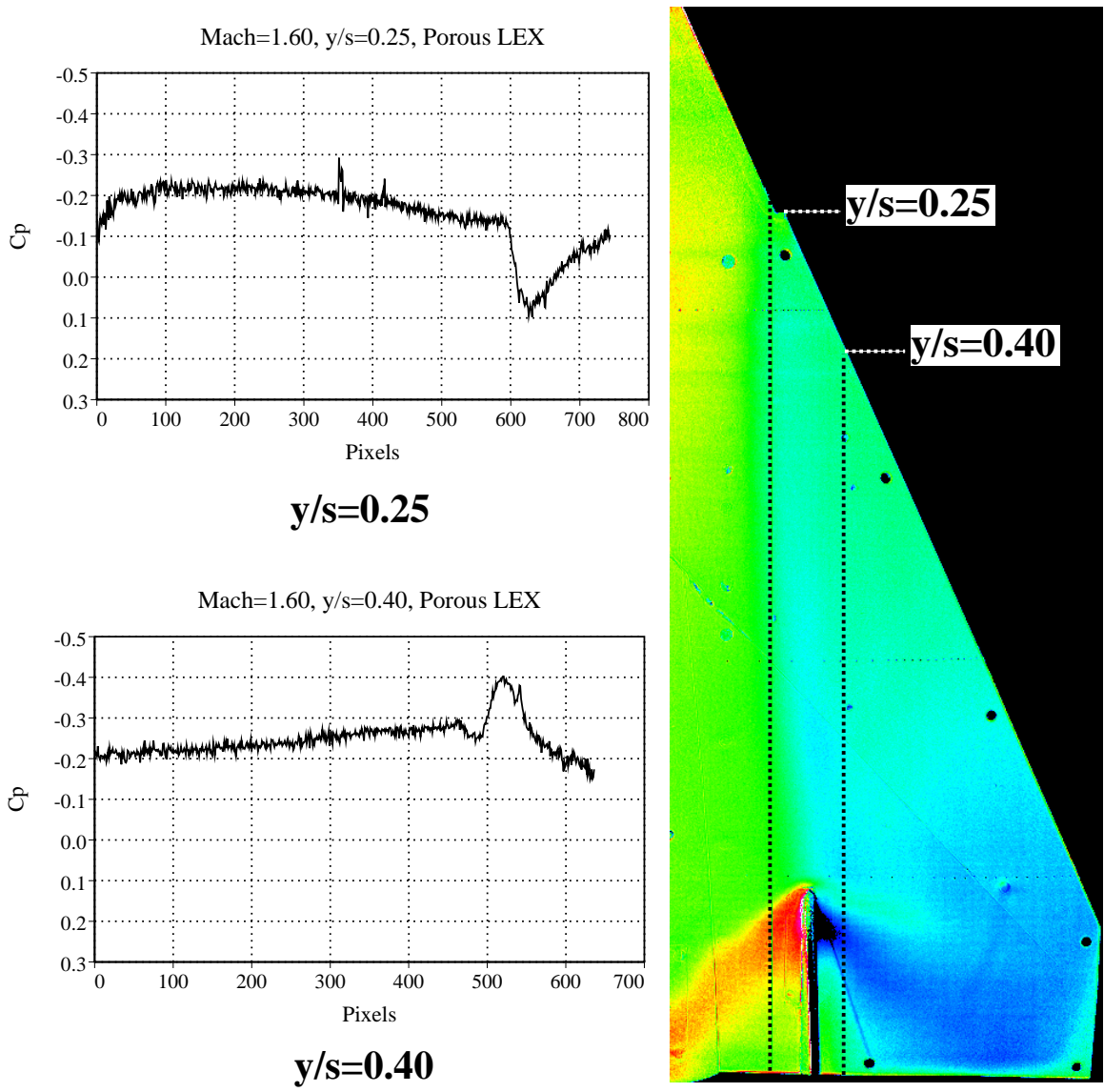
Figure 32. PSP chordwise pressure distributions at y/s = 0.25 and 0.40 with porous LEX and twin vertical tails; $M_\infty = 1.6$, $\alpha = 8^\circ$.

Mach=2.10, y/s=0.25, Solid LEX

y/s=0.25

Mach=2.10, y/s=0.40, Solid LEX

y/s=0.40

y/s=0.25

y/s=0.40

LVS cross−flow image
near wing trailing edge
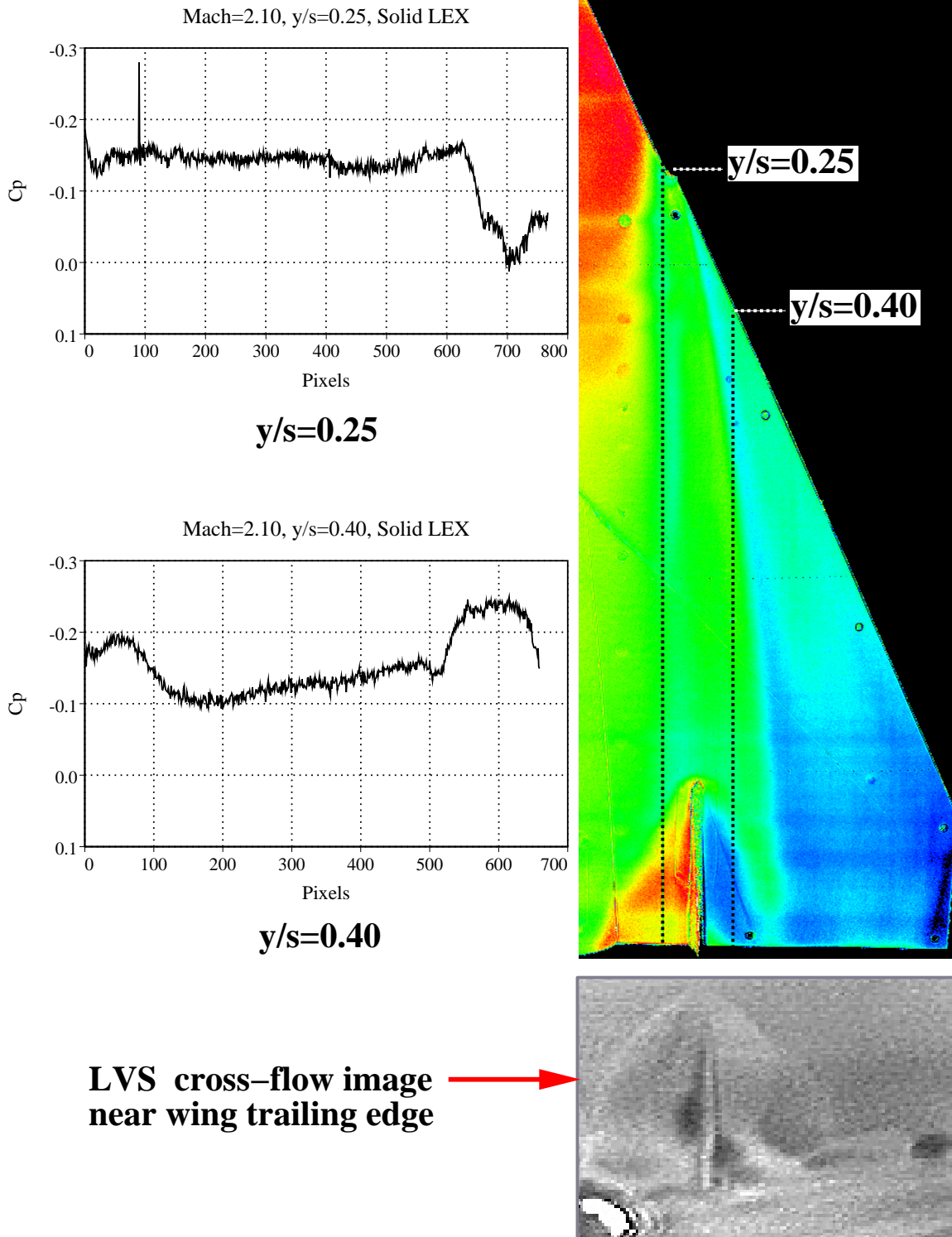
Figure 33. PSP chordwise pressure distributions at y/s = 0.25 and 0.40 with solid
LEX and twin vertical tails; $M_\infty = 2.1$, $\alpha = 8^\circ$.
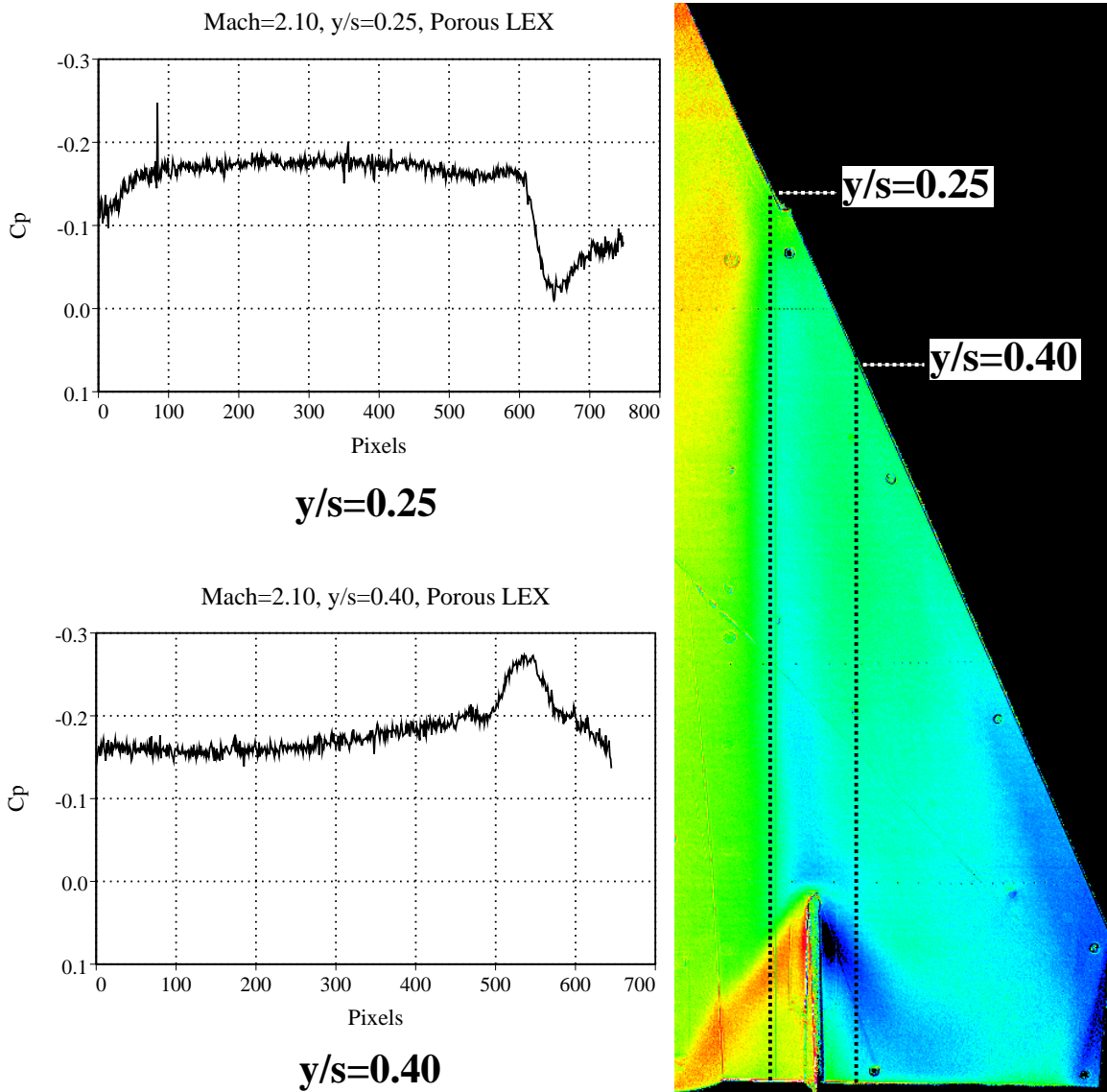
Figure 34. PSP chordwise pressure distributions at y/s = 0.25 and 0.40 with porous LEX and twin vertical tails; $M_\infty = 2.1$, $\alpha = 8^\circ$.

Figure 35. Comparison of PSP chordwise pressure distributions at y/s = 0.25 with solid and porous LEX and twin vertical tails; $M_\infty = 1.6$, $\alpha = 8^\circ$.
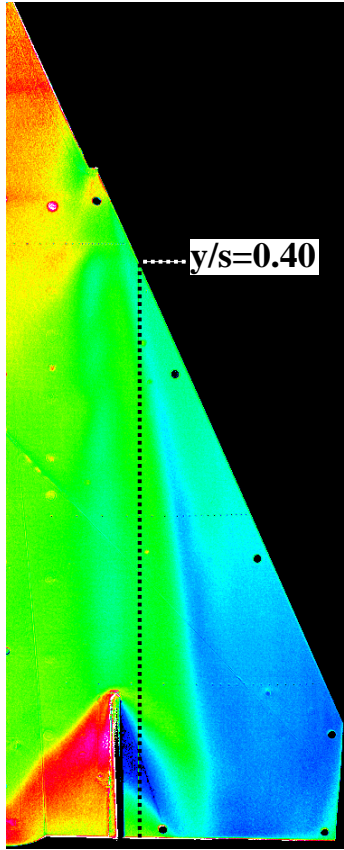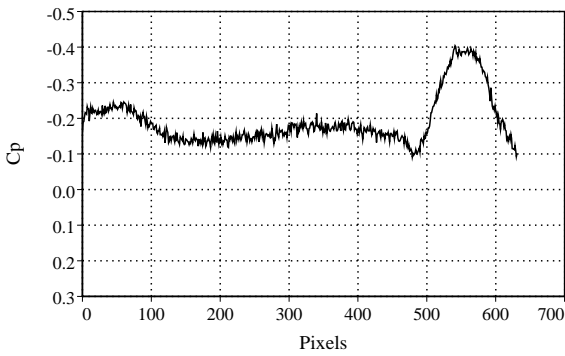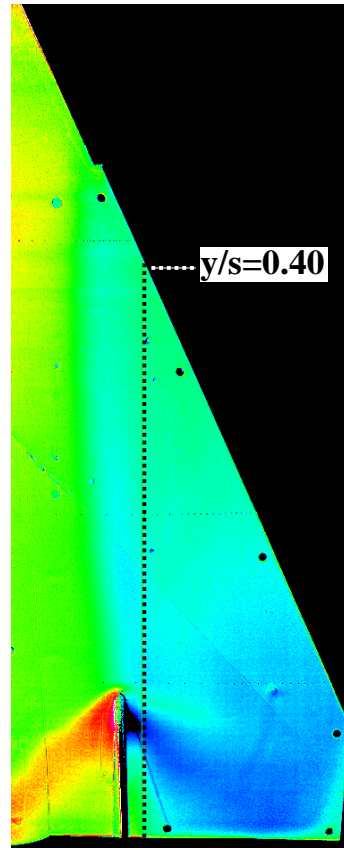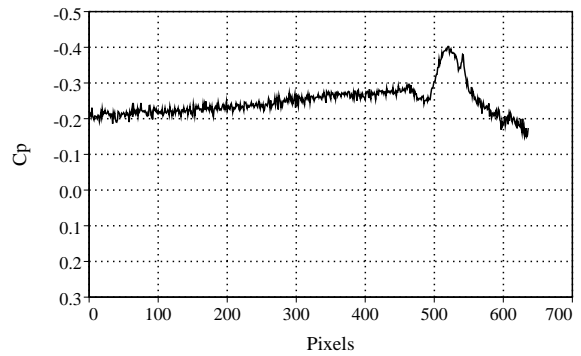
Figure 36. Comparison of PSP chordwise pressure distributions at y/s = 0.40 with solid and porous LEX and twin vertical tails; $M_\infty = 1.6$, $\alpha = 8^\circ$.

y/s=0.25

Mach=2.10, y/s=0.25, Solid LEX

Mach=2.10, y/s=0.25, Porous LEX
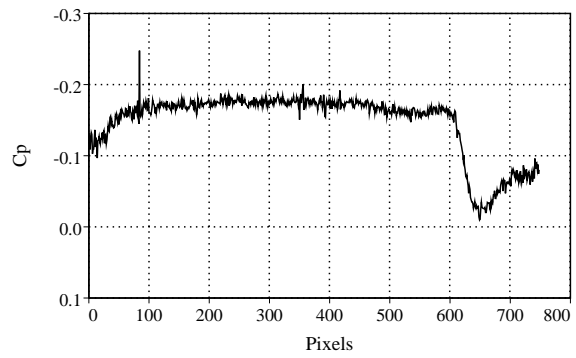
Solid LEX, y/s=0.25

Porous LEX, y/s=0.25

Figure 37. Comparison of PSP chordwise pressure distributions at y/s = 0.25 with solid and porous LEX and twin vertical tails; $M_\infty = 2.1$, $\alpha = 8^o$.
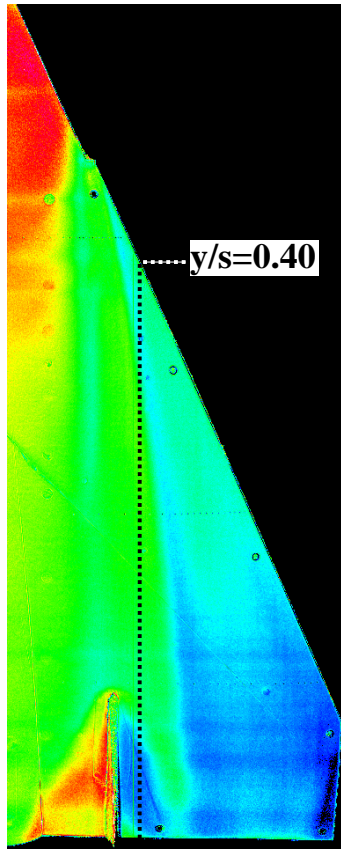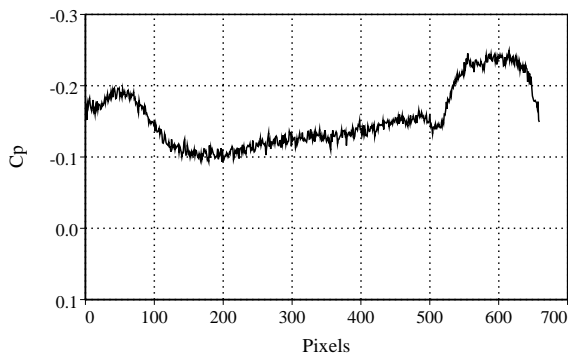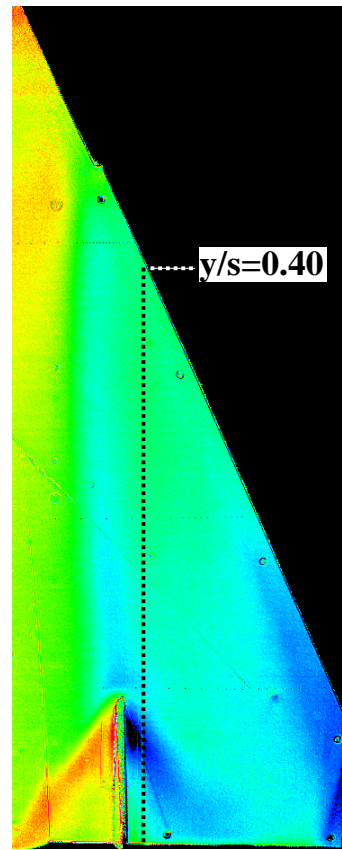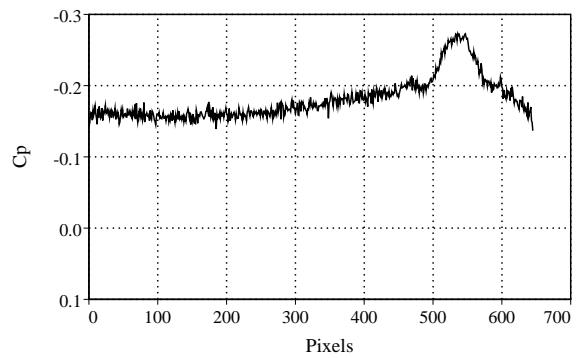
Figure 38. Comparison of PSP chordwise pressure distributions at y/s = 0.40 with solid and porous LEX and twin vertical tails; $M_\infty = 2.1$, $\alpha = 8^o$.
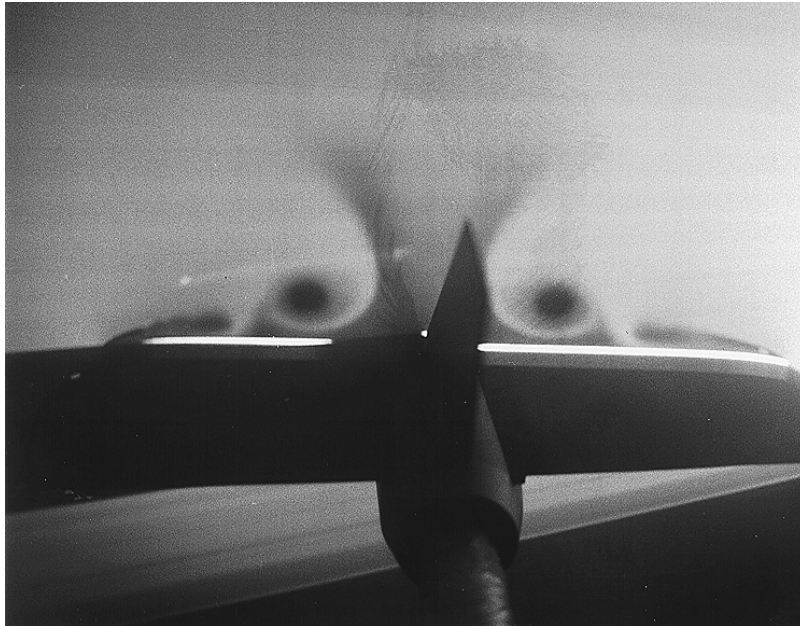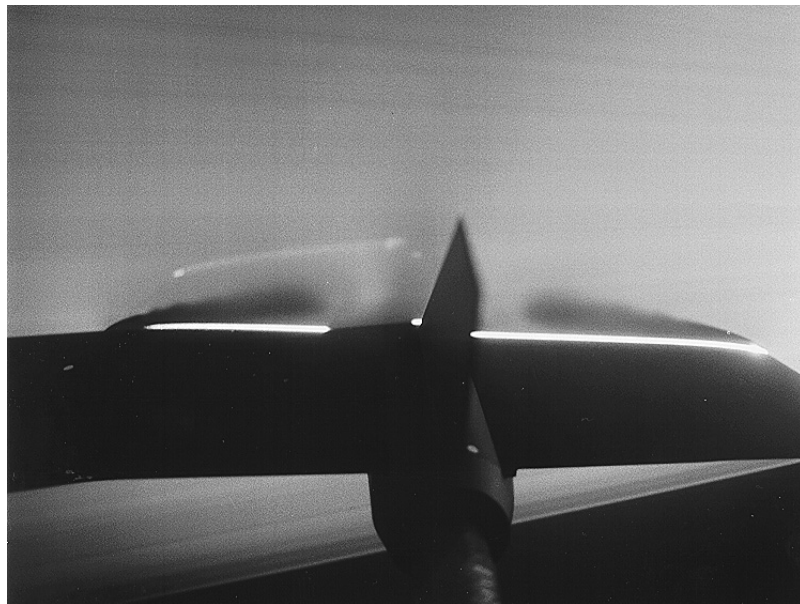
Solid LEX

Porous LEX

(a) $\alpha = 8^{\circ}$.

Figure 39. Comparison of LVS images at $x/c_{r,w}$ = 0.80 with solid and porous LEX and centerline vertical tail; $M_{\infty} = 1.6$.
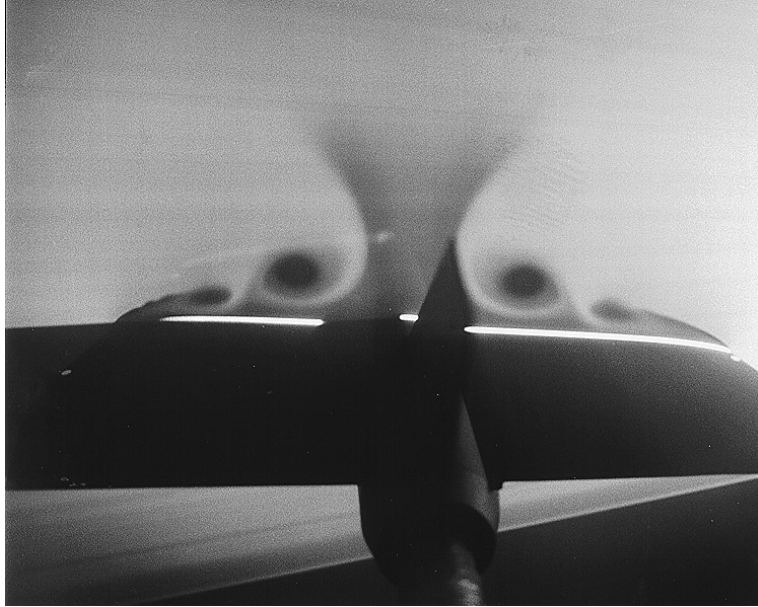
Solid LEX

Porous LEX

(b) $\alpha = 10^{\circ}$.

Figure 39. Concluded.
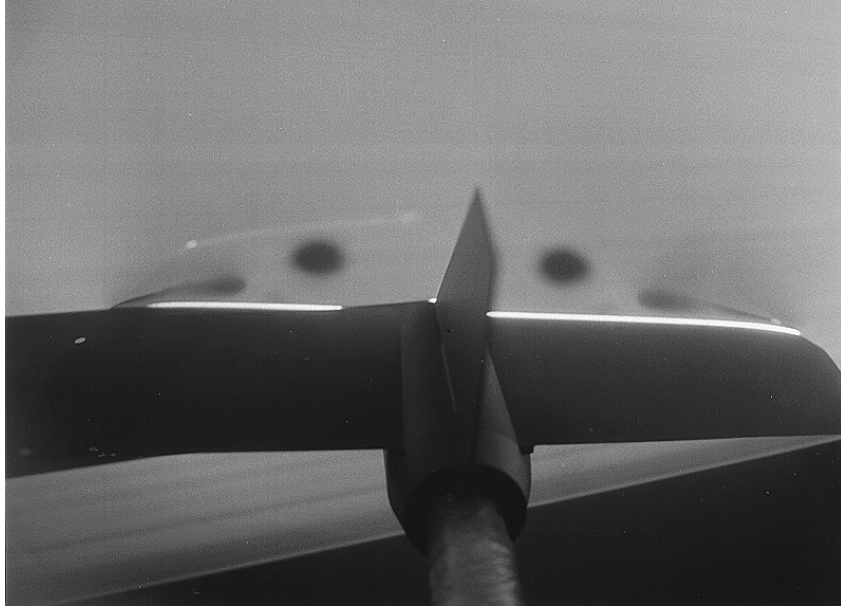
Solid LEX
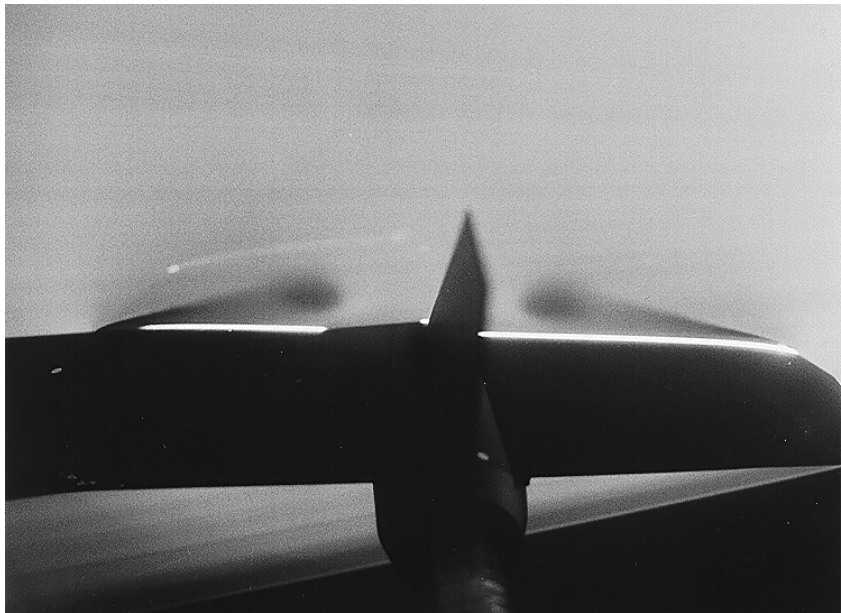
Porous LEX

(a) $\alpha = 8^{\circ}$.

Figure 40. Comparison of LVS images at $x/c_{r,w} = 0.80$ with solid and porous LEX and centerline vertical tail; $M_{\infty} = 2.1$.

82
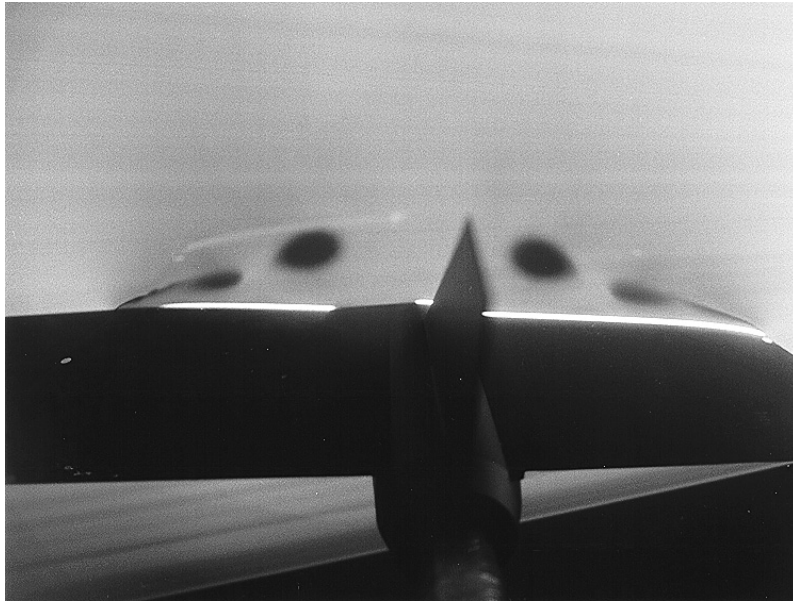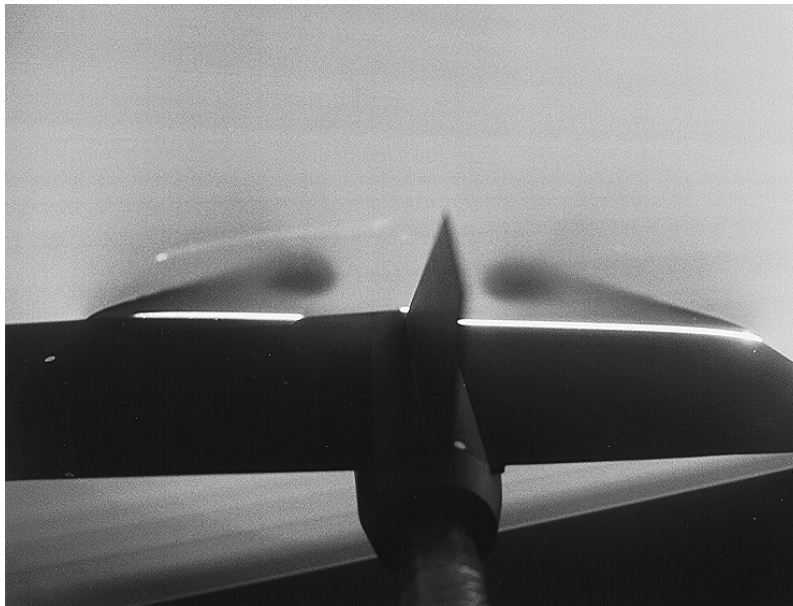
Solid LEX

Porous LEX

(b) $\alpha = 10^{\circ}$.

Figure 40. Continued.
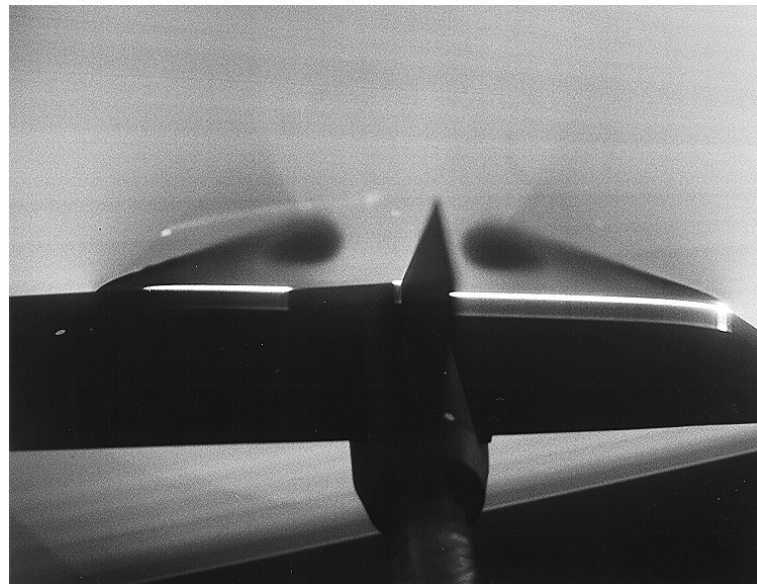
Solid LEX

Porous LEX

(c) $\alpha = 12^{\circ}$.

Figure 40. Continued.
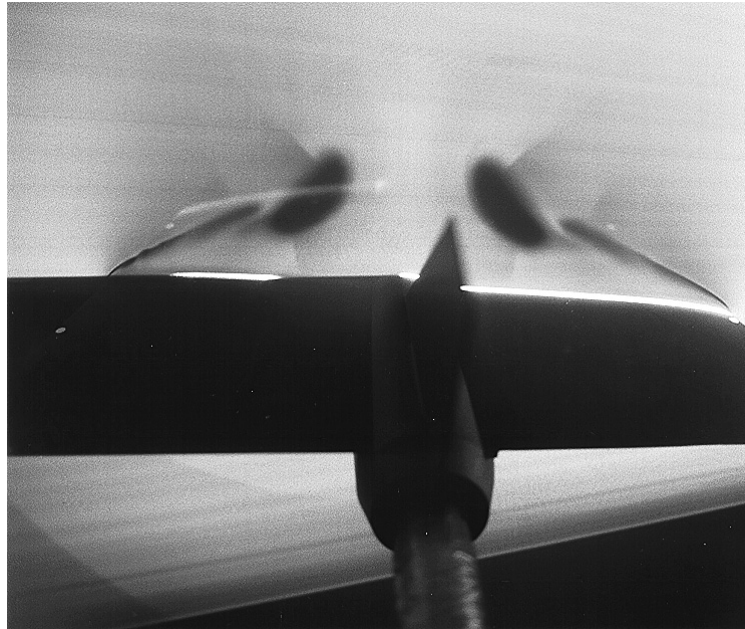
Solid LEX

Porous LEX

(d) $\alpha = 16^o$.
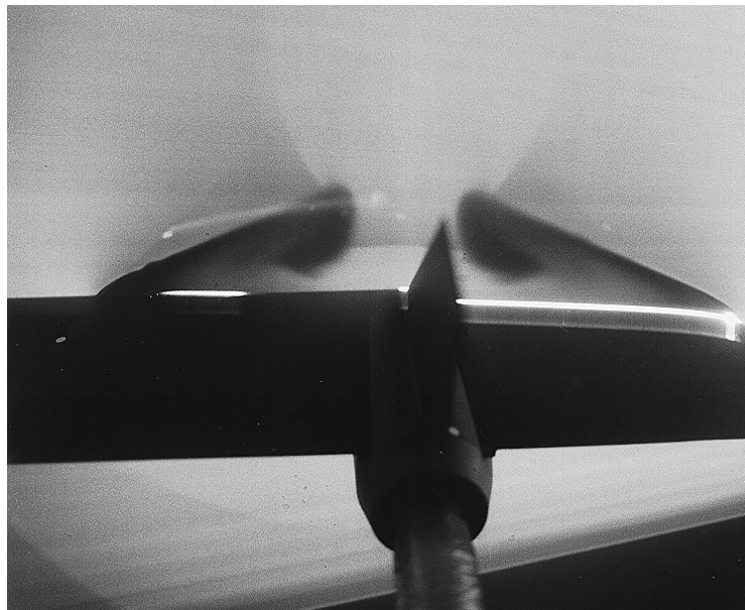
Figure 40. Concluded.
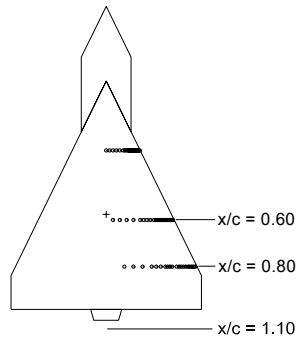
Centerline Tail　　　　　　**Twin Tails**
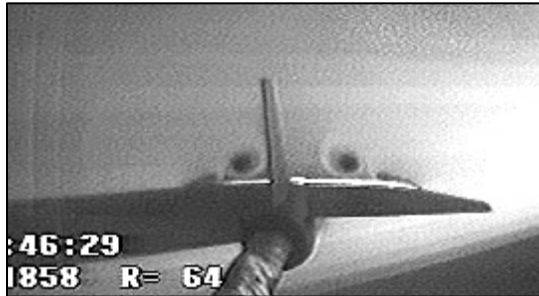
x/c = 0.60

x/c = 0.80

x/c = 1.10

x/c=0.60　　　　　　　　x/c=0.60
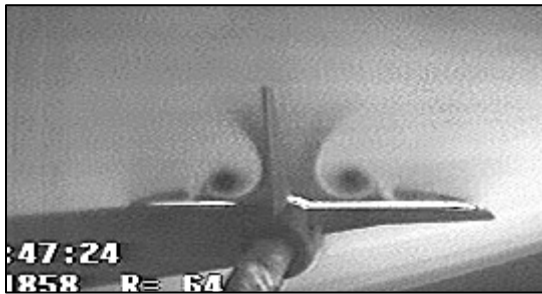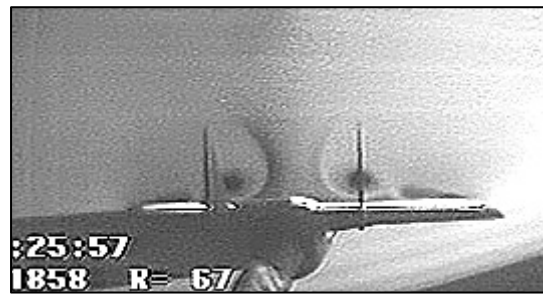
x/c=0.80　　　　　　　　x/c=0.80
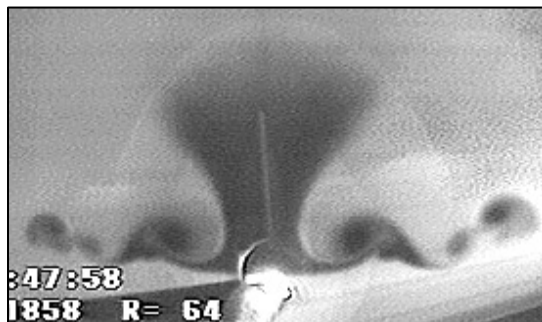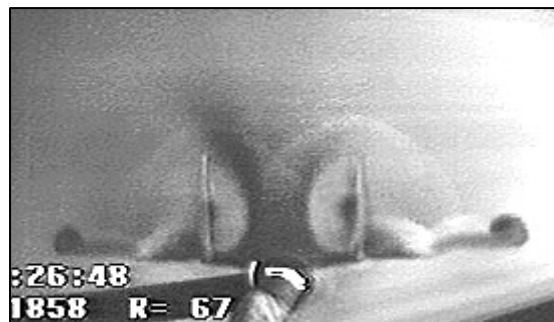
x/c=1.10 (approx.)　　　　　　x/c=1.10 (approx.)

Figure 41. Comparison of LVS images with centerline and twin vertical tails at selected axial locations; solid LEX, $M_\infty = 1.6$, $\alpha = 8^\circ$.

86
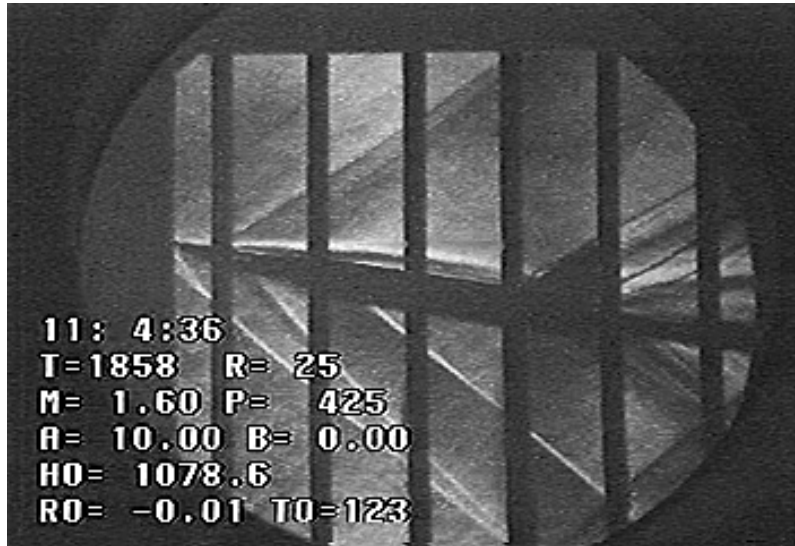
Solid LEX

Porous LEX

Figure 42. Comparison of schlieren images with solid and porous LEX and twin vertical tails; $M_\infty = 1.6$, $\alpha = 10^o$.

Solid LEX

Porous LEX

(a) $\alpha = 12^{\mathrm{o}}$.

Figure 43. Comparison of schlieren images with solid and porous LEX and twin vertical
tails; $M_\infty = 1.8$.

11:48:59
T=1858   R= 28
M= 1.80 P=   470
A= 16.08 B= 0.00
HO= 1153.6
RO=   0.00 TO=124

Solid LEX

11:57:24
T=1858   R= 20
M= 1.80 P=   357
A= 16.03 B=-0.02
HO= 1153.6
RO=   0.01 TO=125

Porous LEX

(b) $\alpha = 16^{o}$.

Figure 43. Continued.

Solid LEX

Porous LEX

(c) $\alpha = 20^o$.

Figure 43. Concluded.
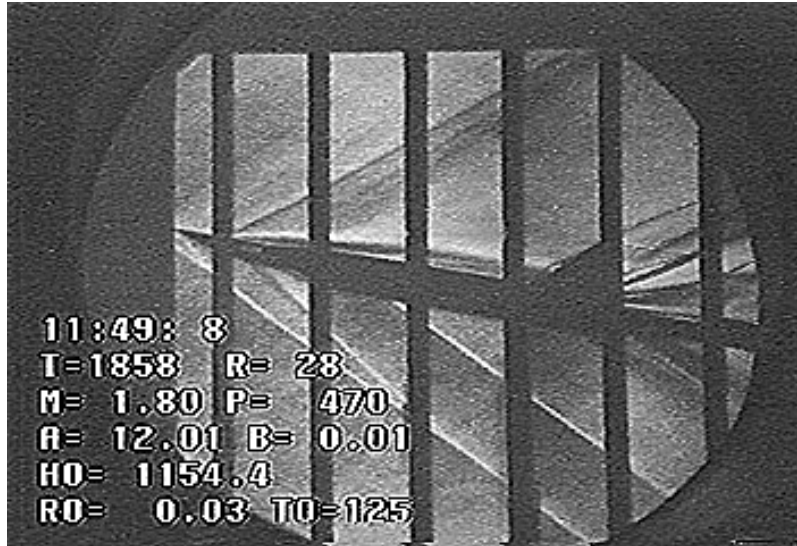
Solid LEX

Porous LEX

(a) $\alpha = 12^{\circ}$.

Figure 44. Comparison of schlieren images with solid and porous LEX and twin vertical
tails; $M_{\infty} = 2.1$.

Solid LEX

Porous LEX

(b) $\alpha = 16^{\mathrm{o}}$.

Figure 44. Continued.

Solid LEX

Porous LEX

(c) $\alpha = 20^{\circ}$.

Figure 44. Concluded.

(a) $\alpha = 8^o$.

(b) $\alpha = 12^o$.
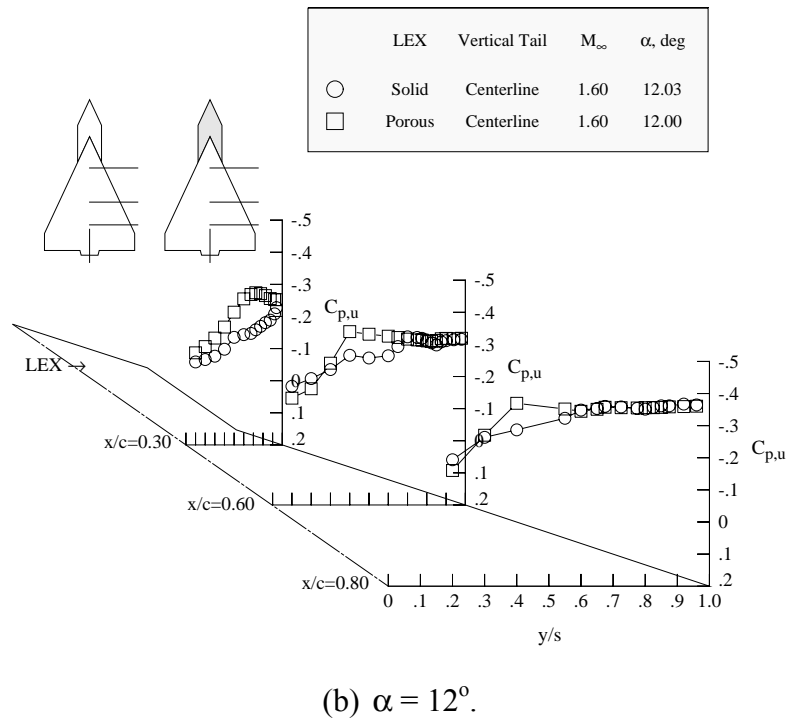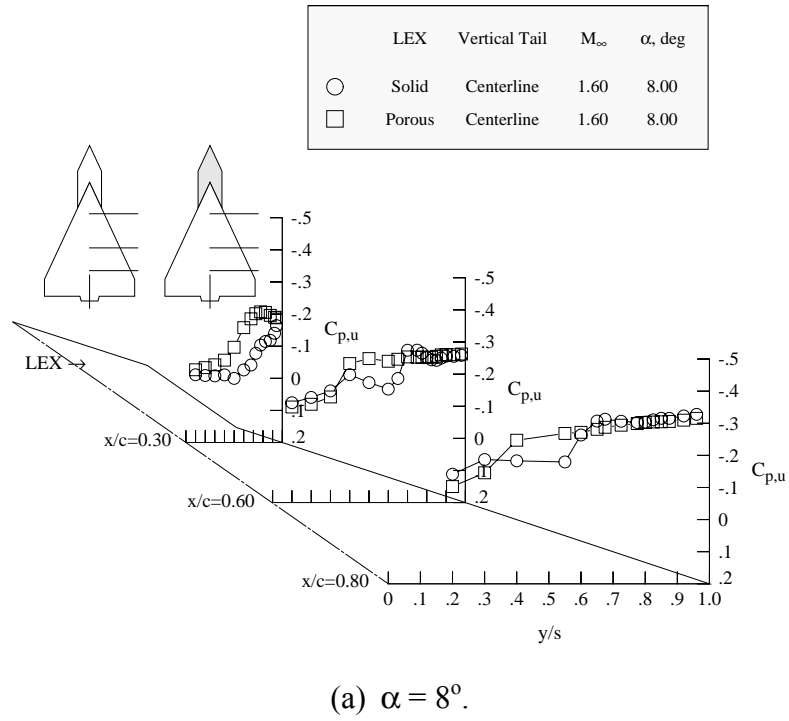
Figure 45. Comparison of ESP pressure distributions with solid and porous LEX; centerline vertical tail, $M_\infty = 1.6$.

94

(a) $\alpha = 12^{o}$.

(b) $\alpha = 16^{o}$.
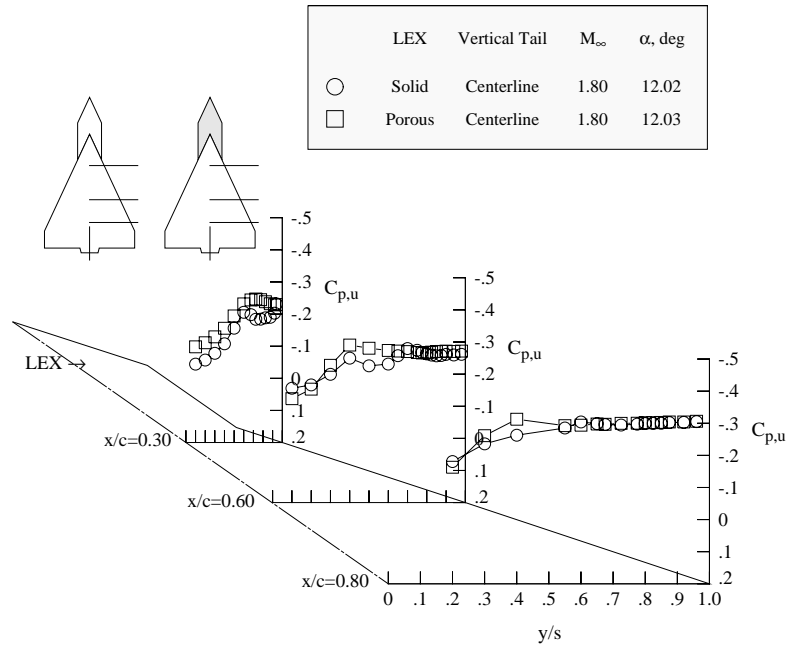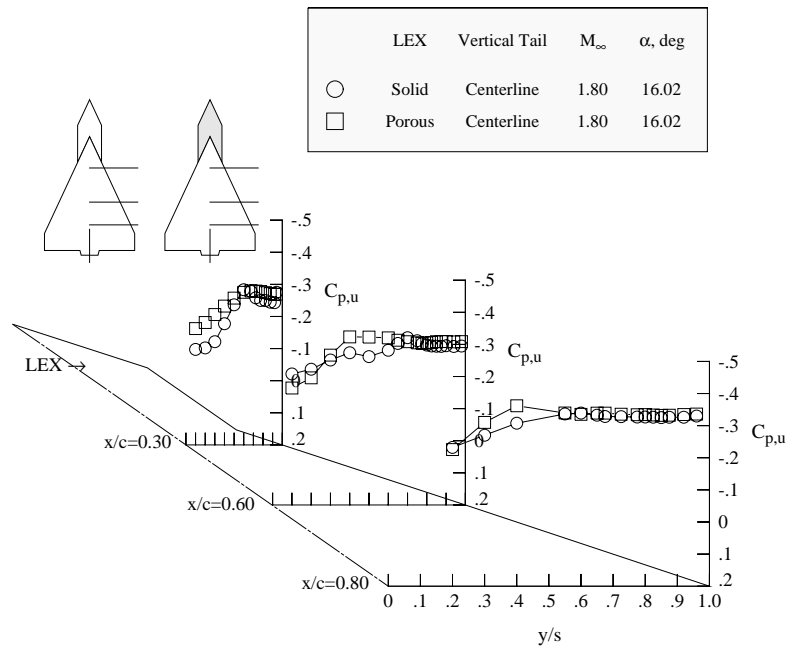
Figure 46. Comparison of ESP pressure distributions with solid and porous LEX; centerline vertical tail, $M_{\infty} = 1.8$.

95
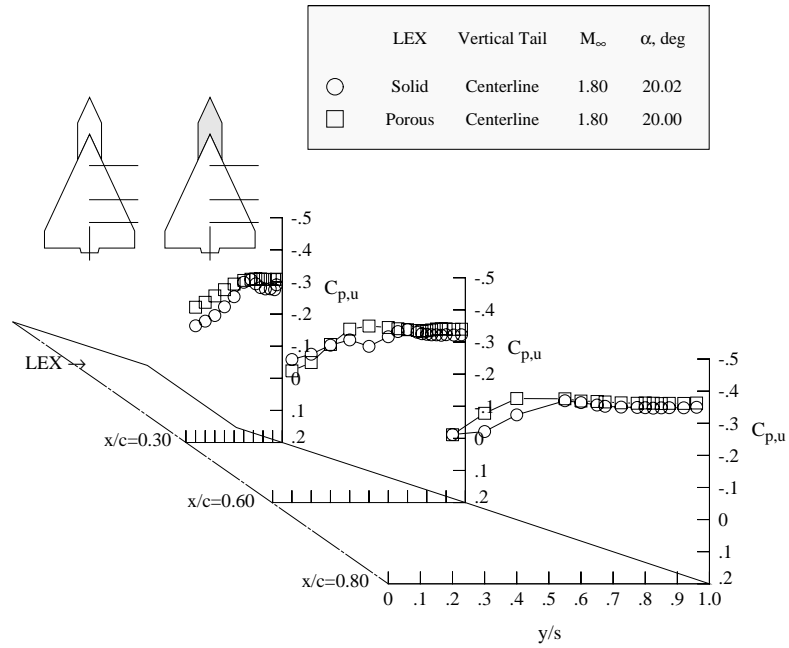
(c) $\alpha = 20^\circ$.

Figure 46. Concluded.
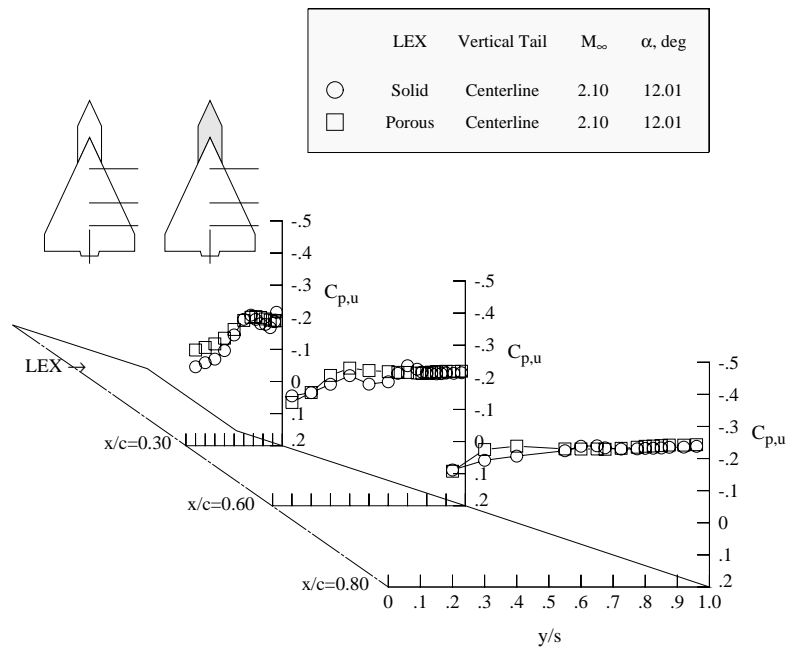
(a) $\alpha = 12^\circ$.
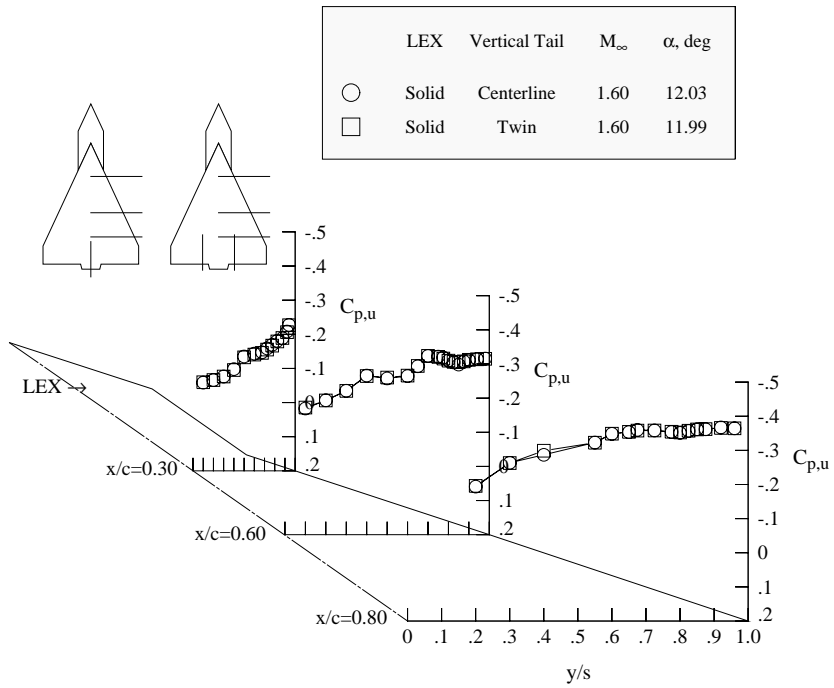
Figure 47. Comparison of ESP pressure distributions with solid and porous LEX; centerline vertical tail, $M_\infty = 2.1$.

96

(b) $\alpha = 16^{o}$.

(c) $\alpha = 20^{o}$.

Figure 47. Concluded.

	PSP	LEX	Vertical Tail	M_∞	α, deg
○	Off	Solid	Centerline	1.60	-4.03
□	Off	Solid	Centerline	1.60	0.03
◇	Off	Solid	Centerline	1.60	3.97
△	Off	Solid	Centerline	1.60	8.00
◁	Off	Solid	Centerline	1.60	12.03

(a) Solid LEX.

	PSP	LEX	Vertical Tail	M_∞	α, deg
○	Off	Porous	Centerline	1.60	-4.00
□	Off	Porous	Centerline	1.60	0.02
◇	Off	Porous	Centerline	1.60	4.00
△	Off	Porous	Centerline	1.60	8.00
◁	Off	Porous	Centerline	1.60	12.00
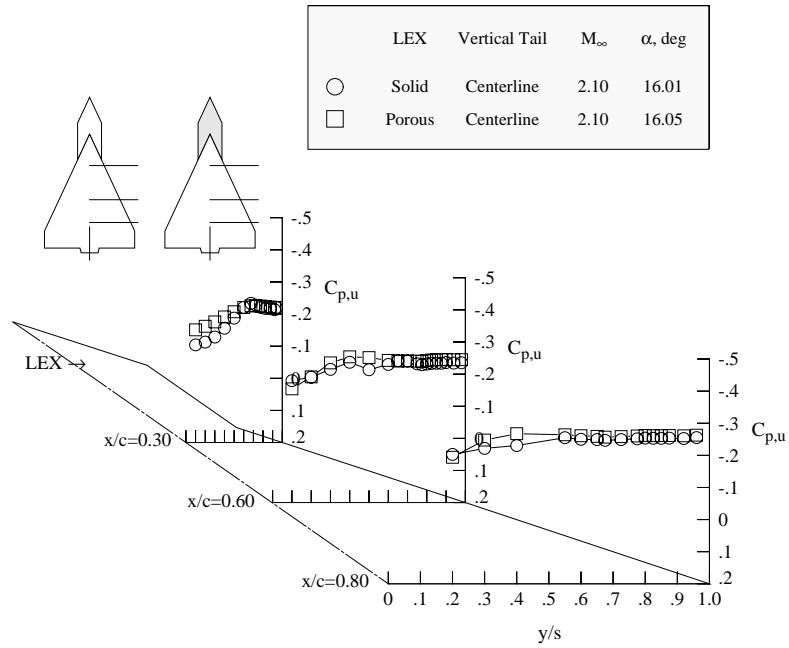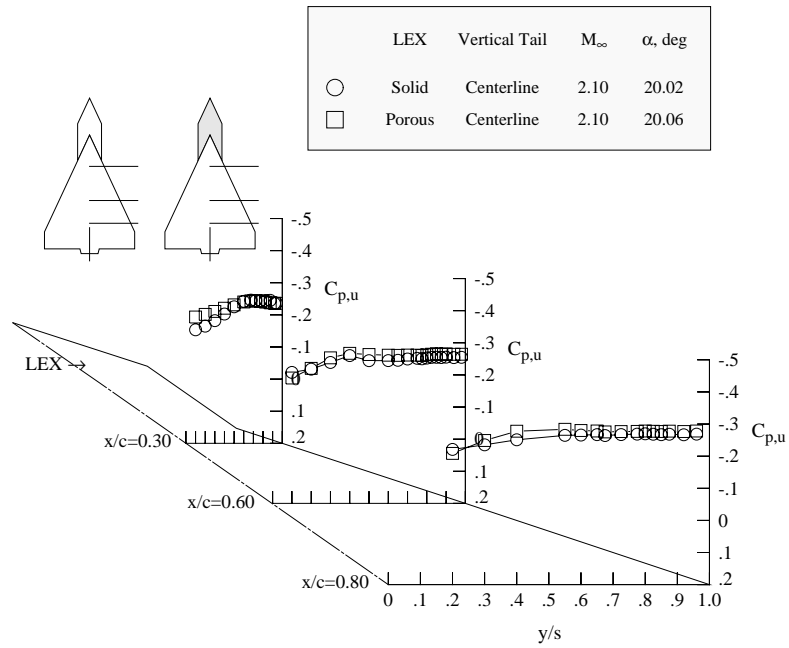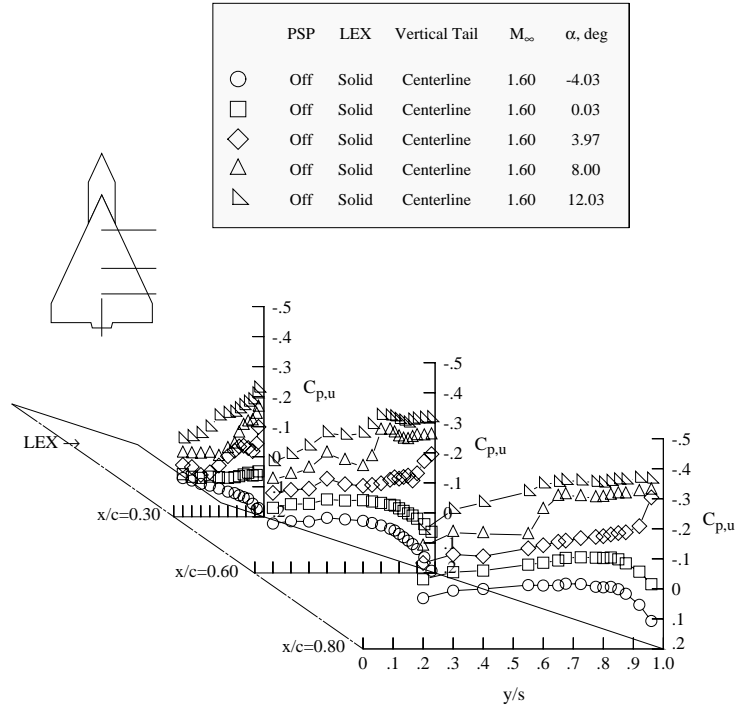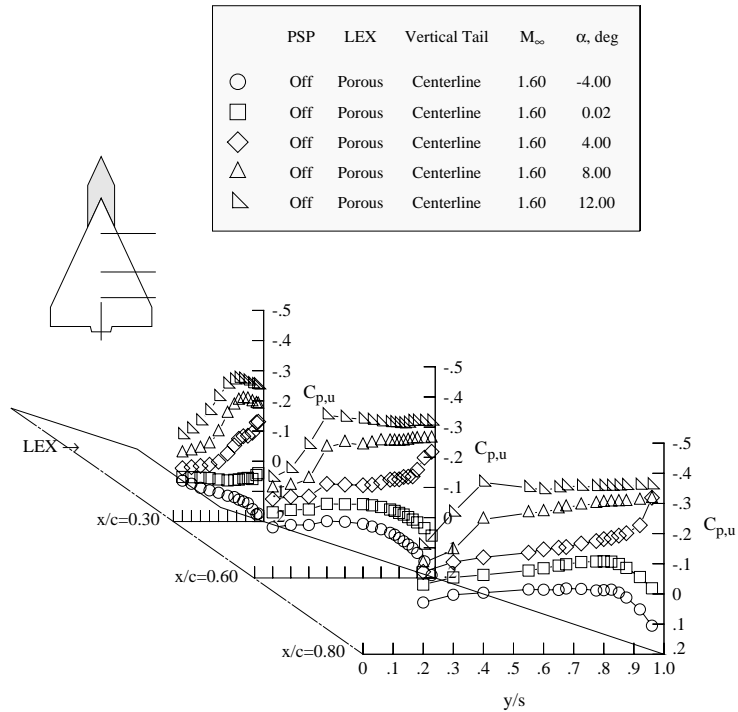
(b) Porous LEX.

Figure 48. Effect of angle of attack on ESP pressure distributions with centerline vertical tail; $M_\infty = 1.6$.

	PSP	LEX	Vertical Tail	M_∞	α, deg
○	Off	Solid	Centerline	1.80	-4.00
□	Off	Solid	Centerline	1.80	0.00
◇	Off	Solid	Centerline	1.80	4.03
△	Off	Solid	Centerline	1.80	8.02
◺	Off	Solid	Centerline	1.80	12.02
◻	Off	Solid	Centerline	1.80	16.02
◠	Off	Solid	Centerline	1.80	20.02

(a) Solid LEX.

	PSP	LEX	Vertical Tail	M_∞	α, deg
○	Off	Porous	Centerline	1.80	-4.02
□	Off	Porous	Centerline	1.80	0.03
◇	Off	Porous	Centerline	1.80	4.01
△	Off	Porous	Centerline	1.80	7.99
◺	Off	Porous	Centerline	1.80	12.03
◻	Off	Porous	Centerline	1.80	16.02
◠	Off	Porous	Centerline	1.80	20.00

(b) Porous LEX.

Figure 49. Effect of angle of attack on ESP pressure distributions with centerline vertical tail; $M_\infty = 1.8$.

99

	PSP	LEX	Vertical Tail	M_∞	α, deg
○	Off	Solid	Centerline	2.10	-4.00
□	Off	Solid	Centerline	2.10	-0.01
◇	Off	Solid	Centerline	2.10	4.02
△	Off	Solid	Centerline	2.10	8.01
◺	Off	Solid	Centerline	2.10	12.01
◿	Off	Solid	Centerline	2.10	16.01
⌂	Off	Solid	Centerline	2.10	20.02

(a) Solid LEX.

	PSP	LEX	Vertical Tail	M_∞	α, deg
○	Off	Porous	Centerline	2.10	-4.02
□	Off	Porous	Centerline	2.10	-0.01
◇	Off	Porous	Centerline	2.10	4.03
△	Off	Porous	Centerline	2.10	8.03
◺	Off	Porous	Centerline	2.10	12.01
◿	Off	Porous	Centerline	2.10	16.05
⌂	Off	Porous	Centerline	2.10	20.06

(b) Porous LEX.

Figure 50. Effect of angle of attack on ESP pressure distributions with centerline vertical tail; $M_\infty = 2.1$.

100

(a) Solid LEX.
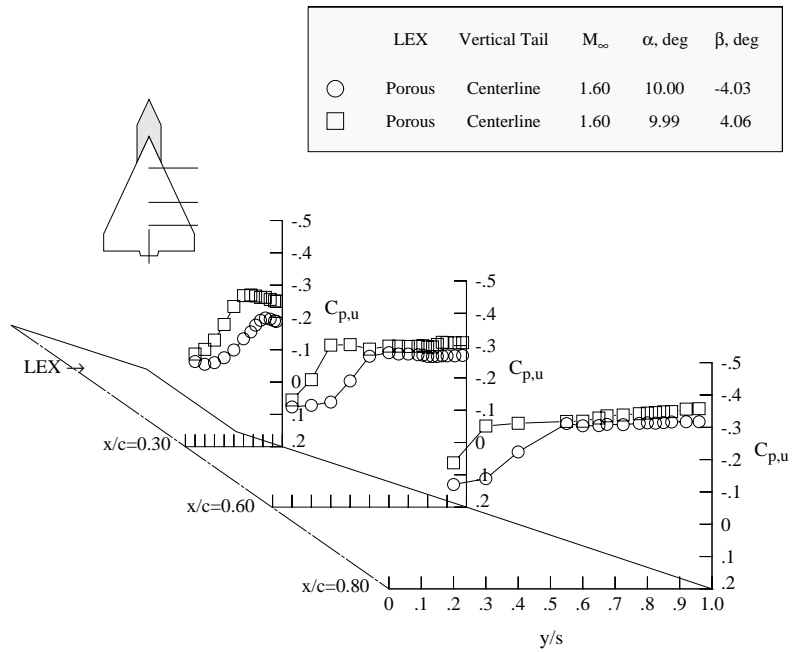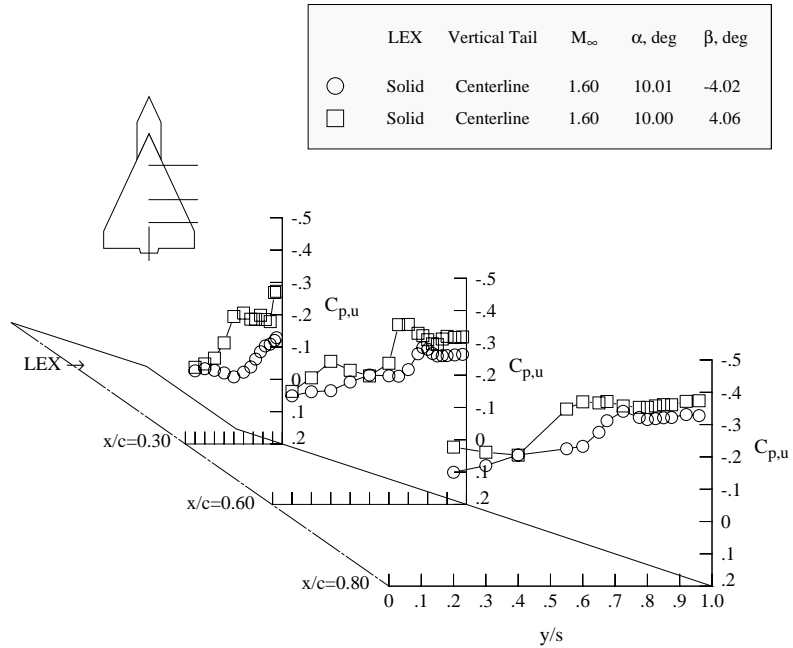
(b) Porous LEX.

Figure 51. Effect of sideslip on ESP pressure distributions with centerline vertical tail; $\alpha = 10^o$; $M_\infty = 1.6$.
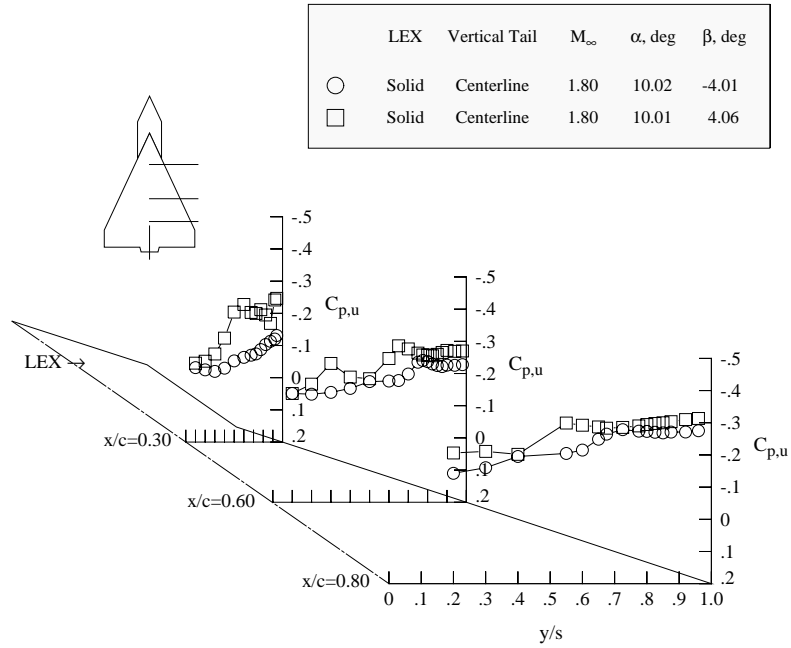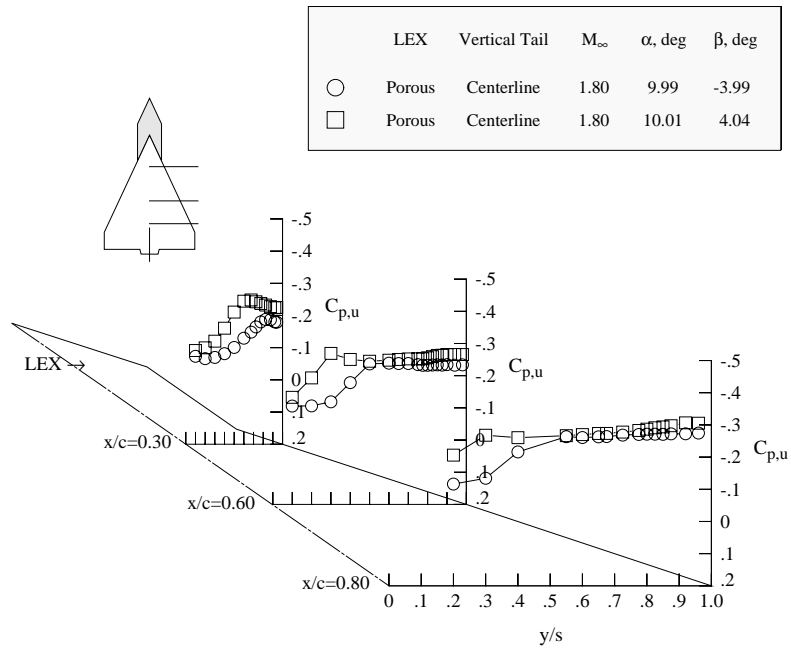
(a) Solid LEX.

(b) Porous LEX.

Figure 52. Effect of sideslip on ESP pressure distributions with centerline vertical tail, $\alpha = 10^o$; $M_\infty = 1.8$.
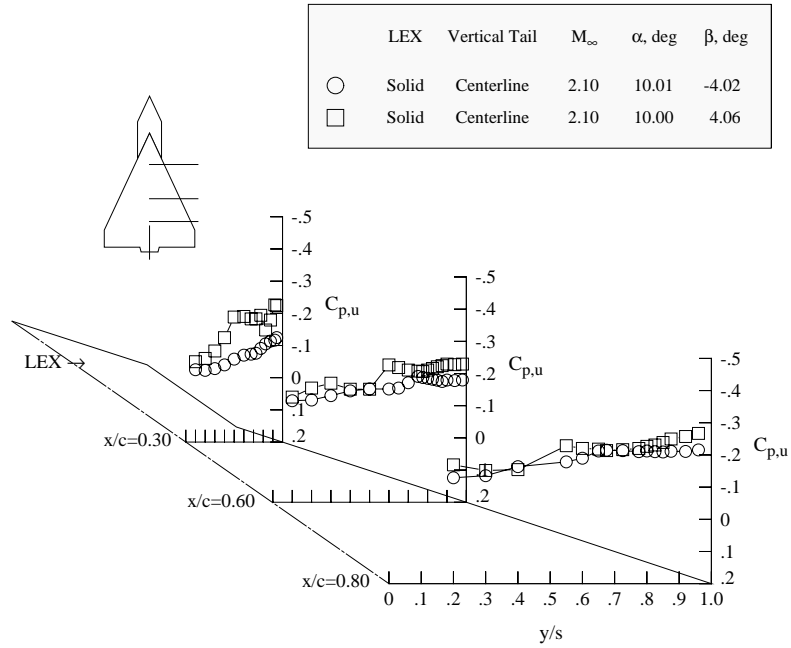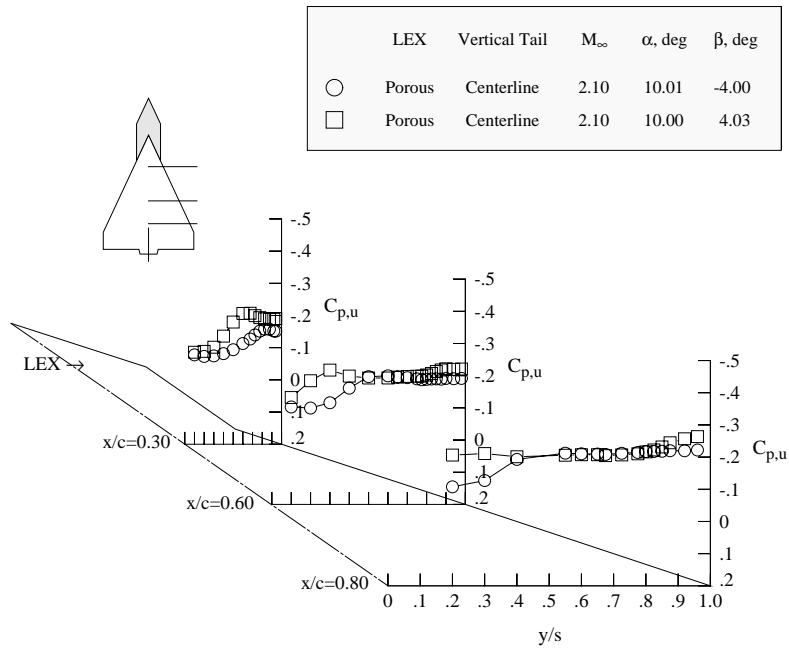
(a) Solid LEX.

(b) Porous LEX.

Figure 53. Effect of sideslip on ESP pressure distributions with centerline vertical tail, $\alpha = 10^o$; $M_\infty = 2.1$.
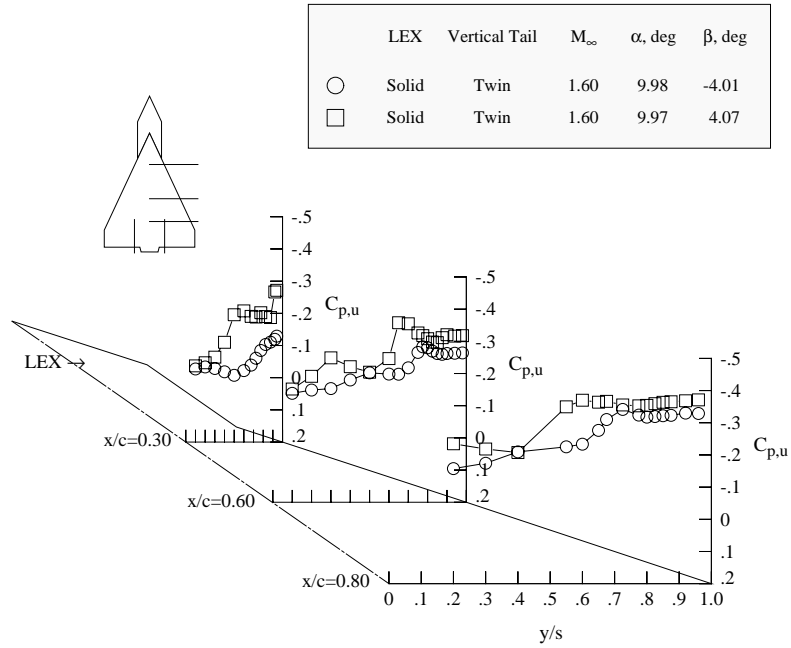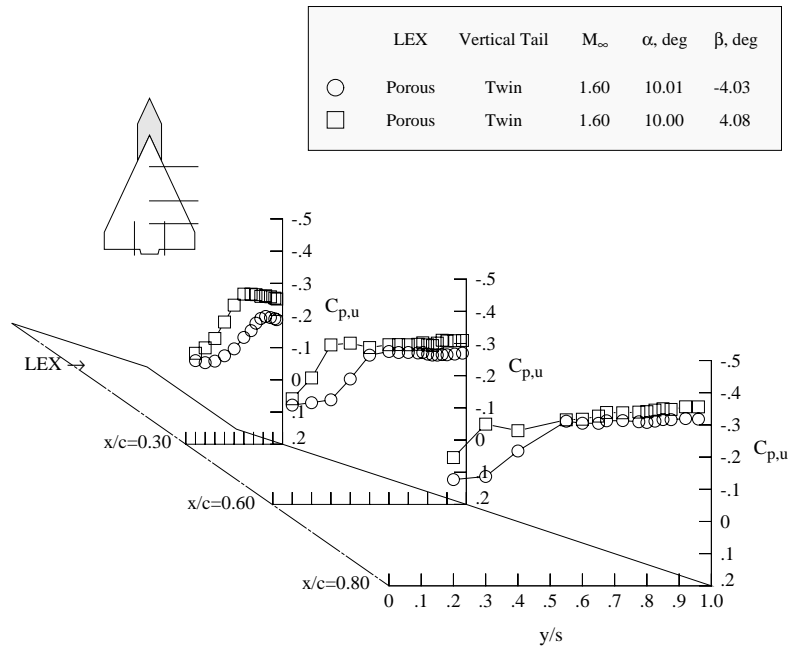
(a) Solid LEX.

(b) Porous LEX.

Figure 54. Effect of sideslip on ESP pressure distributions with twin vertical tails, $\alpha = 10^o$; $M_\infty = 1.6$.
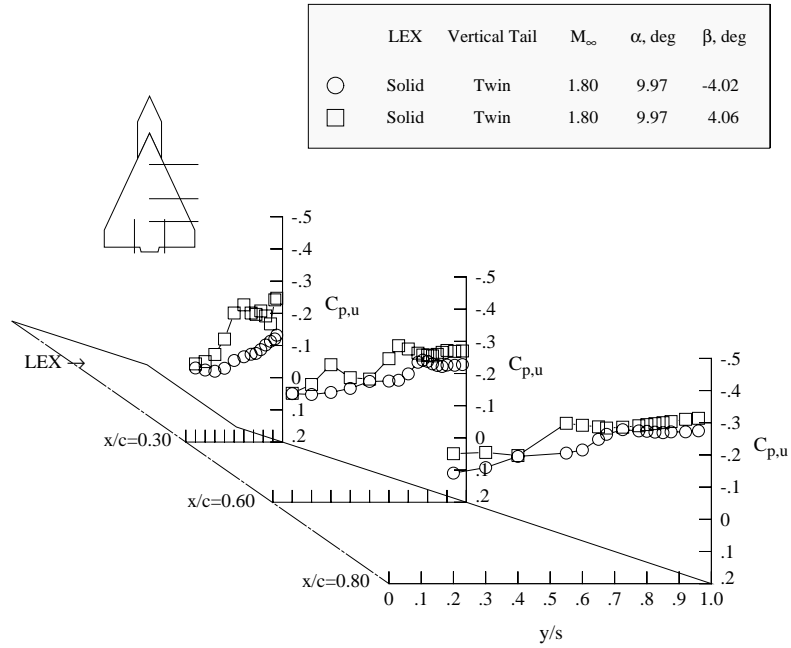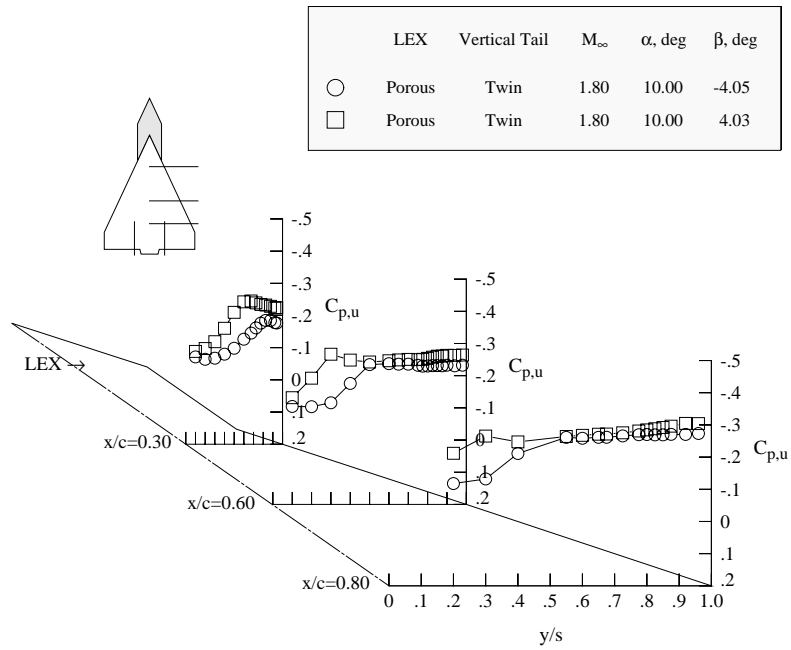
(a) Solid LEX.

(b) Porous LEX.

Figure 55. Effect of sideslip on ESP pressure distributions with twin vertical tails, $\alpha = 10^o$; $M_\infty = 1.8$.
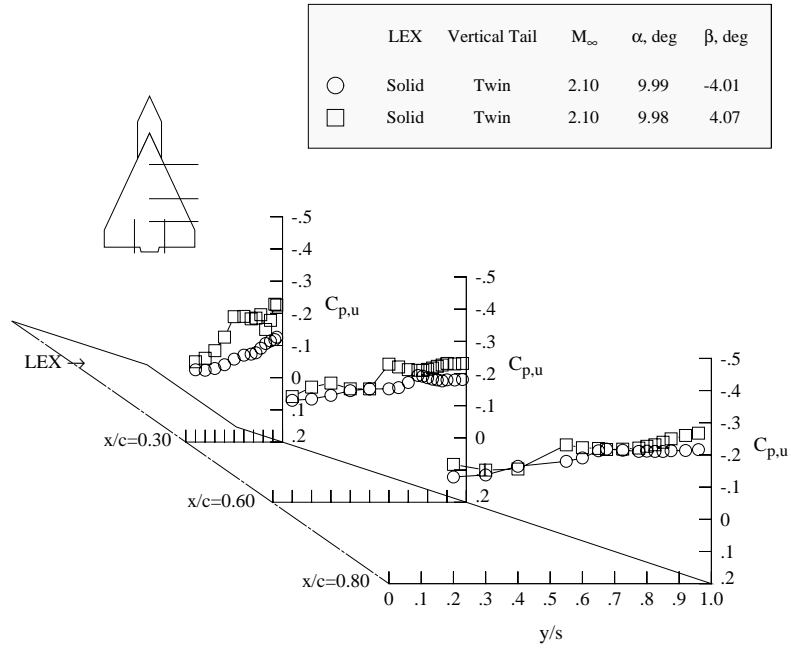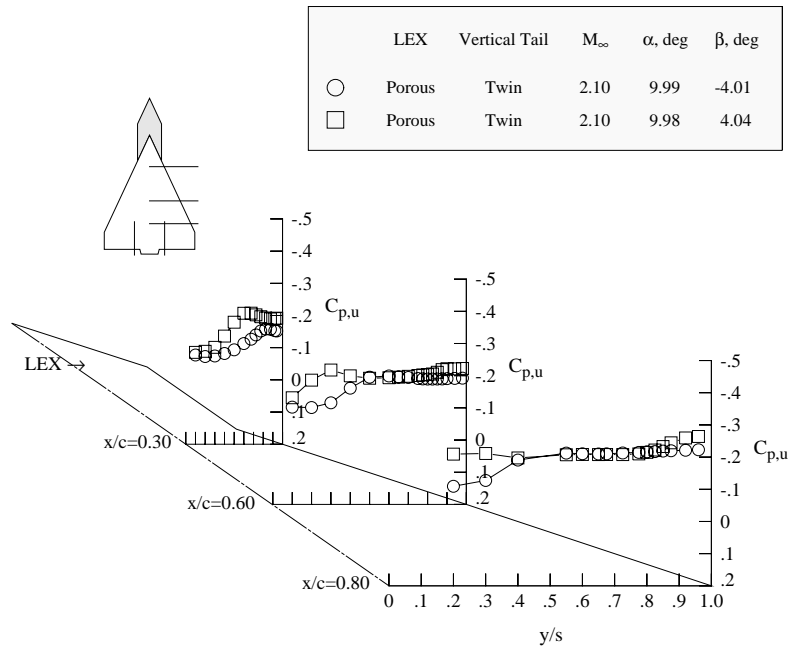
(a) Solid LEX.

(b) Porous LEX.

Figure 56. Effect of sideslip on ESP pressure distributions with twin vertical tails, $\alpha = 10^{o}$; $M_{\infty} = 2.1$.
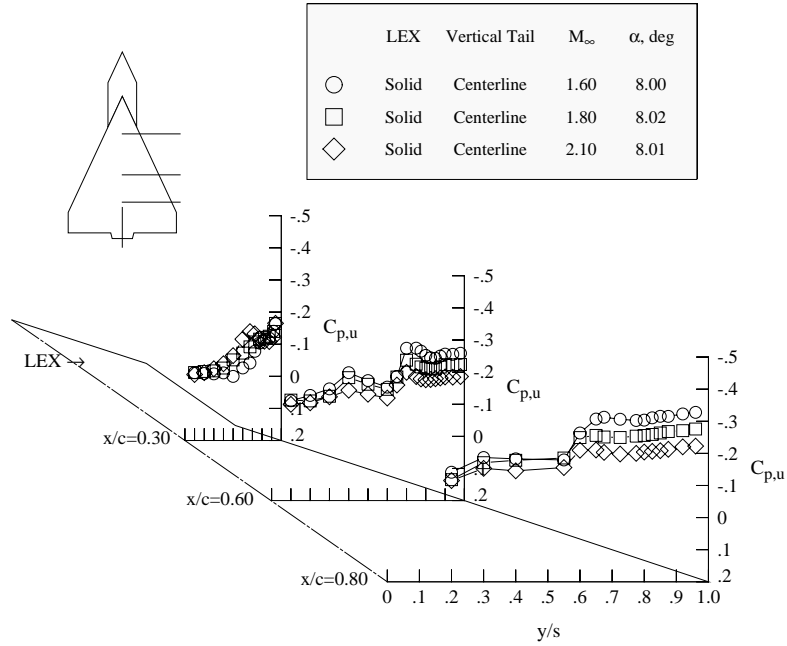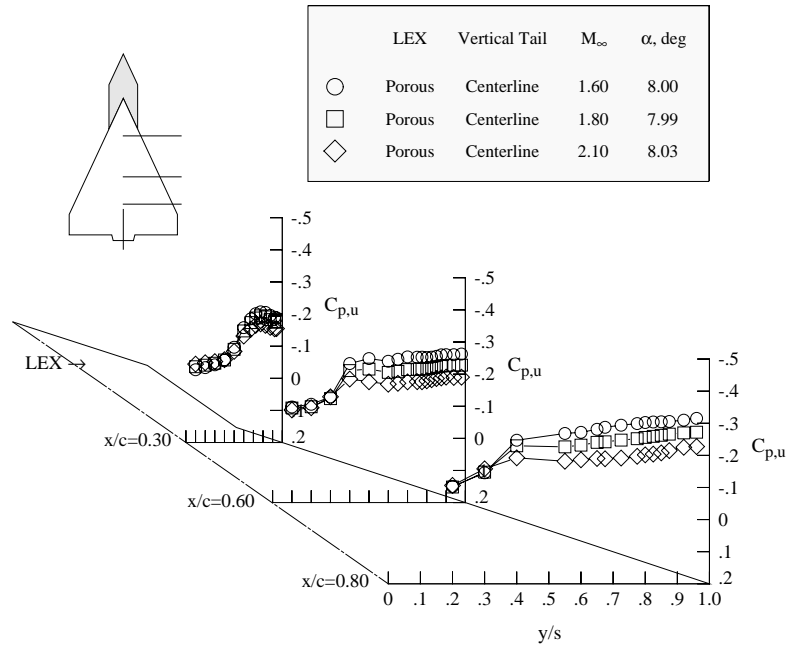
(a) Solid LEX.

(b) Porous LEX.

Figure 57. Effect of Mach number on ESP pressure distributions with centerline
vertical tail, $\alpha = 8^o$.
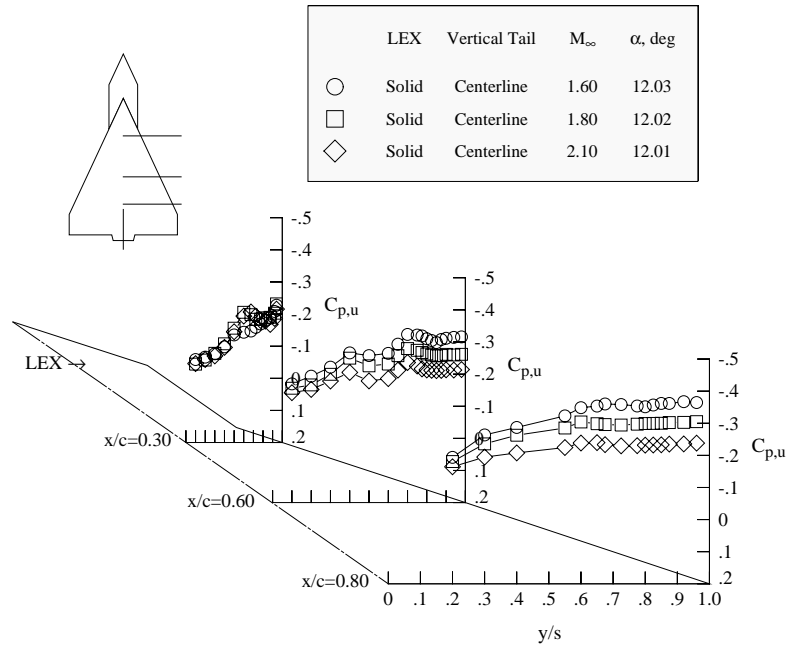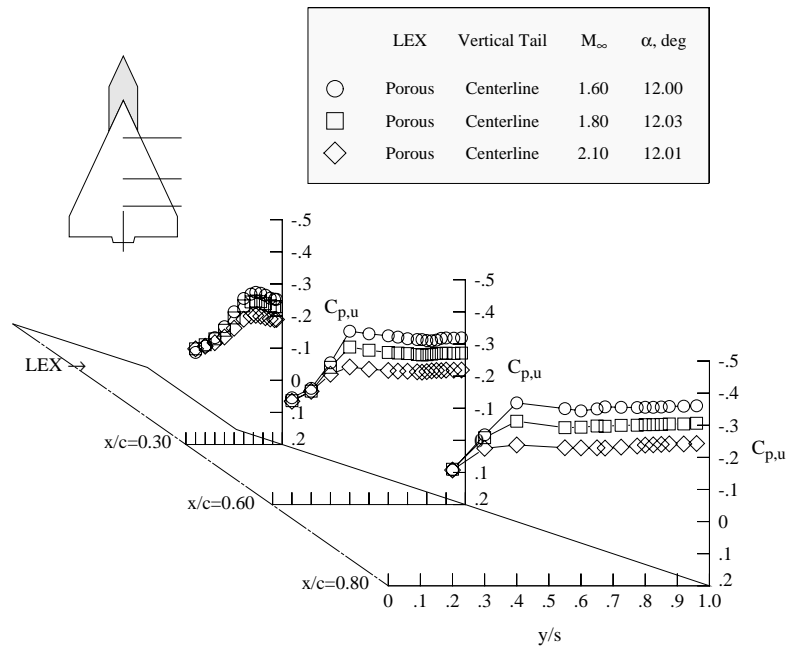
(a) Solid LEX.

(b) Porous LEX.

Figure 58. Effect of Mach number on ESP pressure distributions with centerline vertical tail, $\alpha = 12^o$.
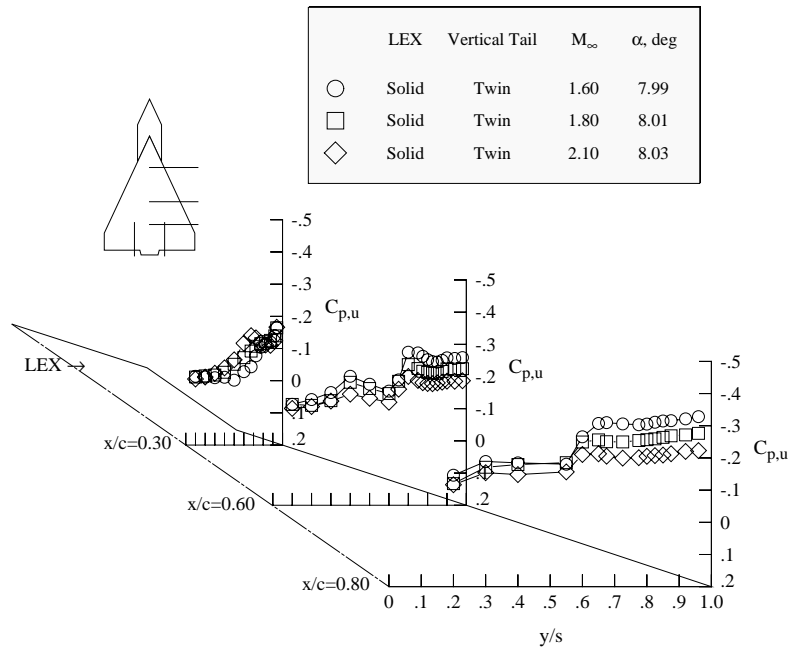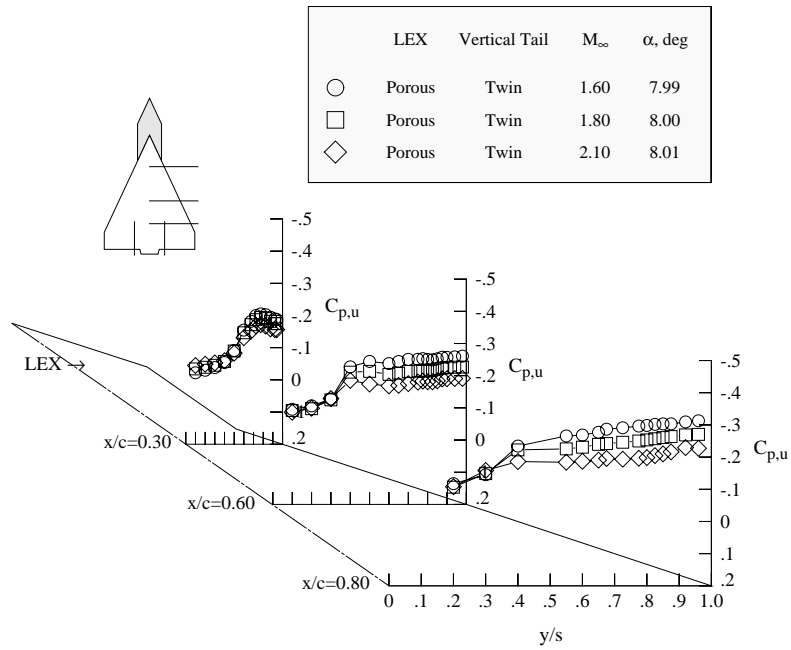
(a) Solid LEX.

(b) Porous LEX.

Figure 59. Effect of Mach number on ESP pressure distributions with twin vertical
tails, $\alpha = 8^{o}$.
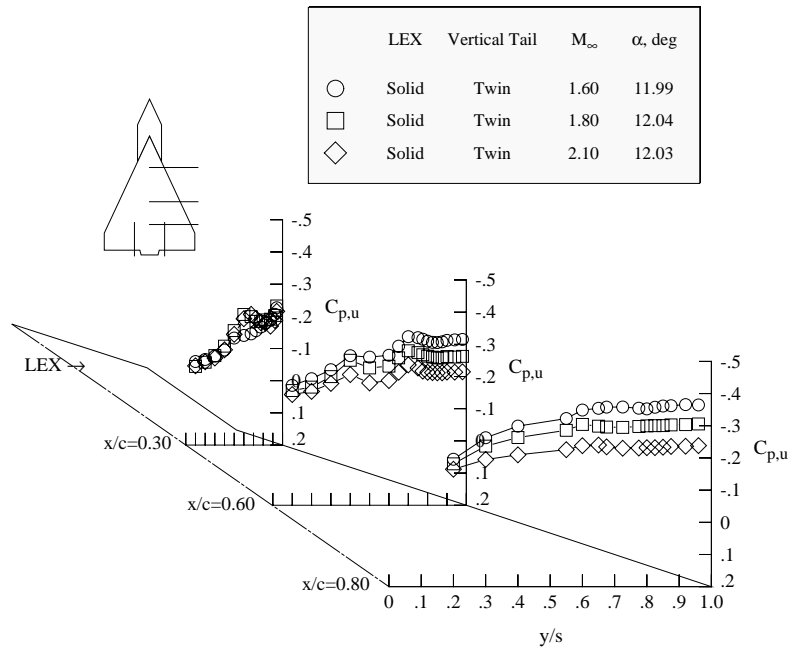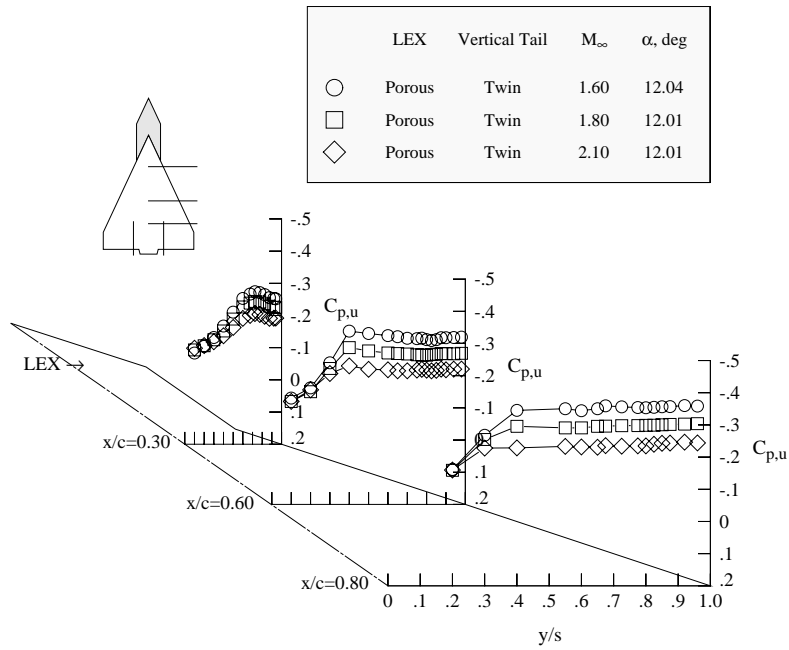
(a) Solid LEX.

(b) Porous LEX.

Figure 60. Effect of Mach number on ESP pressure distributions with twin vertical tails, $\alpha = 12^{o}$.

(a) $\alpha = 8^\circ$.

(b) $\alpha = 12^\circ$.
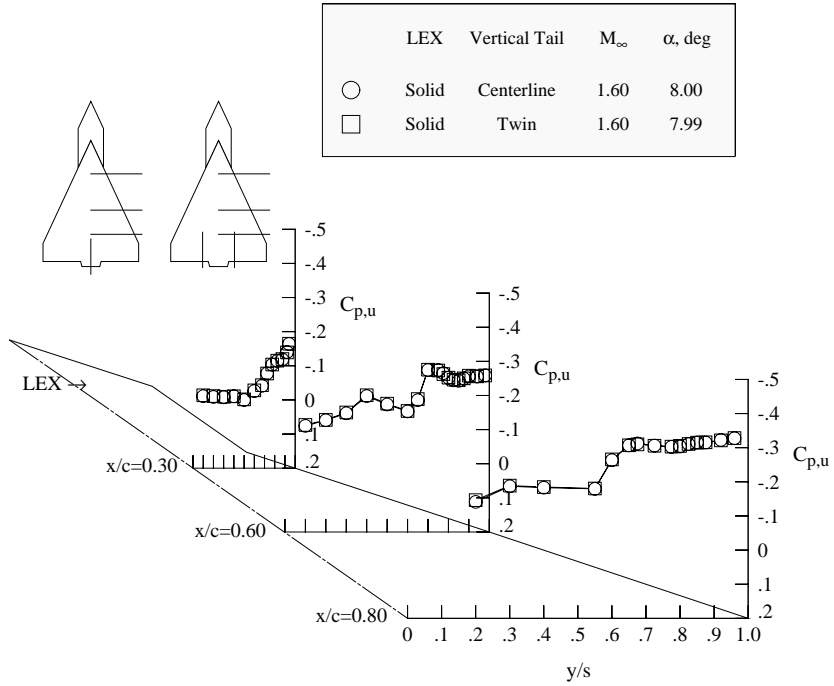
Figure 61. Comparison of ESP pressure distributions with centerline and twin vertical tails; solid LEX, $M_\infty = 1.6$.

111
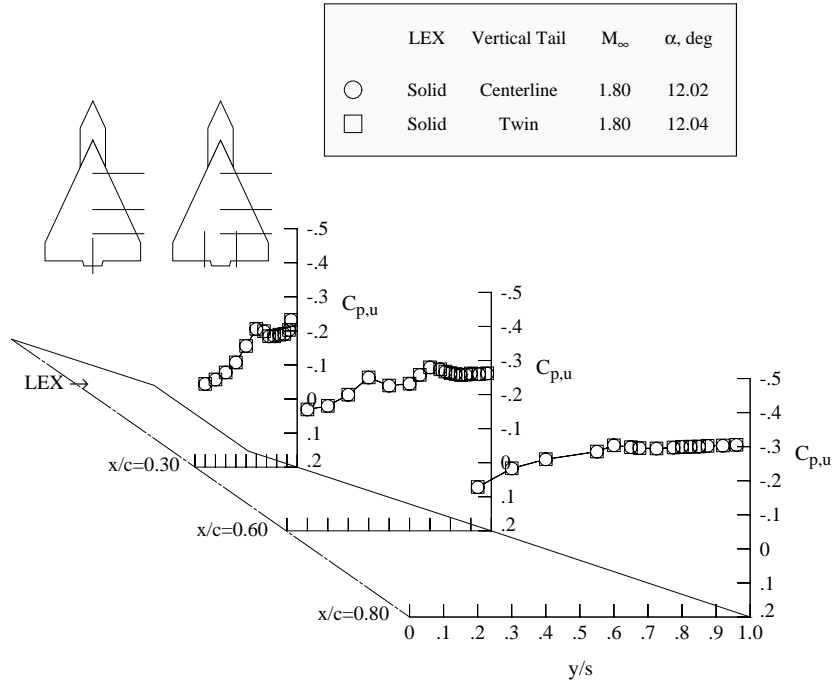
(a) $\alpha = 12^\circ$.
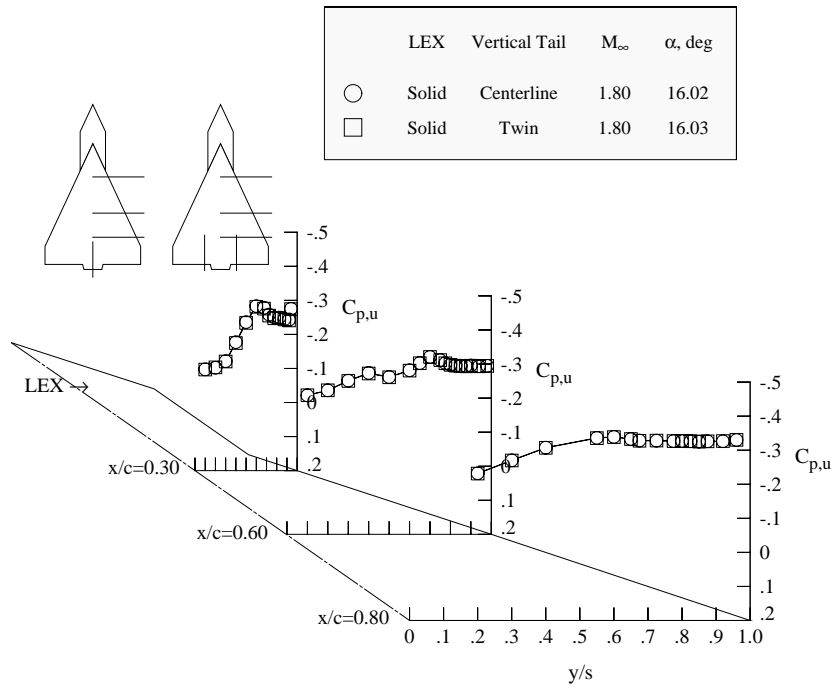
(b) $\alpha = 16^\circ$.

Figure 62. Comparison of ESP pressure distributions with centerline and twin vertical tails; solid LEX, $M_\infty = 1.8$.
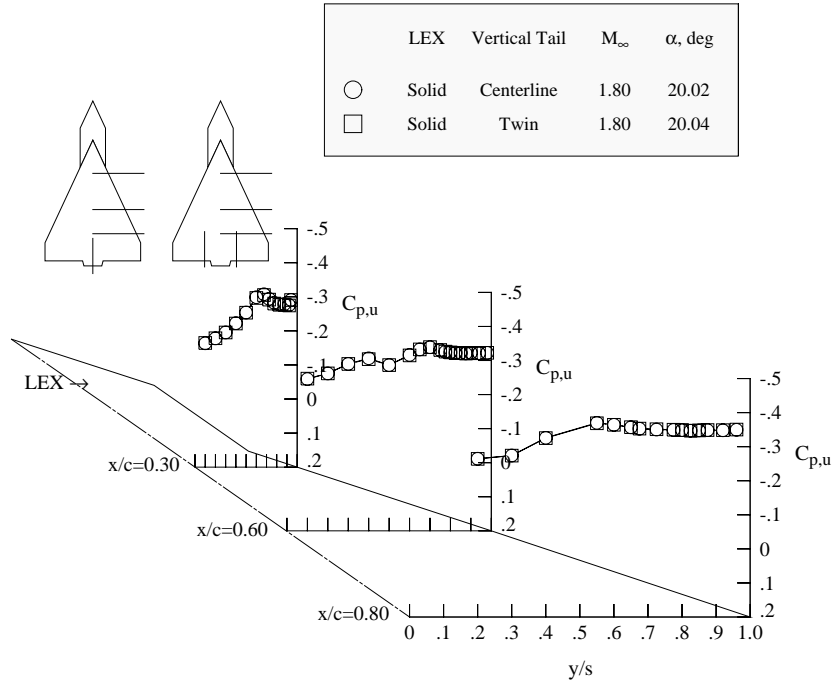
(c) $\alpha = 20^{\circ}$.

Figure 62. Concluded.
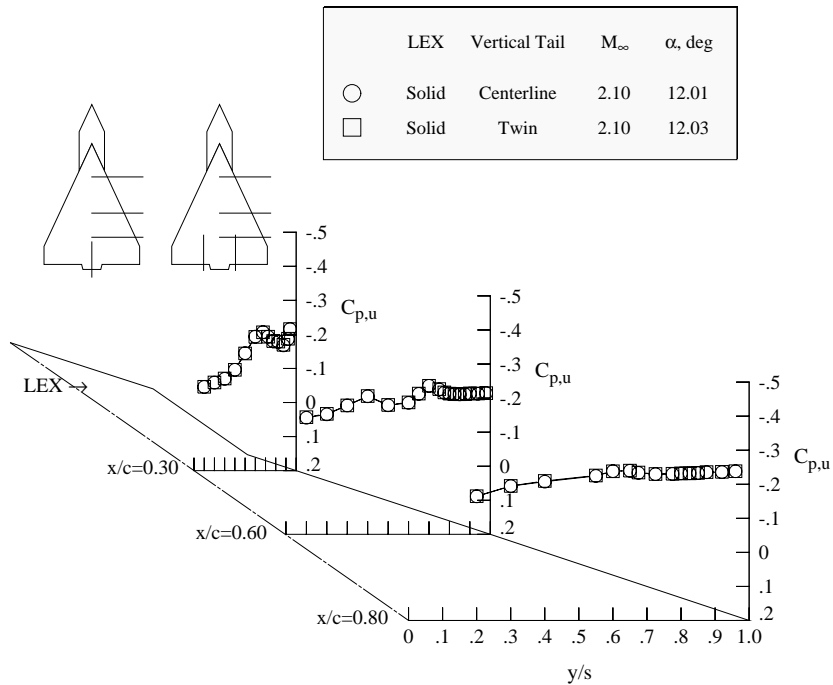
(a) $\alpha = 12^{\circ}$.

Figure 63. Comparison of ESP pressure distributions with centerline and twin vertical tails; solid LEX, $M_{\infty} = 2.1$.

	LEX	Vertical Tail	M_∞	α, deg
○	Solid	Centerline	2.10	16.01
□	Solid	Twin	2.10	16.03

(b) $\alpha = 16°$.

	LEX	Vertical Tail	M_∞	α, deg
○	Solid	Centerline	2.10	20.02
□	Solid	Twin	2.10	20.03
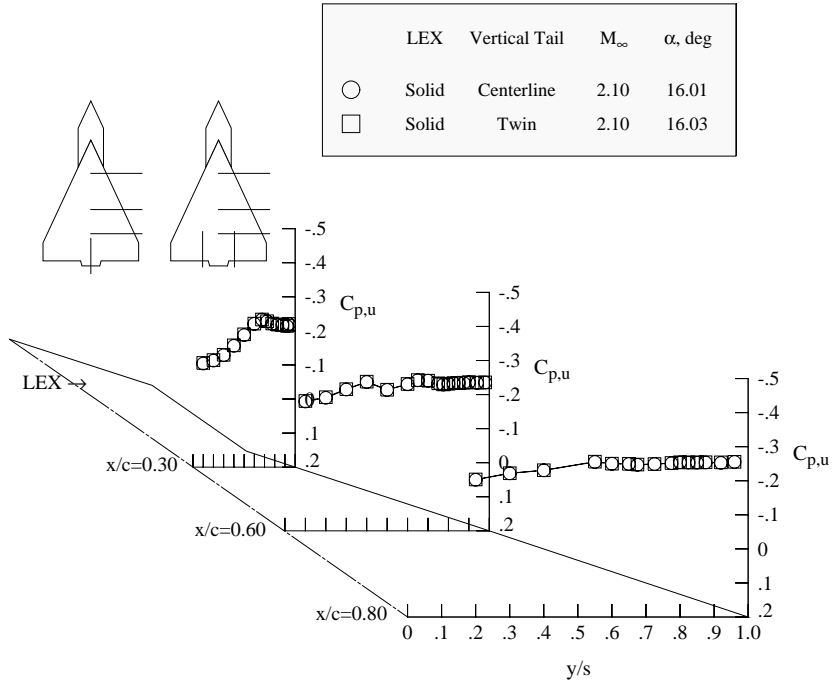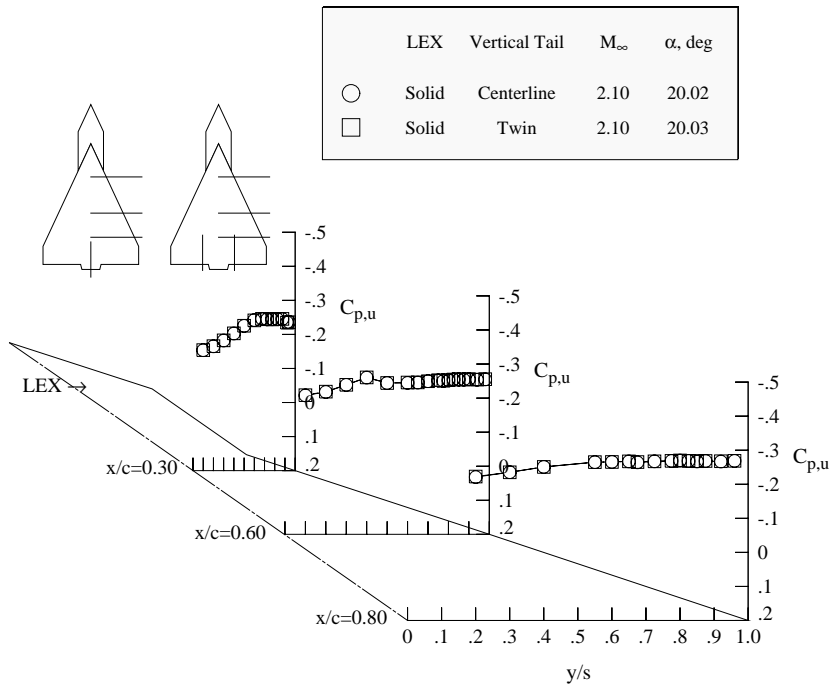
(c) $\alpha = 20°$.

Figure 63. Concluded.

(a) $\alpha = 8^o$.

(b) $\alpha = 12^o$.
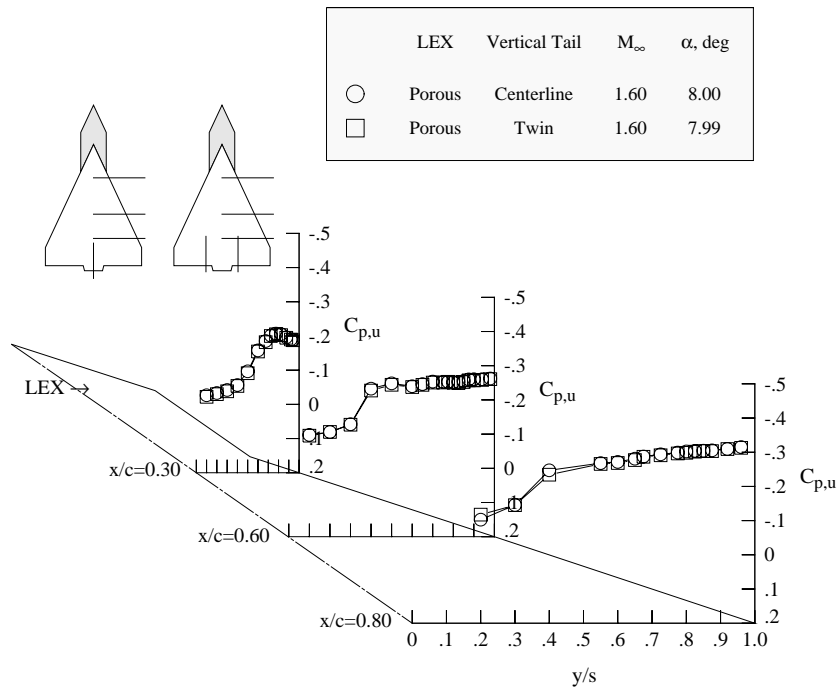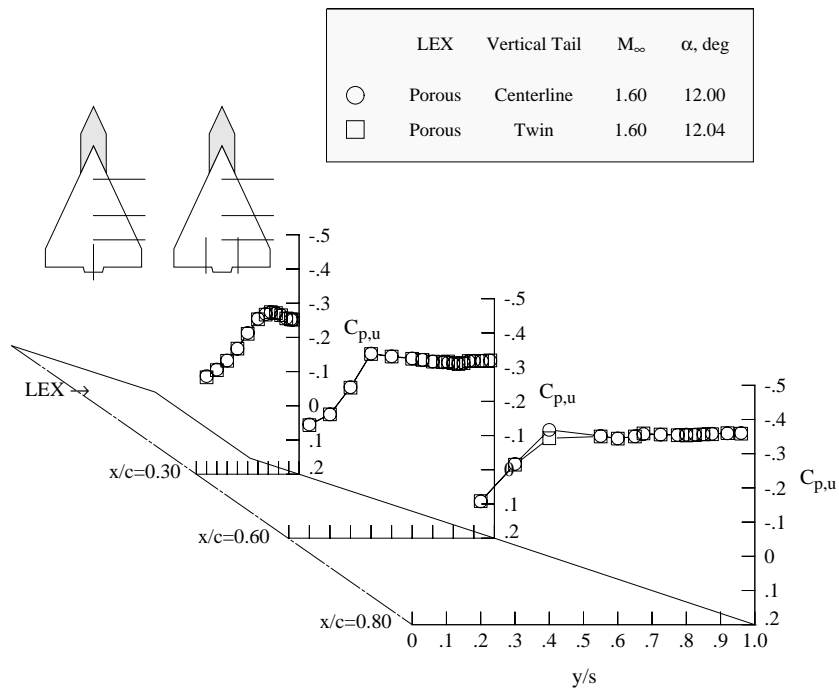
Figure 64. Comparison of ESP pressure distributions with centerline and twin vertical tails; porous LEX, $M_\infty = 1.6$.

(a) $\alpha = 12^{o}$.

(b) $\alpha = 16^{o}$.
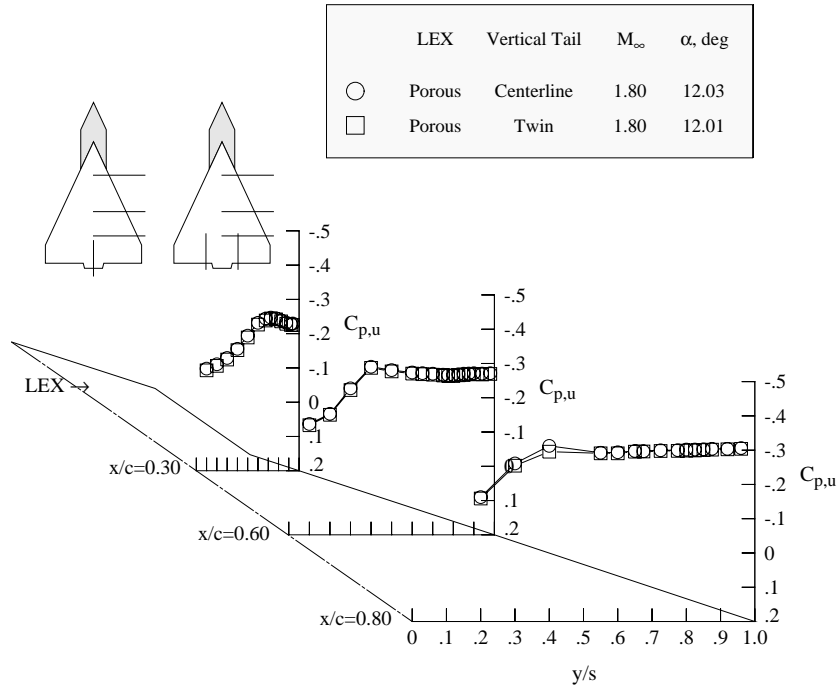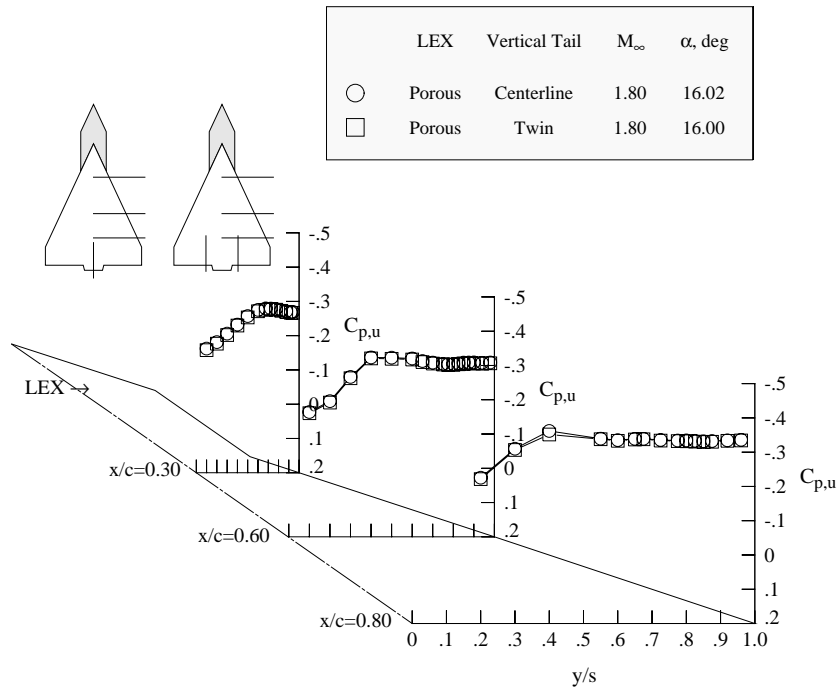
Figure 65. Comparison of ESP pressure distributions with centerline and twin
vertical tails; porous LEX, $M_{\infty} = 1.8$.

116
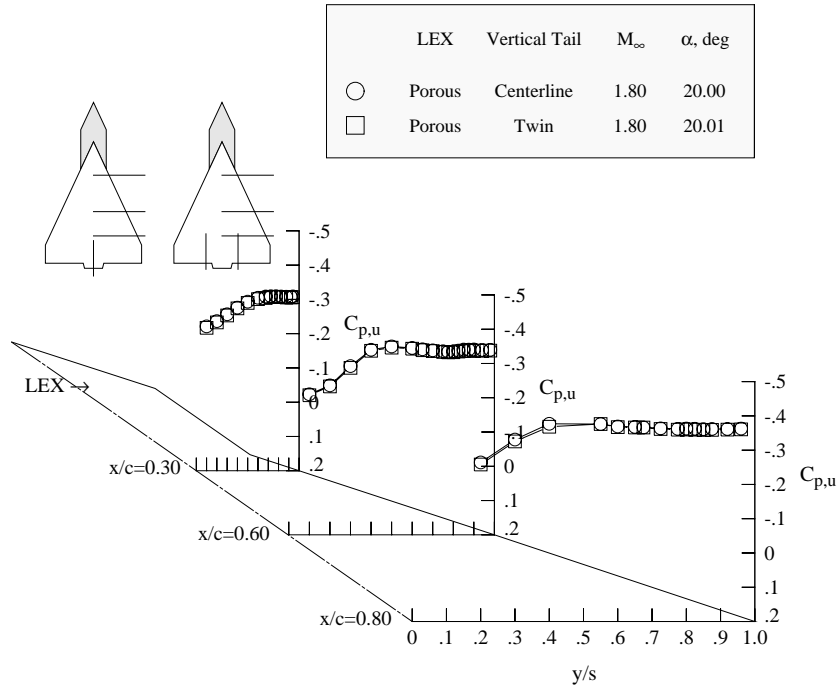
(c) $\alpha = 20^{\circ}$.

Figure 65. Concluded.
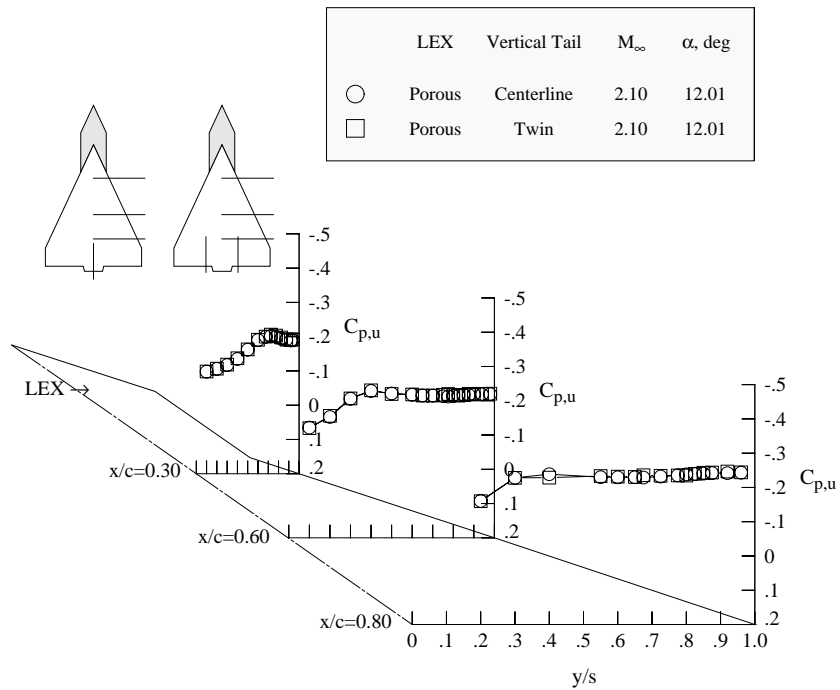
(a) $\alpha = 12^{\circ}$.

Figure 66. Comparison of ESP pressure distributions with centerline and twin vertical tails; porous LEX, $M_{\infty} = 2.1$.

	LEX	Vertical Tail	M_∞	α, deg
○	Porous	Centerline	2.10	16.05
□	Porous	Twin	2.10	16.03

(b) $\alpha = 16^o$.

	LEX	Vertical Tail	M_∞	α, deg
○	Porous	Centerline	2.10	20.06
□	Porous	Twin	2.10	20.01

(c) $\alpha = 20^o$.

Figure 66. Concluded.

118

	M_∞	LEX	Vertical Tail
○	1.60	Solid	Centerline
□	1.60	Porous	Centerline
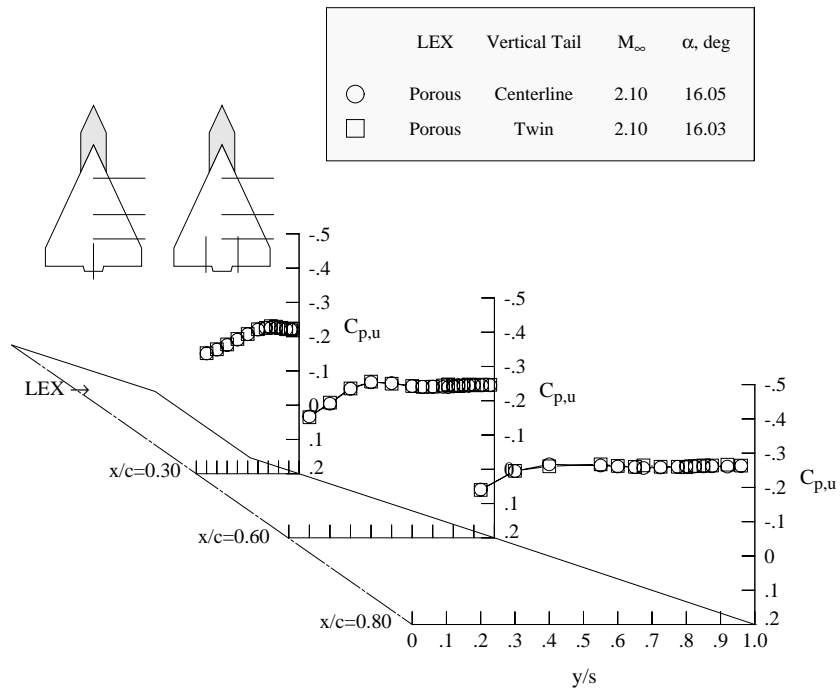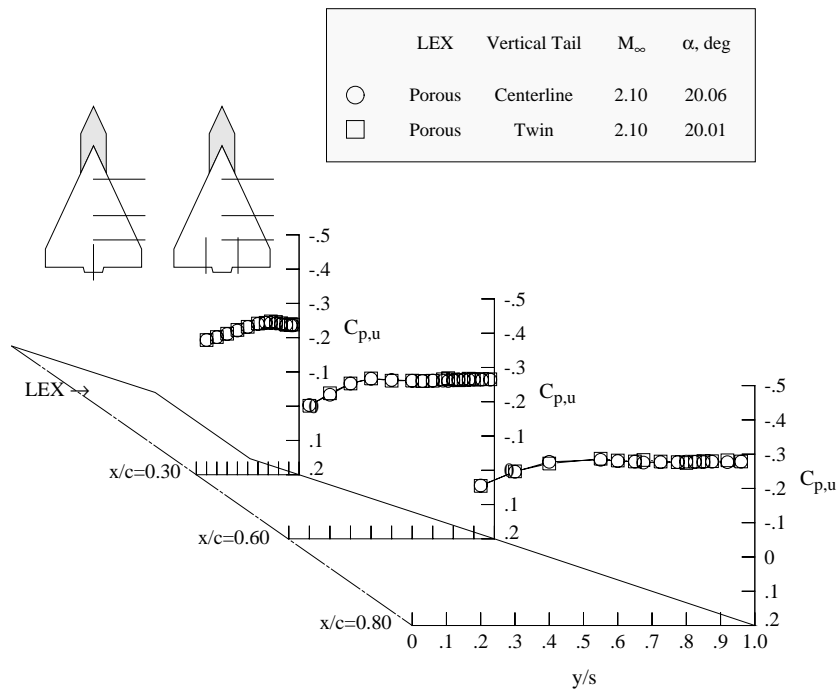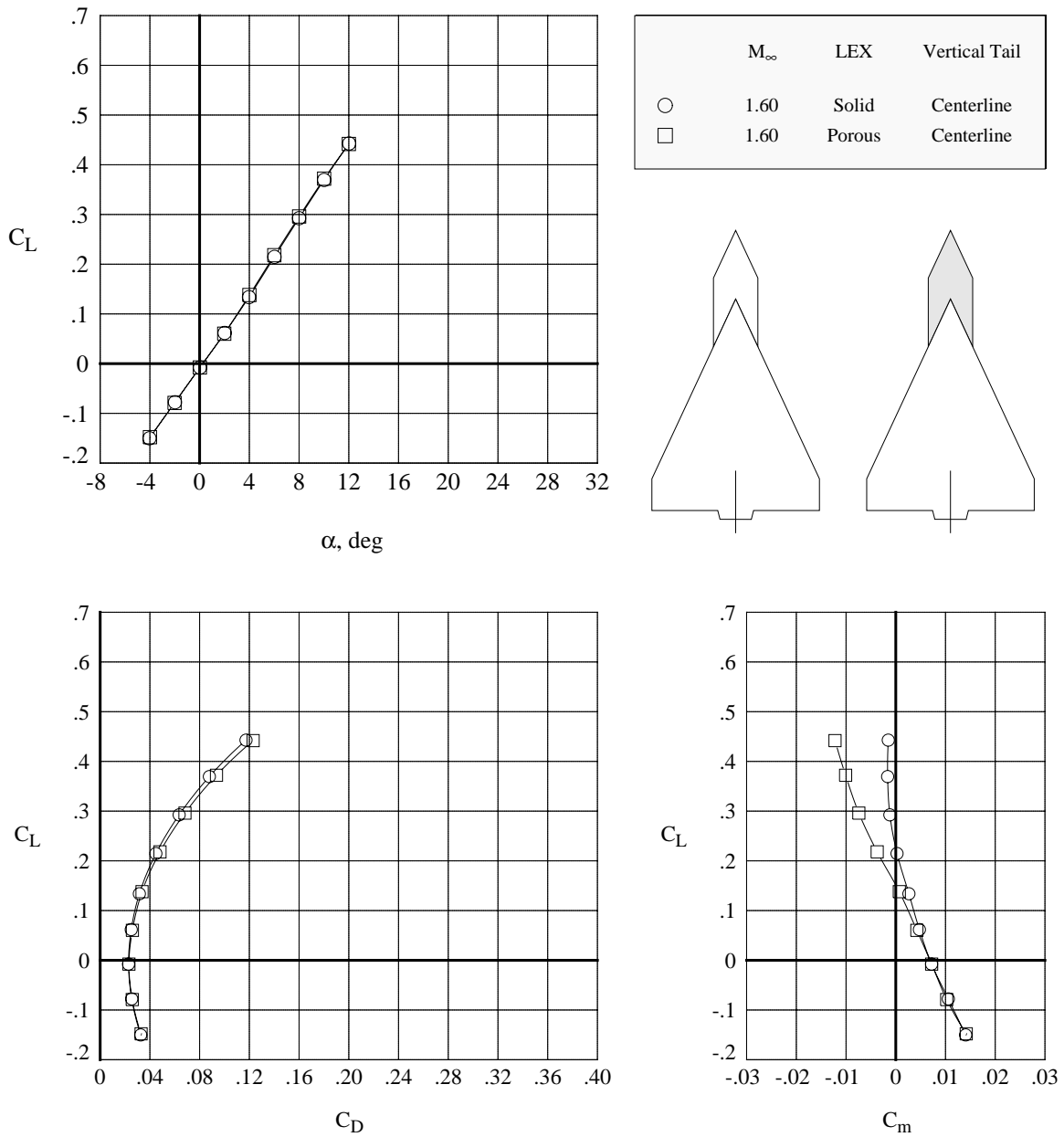
(a) Centerline tail.

Figure 67. Comparison of longitudinal aerodynamic characteristics with solid and porous LEX; $M_\infty = 1.6$.
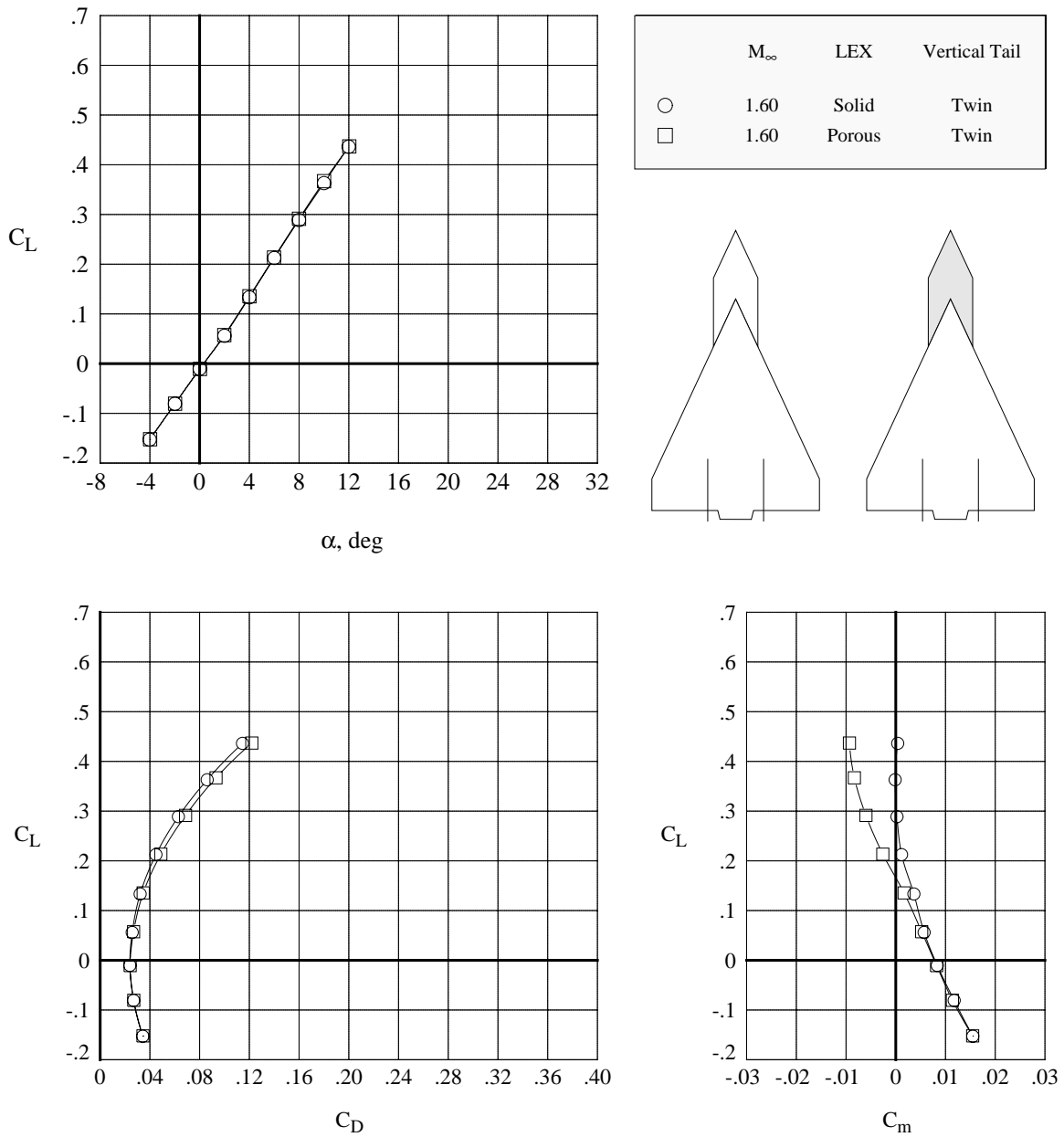
(b) Twin vertical tails.

Figure 67. Concluded.
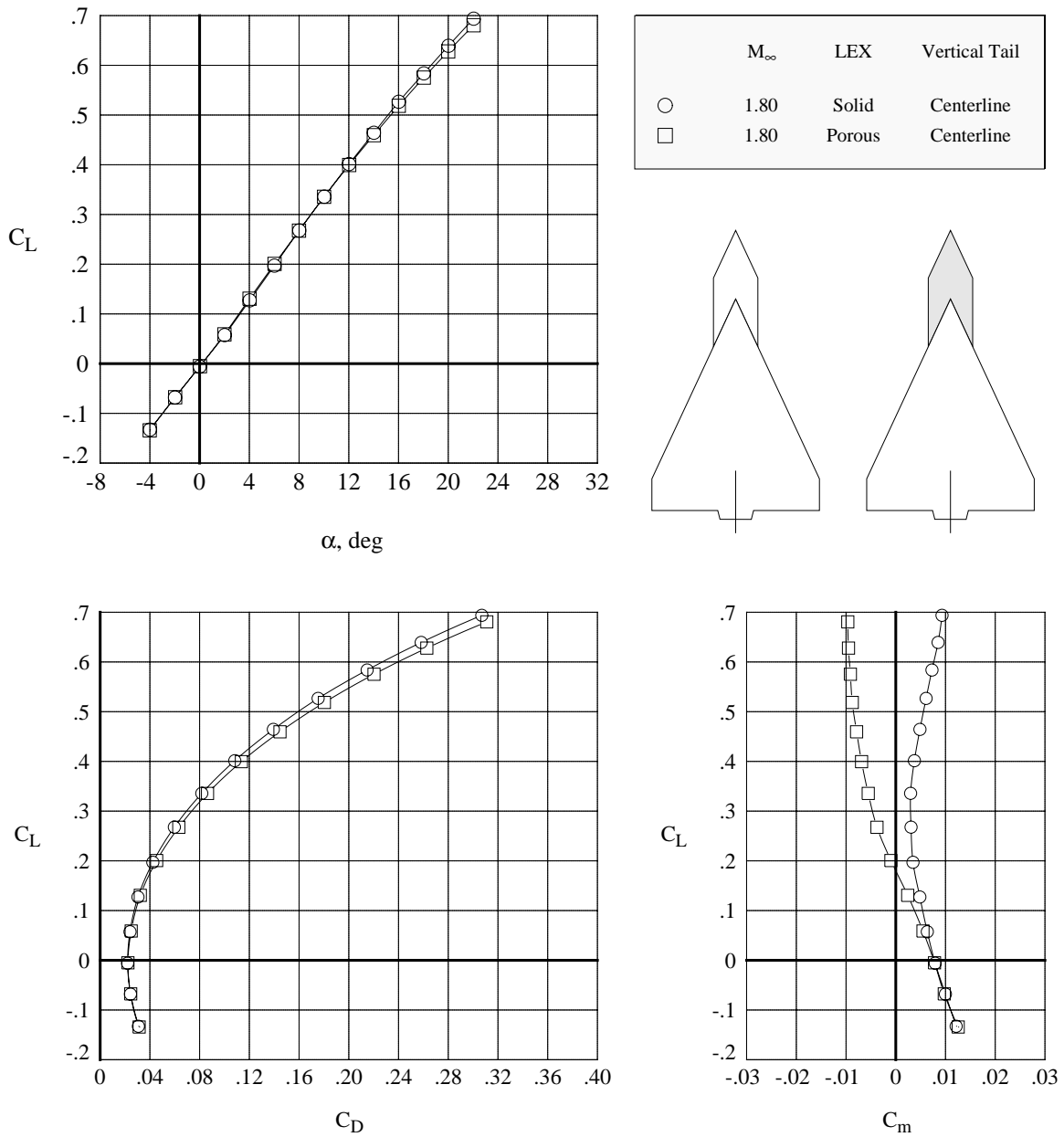
(a) Centerline vertical tail.

Figure 68. Comparison of longitudinal aerodynamic characteristics with solid and porous LEX; $M_\infty = 1.8$.
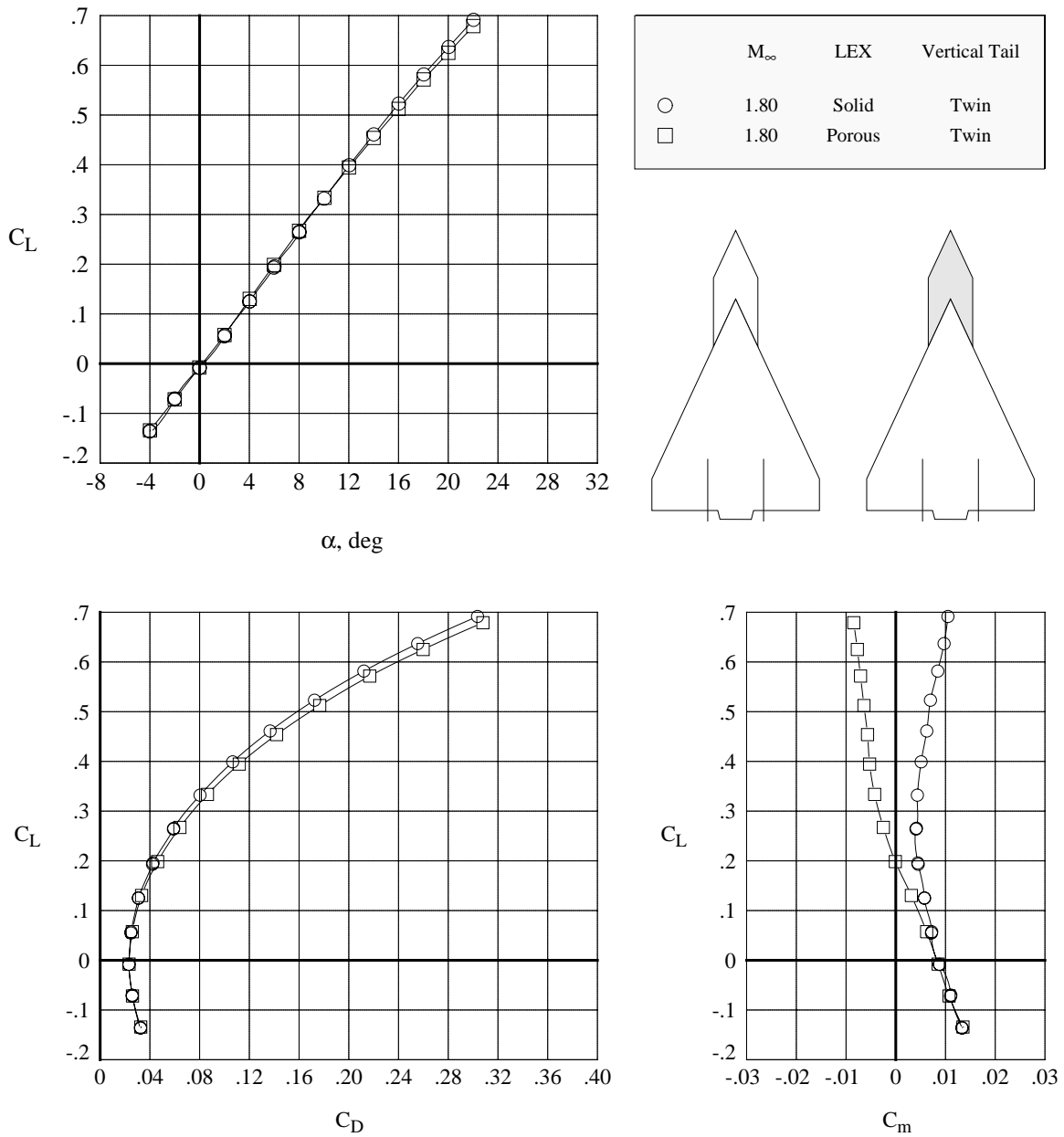
(b) Twin vertical tails.

Figure 68. Concluded.
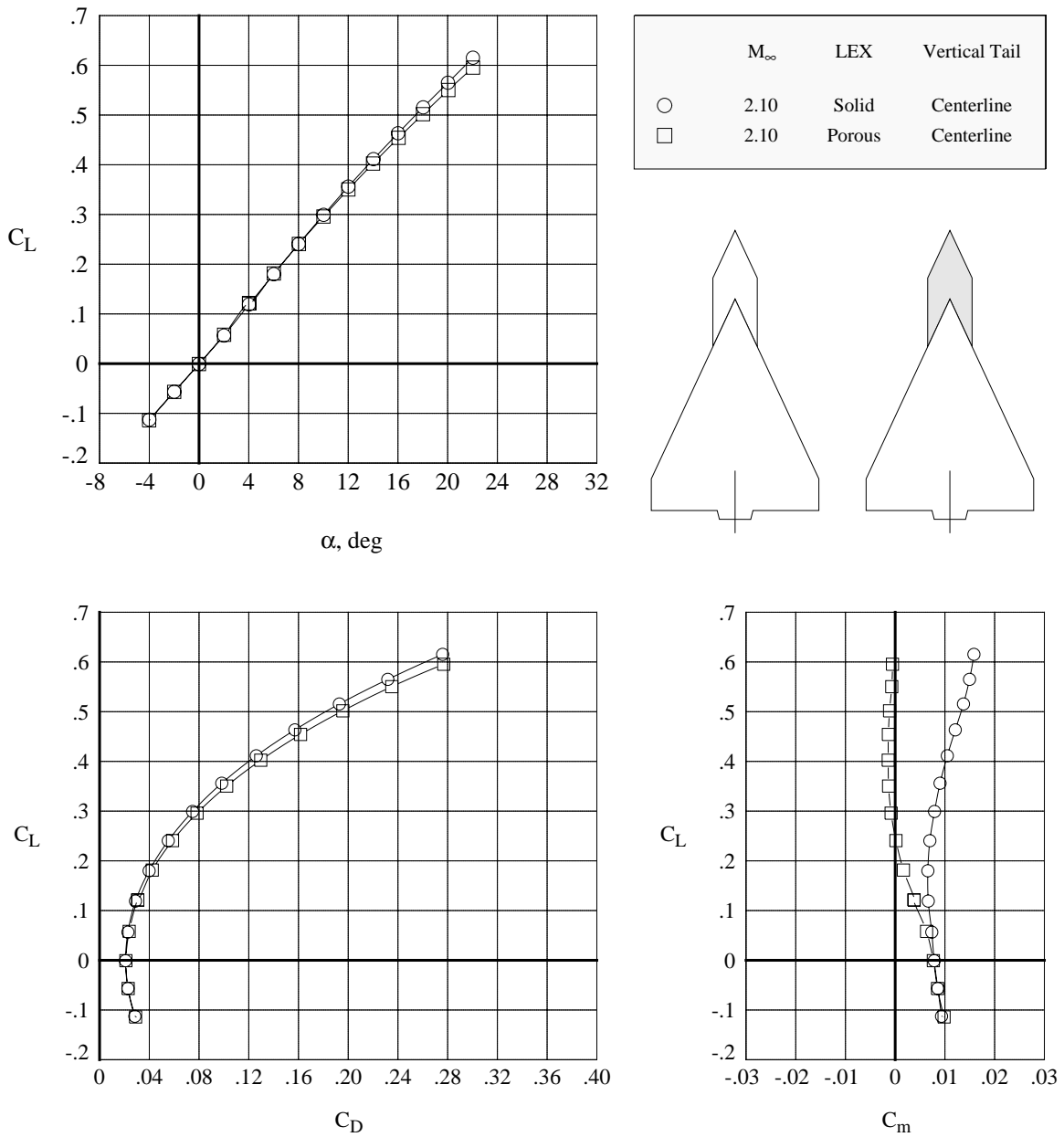
(a) Centerline vertical tail.

Figure 69. Comparison of longitudinal aerodynamic characteristics with solid and porous LEX; $M_\infty = 2.1$.
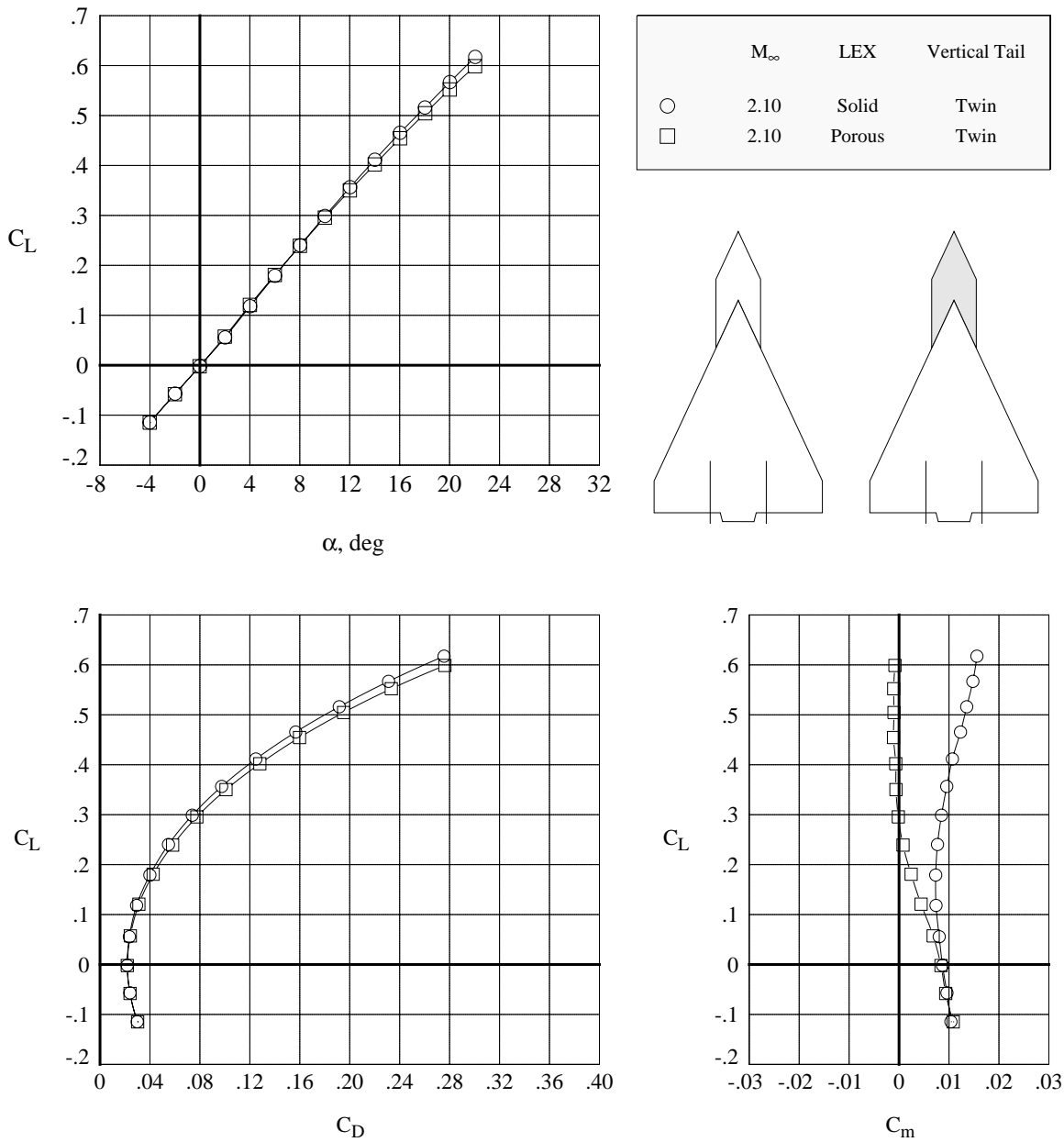
(b) Twin vertical tails.

Figure 69. Concluded.
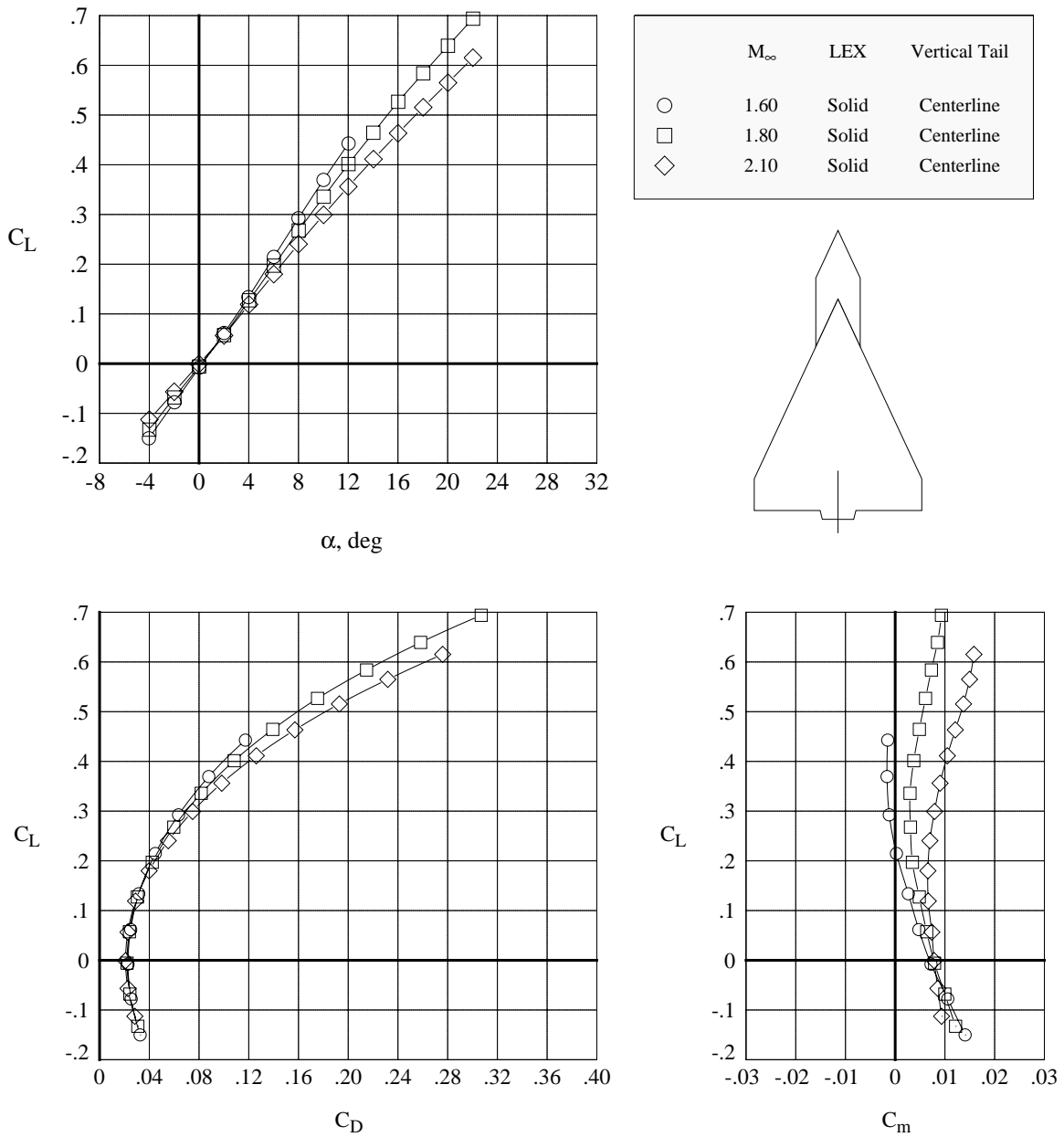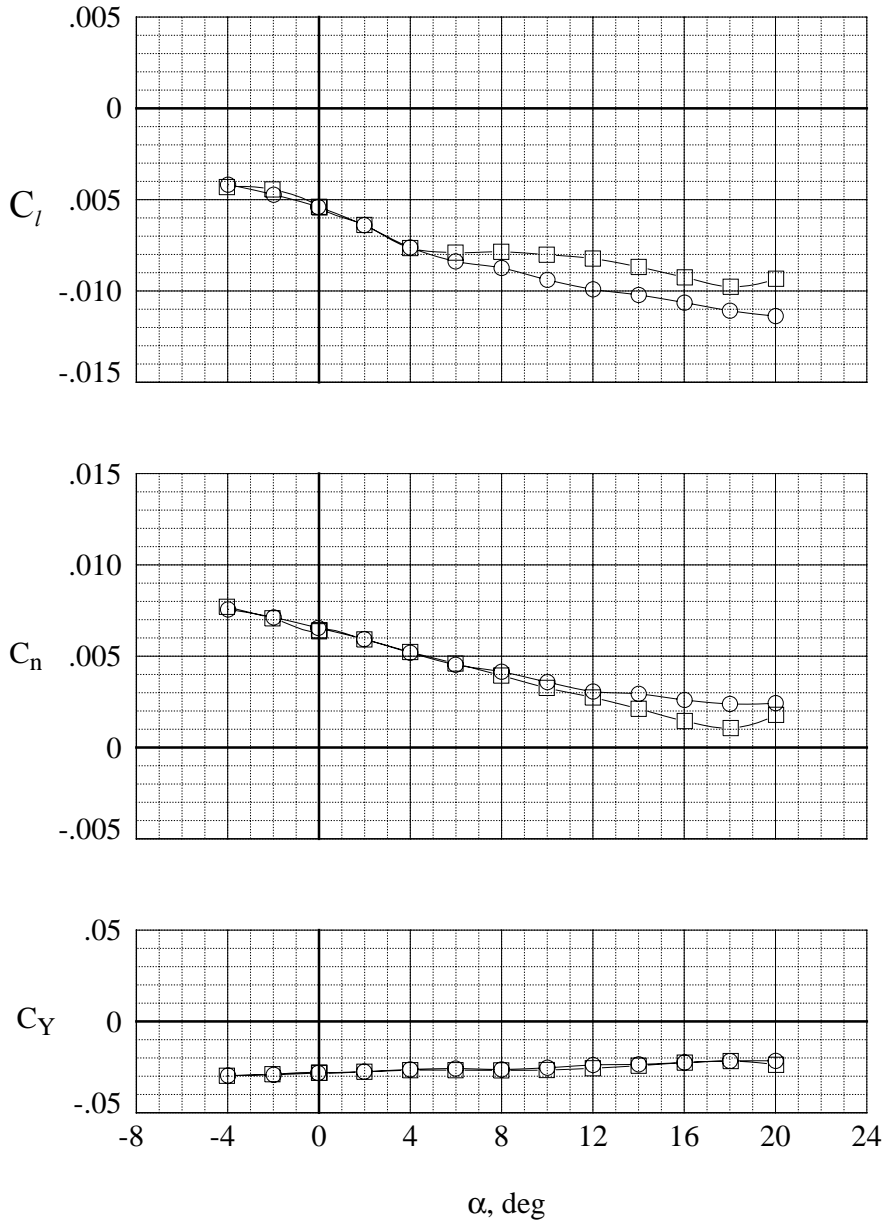
(a) Solid LEX.

Figure 70. Effect of Mach number on the longitudinal aerodynamic characteristics;
centerline vertical tail.

125
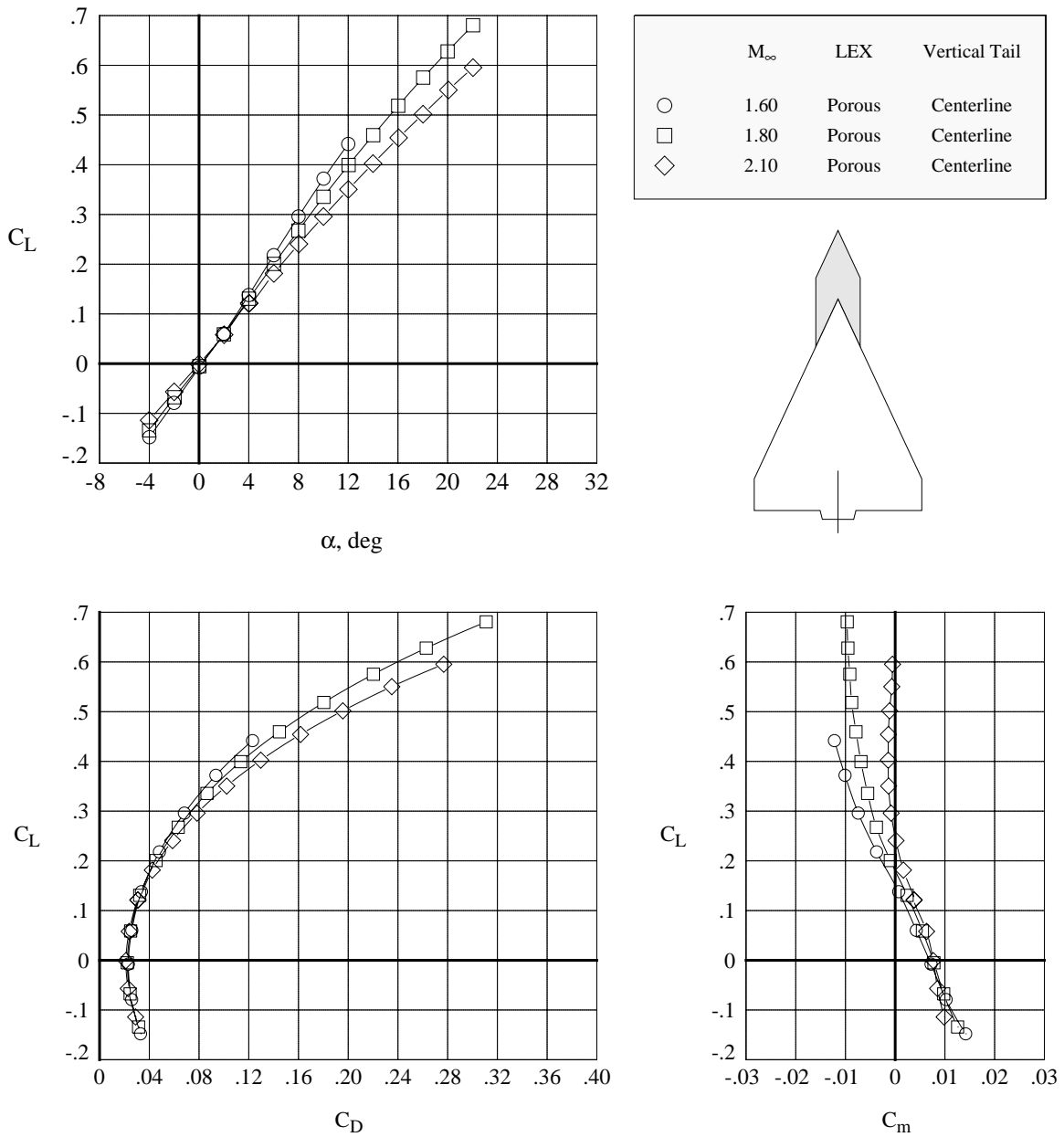
(b) Porous LEX.

Figure 70. Concluded.

126

	M_∞	LEX	Vertical Tail
○	1.60	Solid	Twin
□	1.80	Solid	Twin
◇	2.10	Solid	Twin
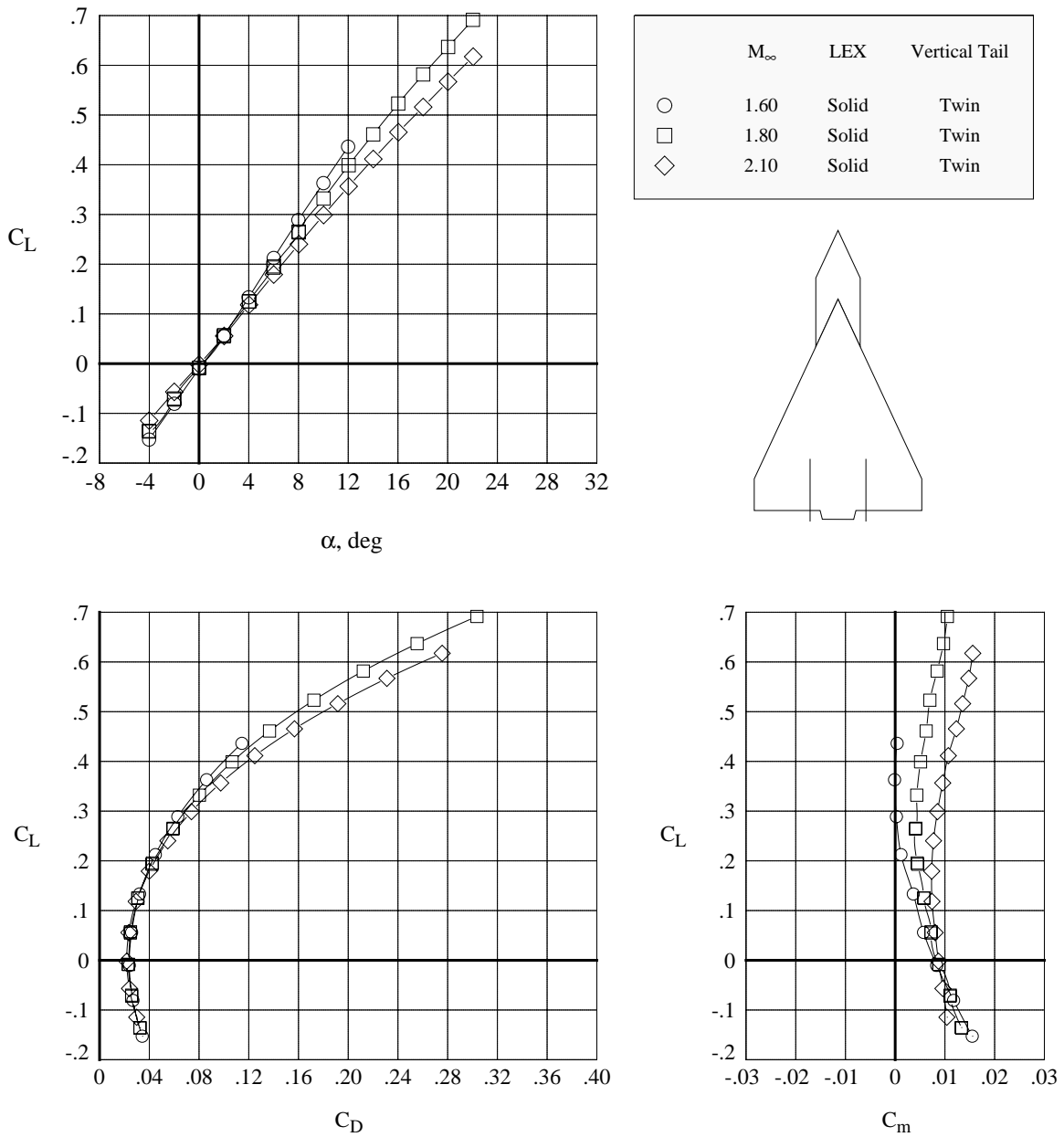
(a) Solid LEX.

Figure 71. Effect of Mach number on the longitudinal aerodynamic characteristics; twin vertical tails.

	M_∞	LEX	Vertical Tail
○	1.60	Porous	Twin
□	1.80	Porous	Twin
◇	2.10	Porous	Twin
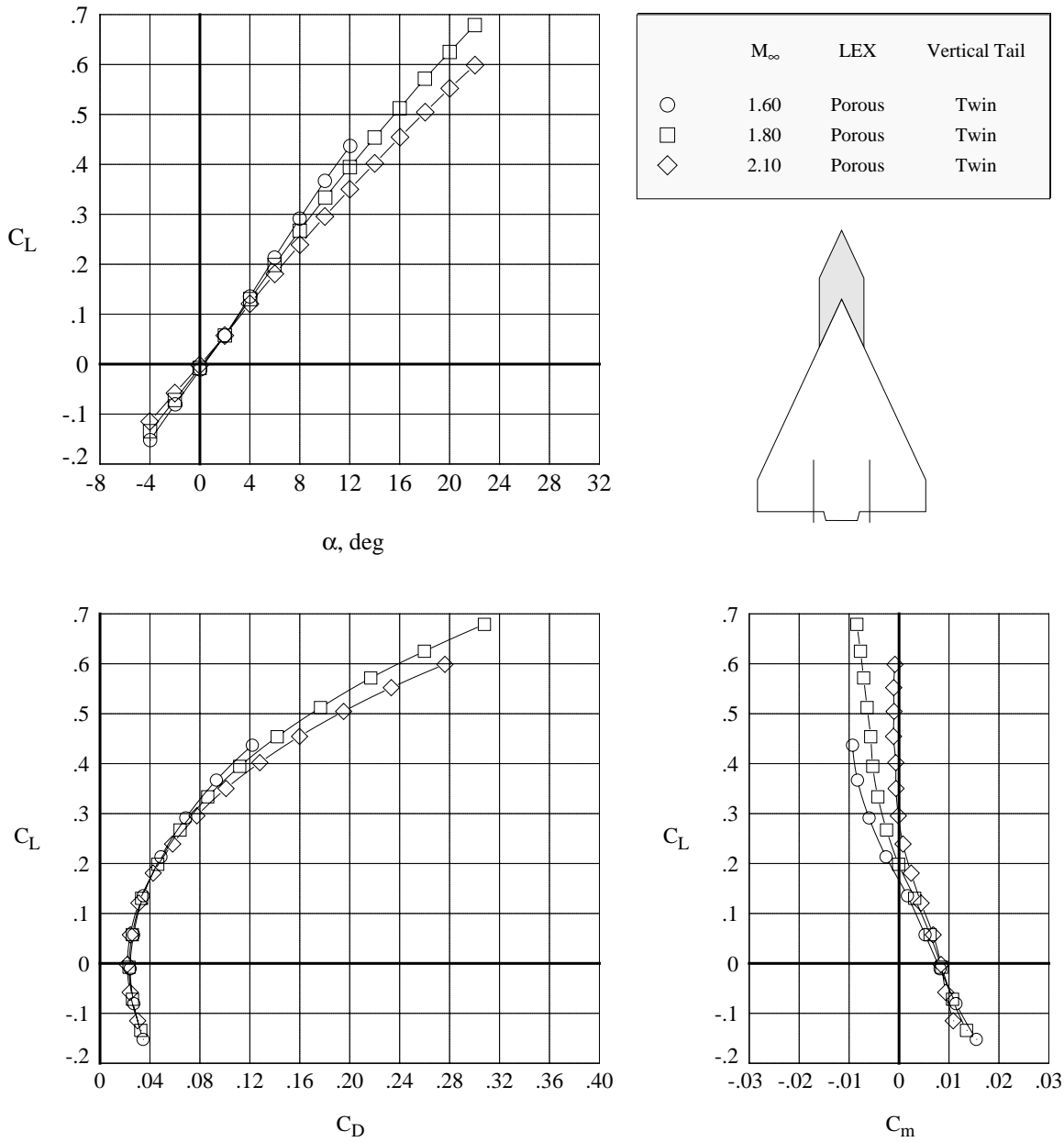
(b) Porous LEX.

Figure 71. Concluded.
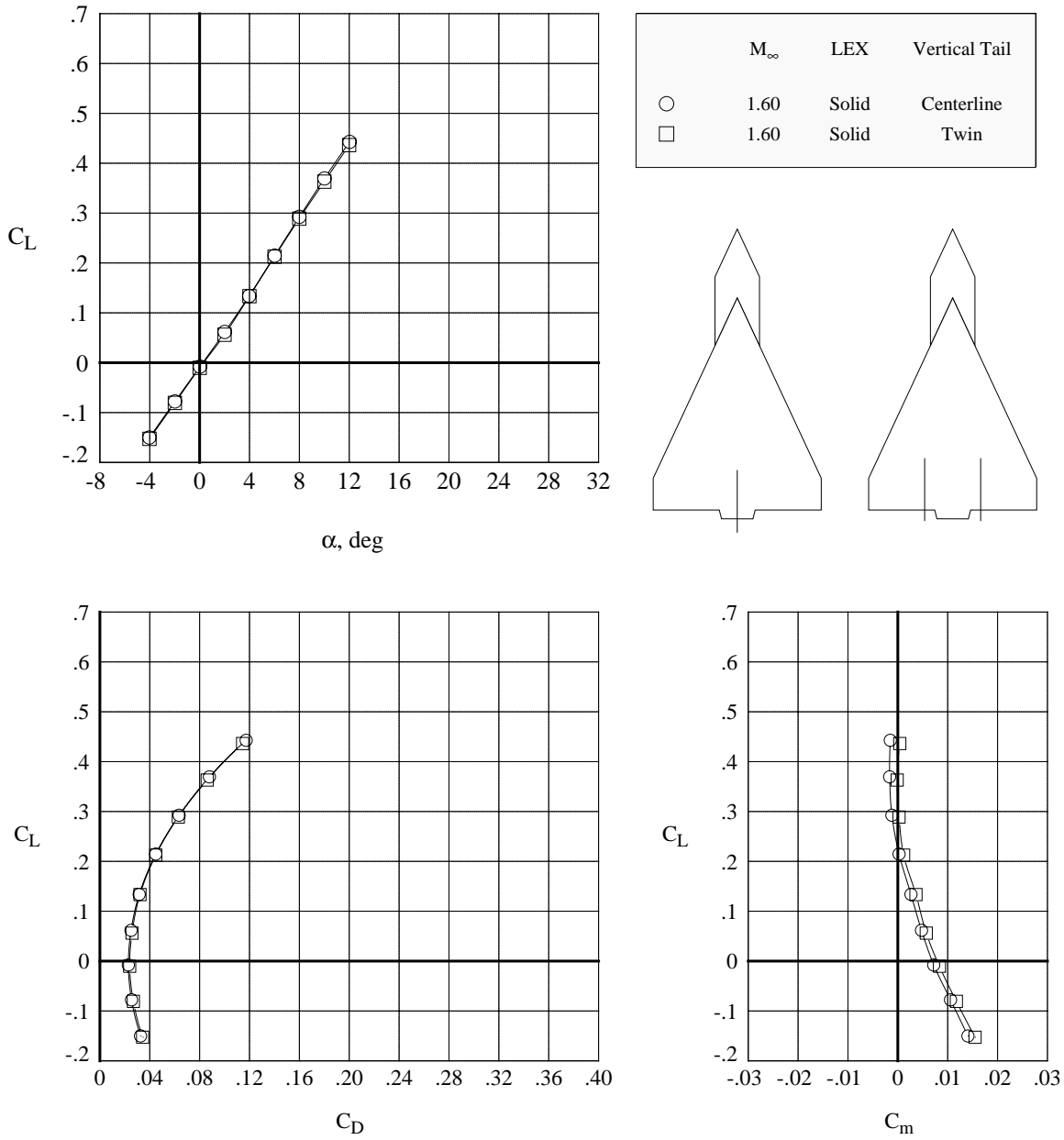
(a) $M_\infty = 1.6$.

Figure 72. Comparison of longitudinal aerodynamic characteristics with centerline and twin vertical tails; solid LEX.
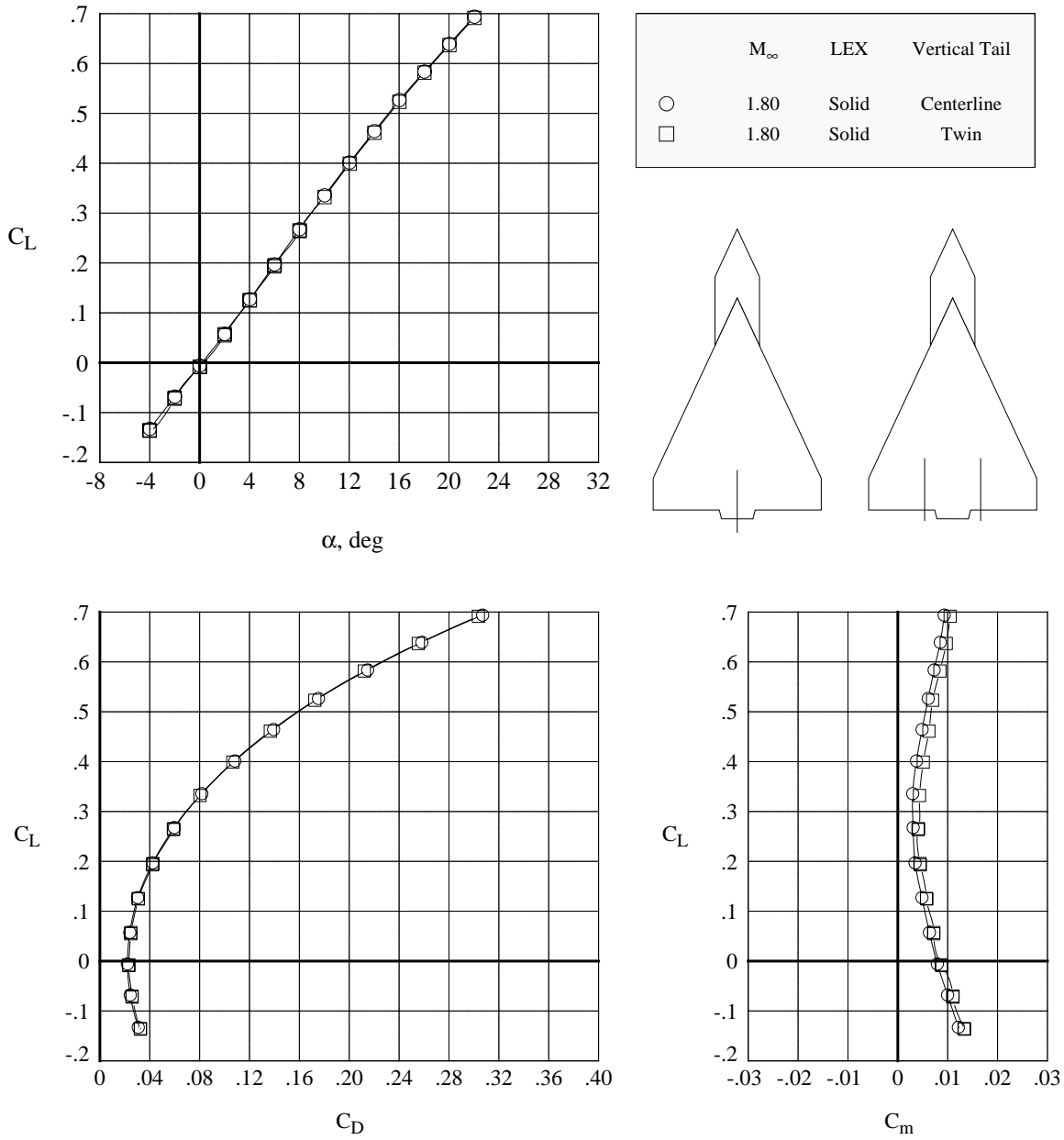
(b) $M_\infty = 1.8$.

Figure 72. Continued.

Legend:

	M_∞	LEX	Vertical Tail
○	2.10	Solid	Centerline
□	2.10	Solid	Twin
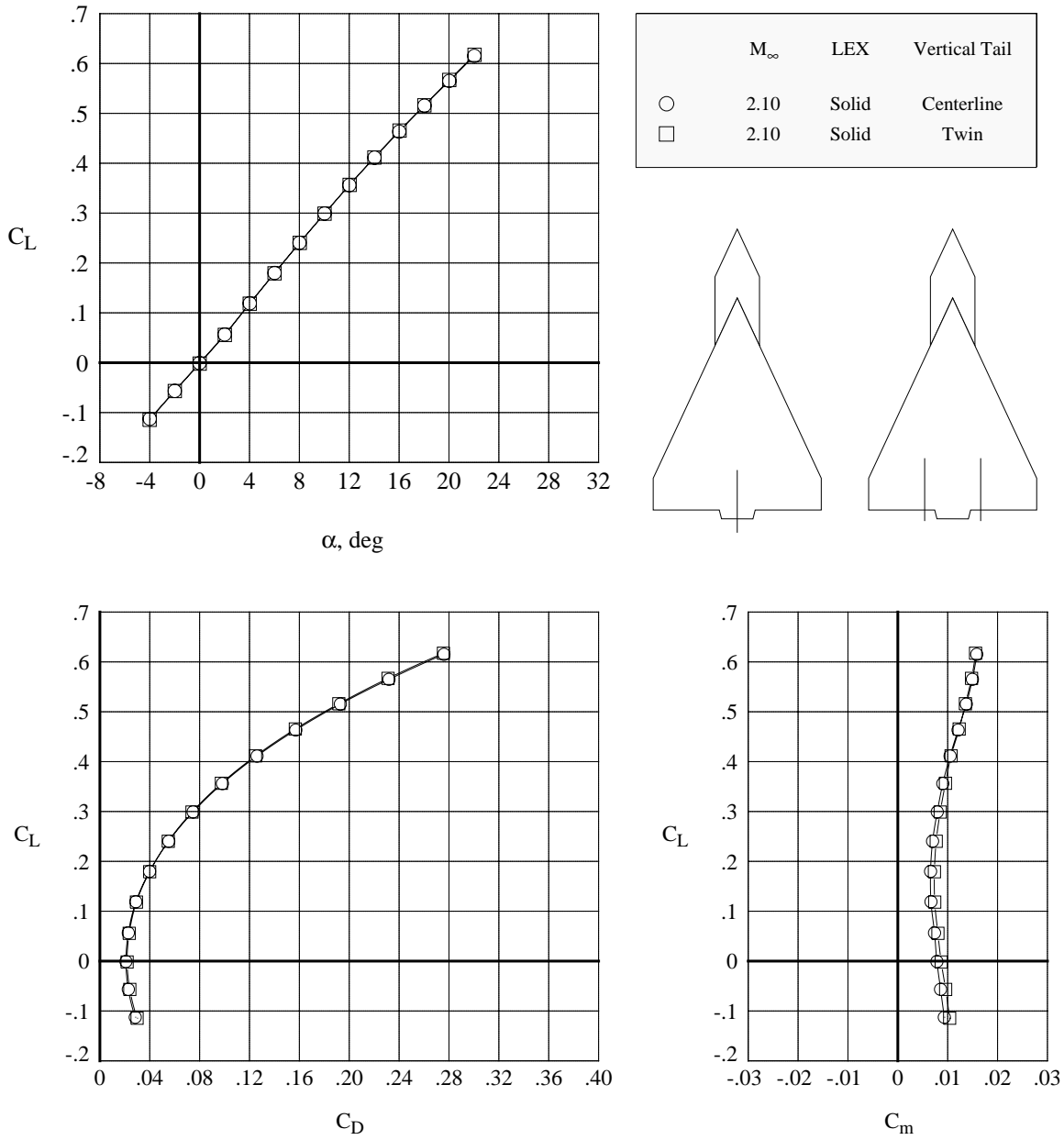
(c) $M_\infty = 2.1$.

Figure 72. Concluded.
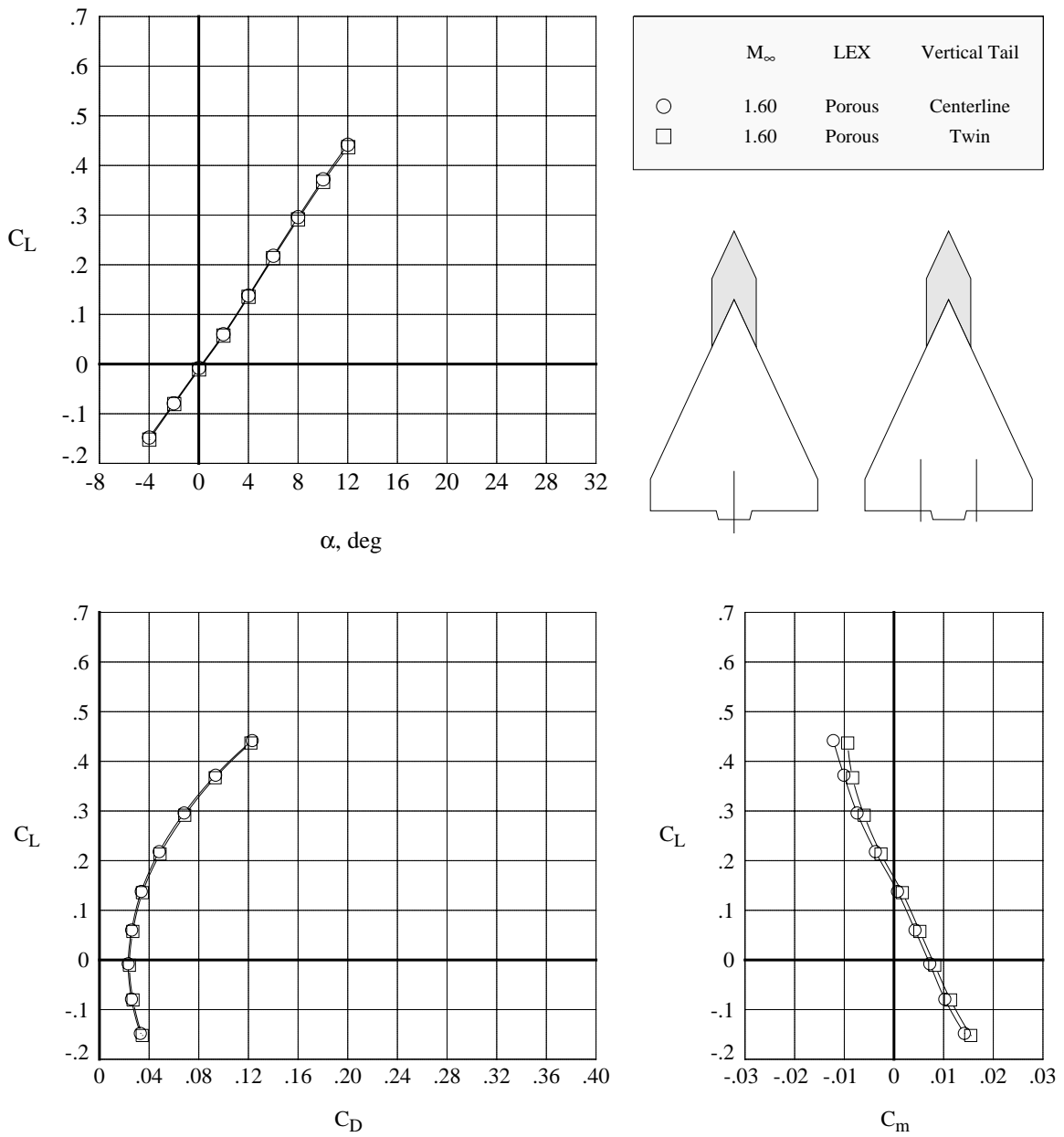
(a) $M_\infty = 1.6$.

Figure 73. Comparison of longitudinal aerodynamic characteristics with centerline and twin vertical tails; porous LEX.

	M_∞	LEX	Vertical Tail
○	1.80	Porous	Centerline
□	1.80	Porous	Twin
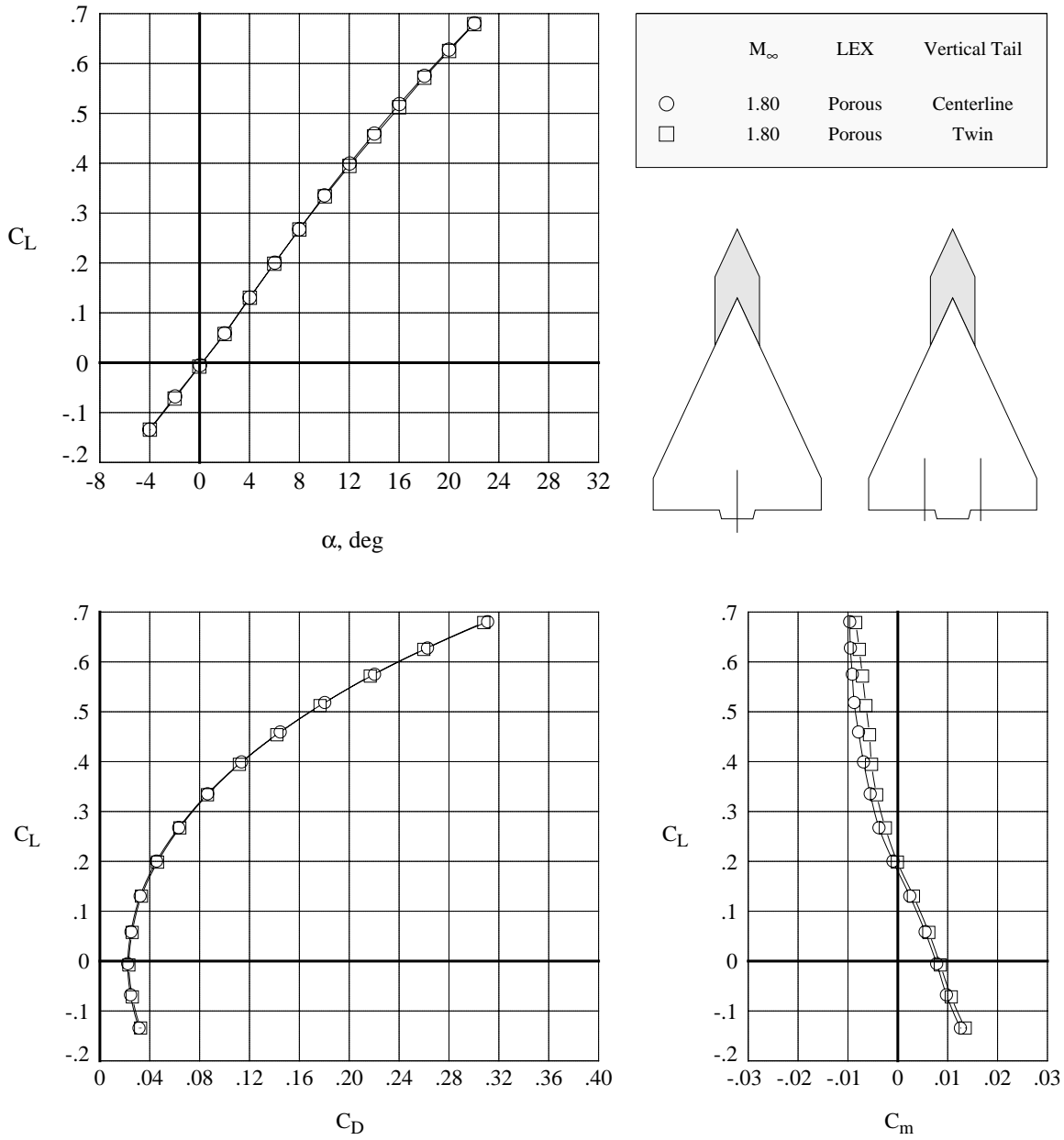
(b) $M_\infty = 1.8$.

Figure 73. Continued.

Legend (top right):

	M_∞	LEX	Vertical Tail
○	2.10	Porous	Centerline
□	2.10	Porous	Twin
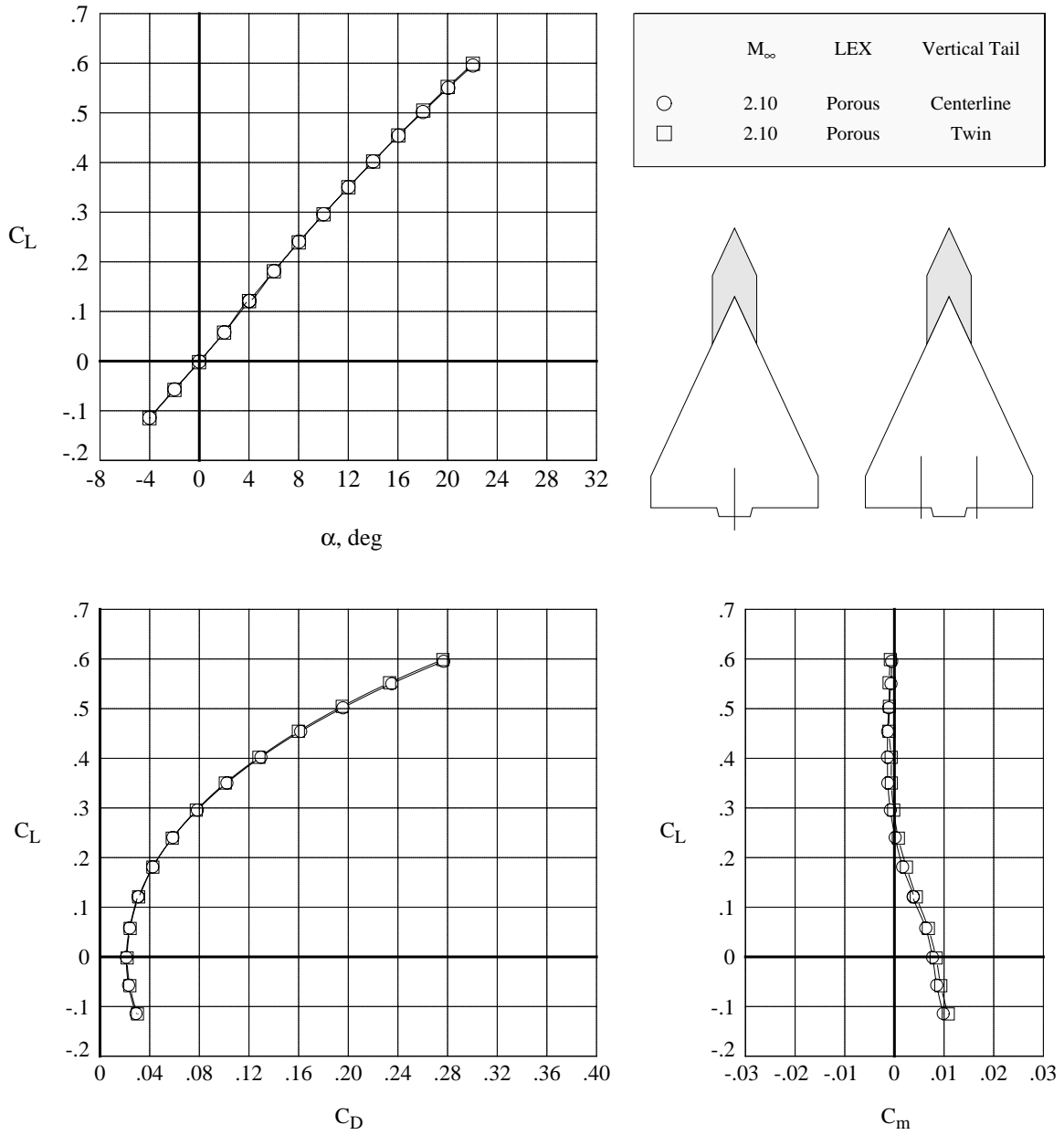
(c) $M_\infty = 2.1$.

Figure 73. Concluded.

134

	M_∞	LEX	Vertical Tail	β, deg
○	1.600	Solid	Centerline	4.04
□	1.600	Porous	Centerline	4.04
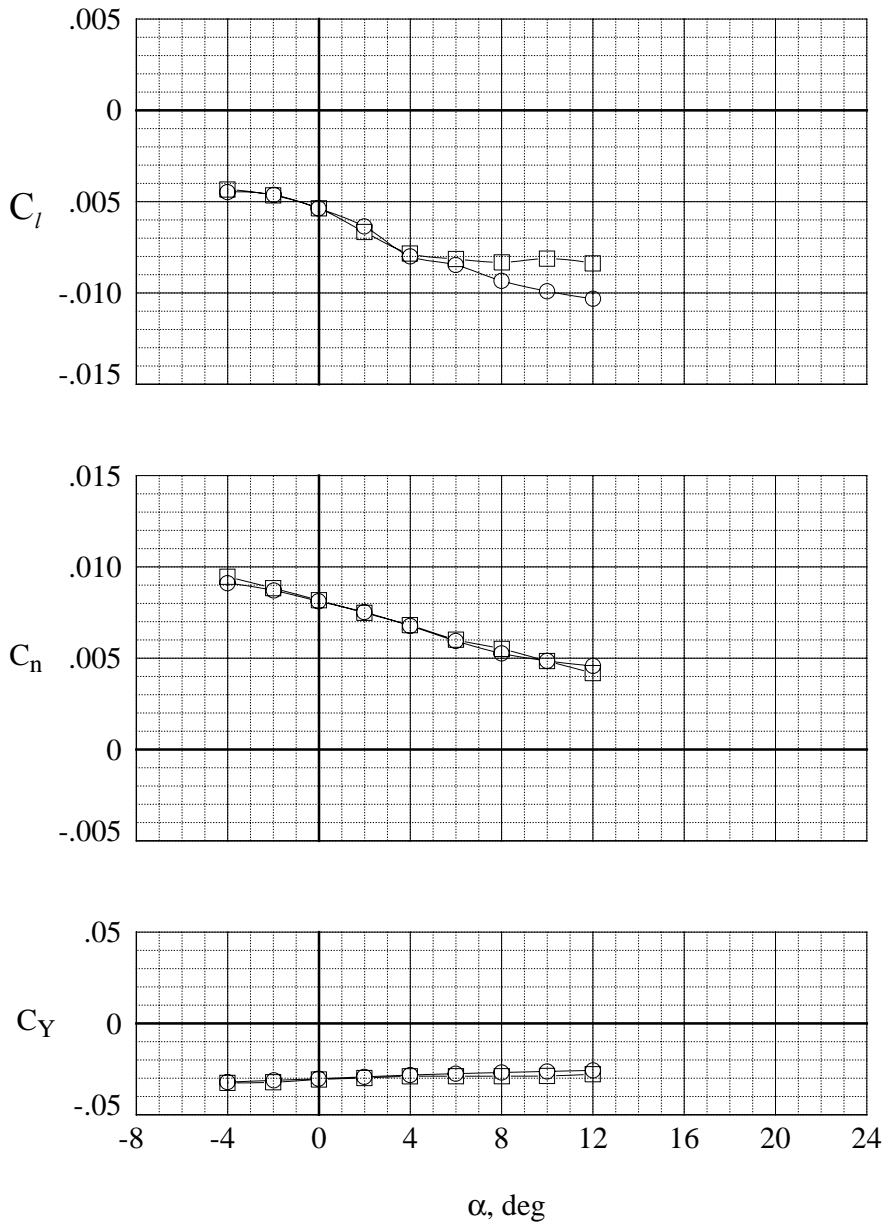
(a) Centerline vertical tail.

Figure 74. Comparison of the lateral aerodynamic characteristics with solid and porous LEX; $M_\infty = 1.6$.

135

	M_∞	LEX	Vertical Tail	β, deg
○	1.600	Solid	Twin	4.04
□	1.600	Porous	Twin	4.03
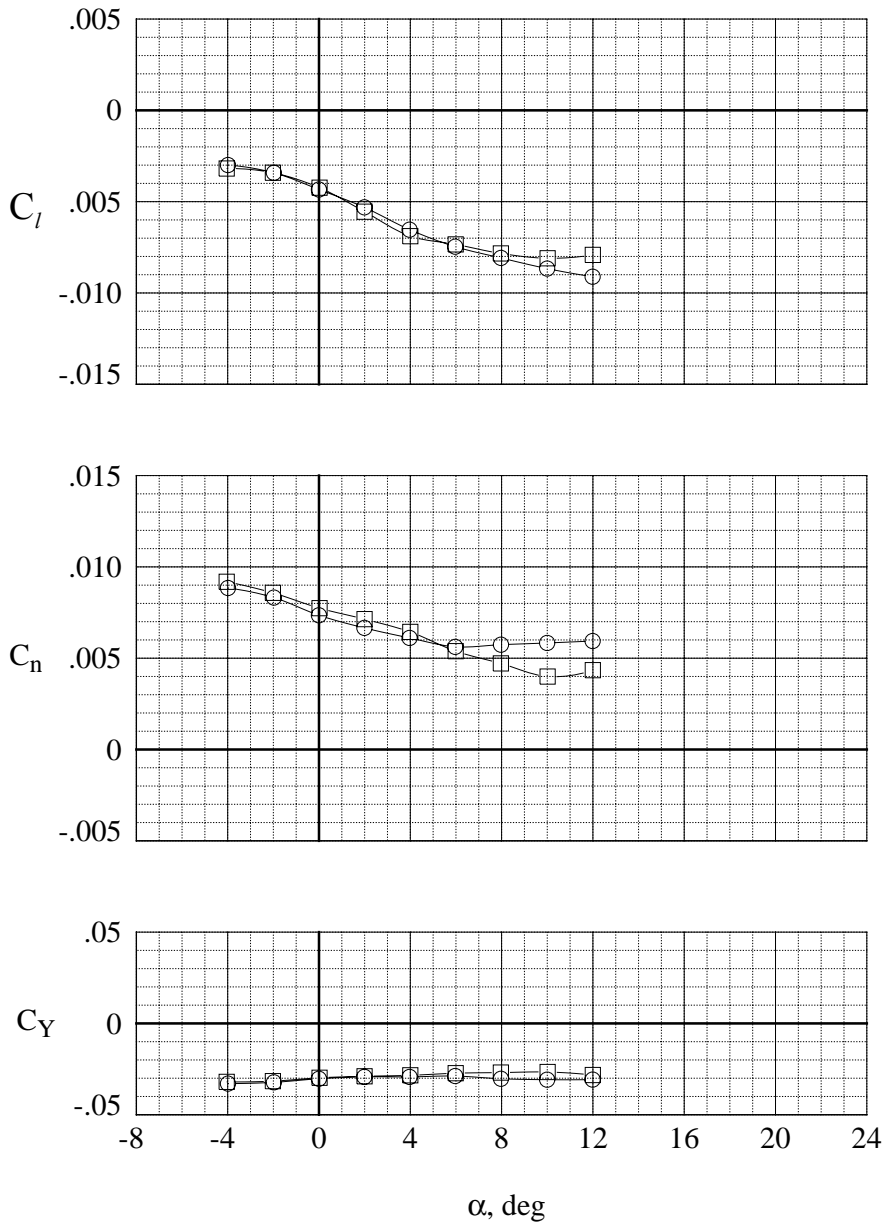
(b) Twin vertical tails.

Figure 74. Concluded.

(a) Centerline vertical tail.

Figure 75. Comparison of the lateral aerodynamic characteristics with solid and porous LEX; $M_\infty = 1.8$.

	M_∞	LEX	Vertical Tail	β, deg
○	1.800	Solid	Twin	4.06
□	1.800	Porous	Twin	4.06

α, deg
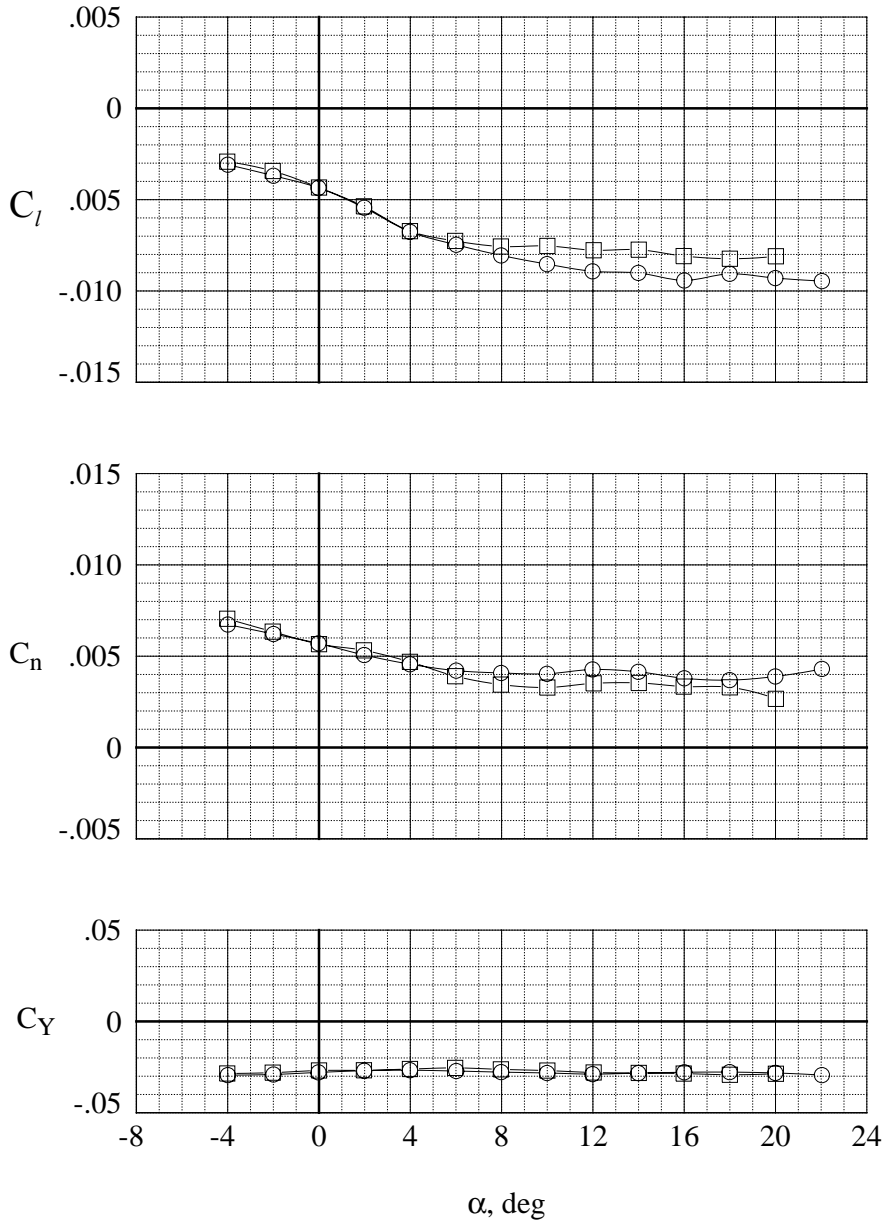
(b) Twin vertical tails.

Figure 75. Concluded.

138

	M_∞	LEX	Vertical Tail	β, deg
○	2.100	Solid	Centerline	4.07
□	2.100	Porous	Centerline	4.07
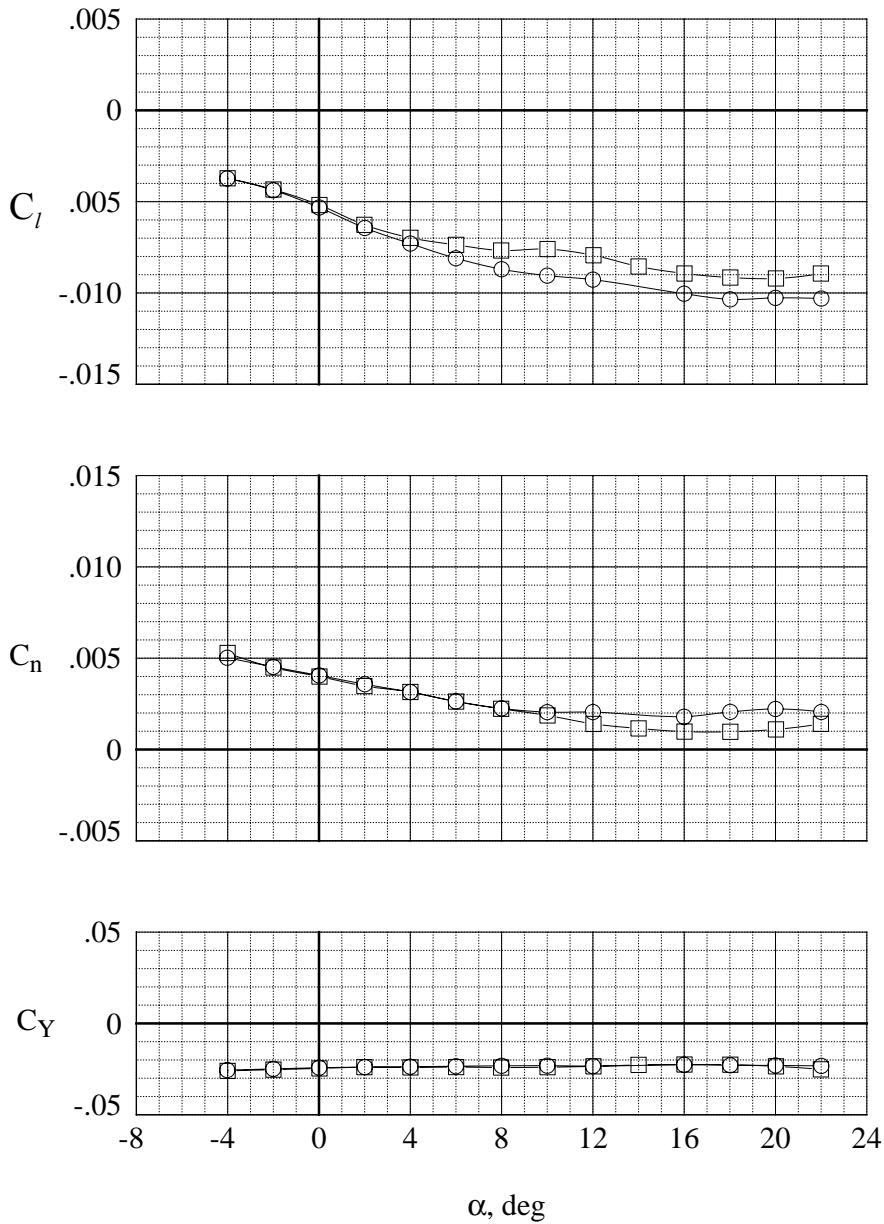
(a) Centerline vertical tail.

Figure 76. Comparison of the lateral aerodynamic characteristics with solid and porous LEX; $M_\infty = 2.1$.

	M_∞	LEX	Vertical Tail	β, deg
○	2.100	Solid	Twin	4.06
□	2.100	Porous	Twin	4.05
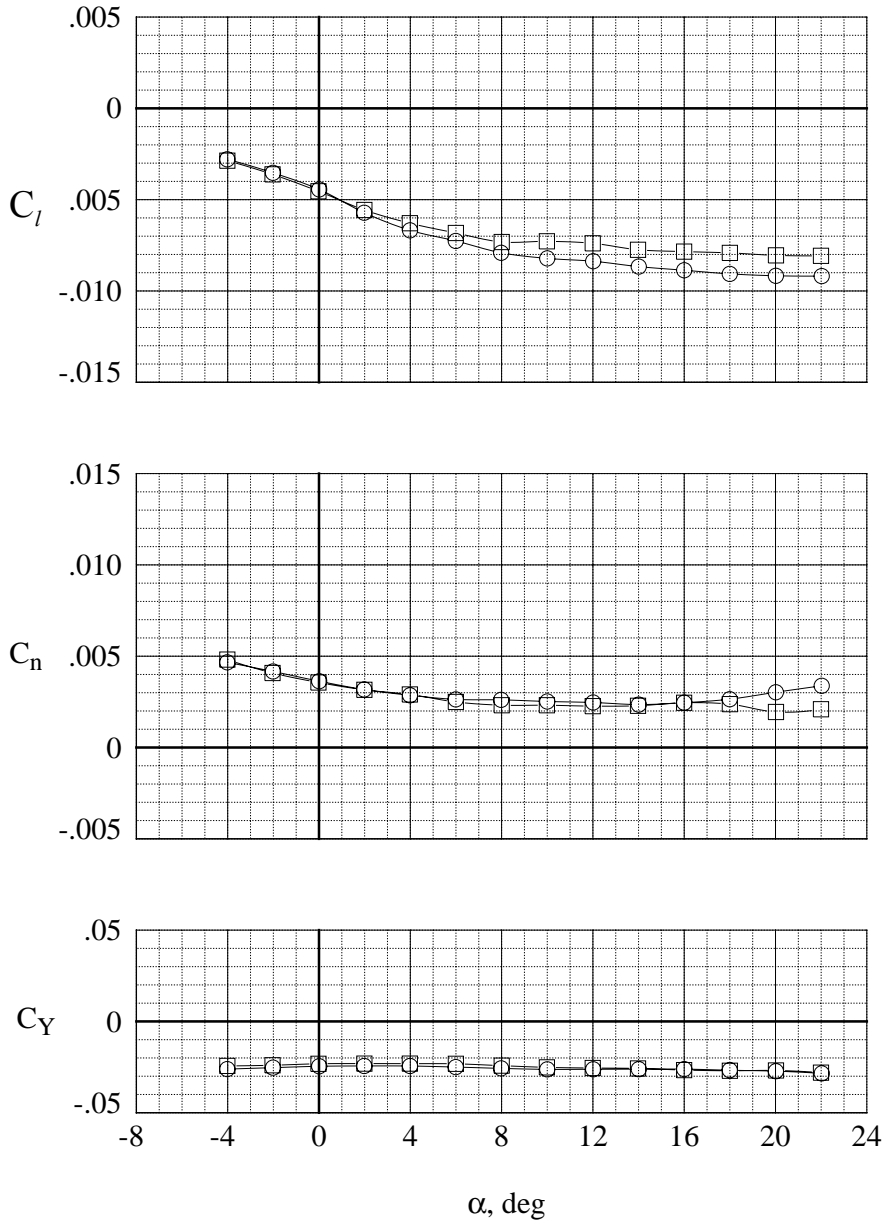
(b) Twin vertical tails.

Figure 76. Concluded.

	M_∞	LEX	Vertical Tail	β, deg
○	1.600	Solid	Centerline	4.04
□	1.800	Solid	Centerline	4.06
◇	2.100	Solid	Centerline	4.07
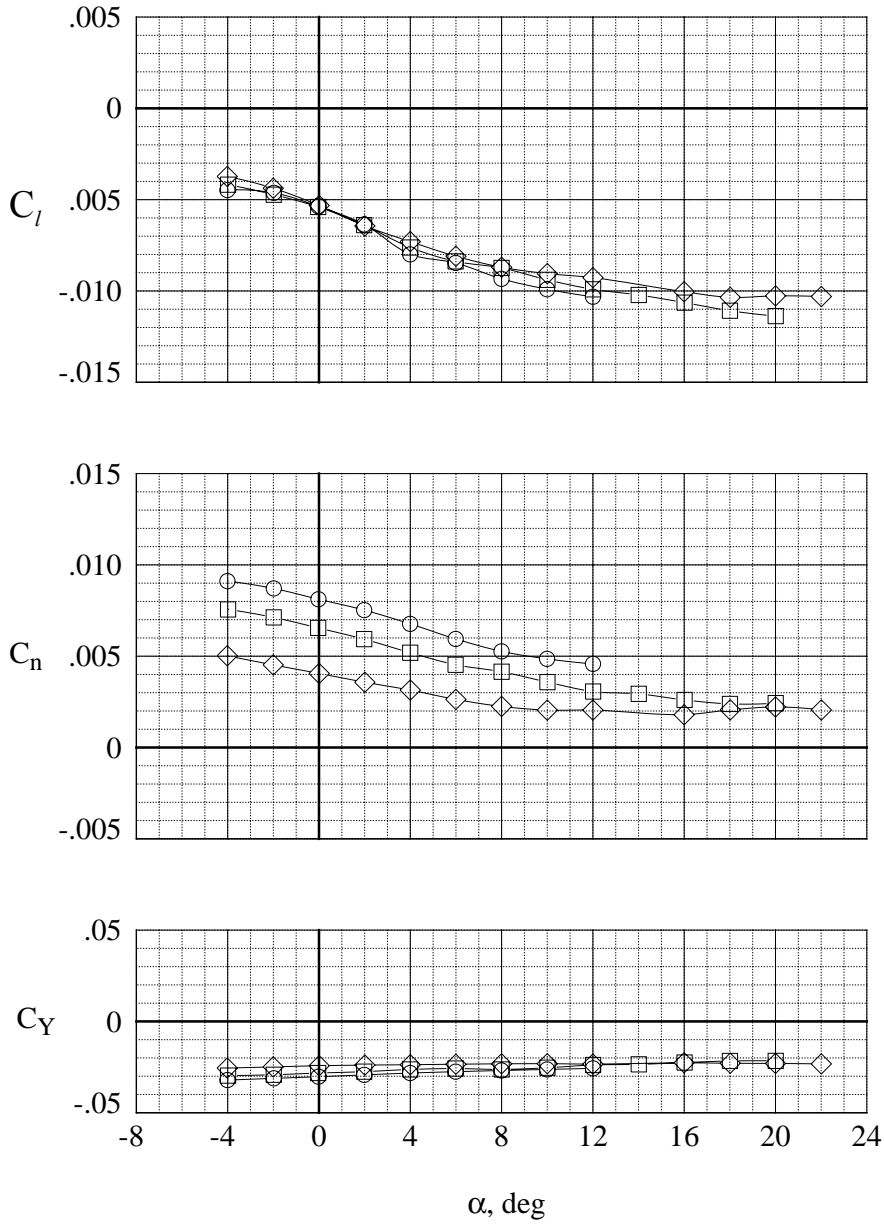
(a) Solid LEX.

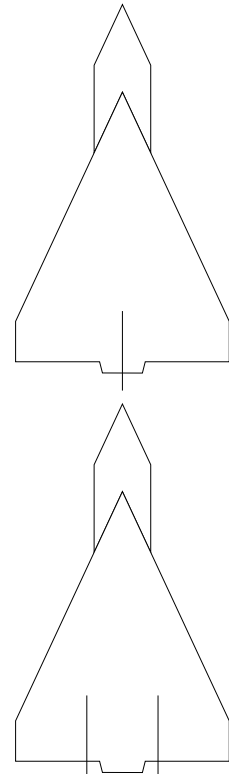Figure 77. Effect of Mach number on the lateral aerodynamic characteristics with centerline vertical tail.
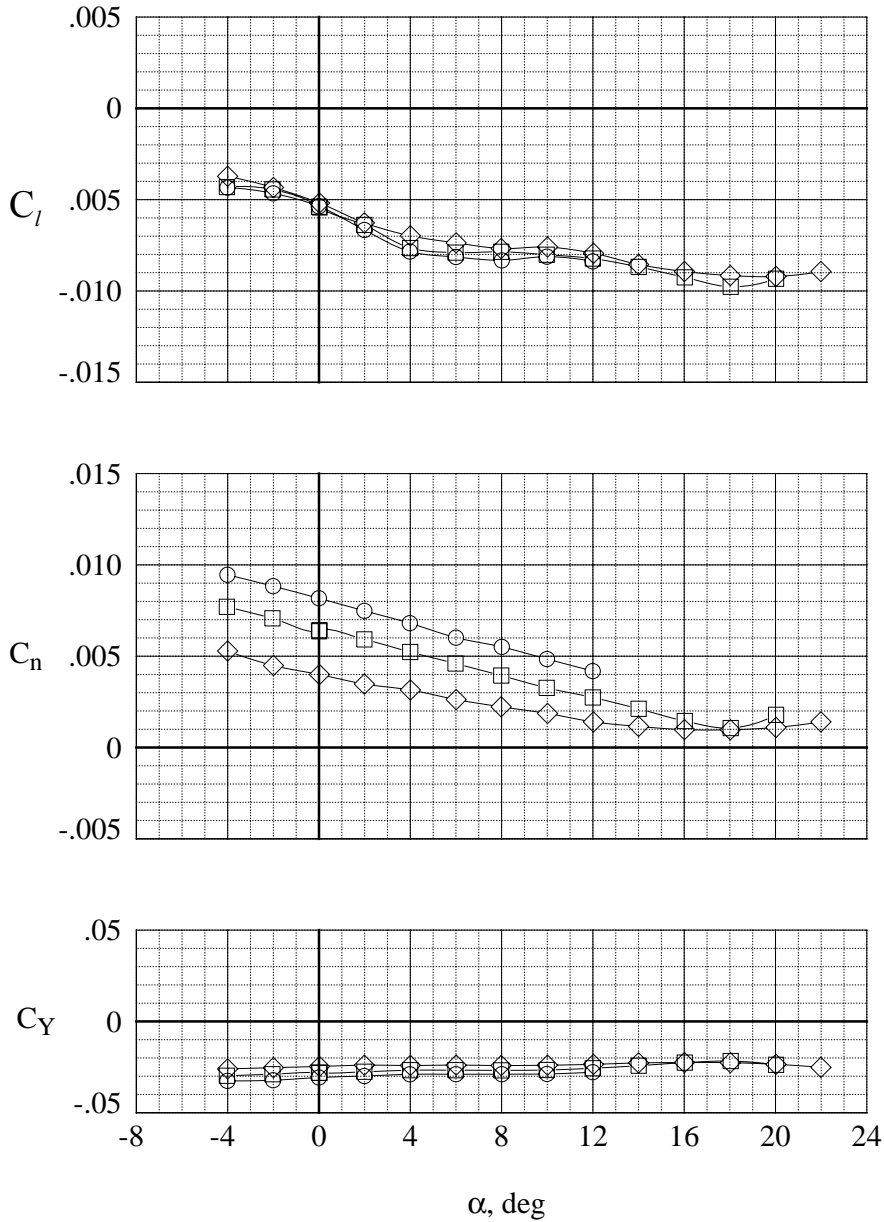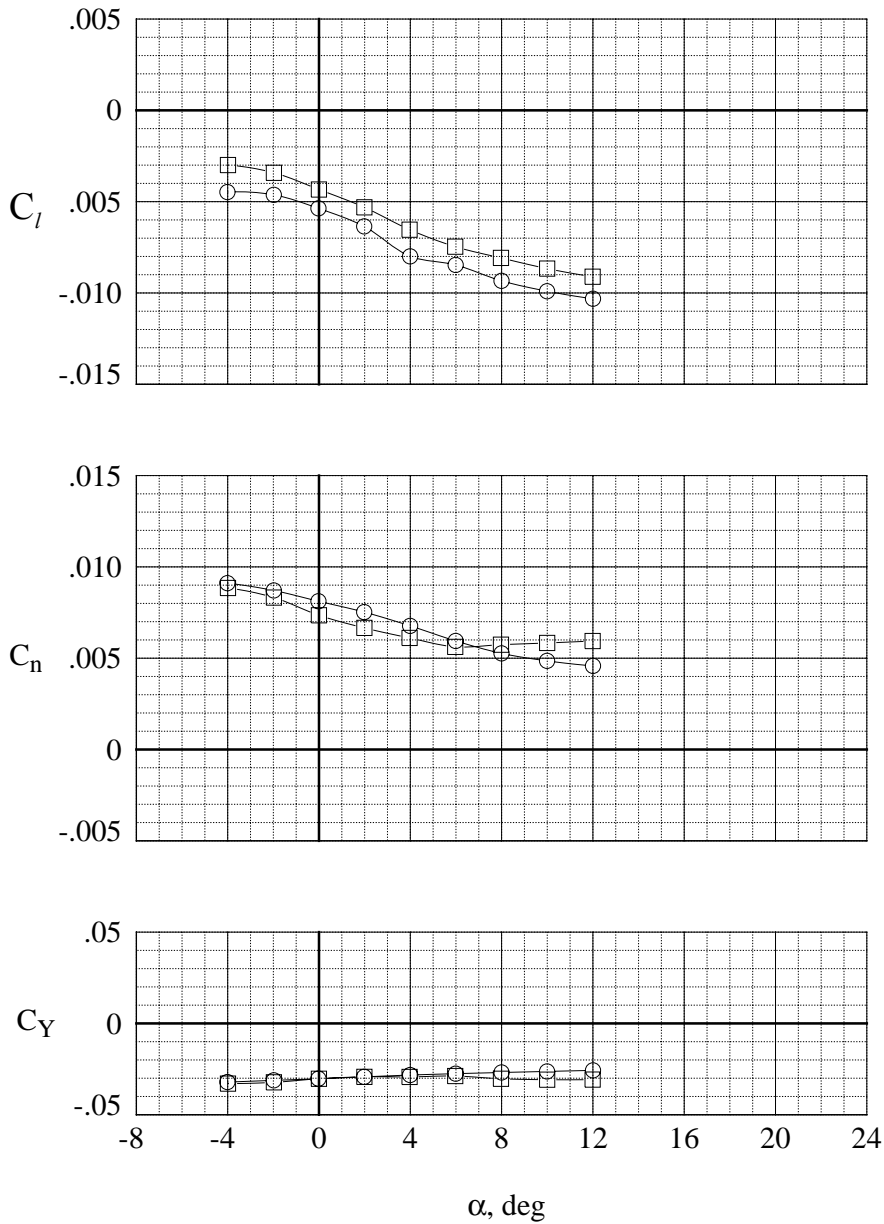
(b) Porous LEX.

Figure 77. Concluded.

	M_∞	LEX	Vertical Tail	β, deg
○	1.600	Solid	Twin	4.04
□	1.800	Solid	Twin	4.06
◇	2.100	Solid	Twin	4.06

α, deg
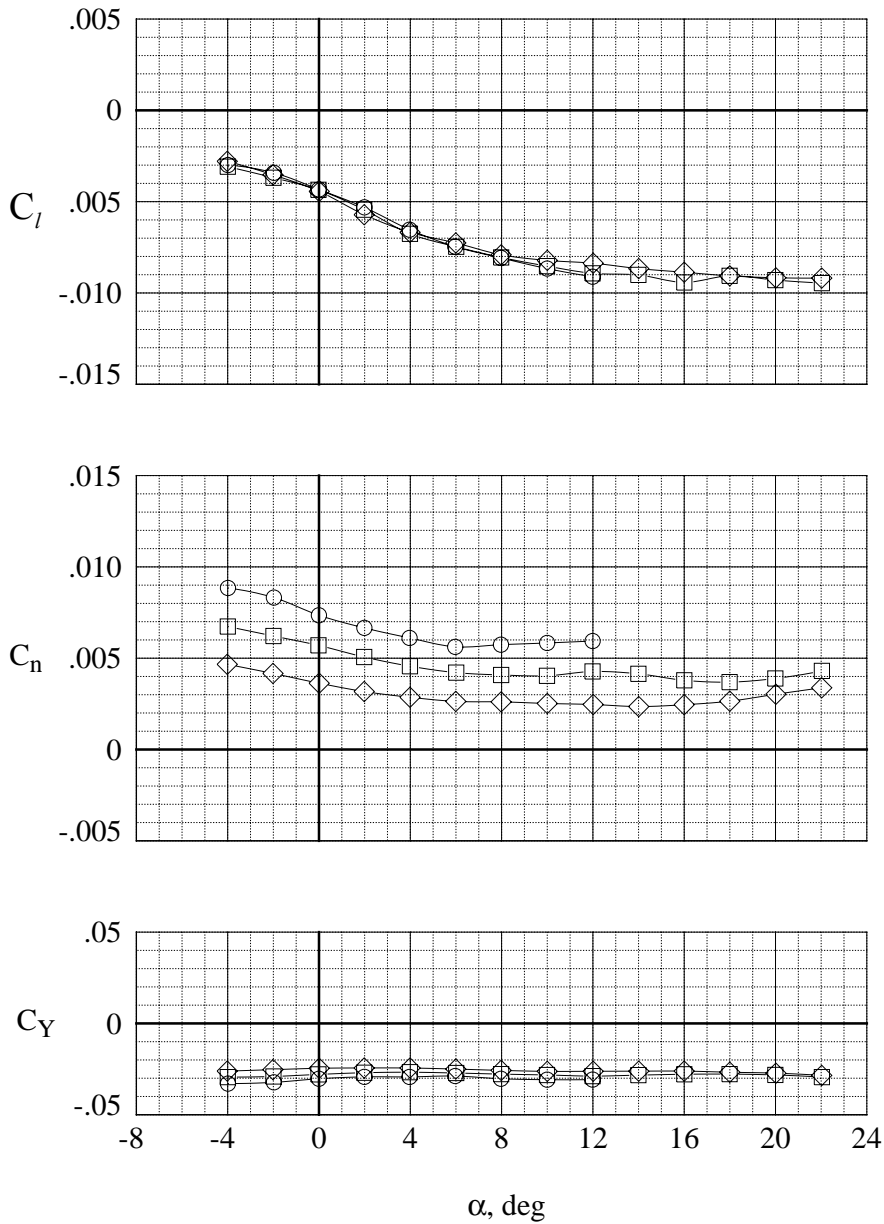
(a) Solid LEX.

Figure 78. Effect of Mach number on the lateral aerodynamic characteristics with twin vertical tails.

143

	M_∞	LEX	Vertical Tail	β, deg
○	1.600	Porous	Twin	4.03
□	1.800	Porous	Twin	4.06
◇	2.100	Porous	Twin	4.05
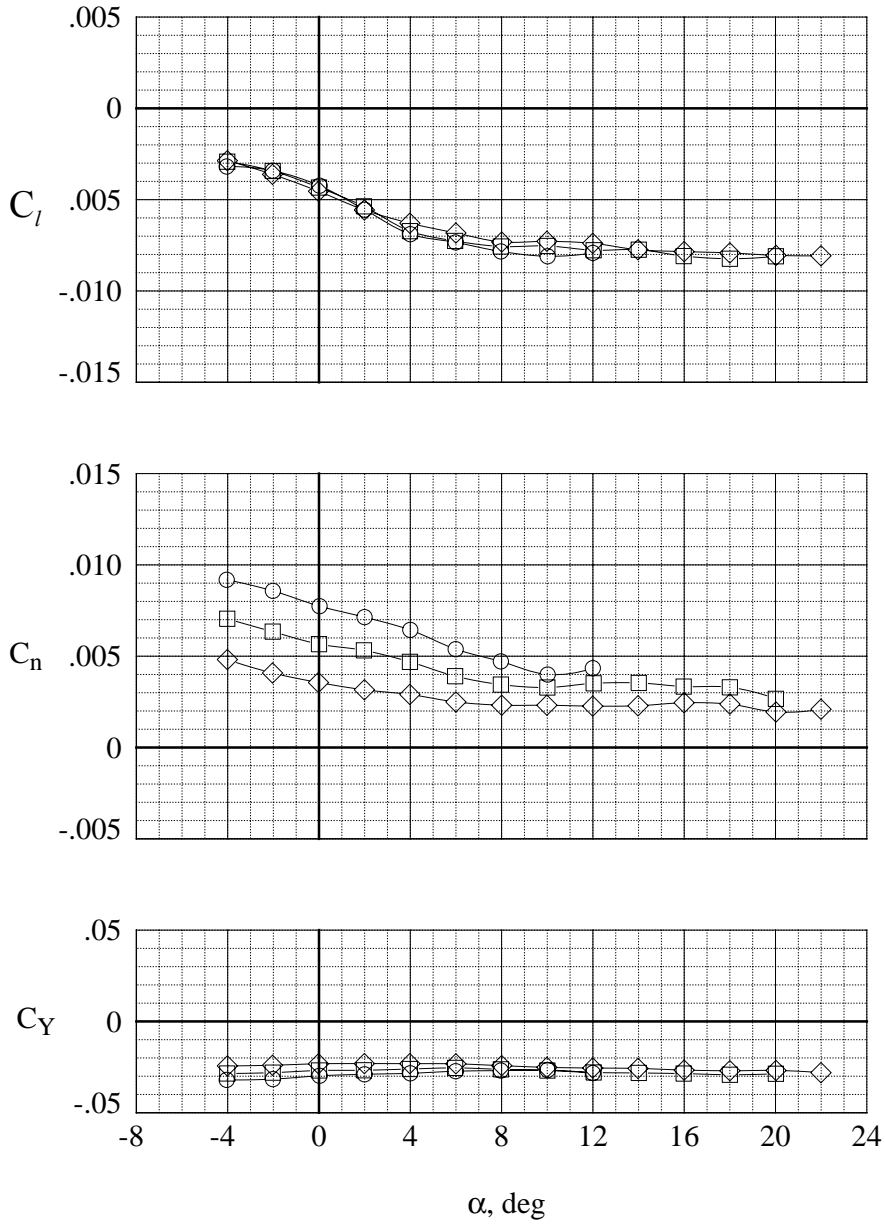
(b) Porous LEX.

Figure 78. Concluded.

	M_∞	LEX	Vertical Tail	β, deg
○	1.600	Solid	Centerline	4.04
□	1.600	Solid	Twin	4.04

(a) Solid LEX.

Figure 79. Comparison of the lateral aerodynamic characteristics with centerline and twin vertical tails; $M_\infty = 1.6$.
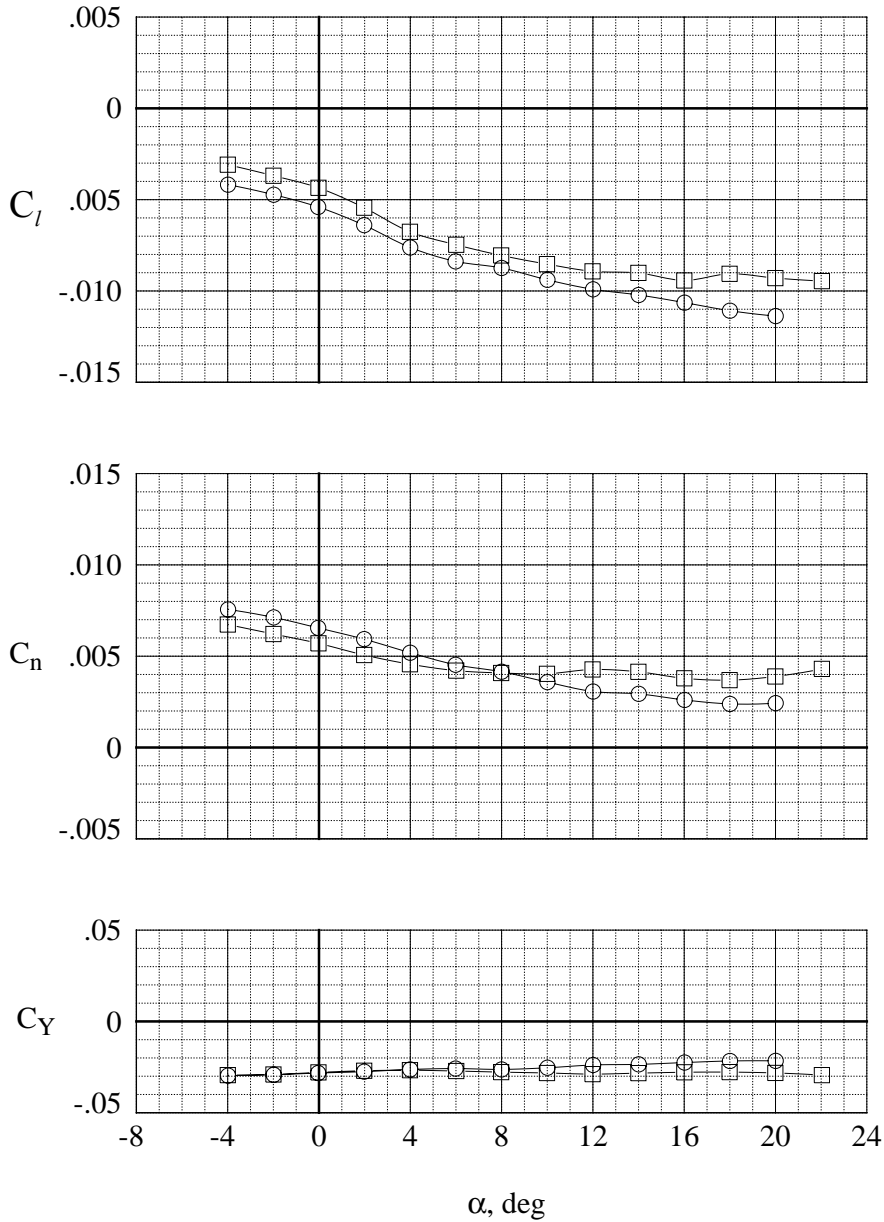
	M_∞	LEX	Vertical Tail	β, deg
○	1.600	Porous	Centerline	4.04
□	1.600	Porous	Twin	4.03
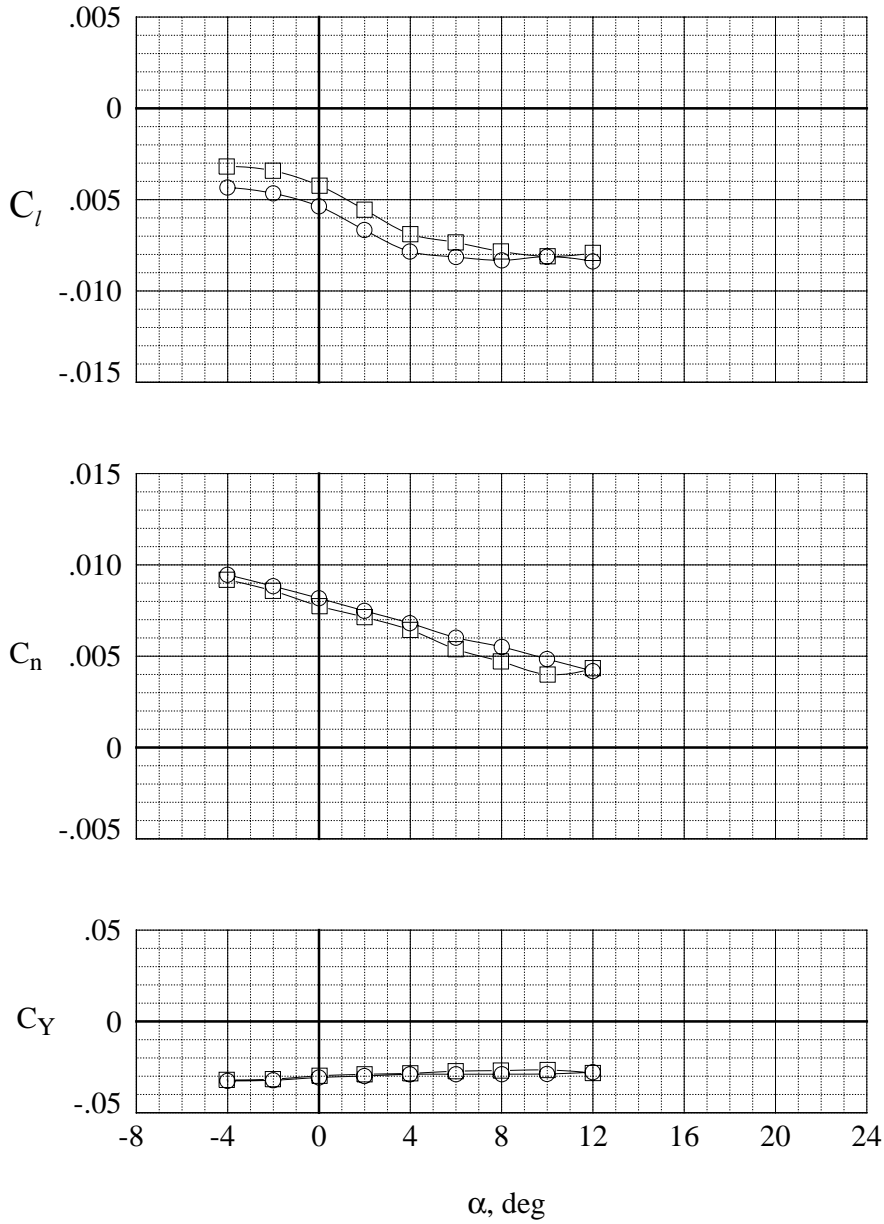
(b) Porous LEX.

Figure 79. Concluded.

146

	M_∞	LEX	Vertical Tail	β, deg
○	1.800	Solid	Centerline	4.06
□	1.800	Solid	Twin	4.06
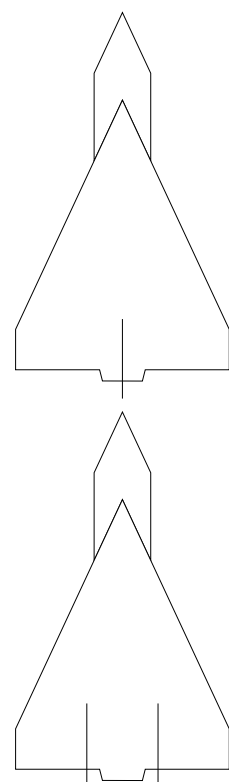
(a) Solid LEX.

Figure 80. Comparison of the lateral aerodynamic characteristics with centerline and
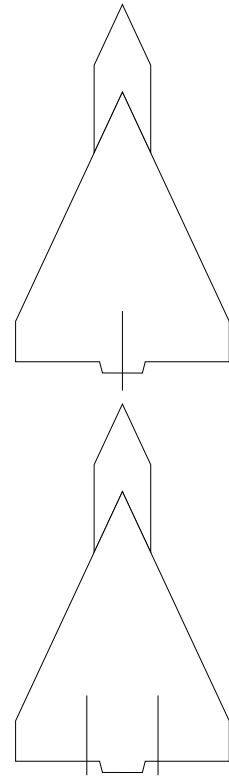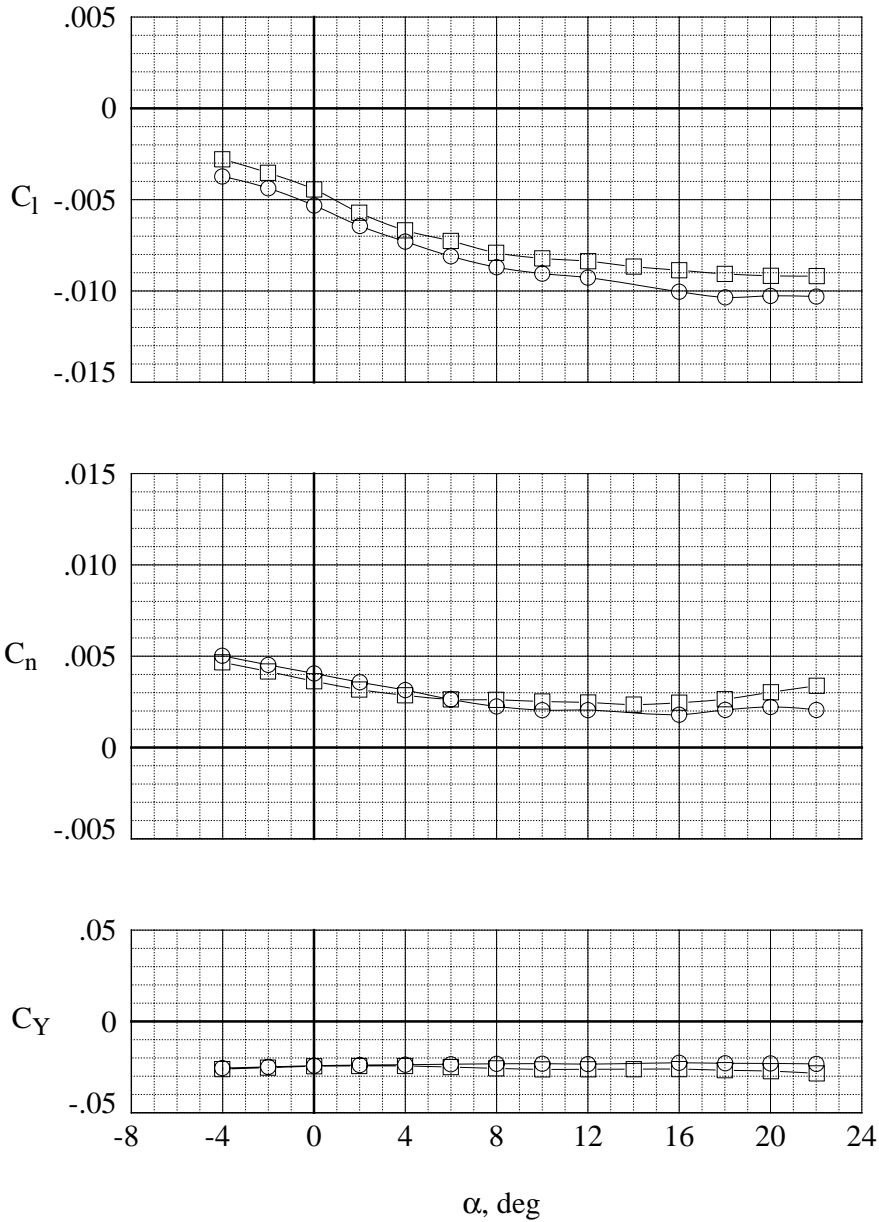twin vertical tails; $M_\infty = 1.8$.

	M_∞	LEX	Vertical Tail	β, deg
○	1.800	Porous	Centerline	4.05
□	1.800	Porous	Twin	4.06
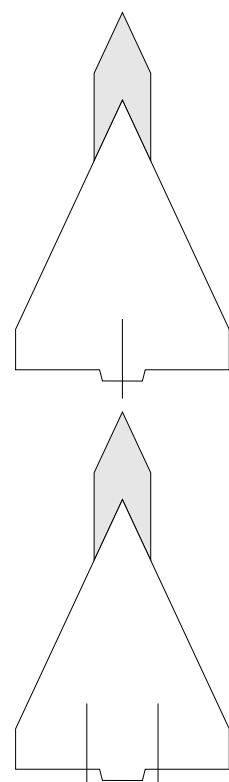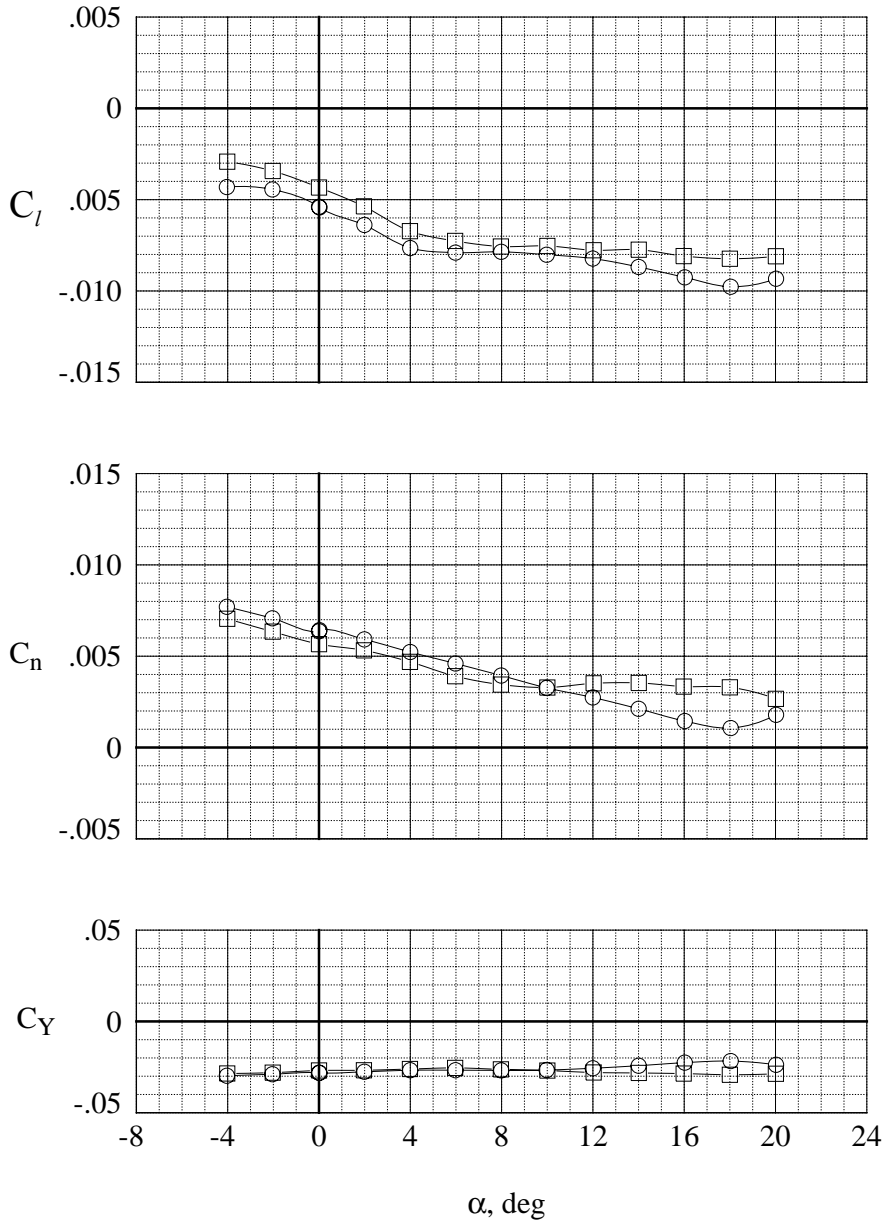
(b) Porous LEX.

Figure 80. Concluded.

	M_∞	LEX	Vertical Tail	β, deg
○	2.100	Solid	Centerline	4.07
□	2.100	Solid	Twin	4.06

(a) Solid LEX.

Figure 81. Comparison of the lateral aerodynamic characteristics with centerline and twin vertical tails; $M_\infty = 2.1$.

	M_∞	LEX	Vertical Tail	β, deg
○	2.100	Porous	Centerline	4.07
□	2.100	Porous	Twin	4.05
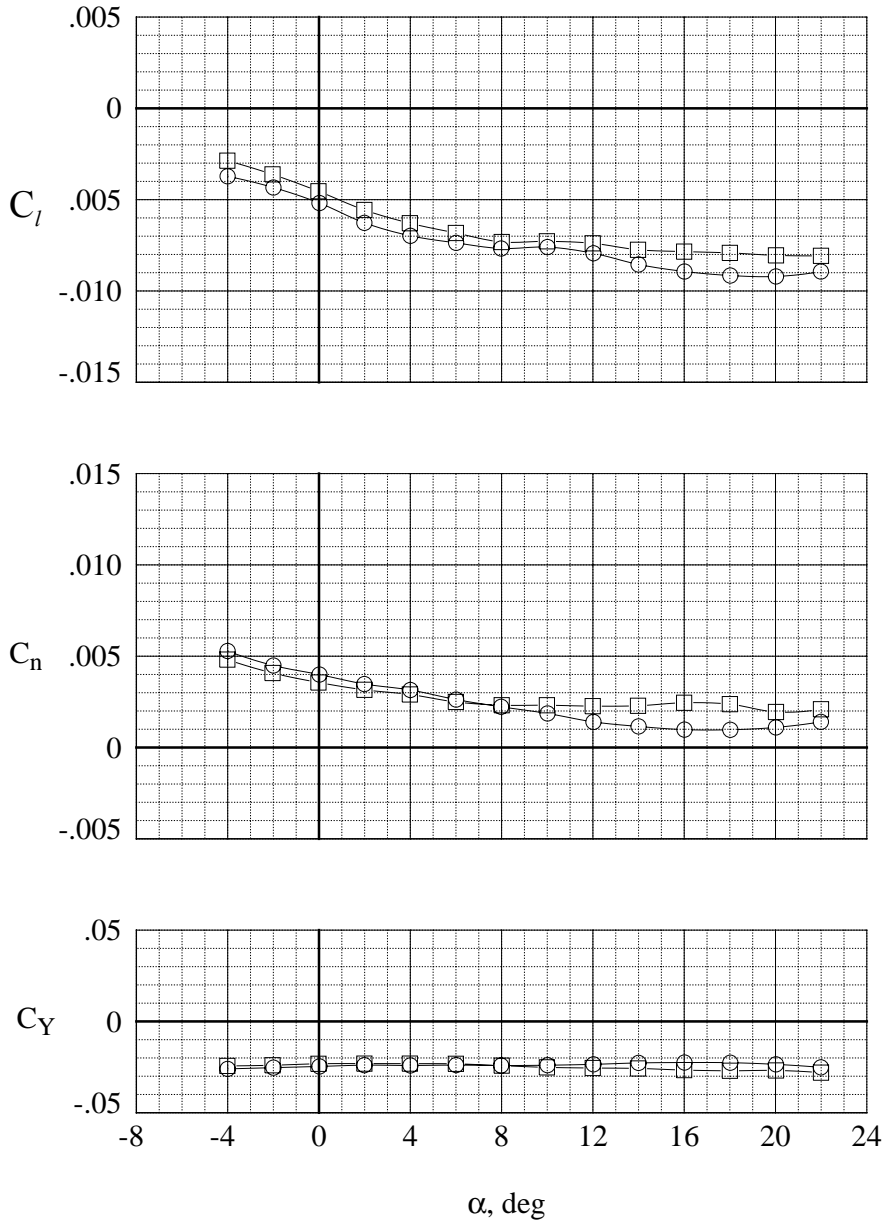
(b) Porous LEX.

Figure 81. Concluded.

REPORT DOCUMENTATION PAGE

Form Approved
OMB No. 0704-0188

1. REPORT DATE *(DD-MM-YYYY)*	2. REPORT TYPE	3. DATES COVERED *(From - To)*
01-10-2007	Technical Memorandum	

4. TITLE AND SUBTITLE

Wind Tunnel Investigation of the Effects of Surface Porosity and Vertical Tail Placement on Slender Wing Vortex Flow Aerodynamics at Supersonic Speeds

5a. CONTRACT NUMBER

5b. GRANT NUMBER

5c. PROGRAM ELEMENT NUMBER

6. AUTHOR(S)

Erickson, Gary E.

5d. PROJECT NUMBER

5e. TASK NUMBER

5f. WORK UNIT NUMBER

136905.02.04.04.01.04

7. PERFORMING ORGANIZATION NAME(S) AND ADDRESS(ES)

NASA Langley Research Center
Hampton, VA 23681-2199

8. PERFORMING ORGANIZATION REPORT NUMBER

L-19401

9. SPONSORING/MONITORING AGENCY NAME(S) AND ADDRESS(ES)

National Aeronautics and Space Administration
Washington, DC 20546-0001

10. SPONSOR/MONITOR'S ACRONYM(S)

NASA

11. SPONSOR/MONITOR'S REPORT NUMBER(S)

NASA/TM-2007-215082

12. DISTRIBUTION/AVAILABILITY STATEMENT

Unclassified - Unlimited
Subject Category 02
Availability: NASA CASI (301) 621-0390

13. SUPPLEMENTARY NOTES

An electronic version can be found at http://ntrs.nasa.gov

14. ABSTRACT

A wind tunnel experiment was conducted in the NASA Langley Research Center (LaRC) Unitary Plan Wind Tunnel (UPWT) to determine the effects of passive surface porosity and vertical tail placement on vortex flow development and interactions about a general research fighter configuration at supersonic speeds. Optical flow measurement and flow visualization techniques were used that featured pressure sensitive paint (PSP), laser vapor screen (LVS), and schlieren. These techniques were combined with conventional electronically-scanned pressure (ESP) and six-component force and moment measurements to quantify and to visualize the effects of flow-through porosity applied to a wing leading-edge extension (LEX) and the placement of centerline and twin vertical tails on the vortex-dominated flow field of a 65-degree cropped delta wing model. Test results were obtained at free-stream Mach numbers of 1.6, 1.8, and 2.1 and a Reynolds number per foot of 2.0 million.

15. SUBJECT TERMS

Aerodynamics; Electronically-scanned pressures; Flow visualization; Forces and moments; Laser vapor screen; Passive porosity; Pressure-sensitive paint; Schlieren; Supersonic; Vortex flows

16. SECURITY CLASSIFICATION OF:

a. REPORT	b. ABSTRACT	c. THIS PAGE	17. LIMITATION OF ABSTRACT	18. NUMBER OF PAGES	19a. NAME OF RESPONSIBLE PERSON
U	U	U	UU	157	STI Help Desk (email: help@sti.nasa.gov)

19a. NAME OF RESPONSIBLE PERSON

STI Help Desk (email: help@sti.nasa.gov)

19b. TELEPHONE NUMBER *(Include area code)*

(301) 621-0390

Standard Form 298 (Rev. 8-98)
Prescribed by ANSI Std. Z39.18